Irradiation de molécules aromatiques hétérocycliques à basse température : le lien avec l'astrochimie

Gabriel Silva Vignoli Muniz

Normandie Université

THESE

Pour obtenir le diplôme de doctorat

Spécialité Physique

Préparée au sein de l'Université de Caen Normandie

Irradiation of aromatic heterocyclic molecules at low temperature : a link to astrochemistry

Présentée et soutenue par
Gabriel SILVA VIGNOLI MUNIZ

Thèse soutenue publiquement le (23 juin 2017) devant le jury composé de		
M. Charles DESFRANÇOIS	Directeur de recherche, LPL - Université Paris 13	Rapporteur
M. Hervé COTTIN	Professeur des universités, LISA - Université Paris-Est Créteil	Rapporteur
M. Thierry CHIAVASSA	Professeur des universités, PIIM – Université Aix -Marseille	Examinateur
M. Giovanni STRAZZULLA	Professeur, INAF – Catania -Italie	Examinateur
Mme Alicja DOMARACKA	Chargé de recherche CNRS,CIMAP	Co-encadrante
M. Philippe BODUCH	Maître de conférences, HDR, Université de Caen Normandie	Directeur de thèse

Thèse dirigée par Philippe BODUCH et Alicja DOMARACKA, laboratoire CIMAP

ED PSIME

UNICAEN
UNIVERSITÉ
CAEN
NORMANDIE

ED 591

CIMAP

List of Figures

List of Tables

List of Equations

List of Appendix

Chapter 1 - Introduction

The aim of this thesis is to explore the radioresistance of aromatic heterocyclic molecules (AHMs) such as nucleobases and pyridine molecules exposed to cosmic ray analogues using the ion beams provided by the accelerator facilities *Grand Accélérateur National d'Ions Lourds* (GANIL-Caen, France) and GSI Helmholtz Center for Heavy Ion Research (GSI-Darmstadt, Germany). Outer space is permeated by corpuscular and electromagnetic radiation and these radiation fields play a key role in the formation and destruction of molecular species. Despite the fact that AHMs have not yet been directly detected in outer space, there is strong evidence of their existence. By irradiating solid samples at temperatures close to those observed in astrophysical environments (typically 10-30 Kelvin) like dense clouds (DCs), interstellar medium (ISM) and the outer solar system, allow to simulate the effects of galactic cosmic rays (CGR) and estimate the survival probability of the complex molecules exposed to the corpuscular radiation.

1.1 Aromatic heterocyclic molecules: nucleobases and pyridine molecules

AHMs are essential for biochemistry. Life, as we know, is impossible without AHMs. In fact, Pullman and Pullman (1962) point out that the most important biomolecules like nucleic acids, proteins and the energy-rich phosphates are conjugated systems or at least present isolated conjugated fragments. It seems that the de-localization of electrons is an important factor for biological systems. Moreover, they claim that this de-localization played an important role in the natural selection of this class of molecules, and point out that all living organisms contain and rely on AHMs. They claim that the electron de-localization leads to higher stability of molecules under UV irradiation and therefore it is an important factor to the natural selection of these molecules in the early Earth permeated

by UV field radiation.

AHMs form important molecules responsible for genetic, energetic, structural and signaling processes. Nucleobases are a class of AHM and compose biomolecules such as deoxyribonucleic acid (DNA) and ribonucleic acid (RNA), known as the nucleic acids. DNA is responsible for storage and transmission of genetic and hereditary information. RNA and DNA are "blueprint" for a number of diverse tasks such as the production of the cell's proteins from the nucleus to the ribosome. Nucleic acids are polymers of nucleotides. Each nucleotide is formed by three units: (1) a sugar (a deoxyribose in DNA and a ribose in RNA), (2) a phosphate group and (3) a nucleobase, see Figure 1.1.

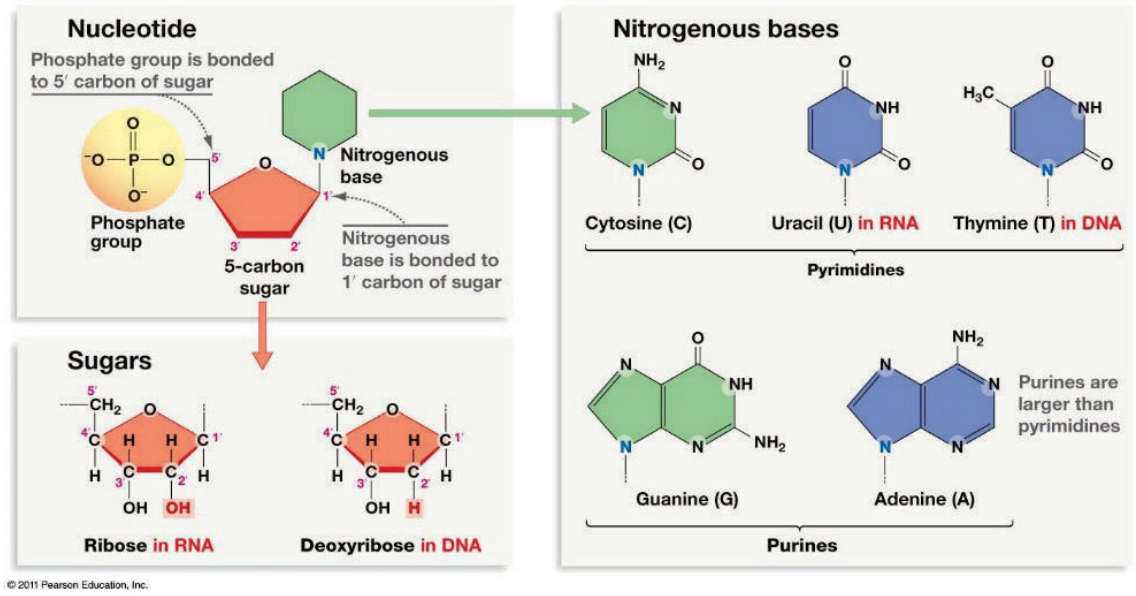

Figure 1.1 – Scheme of nucleotide and the purine and pyrimidine nucleobases present in DNA and RNA. Figure taken from: https://biochemneverland.files.wordpress.com/2014/03/04_01_nucleotide_structure.jpg

The sequence of nucleobases in DNA provides the genetic code. Nucleobases are divided into two groups: purines formed by the union of two heterocyclic rings and pyrimidines constituted by only one heterocyclic ring, see Fig. 1.1. DNA has four different types of nucleobases: adenine ($C_5H_5N_5$), cytosine ($C_4H_4N_3O$), guanine ($C_5H_5N_5O$) and thymine ($C_5H_6N_2O_2$), whereas RNA has the same nucleobases with the exception of thymine

which is replaced by uracil ($C_4H_4N_2O_2$). AHMs are also involved in the production and storage of energy for all living beings. For example, adenosine triphosphate (ATP) fuels the energy used by all cells, since this molecule stores energy in its chemical bonds. The removal of the phosphate group reduces ATP to adenosine diphosphate (ADP) and after that to adenosine monophosphate (AMP) and in turn releases energy for the cell's activities.

Pyridine (C_5H_5N) is also an AHM. This molecule has an electronic density close to benzene (C_6H_6) and in fact, pyridine is a benzene with a C-H group substituted by a nitrogen atom, see Figure 1.2.

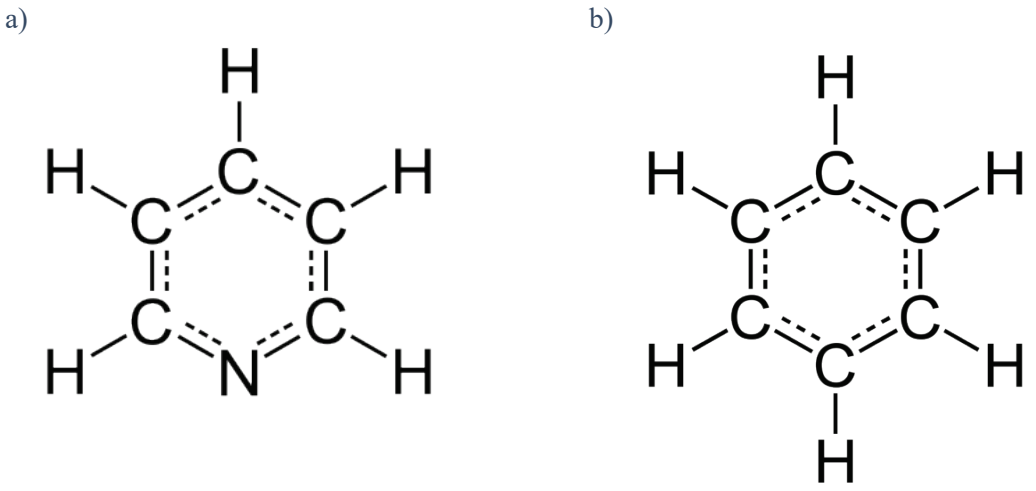

Figure 1.2 - Scheme of pyridine (a) and benzene (b).

Pyridine is part of important coenzymes. A coenzyme is a molecule acting together with an enzyme to catalyze a reaction. Coenzymes are complex organic molecules and can be classified into two groups although, both have the function to assist the reaction of an enzymes and protein. In the prosthetic group, coenzymes are permanently bound to an enzyme. In the cosubstrate group, enzymes are temporarily bound to the enzyme being liberated from the enzyme and later returning to the enzyme. Coenzymes are present in several biochemistry reactions. Present in all living cells, nicotinamide adenine dinucleotide (NAD) is an essential coenzyme within the sequence of chemical reactions

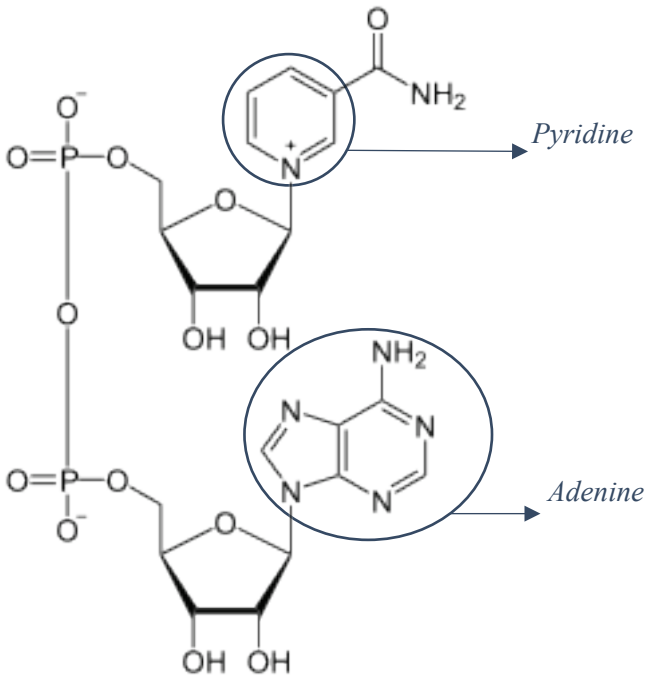

Figure 1.3 – Structure of nicotinamide adenine dinucleotide. Pyridine and adenine molecules are indicated within its general molecular structure.

which produces ATP. This sequence of reactions is known as "respiratory chain". Figure 1.3 displays the scheme of the NAD molecule. Note that the NAD molecule contains a molecule of adenine and of pyridine in its structure. Moreover, pyridine can be absorbed via alimentation in form of nicotid acid, also known as vitamin B3 or PP. Its lack in alimentation can cause several problems and diseases like Pellagra (Shils et al. 2003).

1.2 Formation of complex organic molecules in outer space and under astrophysical conditions

In the 1950s, with the work of Miller and Urey (1953) it became clear that the formation of biomolecules by abiotic processes is possible. Miller and Urey (1953) showed that a mixture of reducing gases (H_2O, NH_3, CH_4 and H_2) exposed to an electrical discharge formed important biomolecules such as amino acids (glycine, α-alanine and β-alanine) and urea. The yield of the production of these complex organic molecules (COMs) were

surprising high. At the time, they believed simulating the early Earth atmosphere, however, analysis of the lithosphere has later shown that the early atmosphere was not reducing. The possibility of formation of COMs under a non-reducing atmosphere was a source of debate. Nowadays, there is a consensus in the scientific community that the formation of these molecules under non-reducing conditions is possible but with smaller yields (Cottin et al. 2015).

It is important to mention that the objective of this chapter is not to do an exhaustive review of different abiotic pathways of formation of biomolecules but simply to highlight selective works which show the possibility of formation of AHMs under astrophysical conditions.

The identification of simple and complex organic molecules in the ISM and in circumstellar envelopes gives support to different hypothesis of life origins. For example, some theories claim that the COMs could have been formed in astrophysical environments later to be delivered to early Earth by comets, meteorites or interplanetary dust particles (Oró 1961; Chyba and Sagan 1992; Love and Brownlee 1993) and leading to the emergence of life. It is important to point out, that although the existence of COMs in different astronomical environments like ISM, DCs, circumstellar envelopes, as well as, in meteorites and comets (Capaccioni et al. 2015; Biver et al. 2015) has been observed. However, the consequences of the bombardment of early Earth by comets and meteorites leading to the emergence of life has yet been established. This topic is recurrently under debate (Cottin et al. 2015).

In contrast to COMs, AHMs have not been detected outside of Earth. Attempts to detect this class of molecules by radio spectroscopy were fruitless (Kuan et al. 2003, 2004), but there is strong evidence of its existence in outer space. For instance, nucleobases and molecules containing pyridine were found in carbonaceous meteorites on Earth. A

possible pollution from the biosphere has been discarded by the isotopic ratio of ^{13}C,^{12}C and H and D, and the amount and structure of the identified material (Shimoyama, Hagishita, and Harada 1990; Martins et al. 2008; Callahan et al. 2011; Smith et al. 2014). Theoretical works show the possibility of formation of AHMs (Roy, Najafian, and von Rague Schleyer 2007; Saladino et al. 2012; Ricca 2001) under astrophysical or early Earth conditions. In addition, experiments mimicking astrophysical conditions have also shown formation of AHMs. Below, some examples will be given of experiments on the formation of COMs from simple molecular species under simulated astrophysical conditions.

The energetic processing of mixtures of ices containing simple organic molecules such as CH_4, NH_3, CO and also more complex molecules detected in the space like methanol and nitriles etc. by electromagnetic radiation (Moore and Hudson 2006; Muñoz Caro et al. 2002; Bernstein et al. 1995, 2002), electrons (Abdulgalil et al. 2013; Kaiser et al. 2013; Jones, Kaiser, and Strazzulla 2014), protons (Hudson et al. 2008; Gerakines, Moore, and Hudson 2004) and heavy ions (Andrade et al. 2014; de Barros 2011a; 2011b) have shown formation of molecules with higher complexity. Recently, Öberg (2016) reviewed the photochemistry of astrophysical ice analogues and also compared the results of photon, electron and ion irradiation of these ices. In this review results of the energetic irradiation of the ices are very similar for different projectiles in terms of formation of complexity of new molecules (e.g. Rothard et al. 2017; Muñoz Caro et al. 2014; Islam, Baratta, and Palumbo 2014). This subject is developed in more detail in Chapters 2 and 7.

Ices composed of mixtures with different proportions of pyrimidine and pure water were irradiated by UV photons (Nuevo et al. 2014, 2009) at low temperature, the analysis of the residues has shown the presence of organic molecules, notably 4(3H)-pyrimidone and uracil. Nuevo et al. (2014) also exposed ice mixtures of ammonia or ammonia-water ice

and pyrimidine at different proportions, at low temperature (~ 15 K) to UV radiation field. They analyzed the obtained residue by using high-performance liquid chromatography and gas chromatography coupled with mass spectrometry. The chromatography experiments exhibited several peaks, however, among them just a few could be assigned to its precursor 4(3H)-pyrimidone and cytosine molecule. Other important biomolecules were also observed like glycine, urea and N-formylglycine. It is important to mention that pyrimidine has been detected in carbonaceous meteorites on Earth (Martins et al. 2008).

Saladino et al. (2016) exposed formamide, an amide already detected in ISM, in the presence of meteorite powders to 363 MeV ^{11}B-(boron) in solid phase (273 K). Using gas chromatography and mass spectrometry (GC-MS) they observed several organic compounds including heterocyclic molecules, among them adenine, guanine, uracil and cytosine. They also detected nucleobase analogues like isocytosine, hypoxanthine and important biomolecules such as pyruvic acid, lactic acid, citric acid. Indeed this beautiful work provides an important clue for the formation of organic compounds in outer space.

Polycyclic aromatic hydrocarbons (PAHs) are a source of carbons in outer space. They are highly abundant, in percentage of about $3 \cdot 10^{-7}$ relative to the number of hydrogen nuclei (Tielens 2008); ISM and circumstellar environments are rich in PAHs (Allamandola, Tielens, and Barker 1989; Ehrenfreund and Cami 2010; Tielens 2008). It has been proposed that the formation of PAHs is due to polymerization of acetylene (Peeters et al. 2005). As already pointed out, AHMs have not yet been detected in outer space. One possible pathway of formation of AHM or polycyclic aromatic nitrogen or oxygen hydrocarbons can be trough energetic processing of ices of PAHs, and water (as source of oxygen) and ammonia (as source of nitrogen). Materese, Nuevo, and Sandford (2015) tested this hypothesis by performing UV irradiation of ices composed of a mixtures of: benzene and water (1:40), water, ammonia and benzene (40:10:1), water and

naphthalene (40:0.2) and water, ammonia and pyridine (40:10:0.2). This work is very interesting because PAHs have already been detected in outer space making the scenario more realistic than those proposed by Nuevo et al. (2014; 2009) and Nuevo, Milam, and Sandford (2012). Using chromatography they observed formation of nitrogen and oxygen heterocycles. To be sure that the oxygen and the nitrogen incorporated in the heterocycles formed by UV irradiation comes from water and ammonia, they used isotopes ^{15}N and ^{18}O. The chromatography experiments showed that the hetero atoms in the heterocyclic compounds undoubtedly originate from the ices used in the experiments. They detected a plethora of new molecules formed from the UV processing, among them pyridine. This experiment shows the possibility that heterocyclic molecules could exist in outer space.

In addition to the possibility of the existence of AHMs in ISM and circumstellar envelope, the formation of these molecules on moons and planets could also be possible. For example, Titan has the only atmosphere in our solar system that is reducing and has a considerable amount of carbon (Hörst et al. 2012; Waite 2005). As observed by (Miller 1953), a reducing atmosphere with carbon reservoir such as (CH_4) (as in Titan's atmosphere) and a source of energy produces COMs like tholins with a high yield. Therefore, the existence of AHMs or biomolecules could be expected. Indeed, molecular ions in the order of hundreds of the atomic mass have been detected in Titan's ionosphere by the Cassini Plasma Spectrometer (CAPS) (Coates et al. 2007; Crary et al. 2009).

Recently, Hörst et al. (2012) produced an aerosol of a mixture of N_2, CH_4 and CO in order to simulate Titan's atmosphere. They used a radio frequency discharge as a source of energy, simulating the energy delivered by solar UV radiation. The discharge produced a dark solid material called tholin (see the pioneering work of Sagan and Khare 1979). Hörst et al. (2012) analyzed the produced tholins and reported the presence of several organic molecules, among them the five nucleobases (adenine, cytosine, guanine, uracil

and thymine) and several amino acids.

The pioneer works of Oró, (1960; 1961) have shown that adenine can be formed under abiotic conditions. In his earlier work, he reported that adenine was formed (0.5 % yield) by a concentrated solution (> 1 mol L^{-1}) of ammonium cyanide (NH_4CN) maintained at 70ºC for several days. With this he demonstrated that adenine can be easily formed through abiosynthesis. Indeed, Ferris, et al. (1978) reported the formation of 4,5-dihydroxypyrimidine, orotic acid, 5-hydroxyuracil, amino acids, 4-aminoimidazole-5-carboxamide and adenine from a diluted solution (0.1 mol L^{-1}) of NH_4CN (pH 9.2) kept in the dark at room temperature between 4 and 12 months. Levy et al. (2000) also reported the formation of adenine, guanine and several amino acids with high concentrations of glycine. Levy, Miller, and Oró (1999) also showed that guanine is produced by the polymerization of NH_4CN but with yields smaller than those reported from the formation of adenine under the same conditions. They also claimed that their results could be a good simulation of frozen regions such as primitive Earth, the Jovian satellite Europa and other icy satellites, and the parent body of the Murchison meteorite.

Moreover, glycine, aliphatic nitriles such as methylamine and ethylamine and phosphorus were detected in the coma of 67P/Churyumov-Gerasimenko (Altwegg et al. 2016). The measurements were done by the ROSINA (Rosetta Orbiter Spectrometer for Ion and Neutral Analysis) *in-situ*, which constitutes an indubitable confirmation of the presence of amino acids and pre-biotic molecules in a comet. Since aliphatic molecules are more radiosensitive than aromatic ones, we can reasonably expect the presence of AHMs in outer space, even if this class of molecules has not yet been detected. In short, the formation of nucleobases (especially adenine) have been shown to occur since the presence of NH_4CN, which is formed by the reaction of NH_3 and HCN. Therefore, the production of nucleobases in astrophysical environments is indeed a realistic scenario.

Therefore, in this thesis, we will assume the presence of nucleobases in astronomical environments.

1.3 Radioresistance of nucleobases and pyridine

Assuming the possibility of the formation and therefore existence of this class of molecules in outer space, it is natural to inquire about radiosensibility, because outer space is permeated by radiation fields which can destroy these molecules. The radioresistance of these molecules can give a clue about their lifetime in outer space and about the possibility of their detection. Furthermore, resistance to ionizing radiation is related to possible survival when travelling in comets and meteorites, and possibly, providing planets with an inventory of biomolecules.

This sub-chapter will give a brief overview of previous works concerning irradiation of nucleobases, the subject is developed further in Chapter 7. In the literature, several authors report work about nucleobases and pyridine radiolysis in the gas phase as isolated molecules or molecular clusters (Alvarado et al. 2007; Schlathölter et al. 2006; Schlathölter, Alvarado, and Hoekstra 2005; Imhoff, Deng, and Huels 2007) and aqueous solution (Improta and Barone 2014; Bahr, Penka, and Lohmann 1979; Abou-Hamdan et al. 2016; Cadet and Wagner 2013; Polverelli and Teoule 1976; Brown and Johns 1968; Ekert and Monier 1960), these experiment revolves around hadron therapy focusing in DNA damage. We also note that those investigations on irradiation of DNA and that of nucleosideos were performed at room temperature (Gromova E. Balanzat B. Gervais R. N 1998; Hüttermann, Schaefer, and Kraft 1989; Gromova, Nardin, and Cadet 1998) However, as these molecules are more complex than simple nucleobases, they will not be discussed in this thesis.

In astrophysical environments, AHMs are expected to existed in the condensed phase at low temperature in a matrix of different elements, notably water, CO_2 and NH_3 (Chakrabarti et al. 2015). As far as we know, only a few experiments were performed under astrophysical conditions: low temperature and solid phase. AHMs at low temperature in a matrix of noble gas (Peeters et al. 2003, 2005) and in the solid phase (thin film or solid samples) (Poch et al. 2014; Pilling et al. 2011; Guan et al. 2010) were exposed to electromagnetic radiation, only Poch et al. (2014) observed new infrared (IR) absorption bands from adenine photodegradation. When the nucleobases are embedded in a noble gas matrix, they exhibit a higher radiosensibilty than in the form of thin film. This finding probably is correlated with the low penetration depth of photons in matter, this is discussed later in Chapter 7. A mixture of pyridine and CO_2 at 14 K was irradiated by Smith et al. (2014) using 0.8 MeV protons, they point out the similarity between the IR spectra of the irradiated pyridine + CO_2 and of the nicotid acid. A solution of uracil was frozen and irradiated by UV photons. Then the residue was dissolved in boiling water and analyzed by IR and UV-visible absorption spectroscopy (Khattak and Wang 1969). Dimerization of the uracil molecules was observed. Solid adenine was exposed to 5 keV electrons by Evans et al. (2011) in order to simulate the effects of protons in adenine at ISM and DCs. They observed new absorption peaks from radiolysis of adenine, see Chapter 7. Huang et al. (2014) exposed solid samples of the four nucleobases (adenine, cytosine, guanine and thymine) to 30 keV Ar^+. They reported a radiosensibility in the following order: thymine < cytosine< guanine< adenine. However, there is no such data about radioresistance of nucleobases at low temperature exposed to swift heavy ions, e.g. cosmic ray analogues. This thesis focuses on heavy ion irradiation : though less than 1% of GCR consists of heavy ions at high energy, it has been shown that their effects on the destruction and formation of new molecules cannot be neglected due to the high cross

sections (e. g. Boduch et al. 2015; Rothard et al. 2017). Some studies have shown that the substrate where nucleobases are adsorbed can play an essential role in their survival to ionizing radiation (Fornaro et al. 2013; Mateo-Martí, Pradier, and Martín-Gago 2009). Therefore, this work is the first study on the resistance of nucleobases in the solid phase to cosmic ray analogues under astrophysical conditions.

References

Abdulgalil, A. G. M., D. Marchione, J. D. Thrower, M. P. Collings, M. R. S. McCoustra, F. Islam, M. E. Palumbo, E. Congiu, and F. Dulieu. 2013. "Laboratory Studies of Electron and Ion Irradiation of Solid Acetonitrile (CH3CN)." *Philosophical Transactions of the Royal Society A: Mathematical, Physical and Engineering Sciences* 371 (1994): 20110586–20110586. doi:10.1098/rsta.2011.0586.

Abou-Hamdan, M., B. Gardette, J. Cadet, B. Gharib, M. De Reggi, T. Douki, and C. Triantaphylides. 2016. "Molecular Hydrogen Attenuates Radiation-Induced Nucleobase Damage to DNA in Aerated Aqueous Solutions." *International Journal of Radiation Biology* 92 (9): 536–41. doi:10.1080/09553002.2016.1206234.

Allamandola, L. J., G. G. M. Tielens, and J. R. Barker. 1989. "Interstellar Polycyclic Aromatic Hydrocarbons - The Infrared Emission Bands, the Excitation/Emission Mechanism, and the Astrophysical Implications." *The Astrophysical Journal Supplement Series* 71 (December): 733. doi:10.1086/191396.

Altwegg, K., H. Balsiger, A. Bar-Nun, J.-J. Berthelier, A. Bieler, P. Bochsler, C. Briois, et al. 2016. "Prebiotic Chemicals--Amino Acid and Phosphorus--in the Coma of Comet 67P/Churyumov-Gerasimenko." *Science Advances* 2 (5): e1600285–e1600285. doi:10.1126/sciadv.1600285.

Alvarado, F., S. Bari, R. Hoekstra, and T. Schlathölter. 2007. "Interactions of Neutral and Singly Charged keV Atomic Particles with Gas-Phase Adenine Molecules." *The Journal of Chemical Physics* 127 (3): 034301. doi:10.1063/1.2751502.

Andrade, D. P. P., A. L. F. de Barros, J. Ding, H. Rothard, P. Boduch, and E. F. da Silveira. 2014. "Acetone Degradation by Cosmic Rays in the Solar Neighbourhood and in the Galactic Centre." *Monthly Notices of the Royal Astronomical Society* 444 (4): 3792–3801. doi:10.1093/mnras/stu1519.

Bahr, A., V. Penka, and W. Lohmann. 1979. “Modification of the Radiation Effect on Nucleobases and Nucleosides by Nitroimidazole-Derivatives and Ascorbic Acid.” In *Annual Meeting of the Deutsche Gesellschaft Für Biophysik*, edited by Gerold Adam and Günther Stark, 20–20. Berlin, Heidelberg: Springer Berlin Heidelberg. doi:10.1007/978-3-642-51881-2_19.

Barros, A. L. F. de, A. Domaracka, D. P. P. Andrade, P. Boduch, H. Rothard, and E. F. da Silveira. 2011. “Radiolysis of Frozen Methanol by Heavy Cosmic Ray and Energetic Solar Particle Analogues: Radiolysis of Frozen Methanol by Heavy Cosmic Ray and Energetic Solar Particle Analogues.” *Monthly Notices of the Royal Astronomical Society* 418 (2): 1363–74. doi:10.1111/j.1365-2966.2011.19587.x.

Barros, A.L.F. de, E. Seperuelo Duarte, L.S. Farenzena, E.F. da Silveira, A. Domaracka, H. Rothard, and P. Boduch. 2011. “Destruction of CO Ice and Formation of New Molecules by Irradiation with 28keV O^{6+} Ions.” *Nuclear Instruments and Methods in Physics Research Section B: Beam Interactions with Materials and Atoms* 269 (9): 852–55. doi:10.1016/j.nimb.2010.12.055.

Bernstein, M. P., J. P. Dworkin, S. A. Sandford, G. W. Cooper, and L. J. Allamandola. 2002. “Racemic Amino Acids from the Ultraviolet Photolysis of Interstellar Ice Analogues.” *Nature* 416 (6879): 401–3. doi:10.1038/416401a.

Bernstein, M. P., S. A. Sandford, L. J. Allamandola, S. Chang, and M. A. Scharberg. 1995. “Organic Compounds Produced by Photolysis of Realistic Interstellar and Cometary Ice Analogs Containing Methanol.” *The Astrophysical Journal* 454 (November): 327. doi:10.1086/176485.

Biver, N., D. Bockelee-Morvan, R. Moreno, J. Crovisier, P. Colom, D. C. Lis, A. Sandqvist, J. Boissier, D. Despois, and S. N. Milam. 2015. “Ethyl Alcohol and Sugar in Comet C/2014 Q2 (Lovejoy).” *Science Advances* 1 (9): e1500863–e1500863. doi:10.1126/sciadv.1500863.

Boduch, P., E. Dartois, A. L. F. de Barros, E. F. da Silveira, A. Domaracka, X.-Y. Lv, M. E. Palumbo, et al. 2015. “Radiation Effects in Astrophysical Ices.” *Journal of Physics: Conference Series* 629 (July): 012008. doi:10.1088/1742-6596/629/1/012008.

Brown, I. H., and H. E. Johns. 1968. “Photochemistry of uracil. intersystem crossing and dimerization in aqueous solution.” *Photochemistry and Photobiology* 8 (4): 273–86. doi:10.1111/j.1751-1097.1968.tb05871.x.

Cadet, J., and J. R. Wagner. 2013. “DNA Base Damage by Reactive Oxygen Species, Oxidizing Agents, and UV Radiation.” *Cold Spring Harbor Perspectives in Biology* 5 (2): a012559–a012559. doi:10.1101/cshperspect.a012559.

Callahan, M. P., K. E. Smith, H. J. Cleaves, J. Ruzicka, J. C. Stern, D. P. Glavin, C. H. House, and J. P. Dworkin. 2011. “Carbonaceous Meteorites Contain a Wide Range of Extraterrestrial Nucleobases.” *Proceedings of the National Academy of Sciences* 108 (34): 13995–98. doi:10.1073/pnas.1106493108.

Capaccioni, F., A. Coradini, G. Filacchione, S. Erard, G. Arnold, P. Drossart, M. C. De Sanctis, et al. 2015. “The Organic-Rich Surface of Comet 67P/Churyumov-Gerasimenko as Seen by VIRTIS/Rosetta.” *Science* 347 (6220): aaa0628-aaa0628. doi:10.1126/science.aaa0628.

Chakrabarti, S. K., L. Majumdar, A. Das, and S. Chakrabarti. 2015. “Search for Interstellar Adenine.” *Astrophysics and Space Science* 357 (1). doi:10.1007/s10509-015-2239-1.

Chyba, C., and C. Sagan. 1992. “Endogenous Production, Exogenous Delivery and Impact-Shock Synthesis of Organic Molecules: An Inventory for the Origins of Life.” *Nature* 355 (6356): 125–32. doi:10.1038/355125a0.

Coates, A. J., F. J. Crary, G. R. Lewis, D. T. Young, J. H. Waite, and E. C. Sittler. 2007. “Discovery of Heavy Negative Ions in Titan’s Ionosphere.” *Geophysical Research Letters* 34 (22). doi:10.1029/2007GL030978.

Cottin, H., J. M. Kotler, K. Bartik, H. J. Cleaves, C. S. Cockell, J.-P. P. de Vera, P. Ehrenfreund, et al. 2015. “Astrobiology and the Possibility of Life on Earth and Elsewhere….” *Space Science Reviews*, September. doi:10.1007/s11214-015-0196-1.

Crary, F.J., B.A. Magee, K. Mandt, J.H. Waite, J. Westlake, and D.T. Young. 2009. “Heavy Ions, Temperatures and Winds in Titan’s Ionosphere: Combined Cassini CAPS and INMS Observations.” *Planetary and Space Science* 57 (14–15): 1847–56. doi:10.1016/j.pss.2009.09.006.

Ehrenfreund, P., and J. Cami. 2010. “Cosmic Carbon Chemistry: From the Interstellar Medium to the Early Earth.” *Cold Spring Harbor Perspectives in Biology* 2 (12): a002097–a002097. doi:10.1101/cshperspect.a002097.

Ekert, B., and R. Monier. 1960. “Effect of X-Rays on Cytosine in Aerated Aqueous Solution.” *Nature* 188 (4747): 309–10. doi:10.1038/188309a0.

Evans, N. L., C. J. Bennett, S. Ullrich, and R. I. Kaiser. 2011. “On the interaction of adenine with ionizing radiation: mechanistical studies and astrobiological implications.” *The Astrophysical Journal* 730 (2): 69. doi:10.1088/0004-637X/730/2/69.

Ferris, JP., Joshi, PC., Edelson, EH., and Lawless, JG. 1978. “HCN: A Plausible Source of Purines, Pyrimidines and Amino Acids on the Primitive Earth.” *J Mol Evol.* 11 (4): 293–311.

Fornaro, T., J. R. Brucato, E. Pace, M. C. Guidi, S. Branciamore, and A. Pucci. 2013. “Infrared Spectral Investigations of UV Irradiated Nucleobases Adsorbed on Mineral Surfaces.” *Icarus* 226 (1): 1068–85. doi:10.1016/j.icarus.2013.07.024.

Gerakines, P.A., M.H. Moore, and R.L. Hudson. 2004. “Ultraviolet Photolysis and Proton Irradiation of Astrophysical Ice Analogs Containing Hydrogen Cyanide.” *Icarus* 170 (1): 202–13. doi:10.1016/j.icarus.2004.02.005.

Gromova E., Balanzat B., Gervais R. N, M. 1998. “The Direct Effect of Heavy Ions and Electrons on Thymidine in the Solid State.” *International Journal of Radiation Biology* 74 (1): 81–97. doi:10.1080/095530098141753.

Gromova, M., R. Nardin, and J. Cadet. 1998. “Direct Effect of Heavy Ions and Electrons on 2′-Deoxyguanosine in the Solid State.” *Journal of the Chemical Society, Perkin Transactions 2*, no. 6: 1365–74. doi:10.1039/a801069b.

Guan, Y. Y., N. Fray, P. Coll, F. Macari, D. Chaput, F. Raulin, and H. Cottin. 2010. "UVolution: Compared Photochemistry of Prebiotic Organic Compounds in Low Earth Orbit and in the Laboratory." *Planetary and Space Science* 58 (10): 1327–46. doi:10.1016/j.pss.2010.05.017.

Hörst, S.M., R.V. Yelle, A. Buch, N. Carrasco, G. Cernogora, O. Dutuit, E. Quirico, et al. 2012. "Formation of Amino Acids and Nucleotide Bases in a Titan Atmosphere Simulation Experiment." *Astrobiology* 12 (9): 809–17. doi:10.1089/ast.2011.0623.

Huang, Q., X. Su, G. Yao, Y. Lu, Z. Ke, J. Liu, Y. Wu, and Z. Yu. 2014. "Quantitative Assessment of the Ion-Beam Irradiation Induced Direct Damage of Nucleic Acid Bases through FTIR Spectroscopy." *Nuclear Instruments and Methods in Physics Research Section B: Beam Interactions with Materials and Atoms* 330 (July): 47–54. doi:10.1016/j.nimb.2014.03.012.

Hudson, R. L., M. H. Moore, J. P. Dworkin, M. P. Martin, and Z. D. Pozun. 2008. "Amino Acids from Ion-Irradiated Nitrile-Containing Ices." *Astrobiology* 8 (4): 771–79. doi:10.1089/ast.2007.0131.

Hüttermann, J., A. Schaefer, and G. Kraft. 1989. "Free Radicals Induced in Solid DNA by Heavy Ion Bombardment." *Advances in Space Research* 9 (10): 35–44. doi:10.1016/0273-1177(89)90421-3.

Imhoff, M., Z. Deng, and M. A. Huels. 2007. "Ionizing Fragmentation of Uracil and 5-Bromouracil by Electron Impact in Gas Phase and Hyperthermal Ar+ Ion Irradiation in Condensed Phase." *International Journal of Mass Spectrometry* 262 (1–2): 154–60. doi:10.1016/j.ijms.2006.11.004.

Improta, R., and V. Barone. 2014. "Excited States Behavior of Nucleobases in Solution: Insights from Computational Studies." In *Photoinduced Phenomena in Nucleic Acids I*, edited by Mario Barbatti, Antonio Carlos Borin, and Susanne Ullrich, 355:329–57. Cham: Springer International Publishing. doi:10.1007/128_2013_524.

Islam, F., G. A. Baratta, and M. E. Palumbo. 2014. "Simultaneous UV- and Ion Processing of Astrophysically Relevant Ices: The Case of CH_3OH:N_2 Solid Mixtures." *Astronomy & Astrophysics* 561 (January): A73. doi:10.1051/0004-6361/201322010.

Jones, B. M., R. I. Kaiser, and G. Strazzulla. 2014. “Uv-vis, infrared, and mass spectroscopy of electron irradiated frozen oxygen and carbon dioxide mixtures with water.” *The Astrophysical Journal* 781 (2): 85. doi:10.1088/0004-637X/781/2/85.

Kaiser, R. I., A. M. Stockton, Y. S. Kim, E. C. Jensen, and R. A. Mathies. 2013. “On the formation of dipeptides in interstellar model ices.” *The Astrophysical Journal* 765 (2): 111. doi:10.1088/0004-637X/765/2/111.

Khattak, M. N., and S. Y. Wang. 1969. “Uracil Photoproducts from Uracil Irradiated in Ice.” *Science* 163 (3873): 1341–42. doi:10.1126/science.163.3873.1341.

Kuan, Y.-J., S. B. Charnley, H.-C. Huang, Z. Kisiel, P. Ehrenfreund, W.-L. Tseng, and C.-H. Yan. 2004. “Searches for Interstellar Molecules of Potential Prebiotic Importance.” *Advances in Space Research* 33 (1): 31–39. doi:10.1016/j.asr.2003.04.004.

Kuan, Y.-J., C.-H. Yan, S. B. Charnley, Z. Kisiel, P. Ehrenfreund, and H.-C. Huang. 2003. “A Search for Interstellar Pyrimidine.” *Monthly Notices of the Royal Astronomical Society* 345 (2): 650–56. doi:10.1046/j.1365-8711.2003.06975.x.

Levy, M., S. L. Miller, and J. Oró. 1999. “Production of Guanine from NH_4CN Polymerizations.” *Journal of Molecular Evolution* 49 (2): 165–68. doi:10.1007/PL00006539.

Love, S. G., and D. E. Brownlee. 1993. “A Direct Measurement of the Terrestrial Mass Accretion Rate of Cosmic Dust.” *Science* 262 (5133): 550–53. doi:10.1126/science.262.5133.550.

Martins, Z., O. Botta, M. L. Fogel, M. A. Sephton, D. P. Glavin, J. S. Watson, J. P. Dworkin, A. W. Schwartz, and P. Ehrenfreund. 2008. “Extraterrestrial Nucleobases in the Murchison Meteorite.” *Earth and Planetary Science Letters* 270 (1–2): 130–36. doi:10.1016/j.epsl.2008.03.026.

Mateo-Martí, E., C.-M. Pradier, and J.-A. Martín-Gago. 2009. “Ultraviolet Photostability of Adenine on Gold and Silicon Surfaces.” *Astrobiology* 9 (6): 573–79. doi:10.1089/ast.2008.0317.

Materese, C. K., M. Nuevo, and S. A. Sandford. 2015. "*N* - AND *O* -heterocycles produced from the irradiation of benzene and naphthalene in H_2O/NH_3 -containing ices." *The Astrophysical Journal* 800 (2): 116. doi:10.1088/0004-637X/800/2/116.

Miller, S. L. 1953. "A Production of Amino Acids Under Possible Primitive Earth Conditions." *Science* 117 (3046): 528–29. doi:10.1126/science.117.3046.528.

Levy, M.., S. L. Miller, K. Brinton, and J.L. Bada. 2000. "Prebiotic Synthesis of Adenine and Amino Acids Under Europa-like Conditions." *Icarus* 145 (2): 609–13. doi:10.1006/icar.2000.6365.

Moore, M. H., and R. L. Hudson. 2006. "Production of Complex Molecules in Astrophysical Ices." *Proceedings of the International Astronomical Union* 1 (S231): 247. doi:10.1017/S1743921306007241.

Muñoz Caro, G. M., E. Dartois, P. Boduch, H. Rothard, A. Domaracka, and A. Jiménez-Escobar. 2014. "Comparison of UV and High-Energy Ion Irradiation of Methanol:ammonia Ice." *Astronomy & Astrophysics* 566 (June): A93. doi:10.1051/0004-6361/201322983.

Muñoz Caro, G. M., U. J. Meierhenrich, W. A. Schutte, B. Barbier, A. Arcones Segovia, H. Rosenbauer, W. H.-P. Thiemann, A. Brack, and J. M. Greenberg. 2002. "Amino Acids from Ultraviolet Irradiation of Interstellar Ice Analogues." *Nature* 416 (6879): 403–6. doi:10.1038/416403a.

Nuevo, M., Y.-J. Chen, W.-J. Hu, J.-M. Qiu, S.-R. Wu, H.-S. Fung, C.-C. Chu, T.-S. Yih, W.-H. Ip, and C.-Y. R. Wu. 2014. "Irradiation of Pyrimidine in Pure H_2O Ice with High-Energy Ultraviolet Photons." *Astrobiology* 14 (2): 119–31. doi:10.1089/ast.2013.1093.

Nuevo, M., S. N. Milam, and S. A. Sandford. 2012. "Nucleobases and Prebiotic Molecules in Or ganic Residues Produced from the Ultraviolet Photo-Irradiation of Pyrimidine in NH_3 and $H_2O + NH_3$ Ices." *Astrobiology* 12 (4): 295–314. doi:10.1089/ast.2011.0726.

Nuevo, M., S. N. Milam, S. A. S., J. E. Elsila, and J. P. Dworkin. 2009. "Formation of Uracil from the Ultraviolet Photo-Irradiation of Pyrimidine in Pure H_2O Ices." *Astrobiology* 9 (7): 683–95. doi:10.1089/ast.2008.0324.

Öberg, K. I. 2016. “Photochemistry and Astrochemistry: Photochemical Pathways to Interstellar Complex Organic Molecules.” *Chemical Reviews* 116 (17): 9631–63. doi:10.1021/acs.chemrev.5b00694.

Oró, J. 1960. “Synthesis of Adenine from Ammonium Cyanide.” *Biochem. Biophys. Res. Commun.* 2: 407–12.

Oró, J. 1961. “Comets and the Formation of Biochemical Compounds on the Primitive Earth.” *Nature* 190 (4774): 389–90. doi:10.1038/190389a0.

Peeters, Z., O. Botta, S. B. Charnley, Z. Kisiel, Y.-J. Kuan, and P. Ehrenfreund. 2005. “Formation and Photostability of N-Heterocycles in Space: I. The Effect of Nitrogen on the Photostability of Small Aromatic Molecules.” *Astronomy and Astrophysics* 433 (2): 583–90. doi:10.1051/0004-6361:20042443.

Peeters, Z., O. Botta, S. B. Charnley, R. Ruiterkamp, and P. Ehrenfreund. 2003. “The Astrobiology of Nucleobases.” *The Astrophysical Journal* 593 (2): L129–32. doi:10.1086/378346.

Pilling, S., D. P. P. Andrade, E. M. do Nascimento, R. R. T. Marinho, H. M. Boechat-Roberty, L. H. de Coutinho, G. G. B. de Souza, et al. 2011. “Photostability of Gas- and Solid-Phase Biomolecules within Dense Molecular Clouds due to Soft X-Rays: Photostability of Biomolecules in ISM.” *Monthly Notices of the Royal Astronomical Society* 411 (4): 2214–22. doi:10.1111/j.1365-2966.2010.17840.x.

Poch, O., S. Kaci, F. Stalport, C. Szopa, and P. Coll. 2014. “Laboratory Insights into the Chemical and Kinetic Evolution of Several Organic Molecules under Simulated Mars Surface UV Radiation Conditions.” *Icarus* 242 (November): 50–63. doi:10.1016/j.icarus.2014.07.014.

Polverelli, M., and R. Teoule. 1976. “ChemInform Abstract: γ-Radiolysis of Aerated Aqueous Solution of Cytosine. Part 3. Identification of Two Radiolysis Products: 1-Carbamoyl-5-hydroxyhydantoin and N-Formylbiuret.” *Chemischer Informationsdienst* 7 (35): no-no. doi:10.1002/chin.197635082.

Pullman, B., and A. Pullman. 1962. “Electronic Delocalization and Biochemical Evolution.” *Nature* 196 (4860): 1137–42. doi:10.1038/1961137a0.

Ricca, A. 2001. “A Computational Study of the Mechanisms for the Incorporation of a Nitrogen Atom into Polycyclic Aromatic Hydrocarbons in the Titan Haze.” *Icarus* 154 (2): 516–21. doi:10.1006/icar.2001.6694.

Rothard, H., A. Domaracka, P. Boduch, M. E. Palumbo, G. Strazzulla, E. F. da Silveira, and E. Dartois. 2017. “Modification of Ices by Cosmic Rays and Solar Wind.” *Journal of Physics B: Atomic, Molecular and Optical Physics* 50 (6): 062001. doi:10.1088/1361-6455/50/6/062001.

Roy, D., K. Najafian, and P. von Rague Schleyer. 2007. “Chemical Evolution: The Mechanism of the Formation of Adenine under Prebiotic Conditions.” *Proceedings of the National Academy of Sciences* 104 (44): 17272–77. doi:10.1073/pnas.0708434104.

Sagan, C., and B. N. Khare. 1979. “Tholins: Organic Chemistry of Interstellar Grains and Gas.” *Nature* 277 (5692): 102–7. doi:10.1038/277102a0.

Saladino, R., E. Carota, G. Botta, M. Kapralov, G. N. Timoshenko, A. Rozanov, E. Krasavin, and E. Di Mauro. 2016. “First Evidence on the Role of Heavy Ion Irradiation of Meteorites and Formamide in the Origin of Biomolecules.” *Origins of Life and Evolution of Biospheres*, April. doi:10.1007/s11084-016-9495-0.

Saladino, R., C. Crestini, S. Pino, G. Costanzo, and E. Di Mauro. 2012. “Formamide and the Origin of Life.” *Physics of Life Reviews* 9 (1): 84–104. doi:10.1016/j.plrev.2011.12.002.

Schlathölter, T., F. Alvarado, and R. Hoekstra. 2005. “Ion–biomolecule Interactions and Radiation Damage.” *Nuclear Instruments and Methods in Physics Research Section B: Beam Interactions with Materials and Atoms* 233 (1–4): 62–69. doi:10.1016/j.nimb.2005.03.087.

Schlathölter, T., F. Alvarado, S. Bari, and R. Hoekstra. 2006. “Ion-Induced Ionization and Fragmentation of DNA Building Blocks.” *Physica Scripta* 73 (4): C113–17. doi:10.1088/0031-8949/73/4/N01.

Shils, M. E., and ed. 2003. *Tratado de nutriçao moderna na saude e na doença*. Barueri, SP: Manole.

Shimoyama, A., S. Hagishita, and K. Harada. 1990. “Search for Nucleic Acid Bases in Carbonaceous Chondrites from Antarctica.” *GEOCHEMICAL JOURNAL* 24 (5): 343–48. doi:10.2343/geochemj.24.343.

Smith, K. E., M. P. Callahan, P. A. Gerakines, J. P. Dworkin, and C. H. House. 2014. “Investigation of Pyridine Carboxylic Acids in CM2 Carbonaceous Chondrites: Potential Precursor Molecules for Ancient Coenzymes.” *Geochimica et Cosmochimica Acta* 136 (July): 1–12. doi:10.1016/j.gca.2014.04.001.

Tielens, A.G.G.M. 2008. “Interstellar Polycyclic Aromatic Hydrocarbon Molecules.” *Annual Review of Astronomy and Astrophysics* 46 (1): 289–337. doi:10.1146/annurev.astro.46.060407.145211.

Waite, J. H. 2005. “Ion Neutral Mass Spectrometer Results from the First Flyby of Titan.” *Science* 308 (5724): 982–86. doi:10.1126/science.1110652.

Chapter 2 - Galactic cosmic rays, solar wind and interaction of ionizing radiation with matter

In the previous chapter, we discussed the possibility of the existence of AHMs in outer space. Also, we pointed out that ionizing radiation can have damaging effects on these molecules. In this chapter, we will present a short overview about ionizing radiations which are present in astrophysical environments. We will focus our attention on corpuscular radiation that hereafter we divide into two categories: galactic cosmic rays (CGRs) and solar wind (SW). We will also briefly talk about electromagnetic radiation fields omnipresent in astronomical environments. Similarities and differences of the process of energy deposition in matter by GCRs, SW and electromagnetic radiation will be also presented.

2.1 – Corpuscular radiation – ions in outer space

Space is permeated by radiation from different sources. Electromagnetic radiation includes ultra-violet (UV) photons, X-rays, and the non-ionizing 2.7 K cosmic microwave background. Furthermore, there is corpuscular radiation: electrons, positrons, nuclei and other massive particles. In ISM and dense clouds (DCs) the dominating corpuscular radiation are nuclei from neighboring stars and from remnants of supernova explosions. Galactic cosmic rays (GCRs) are corpuscular radiation with extraterrestrial origin and with an energy range of few MeV per nucleon to several GeV per nucleon. CRGs are composed almost exclusively by nuclei, only 2% are electrons or positrons. Among these nuclei, protons are the most abundant (~89%), followed by alpha particles (~10%) and heavy ions (~1%). The GCRs interact with ISM hydrogen and helium, this strips off their

electrons increasing their charge state (Spurio 2014; Lave 2012)

Solar or stellar wind, i.e., the outer part of the solar or stellar corona, is in continuous expansion. In the case of our Sun, the expansion of its corona fills the interplanetary medium with plasma consisting of ionized atoms and electrons with energies ranging from a few keV per nucleon to few hundreds of keV. Space affected by the solar wind is known as the heliosphere, we will come back to this subject in sub-section 2.2.

Note that GCRs are orders of magnitude more energetic than solar wind. Typically SW are within a range of energy of a few keV per nucleon, whereas GCRs have energies of a few MeV/n to TeV/n. Therefore, the interaction between solar wind particles and matter may differ from that of GCR. The most energetic particles will interact via inelastic collisions with the electrons of the targets provoking excitations and ionizations, while the less energetic particles interact via elastic collisions with the target nuclei, we will discuss this processes in section 2.3.

2.1.1 Galactic cosmic rays

The origin of GCRs is still a theme of debate in the literature, but it has been accepted by the academic community that GCRs are remnants from supernova explosions (Biermann *et al*. 2010). Their flux is under steady-state conditions and GCRs are isotropic due to the deflections and scattering by the magnetic fields in the galaxy (Lave 2012). GCRs are classified into two different categories: primary and secondary GCRs. The primary GCRs are those produced and accelerated at astrophysical sources. Secondary GCRs are the product of the nuclear fragmentation of heavy ions colliding with gas in the ISM, this phenomenon is known as spallation. It is observed that there is a similar pattern between the relative abundance of elements in GCRs and in the Solar System (Drury, Ellison, and

Meyer 2000). In CGRs notably light elements such as Li, Be, B; and some heavy species like scandium, titanium and vanadium are a few exceptions that do not follow this pattern of relative abundance. The abundance of these elements is too small and therefore not taken into consideration in this thesis. Table 2.1 displays the relative abundances of the ten most abundant ions that compose GCRs, their relative abundance in the solar system is also included.

Table 2.1 – Relative abundance of the ten more abundant elements in the GCRs, its abundance in the solar wind is also included. Data adapted from Drury, Ellison, and Meyer (2000).

Element	Relative abundance GCRs	Relative solar wind
H	1.0×10^{6}	1.0×10^{6}
He	6.3×10^{4}	2.0×10^{5}
C	2.5×10^{3}	2.5×10^{2}
O	3.1×10^{3}	6.3×10^{2}
Mg	6.3×10^{2}	4.0×10^{1}
Si	6.3×10^{2}	4.0×10^{1}
Fe	6.3×10^{2}	3.2×10^{1}
S	8.0×10^{1}	1.6×10^{1}
Al	5.0×10^{1}	3.1×10^{0}
Ca	4.0×10^{1}	2.0×10^{0}

The differential flux of GCRs (i.e., the number of incoming particles at a given energy interval, per unit of time, per unit of area and per solid angle) follows a power law as a function of the specific energy. This quantity hereafter is called energy spectrum, $\Phi(E, Z)$. At energies bellow 10^{15} eV per nucleon the spectrum of CGRs strongly decreases with the energy $\Phi(E, Z) \sim E^{-2.7}$. At energies of about 5×10^{15} eV, there is a deformation in the spectrum known as “knee”, and at energies of about 3×10^{17} eV the spectrum dips slightly, this is known as a second “knee” (Fig.2.1). Within the ranges of energies between the first “knee” and energies up to 10^{18} eV, $\Phi(E, Z)$ roughly follows the power law:

$\Phi(E, Z) \sim E^{-3.0}$. A second deformation in the spectrum occurs even at higher energies (up to 10^{18} eV) and it is known as "ankle". GCRs at energies up to 10^{19} eV are difficult to observe from Earth because they interact with the 2.7 K cosmic microwave background radiation. This effect is known as the Greisen-Zatsepin-Kuzmin (GZK) cutoff (Šmída, 2009). As discussed above the flux of cosmic rays strongly depends on the energy. Table 2.2 displays the approximate of energies.

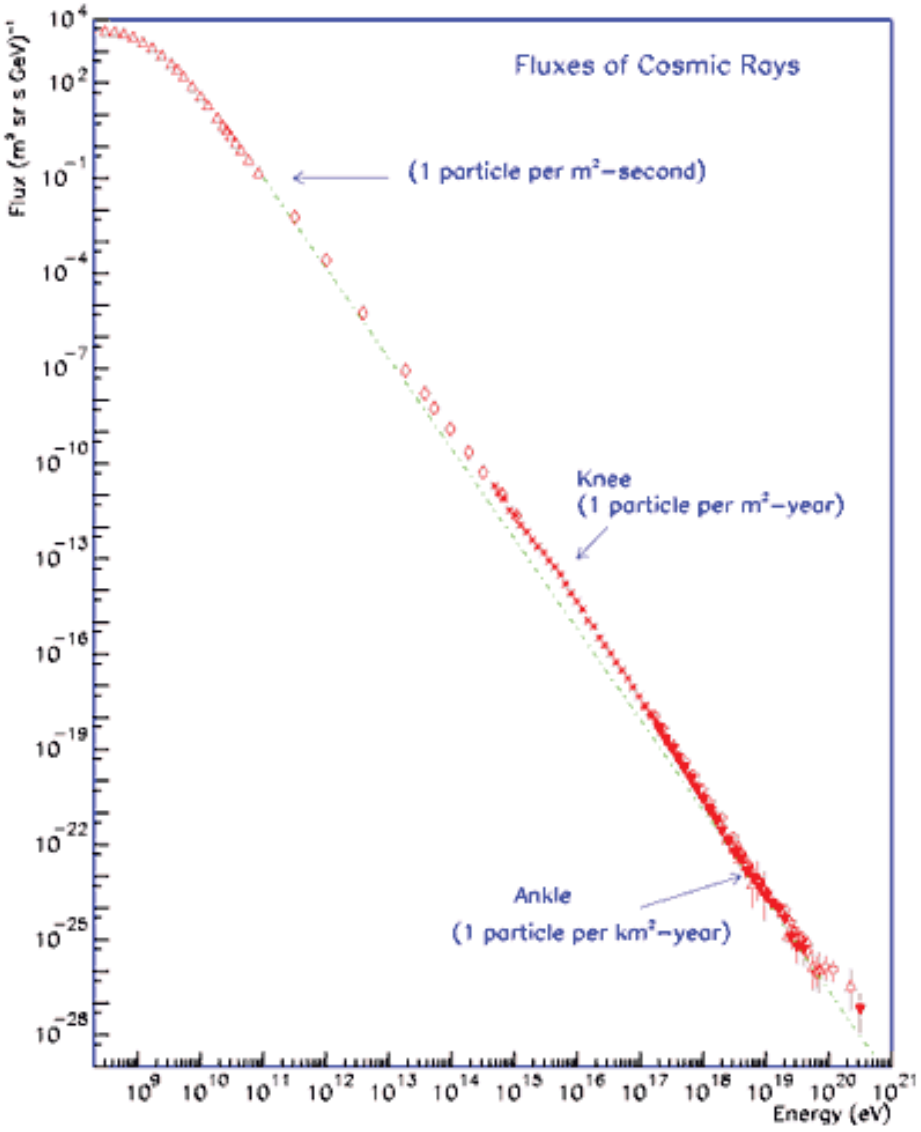

Figure 2.1 – Energy spectrum of GCRs made by a compilation of several experiments. This figure is adapted by W. Hanlon (https://www.physics.utah.edu/~whanlon/spectrum.html)

Table 2.2 – The approximate flux of GCRs within different ranges of energy.

Energy range	Flux
$>10^3$ MeV	1000 particles s^{-1} m^{-2}
$>10^{12}$ MeV	1 particle $year^{-1}$ m^{-2}
$>10^{14}$ MeV	1 particle $century^{-1}$ km^{-2}

In this thesis, we will focus our attention on GCRs in the energy ranges from 10^{-1} to 10^3 MeV per nucleon, because the flux is more abundant in this interval of energy. Also the loss of energy is due to interactions with the target electrons (electronic stopping power domain), more details see section 2.2 and Chapter 6.

The determination of a GCRs' spectrum is performed by using satellites, balloon-borne detectors, ground detectors and space probes. All these measurements were done inside the heliosphere (Cooper et al. 2003; Padovani and Galli 2013). The solar magnetic field and winds affect the incoming GCRs, specially the particles at low energies which can be expelled from the heliosphere by solar winds and planetary magnetic fields. The spectra of cosmic rays observed from Earth or inside the heliosphere are therefore modulated and hence the deduced flux of cosmic rays is full of uncertainties, especially at low energies (Padovani and Galli, 2013; Shen *et al*., 2004). A more accurate spectrum of GCRs may possibly be obtained when the spacecrafts Pioneer and Voyager will have left the heliosphere.

Webber and Yushak (1983) using the data from a meteorological balloon and the *Voyager* data showed that the spectrum of GCRs $\Phi(E, Z)$ can be described by

Eq. 2.1 $$\Phi(E, Z) = \frac{C(Z)\, E^{0.3}}{(E+E_0)^3}$$

Here C (Z) is a normalization constant, which is proportional to the ion abundance in ISM. The numerical values of the constant C,(Z) can be found in the Appendix **(Appx. 1).**

E_0 is a parameter that modifies the flux at low energy but does not have an impact at high energies. In the model proposed by Webber and Yushak (1983), it represents the solar modulation and assumes values between 0 and 940 MeV. According to Shen et al. (2004), E_0 = 400 MeV per nucleon is the most accurate value to simulate the observed cosmic ray ionization rates of ISM and DCs. As an example, using equation 2.1 we plotted the differential flux of H, O and Fe ions in ISM.

Dartois *et al* (2013) showed that, although equation 2.1 is just an estimation of the flux of cosmic rays, with different values of the parameter E_0 (200, 400 and 600 MeV/n), it is possible to evaluate cosmic ray ionization rates of hydrogen, which are in agreement with astronomical observations (Indriolo et al. 2007). Following this procedure, we adopted different values of the parameter E_0 (200, 400 and 600 MeV/n) to simulate the CGR differential flux. As an example, we plotted the iron flux in the cosmic rays using the three different values of the parameter E_0 in Figure 2.2.

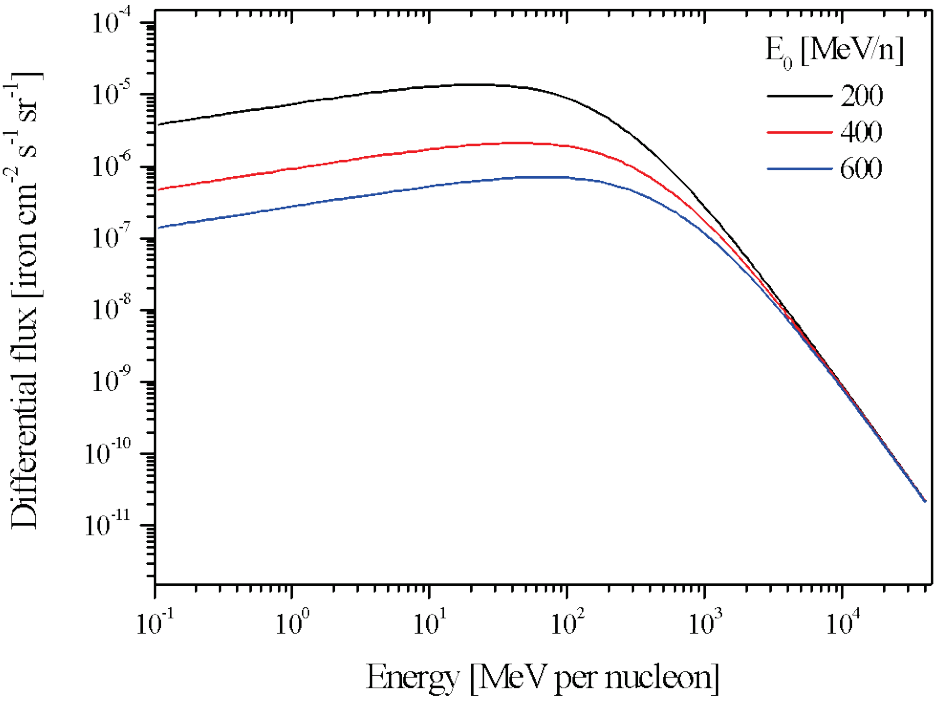

Figure 2.2 – Flux distribution of iron at GCRs with three different values for the parameter E_0 (200, 400 and 600 MeV/n).

Note that at high energies (> 1GeV/n) the impact of the E_0 parameter in the differential flux (Eq. 2.1) becomes negligible. Therefore equation 2.1 is able to describe a differential flux quite similar to the observed one. The abundance of elements which compose the GCRs is similar to that observed in ISM; here we plotted, using equation 2.1, the differential flux for protons, oxygen and iron ions (Fig. 2.3).

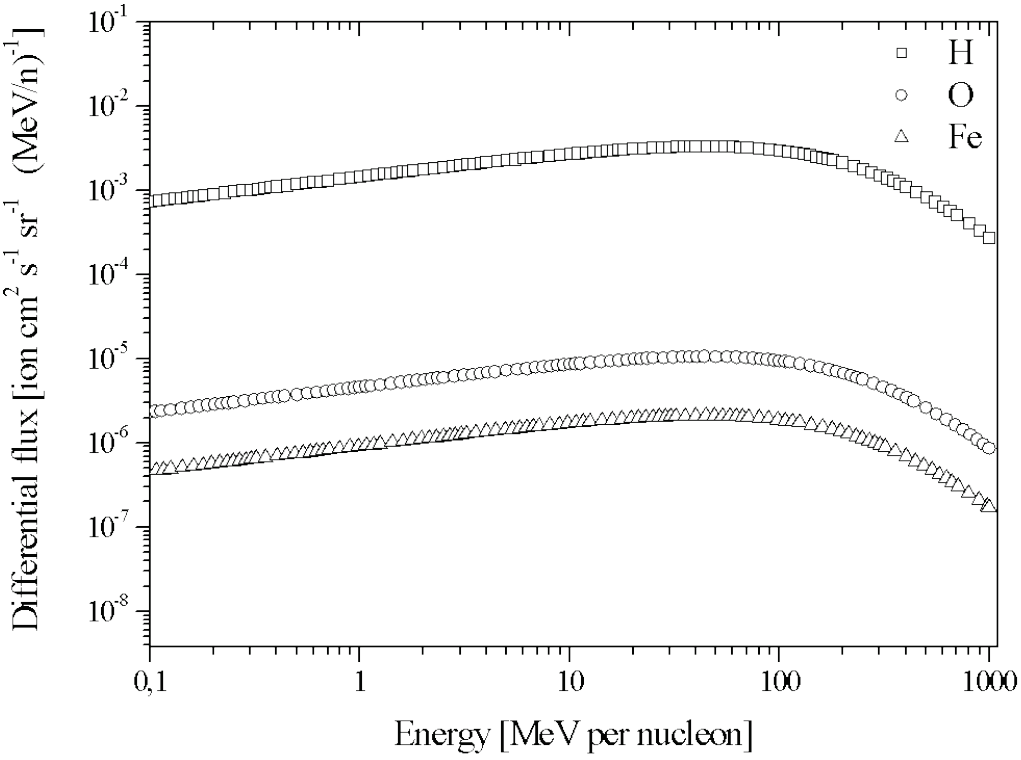

Figure 2.3 – Differential flux of cosmic ray particles (H, O, and Fe), E_0 = 400 MeV/n.

Figure 2.3 and Table 2.1 indicate that protons are the most abundant element in the GCRs. However, several studies have shown that heavy ions, even at low abundance (~1%) have an essential role in the survival and in the production of new molecules in astrophysical environments, due to their orders of magnitude higher electronic stopping power compared to that of protons (see reviews, Rothard et al. 2017; Boduch et al. 2015).

2.1.2 Solar wind

Solar wind (SW) consists of ions ejected by the expansion of the solar corona. The composition of the solar wind consists in approximately 95% of protons, 4% of α-particles and less than 1% of heavy elements (Johnson 1990). It is possible to find more energetic particle from solar flares but the energy range of the ions in the SW ranges from a few keV per nucleons to hundreds of MeV per nucleons, see Figure 2.4 (extracted from de Barros et al. (2011). These authors also determined an empirical formula to generate the observed SW differential flux to fit the SW spectrum data extracted from (Mewaldt, RA et al. 2001).

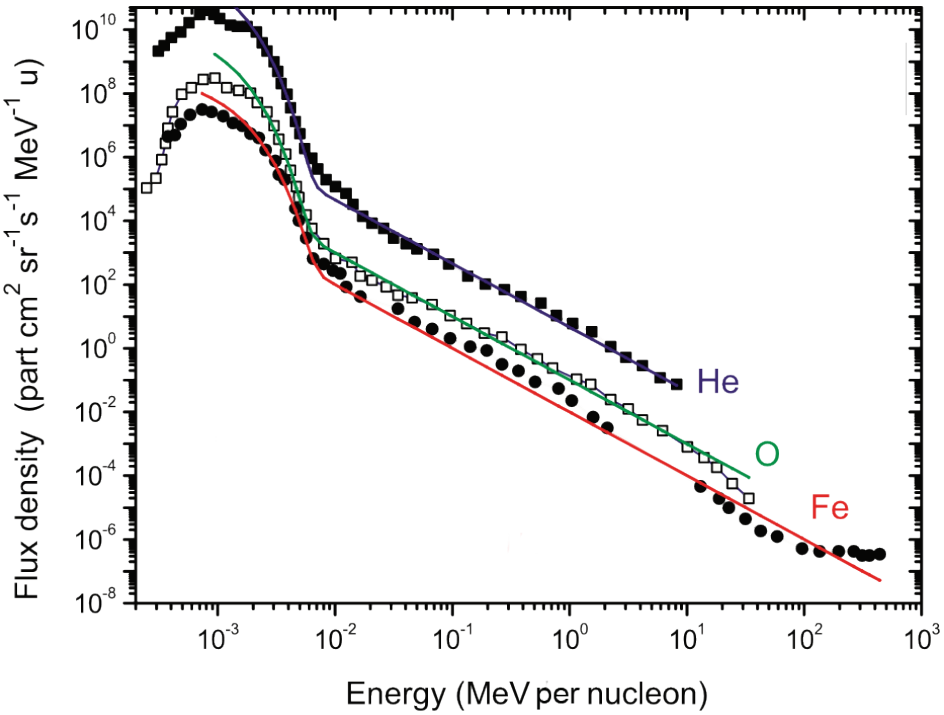

Figure 2.4 – SW differential flux as a function of the specific energy. It is included the energy distribution for He, O and Fe (de Barros et al. 2011).

An important interaction exists between the planetary magnetosphere and SW. The ions can be trapped by the planetary magnetic fields. It is expected that those ions trapped in the magnetosphere play a key role in the chemical evolution of the molecules present in the ice of moons and giant planets (Ding et al. 2013; Lv et al. 2014; Boduch et al. 2015).

2.2 Interaction of radiation with matter

Electromagnetic and corpuscular radiation have different mechanism of energy deposition in matter. In this sub-section, we will briefly present the differences and similarities between the effects of energetic photons, slow and swift light and heavy projectiles.

2.2.1 – Corpuscular radiation

Solids processed by energetic ion irradiation present modifications such as chemical alterations, structural modifications and sputtering. The collisional mechanism of transfer of momentum can be divided into two categories: elastic collisions with the target nuclei (1) and inelastic collision with target electrons (2). Slow particles (SW), interact mainly via elastic collisions, while swift particles, (GCRs) interact mainly via inelastic process leading ionizations, excitations, electron capture. Because almost all of the experiments performed for this thesis concern swift particles, we will focus our attention on this latter process. Along to their trajectory swift projectiles deposit a large amount of energy leading to production of secondary electrons, called as δe^-, also production of radicals and structural modifications. This region is known as ion track. The typical track diameter is about 5 to 10 nm. Figure 2.5 schematically presents basic processes occurring during the swift heavy ion penetration of solid (Neugebauer, 2001) :

- Ion track (multiple ionizations)
- Secondary electrons emissions (δe^-)
- Radical productions (chemical modifications)
- sputtering

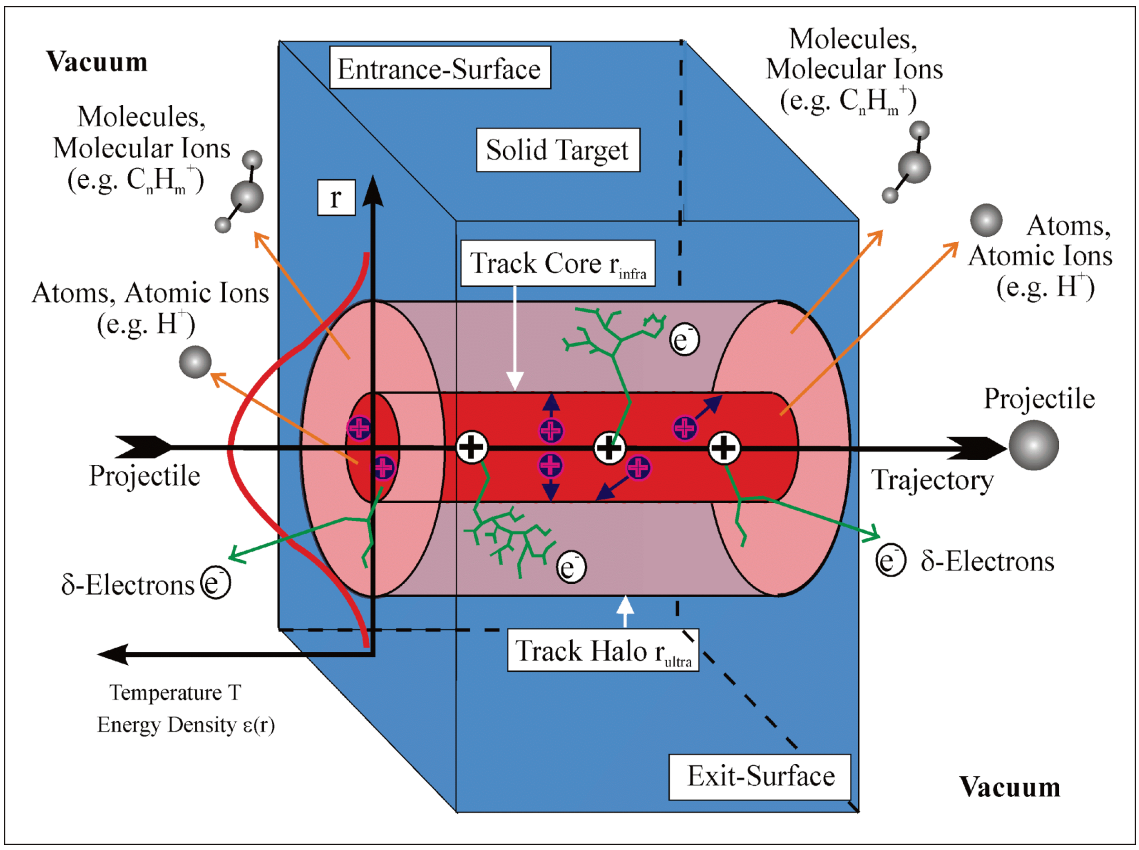

Figure 2.5 – Schematic view of swift ion irradiation of a solid, including the ion track and subsequent events such as secondary electrons emission, sputtering and chemical modifications. Extracted from Neugebauer (2001).

2.2.1.1 – Stopping power

The stopping power corresponds to the energy loss per unit of path length ($^{dE}/_{dx}$). Stopping power can be divided in two groups: (1) electronic stopping power (S_e) which results from the interaction of swift ions with the electronic cloud of the target molecules and (2) nuclear stopping power (S_n) which results from the interaction of slow projectiles with the target nuclei via elastic collisions. The total stopping power (S_{total}) is the sum of these two contributions:

Eq. 2.2 $$\boldsymbol{S_{total} = -\frac{dE}{dx} = -(\frac{dE}{dx})_e - (\frac{dE}{dx})_n = S_e + S_n}$$

Moreover, from the stopping power we can determine the penetration depth (P_d), i.e., how deep the projectile can penetrate into the solid.

Eq. 2.3 $$P_d = \int_0^{E_0} \left(-\frac{dE}{dx}\right)^{-1}$$

E_0 is the projectile initial energy.

When the thickness of the solid is higher than P_d the projectile remains implanted in the solid, this can lead to chemical reactions (Lv et al. 2014; Ding et al. 2013) with reactive projectiles.

Figure 2.6 is a scheme that shows the different process of energy loss as a function of the projectile energy. Note that the kinetic energy of the projectiles determines which processes of energy loss is the dominant one.

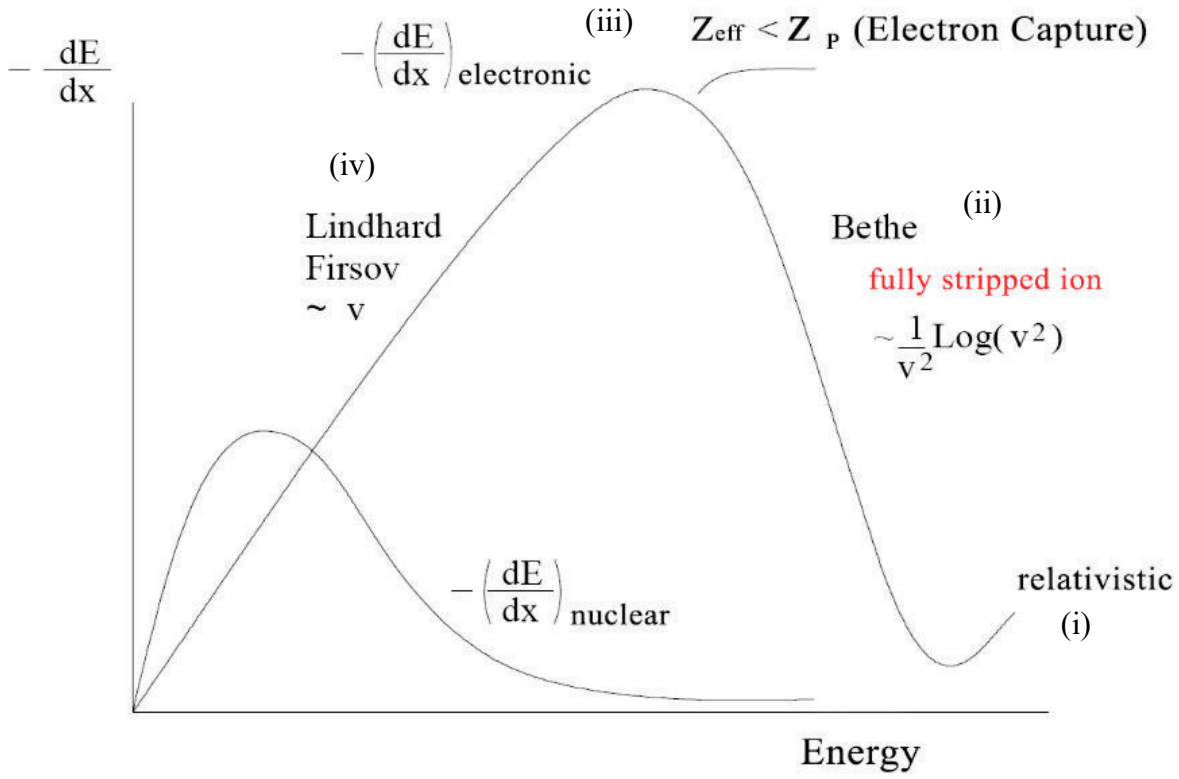

Figure 2.6 - A scheme of the stopping power as a function of the energy. It is indicate the regions of dominance of the nuclear and electronic loss of energy and the four different regime of the electronic stopping power.

Nuclear stopping power (S_n)

At low velocities, projectile-target atom collisions dominate (nuclear stopping, elastic, leading e.g. to sputtering). The interaction of slow projectile and the target nuclei occurs via purely coulombian interactions which can be treated by the laws of classic mechanics as an elastic shock between two particles. The momentum transferred from the ion to the solid may provoke a displacement of the target atoms. A theoretical description for the nuclear loss as function of the projectile energy was given by Biersack (1968).

Eq. 2.4 $$S_n = -4\pi a^2 N Z_p Z_t e^2 \frac{M_p}{(M_t+M_p)} \frac{\ln \varepsilon}{2\varepsilon\,(1-\varepsilon^{-3/2})}$$

Where a Z_p and Z_t are the atomic number of the projectile and the target, respectively, and $a = \frac{0.8853\, a_0}{(Z_p^{1/2}+Z_t^{1/2})^{1/3}}$, where a_0 is the radius of the hydrogen atom. M_p and M_t are the mass of the projectile and the target and e is the elementary charge. The dimensionless Ɛ is given by the following equations:

$$\varepsilon = \left(\frac{M_t}{M_p M_t}\right)\left(\frac{E\, a}{Z_p Z_t e^2}\right)$$

Electronic stopping power

At “high” projectile velocity, the energy loss is mainly due to projectile-target electron interactions (electronic stopping, inelastic). At medium energy, charge exchange comes into play: electron capture, electron loss, formation of excited projectile states versus radiative de-excitation or Auger electron emission may occur. The energy loss in the high energy regime can be estimated from the transfer of energy or momentum in binary ion-electron collisions (Bohr, Lindhard). Starting with a binary collision of a projectile ion

with a target electron due to Coulomb scattering, the momentum transfer to the electron and the associated energy loss of the projectile can be calculated. Other approaches are the dielectric theory, i.e. the macroscopic description using a dielectric function (Sigmund 2008), and quantum mechanics (perturbation theory) (Bethe, Bloch), but all yield similar results: the stopping power is proportional to (Z_p^2/V_p^2).

In the electronic energy loss regime, the projectiles interact with the electronic cloud of the target atoms provoking, electronic excitations and ionization leading the production of δe^-. The theoretical approach for the electronic stopping power is divided into four regimes of velocities. These four regimes are determined by the quantity $Z_p^{2/3}\, v_0$, where Z_p is the atomic number of the projectile and v_0 is the Bohr velocity, i.e., the orbital velocity of the electron 1s in the hydrogen atom ($v_0 = 2.2 \times 10^6$ m/s), this velocity also is the average velocity of the target electrons according Thomas-Fermin model. The four regimes are defined by:

(i) $V_p > 0.1\ c$

(ii) Regime of high velocities: $c >> V_p << Z_p^{2/3}\, V_0$

(iii) Regime of intermediary velocities $V_p \approx Z_p^{2/3}\, V_0$

(iv) Regime of low velocities $V_p >> Z_p^{2/3}\, V_0$

c is the velocity of light in the vacuum

Regime of high velocities ($c >> V_p << Z_p^{2/3}\, V_0$)

Under this condition, the electrons of the projectile ion are full stripped out and therefore it can be considered as a point charge, Z_p e. The Bethe-Bloch equation describes the

electronic stopping power for projectiles at high energies (Bethe 1930). The stopping power is proportional to square of the projectile atomic number (Z_p^2) and approximately inversely proportional to the square of projectile energy (V_p^2).

$$S_e = \frac{4\,\pi\, Z_p^2 Z_t n}{m_e\, V_p^2}\, e^4 \ln \frac{2\, m_e V_p^2}{I}$$

Where n is the density of the target atoms, m_e is the electrons mass and I is the average excitation potential.

Regime of relativistic velocities ($V_P > 0.1$ c)

At relativistic velocities there is a deviation of the Beth-Bloch equation and correction are mandatory, here wed show the complete Beth-Bloch which includes the correction for very high velocities:

$$S_e = \frac{4\,\pi\, Z_p^2 Z_t n}{m_e\, V_p^2}\, e^4 \left(\ln \frac{2\, m_e V_p^2}{I} + \ln \frac{1}{1-\beta^2} - \beta^2 - {}^{C}/_{Z_t} \right)$$

Where $\beta = {}^{V_p}/_{c}$. The first term of the equation is the same of the classical Beth-Boch equation. The other terms come from the relativistic corrections, the last term of this equation is correlated to the "shell effects".

Regime of intermediary velocities ($V_p \approx Z_p^{2/3} V_0$)

The Beth-Bloch equation is just valid when the velocity of the projectiles is much higher than that of the target electrons. When the velocity of the projectile is close to the average velocity of the bound electrons a correction in the Bethe-Bloch equation becomes

mandatory. Due to the electron capture, the atomic number of Z_p should be corrected by introducing the effective charge number (Z_{eff}) in the Beth Bloch formula (Spohr and Bethge 1990). A simple a semi-empirical formula for Z_{eff} is

$$Z_{eff} = Z_p(1 - e^{-V_p / V_0 Z_p^{2/3}})$$

Regime of low energy regime – $V_p >> Z_p^{2/3} V_0$

In this "adiabatic" regime of energy there is an overlap between the wave functions of the projectile and the target, thus forming a quasi –molecule Lindhard et al. (1963) ,and Firsov. (1959) developed independently equations which can describe the electronic energy loss under this condition. Here, for simplicity and as an example we show the Lindhard equation:

$$\text{(i)} \qquad S_e = Z_p^{1/6}\, 8\,\pi\, a_0 n\, \frac{Z_p Z_t}{(Z_p^{2/3}+Z_t^{2/3})^{3/2}}\, \frac{v_p}{v_0}$$

The linear dependence of the projectile velocity ($S_e \sim V_p$) resembles the friction of a body moving on a surface or in a liquid.

Numerical simulations: the SRIM code

SRIM (Ziegler, Ziegler, and Biersack, 2008) provides estimations of S_e and S_n as tables, and also a Monte Carlo simulation of particle trajectories. This feature allows determining ranges and implantation profiles. With this software it is possible to generate to parameters for all ions (S_e, S_n, and P_d) in different materials up to projectiles energies of 1 GeV per nucleon. As an example, we plotted the electronic and nuclear stopping power

to uranium (heavy ion) and hydrogen as a function of the specific energy in solid of guanine, Figure 2.7.

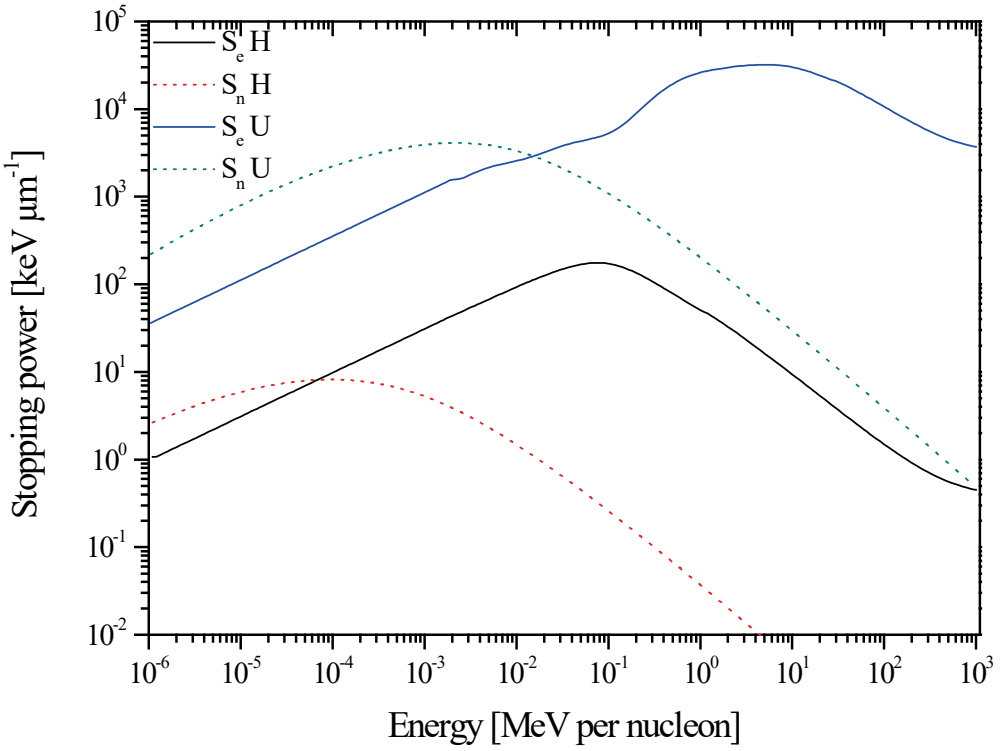

Figure 2.7 – Electronic and nuclear stopping power of H and U in solid guanine.

From the Figure 2.7 turns out that at first that the heavy ions deposit more energy than the light ones and that within the range of energies from 10^{-6} to 10^{-3} MeV/n the projectile loss of energy is driven by the nuclear loss. At energies above 10^{-1} MeV/n there is a dominance of the electronic stopping power and the nuclear loss can be neglected. For most of the experiments performed for this thesis, we worked in the electronic regime of loss of energy, see Chapter 5.

It is important to point out that at energies higher than 1 GeV/n, nuclear reactions becomes more and more important. Here, we will not to take into account the possible nuclear reactions induced in AHMs irradiated by such energetic projectiles, neither the effects from projectile fragmentation. Note also that abundance of GCRs at such high energy

(above of 1GeV per nucleon) is much smaller than those within the energies ranges of MeV per nucleon (Table 2.2).

2.2.2 – Electromagnetic radiation

Electromagnetic radiation interaction with matter leads to electronic excitations and ionization of the target atoms. There is a similarity between the deposition of energy in the matter between ions at electronic loss of energy regime and electromagnetic radiation; both interact with the electronic cloud of the targets. Indeed, several works have reported a similar evolution in terms of new molecules and of ices irradiated by UV photons and ions at loss energy domain, in terms of formation of new molecules from the ice degradation if the dose deposited by ions or photons was equal (Gerakines, Moore, and Hudson 2004; Öberg 2016; Baratta, Leto, and Palumbo 2002; Muñoz Caro *et al*. 2014).

Although photons and ions present some similarities concerning the formation of new molecules and the electronic target excitation, photons do not travel large distances inside matter, their intensity decays exponentially following the Beer-Lambert law, equation 2.5.

Eq. 2.5 $$I(\lambda) = I_0(\lambda)e^{-\sigma_{ab}(\lambda)N}$$

Here $I_0(\lambda)$ is the intensity of the light at a given wavelength (λ) from the source, $I(\lambda)$ the intensity of the light at a given wavelength which arrives at the detector after travelling the matter. $\sigma_{ab}(\lambda)$ is the absorption cross section at a given wavelength and N is the column density (molecules per unit of area) of the target. Therefore, the deposited energy of the photon in the matter will be proportional to the difference between $I(\lambda)$ and $I_0(\lambda)$. For a light with different wavelength the deposited energy will be proportional to

$I_0 \sum_\lambda (1 - e^{\sigma_{ab}(\lambda) N})$. Note the σ_{ab} is an essential parameter to determine the local dose (energy per molecule) deposit by photons. The summation is done for all wavelengths of the light used in the irradiation.

There is a limitation in the penetration of the photons in the matter imposed by the Beer-Lambert law, however, energetic ions like GCRs deposit constant amounts of energy along their trajectory in matter, since their penetration depth is much higher than the thickness of the target.

Moreover, energetic photons are easily scattered (Rayleigh scattering) by dust or grains, therefore in the core of astrophysical region like DCs energetic photons from the neighboring stars are not present. It is important to mention that electromagnetic radiation fields indeed exist in these environments but they are also produced by impact of GCRs on hydrogen and hereafter referred as secondary photons (Ehrenfreund *et al.* 2001; Prasad and Tarafdar 1983).

Due the differences between ions and photons is important to use a scaling parameter to compare their effects in a solid. Here, we will use the radiation G yield value to compare the destruction of the molecules induced by photon or ion irradiation. Here we define the radiation G yield as the number of molecules destroyed per 100 eV deposited. Equation 2.6 displays the radiation G yield for ions

Eq. 2.6 $$G = 100 \frac{\sigma_d}{S_e}$$

Where σ_d is the destruction cross section. In this work, we are used the radiation G yield in units of eV^{-1}, thus to calculate the radiation G we use the σ_d in cm^2 and the S_e in units of eV cm^{-2} $molecule^{-1}$. In the case of electromagnetic irradiation the radiation G yield is

Eq. 2.7

$$G = \frac{100}{E_\lambda} \frac{\sigma_d(\lambda)}{\sigma_{ab}(\lambda)}$$

Where $\sigma_d(\lambda)$ and E_λ are the destruction cross section at a given wavelength and the energy of the photon, respectively.

References

Baratta, G. A., G. Leto, and M. E. Palumbo. 2002. “A Comparison of Ion Irradiation and UV Photolysis of CH_4 and CH_3OH.” *Astronomy and Astrophysics* 384 (1): 343–49. doi:10.1051/0004-6361:20011835.

Barros, A. L. F. de, A. Domaracka, D. P. P. Andrade, P. Boduch, H. Rothard, and E. F. da Silveira. 2011. “Radiolysis of Frozen Methanol by Heavy Cosmic Ray and Energetic Solar Particle Analogues: Radiolysis of Frozen Methanol by Heavy Cosmic Ray and Energetic Solar Particle Analogues.” *Monthly Notices of the Royal Astronomical Society* 418 (2): 1363–74. doi:10.1111/j.1365-2966.2011.19587.x.

Bethe, H. 1930. “Zur Theorie des Durchgangs schneller Korpuskularstrahlen durch Materie.” *Annalen der Physik* 397 (3): 325–400. doi:10.1002/andp.19303970303.

Biermann, P. L., J. K. Becker, J. Dreyer, A. Meli, E.-S. Seo, and T. Stanev. 2010. “The origin of cosmic rays: explosions of massive stars with magnetic winds and their supernova mechanism.” *The Astrophysical Journal* 725 (1): 184–87. doi:10.1088/0004-637X/725/1/184.

Boduch, P., E. Dartois, A. L. F. de Barros, E. F. da Silveira, A. Domaracka, X.-Y. Lv, M. E. Palumbo, et al. 2015. “Radiation Effects in Astrophysical Ices.” *Journal of Physics: Conference Series* 629 (July): 012008. doi:10.1088/1742-6596/629/1/012008.

Cooper, J. F., E. R. Christian, J. D. Richardson, and C. Wang. 2003. “Proton Irradiation of Centaur, Kuiper Belt, and Oort Cloud Objects at Plasma to Cosmic Ray Energy.” *Earth, Moon, and Planets* 92 (1–4): 261–77. doi:10.1023/B:MOON.0000031944.41883.80.

Ding, J.J., P. Boduch, A. Domaracka, S. Guillous, T. Langlinay, X.Y. Lv, M.E. Palumbo, H. Rothard, and G. Strazzulla. 2013. “Implantation of Multiply Charged Sulfur Ions in Water Ice.” *Icarus* 226 (1): 860–64. doi:10.1016/j.icarus.2013.07.002.

Drury, Lo’C, Dc Ellison, and J-P Meyer. 2000. “Interpreting the Cosmic Ray Composition.” *Nuclear Physics A* 663–664 (January): 843c–846c. doi:10.1016/S0375-9474(99)00728-9.

Ehrenfreund, P., M. P. Bernstein, J. P. Dworkin, S. A. Sandford, and L. J. Allamandola. 2001. “The Photostability of Amino Acids in Space.” *The Astrophysical Journal* 550 (1): L95–99. doi:10.1086/319491.

Firsov, O. B. 1959. “A Qualitative Interpretation of the Mean Electron Excitation Energy in Atomic Collisions.” *Zh. Eks. Teor. Fiz.* 36.

Gerakines, P.A., M.H. Moore, and R.L. Hudson. 2004. “Ultraviolet Photolysis and Proton Irradiation of Astrophysical Ice Analogs Containing Hydrogen Cyanide.” *Icarus* 170 (1): 202–13. doi:10.1016/j.icarus.2004.02.005.

Indriolo, N., T. R. Geballe, T. Oka, and B. J. McCall. 2007. H_3^+ in diffuse interstellar clouds: a tracer for the cosmic ray ionization rate.” *The Astrophysical Journal* 671 (2): 1736–47. doi:10.1086/523036.

Johnson, R. E. 1990. *Energetic Charged-Particle Interactions with Atmospheres and Surfaces*. Berlin, Heidelberg: Springer Berlin Heidelberg. doi:10.1007/978-3-642-48375-2.

Lave, K. 2012. Dissertation “The Interstellar Transport of Galactic Cosmic Rays.” USA: Washington University in St. Louis.

Lindhard, J., Scharff, M., and Schiott, H. E. 1963. “Range Concepts and Heavy Ion Ranges (Notes on Atomic Collisions, II).” *Kgl. Danske Videnskab. Selskab. Mat. Fys. Medd.* 33 (1–42).

LV, X. Y., P. Boduch, J. J. Ding, A. Domaracka, T. Langlinay, M. E. Palumbo, H. Rothard, and G. Strazzulla. 2014. “Sulfur Implantation in CO and CO_2 Ices.” *Monthly Notices of the Royal Astronomical Society* 438 (2): 922–29. doi:10.1093/mnras/stt2004.

Mewaldt, RA, Spalding, JD., Stone, EC., and Vogt, RE. 2001. “High Resolution Measurements of Solar Flare Isotopes.” *Proc 17th Int. Cosmic Ray Conf. 3.*

Muñoz Caro, G. M., E. Dartois, P. Boduch, H. Rothard, A. Domaracka, and A. Jiménez-Escobar. 2014. “Comparison of UV and High-Energy Ion Irradiation of Methanol:ammonia Ice.” *Astronomy & Astrophysics* 566 (June): A93. doi:10.1051/0004-6361/201322983.

Öberg, K. I. 2016. “Photochemistry and Astrochemistry: Photochemical Pathways to Interstellar Complex Organic Molecules.” *Chemical Reviews* 116 (17): 9631–63. doi:10.1021/acs.chemrev.5b00694.

Padovani, M., and D. Galli. 2013. “Cosmic-Ray Propagation in Molecular Clouds.” In *Cosmic Rays in Star-Forming Environments*, edited by Diego F. Torres and Olaf Reimer, 34:61–82. Berlin, Heidelberg: Springer Berlin Heidelberg. http://link.springer.com/10.1007/978-3-642-35410-6_6.

Portugal, W., S. Pilling, P. Boduch, H. Rothard, and D. P. P. Andrade. 2014. “Radiolysis of Amino Acids by Heavy and Energetic Cosmic Ray Analogues in Simulated Space Environments: -Glycine Zwitterion Form.” *Monthly Notices of the Royal Astronomical Society* 441 (4): 3209–25. doi:10.1093/mnras/stu656.

Prasad, S. S., and S. P. Tarafdar. 1983. “UV Radiation Field inside Dense Clouds - Its Possible Existence and Chemical Implications.” *The Astrophysical Journal* 267 (April): 603. doi:10.1086/160896.

Neugebauer, R. 2001. “Auf Der Spur Des Ursprungs Und Der Evolution von Sekundarionen Aus Ion-Festkorper-Stoben.” Frankfurt, Germany: Universitat in Frankfurt am Main.

Rothard, H., A. Domaracka, P. Boduch, M. E. Palumbo, G. Strazzulla, E. F. da Silveira, and E. Dartois. 2017. “Modification of Ices by Cosmic Rays and Solar Wind.” *Journal of Physics B: Atomic, Molecular and Optical Physics* 50 (6): 062001. doi:10.1088/1361-6455/50/6/062001.

Shen, C. J., J. M. Greenberg, W. A. Schutte, and E. F. van Dishoeck. 2004. “Cosmic Ray Induced Explosive Chemical Desorption in Dense Clouds.” *Astronomy and Astrophysics* 415 (1): 203–15. doi:10.1051/0004-6361:20031669.

Sigmund, P. 2008. Particle Penetration and Radiation Effects: General Aspects and Stopping of Swift Point Charges. Berlin; New York: Springer. http://www.myilibrary.com?id=134987.

Šmída, R. 2009. Thesis “Cosmic-Ray Physics with the Pierre Auger Observatory.” Prague: Institute of Physics Academy of Sciences of the Czech Republic.

Spohr, R., and K. Bethge 1990. Ion Tracks and Microtechnology: Principles and Applications: Informatica International, Incorporated.

Spurio, M. 2014. Particles and Astrophysics. New York: Springer.

Webber, W. R., and S. M. Yushak. 1983. “A Measurement of the Energy Spectra and Relative Abundance of the Cosmic-Ray H and He Isotopes over a Broad Energy Range.” *The Astrophysical Journal* 275 (December): 391. doi:10.1086/161541.

Ziegler, J. F., M. D. Ziegler, and J. P. Biersack. n.d. *SRIM 2012. www.srim.com*.

Chapter 3 - Experimental methodology

This chapter is dedicated to present the experimental techniques and methods of infrared (IR) spectroscopy and time-of-flight (TOF) techniques used in this work, as well as to point out their advantages and limitations.

3.1 Sample preparation

In the literature there are several different manners to prepare solid nucleobases: by crystallization (Mohamed Mathlouthi, Seuvre, and Koenig 1986a), sublimation and condensation of the nucleobase onto a substrate (Saïagh et al. 2015), as well as preparation of a solution of the nucleobase followed of the evaporation of the solvent (Pilling et al. 2011). In this work, the two latter methods of sample preparation were adopted in virtue of their simplicity.

Nucleobase powders (≥99% pure, guanine which is ≥ 98% pure) purchased from Sigma-Aldrich were dissolved in a solution of ethanol and water (60.8% ethanol in water v/v) at different concentrations: adenine (1.0 mg ml^{-1}), cytosine (1.5 mg ml^{-1}) and uracil (1.5 mg ml^{-1}). Thymine was dissolved directly in pure ethanol at a concentration of 1.5 mg ml^{-1}. Each solution was exposed to ultrasound until all solid material had been visibly dissolved. Then, drops of these solutions were applied directly onto ZnSe windows except for the thymine solution for which a CsI window was used. Afterwards, the windows were heated up to 100ºC until to the entire evaporation of the solvent, thus obtaining a solid sample. Hereafter, samples prepared in this manner will be referred to as "grainy" because of their grainy aspect under the optical microscopy, see Chapter 4.

Due to the insolubility of guanine in ethanol and water, the sample preparation was

modified. Uniform films were prepared by the sublimation of nucleobase powders at low pressure (10^{-5} mbar) using an oven. This oven consists in a resistance of 0.8 Ω plugged to a direct current generator and a temperature sensor, Figure 3.1. The temperature to sublimate was chosen according to each molecule, below their thermal decomposition temperature: adenine (150ºC), cytosine (150ºC), thymine (100ºC), uracil (100ºC) and guanine (260ºC). A similar methodology was adopted by by Saïagh et al. (2015); Saïagh et al. (2014) and Guan et al (2010) in order to obtain uniform nucleobase films.

The optical microscopy and the profilometry experiments confirm that these samples are

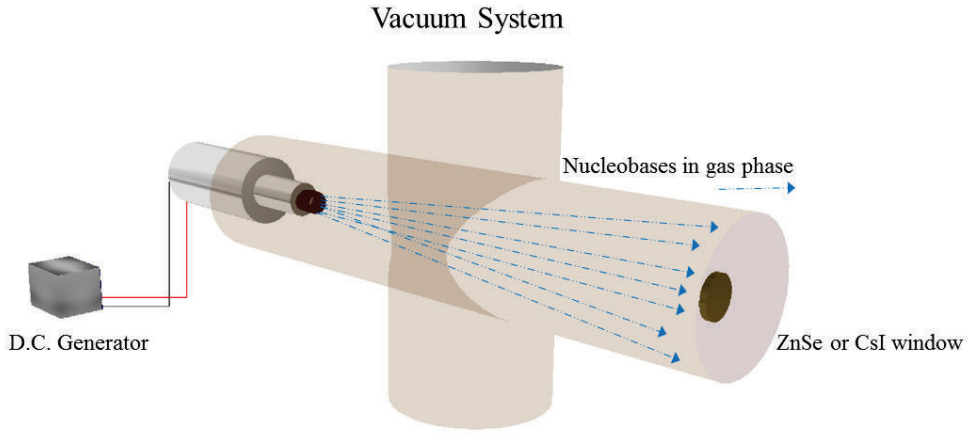

Figure 3.1 – A scheme of the oven used in this work. The oven is constituted by resistance of 0.8 ohms plugged to a direct current generator.

uniform thin films, therefore, hereafter for the sake of simplicity these samples are referred to as "films". The spectra of the nucleobases films are in good agreement with those reported in the literature, see Chapter 4, proving that the process of heating does not destroy these molecules**.** Figure 3.2 presents a picture of a prepared cytosine film.

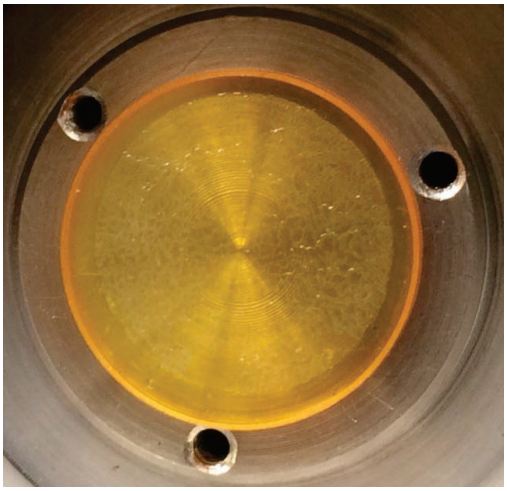

Figure 3.2 – Picture of cytosine film deposited on ZnSe window.

3.2 Ion beam facilities

This sub-section presents a short introduction to the beam lines employed in this work. *Grand Accélérateur National d'Ions Lourds* (GANIL) and *Helmholtzzentrum für Schwerionenforschung* (GSI) are two heavy ion research centers. We used the beam lines *Irradiation Sud* (IRRSUD), *Sortie Moyenne Energie* (SME), and *Accélérateurs de Recherche avec les Ions de Basse Energie* (ARIBE) of GANIL, and of M-branch of the *Universal Linear Accelerator* (UNILAC) at GSI to study the effects of corpuscular radiation on our samples. The beam lines ARIBE, IRRSUD and SME provide different ranges of energy respectively: a few keV/q, about 1MeV/n and between 4-13 MeV/n; at GSI we used a 190 MeV Ca^{10+} beam.

As an example, we plotted the loss of energy per unit of path length of the most abundant heavy ion in the cosmic rays, iron, as a function of the projectile energy in solid adenine, Figure 3.3, both electronic (S_e) and nuclear (S_n) stopping power are included.

Figure 3.3 shows that the beam line of ARIBE is in general in nuclear stopping power

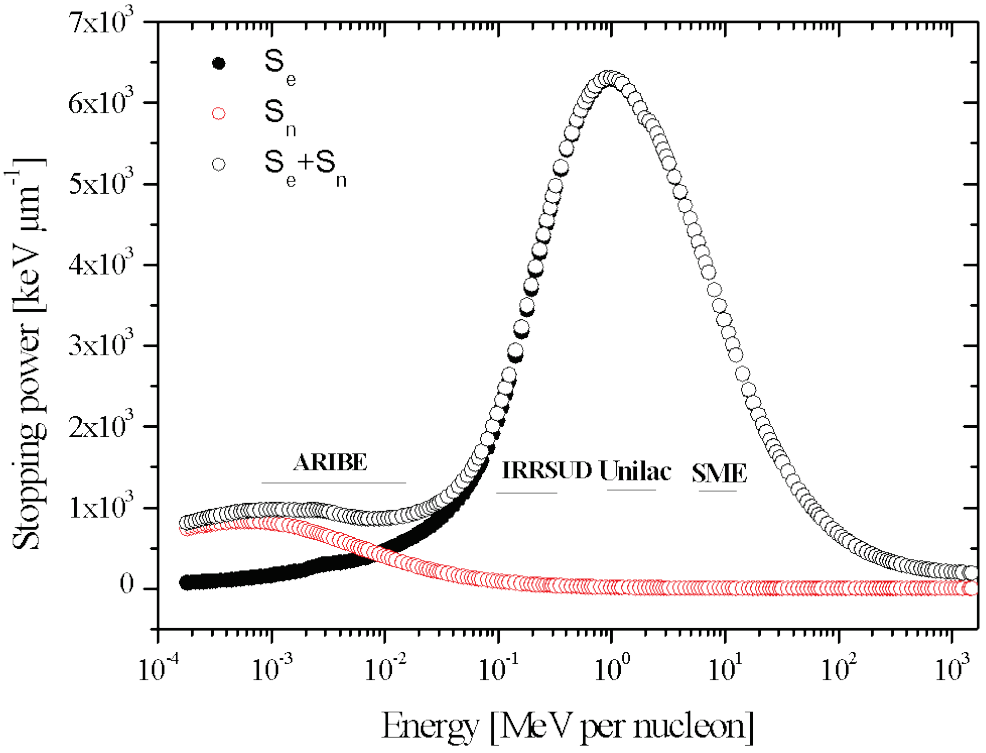

Figure 3.3 – Electronic stopping power (S_e), nuclear stopping power (S_n) and the total stopping power (S_e + S_n) of solid adenine as iron as a function of the specific energy.

domain of deposition of energy. However, the electronic energy loss in those ion beams is not negligible. The other high energy (above 10^{-3} MeV/n) beams clearly are in the electronic regime of energy deposition. The ARIBE platform delivers ion beams which can be considered as solar wind analogues, whereas IRSSUD, SME and M-branch present good conditions to mimic GCR interaction.

3.2.1 IRRSUD and SME – ion beams in the electronic stopping power domain.

This work was carried out mainly with ion beams in the MeV/n range (electronic loss energy domain). We will describe the ion beam lines IRRSUD and SME of GANIL and the beam line M-branch of GSI briefly since it is similar to the beam lines of GANIL. An Electron Cyclotron Resonance (ECR) source supplies ions to a cyclotron (C01 or C02) where they are accelerated up to energies of about 1 MeV/n, see Figure 3.4. The two

injector cyclotrons allow to simultaneously use the IRRSUD line and to inject ions into larger cyclotron CSS1. They are accelerated to higher energies of about 3-14 MeV/n and delivered to the SME beam line.

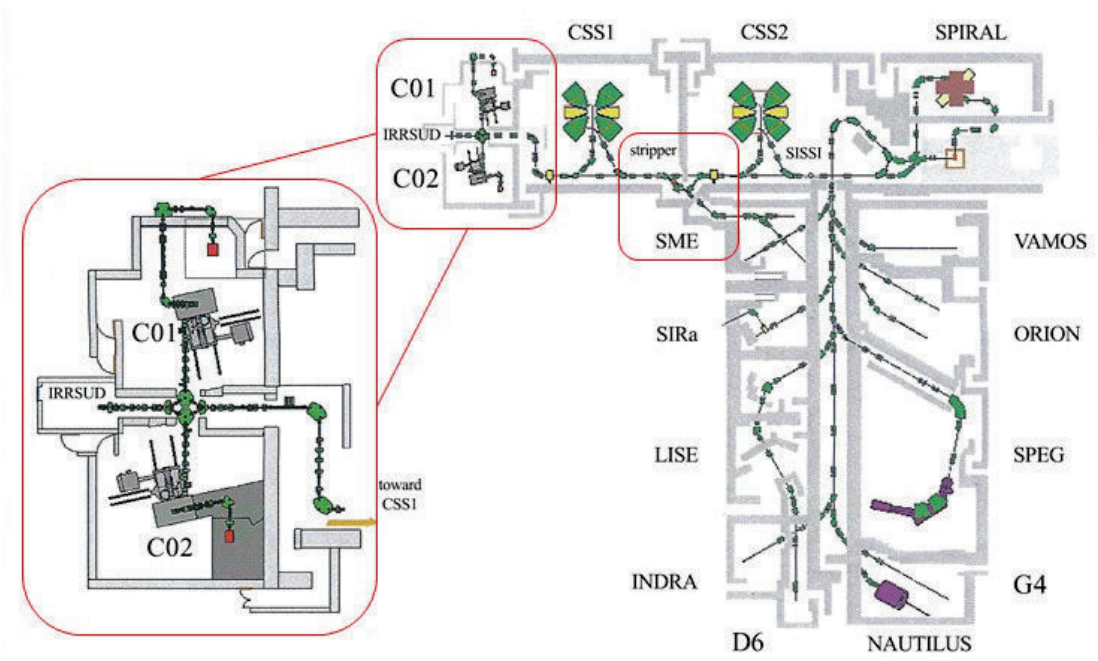

Figure 3.4 – Schematic of beam lines of the accelerator at GANIL (SME, IRRSUD)

In order to irradiate uniformly the samples, the ion beams are swept horizontally and vertically by a pair of magnets. A periodic voltage is applied on the sweeping device, to avoid Lissajous figures, the frequencies applied in the horizontal and in the vertical were set at few hertz and hundreds of hertz, respectively (Seperuelo Duarte et al. 2009). A collimator in front of a Faraday cup allows to determine the flux, the fluence and to check the stability of the ion beams.

The fluence, i.e. the accumulated number of projectile ions per unit of area (cm^2), is proportional to the charge accumulated in the collimator and can be calculated by the following equation 3.1

Eq. 3.1

$$F = \frac{Q}{e\, q\, \frac{I_{COLL}}{I_{FC}} A}$$

Where Q is the charge accumulated in the collimator, e is the elementary charge ($1.6 \cdot 10^{-19}$ C), q is the state charge of the incoming ions and A is the area of the Faraday cup. The typical flux in our experiments in GANIL were about 10^9 ions cm^{-2} s^{-1}.

3.2.1.1 M-branch beam line of UNILAC at GSI.

UNILAC can delivery ion beams from protons to U^{9+} at energies up to 11.4 MeV/n (Hubert, 2016). We performed experiments at GSI employing 190 MeV Ca^{10+} ion beams to irradiate our samples.

Ions are extracted from an ions source, then bunched and accelerated by radio frequency quadrupole, followed by a gas stripper which increases the charge state of the ions. An accelerator increases the energy of the ions and finally they are injected into the M-branch line. The ions flux at GSI was about 10^8 ions s^{-1} cm^{-2}.

3.2.1.2 ARIBE platform – low energy ion beam.

The ARIBE platform delivers low energy ion beams within the energy range of a few dozen keV (5-25 keV/q). The source of ions here is also an ECR. The ions are extracted by a voltage (U), being the energy of the ion E = q U, where q is the charge state of the projectiles. At ARIBE, we also used a sweeping device in order to irradiate the samples uniformly. Figure 3.5 is a scheme adapted from Ding (2014) that displays our set-up used for the experiments at ARIBE. The ratio between the current in the collimator and the current in the Faraday cup was measured in order to calculate the fluence (F), see equation 3.1.

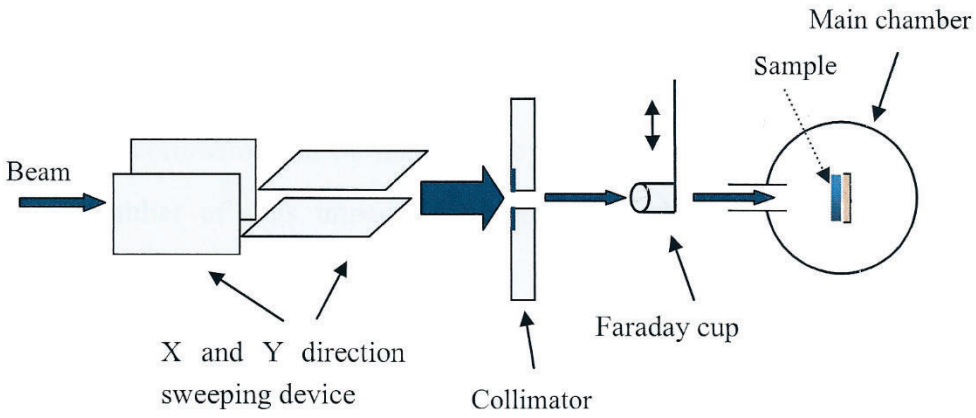

Figure 3.5 - Scheme of the experimental set-up used at ARIBE, adapted from Ding (2014)

3.3 Infrared absorption spectroscopy

Infrared (IR) absorption spectroscopy is an analytical non-destructive technique. The energy of a photon can also be expressed in terms of wavenumber ($k = 1/\lambda$). Among spectrocopists this is the most common manner to refer to a photon, in cm^{-1}. We shall adopt this form now on.

The energy of molecules and atoms due to vibrations and rotations are quantized. For the absorption of the photon to occur, its energy needs to match the energy of the molecular vibration or rotation, this process is called resonant absorption. It is common to refer to IR and Raman as vibrational spectroscopy techniques.

In large molecules the rotation or vibration of functional groups have little influence on the rest of the molecule, that means that the absorption of electromagnetic radiation by the same functional groups in different molecules will be within the same range (energy or frequency). This makes IR absorption spectroscopy a powerful technique in identifying functional groups and molecules.

The infrared spectrum is usually divided in three distinct regions: near infrared region (14000-4000 cm^{-1}), mid infrared (4000-400 cm^{-1}) and the far infrared (400-4 cm^{-1}). The

molecules studied in this work (nucleobases and pyridine) are composed of H, C, N and O. Hence, we work in the mid infrared range of the electromagnetic spectrum. It is important to point out that nitrogen heterocyclic compounds have a strong absorption in the UV range and therefore UV-visible spectroscopy can also be used also to perform a similar study.

The molecular vibration is a function of different parameters such as the mass of the bonded atoms, and the force of the chemical bond between them allowing the detection of different isotopes, functional groups and isomers (Günzler and Gremlich 2002)**.** In the first approximation, diatomic molecules can be described by a quantum harmonic oscillator, to atoms bound by an elastic force with quantized energies and vibrations which can be expressed by the following equations:

Eq. 3.2 $$\nu = {}^{1}/_{2\,\pi}\sqrt{{}^{k}/_{\mu}}$$

Here ν is the frequency of vibration, k the constant of proportionality of the force binding the atoms, μ is the reduced mass, i.e. ${}^{m_1 m_2}/_{(m_1+m_2)}$ m_1 and m_2 are the mass of the bounded atoms. The associated energy of those molecules can be determine through the equation 3.3 – energy of the quantum harmonic oscillator (Griffiths 2017), as discussed earlier in this section, the absorption of a photon occurs when its energy matches with the energy associated to a vibrational or rotational of the molecule.

Eq. 3.3 $$E_\nu = h\,\nu\left(n + {}^{1}/_{2}\right) with\ n = 0,1,2,\ldots$$

Equation 3.3 shows that the minimal energy of the is $E_0 = {}^{h\,\nu}/_{2}$. That means that molecules always are in motion.

A system with N free atoms has 3 N degrees of freedom corresponding to the three

coordinates: x, y, and z. When atoms form a molecule, it still has 3 N degrees of freedom. However, the position of the molecule and its bond-angles are fixed. Thus, three degrees are determined by the translation of the center of mass. The rotational movements of non-linear molecules occupy more three degree of freedom. Therefore, in non-linear molecules remain 3N-6 degrees of freedom for the vibrations. Linear molecules do not rotate around the intermolecular axis; those molecules have 3N-5 degrees of freedom for the vibrations**.** The degrees of freedom correspond to the different normal modes of vibrations of the molecule.

However, generally the number of different modes of vibrations does not correspond to the number of peaks of bands observed in the IR absorption spectra. This can be explained by the following reasons:

- Bands of combination – It is linear combinations of the normal frequencies of vibrations, e. g. if ν_2 and ν_4 are to frequencies of vibrations of a given mode normal of vibration it is possible occurs bands of combination as $\nu_2 + 2\nu_4$.
- Overtone – It is a band with value of frequency which corresponds to interger numbers of those of the normal vibrations, e. g, let ν_1 be the value of a given mode normal of vibration. The overtone occurs within the values: $2\nu_1, 3\nu_1, 4\nu_1$.
- Degeneracy – Different vibrations can have the same energy and therefore their absorptions peaks will be overlapped in the IR spectrum.
- Symmetric vibrations –Symmetric vibrations do not change the dipole momentum and they are IR inactive so do not produce an absorption peak.

As an illustrative example, Figure 3.6 displays the IR spectrum of methane, a simple and important organic molecule. Note that the absorption peaks correspond to a linear combination of the different modes of vibration of this molecule.

IR absorption spectroscopy also gives information about the structure of the molecules and its neighborhood, e.g. amorphous water ice and crystalline display different IR

absorption spectra (Dartois et al. 2013). In addition to allowing the identification of functional groups and molecules, IR absorption spectroscopy also allows an estimation or determination of its concentration or column density (number of molecules per centimeter square). The Lambert-Beer equation describes the relationship between the quantity of molecules and the intensity of absorbed light at a given frequency, equation 2.5.

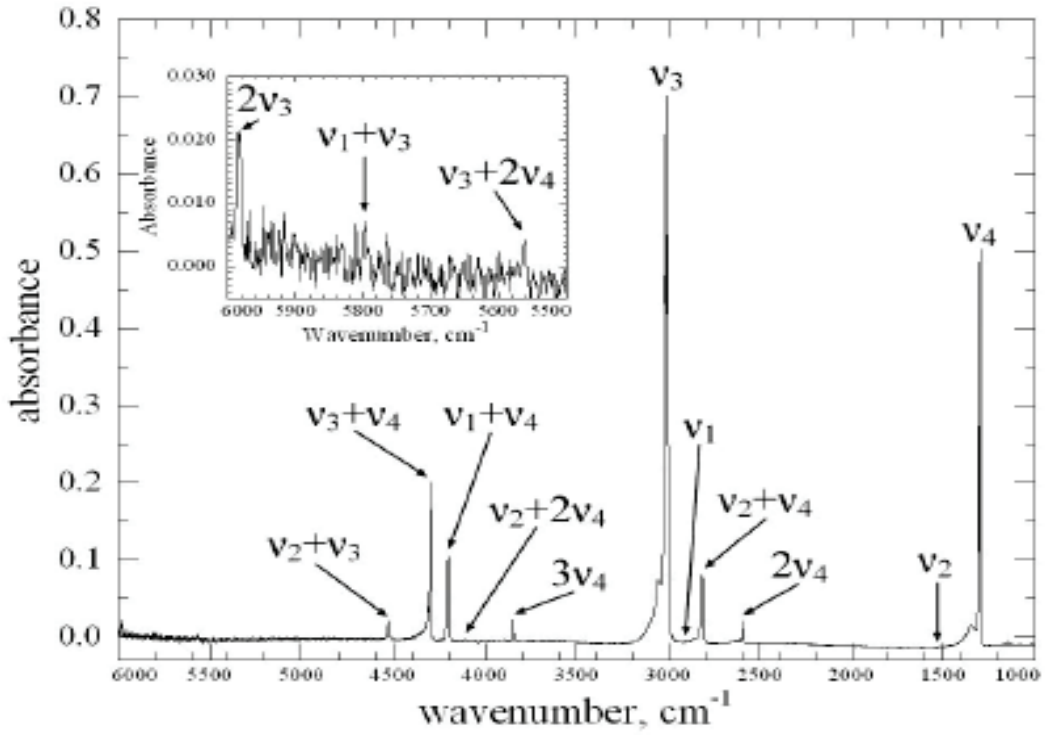

Figure 3.6 – Methane (CH_4) IR spectrum adapted from Bennett et al. (2006).

There are different ways to represent an infrared spectrum, all of them based on Eq. 2.5. At ordinate is possible to present it as absorbance (A) Eq. 3.4, Transmittance (T) Eq. 3.5 or optical depth (τ) Eq. 3.6 and in the abscissa is possible to represent in wavenumber, wavelength, frequency or energy.

Eq. 3.4 $$A = log \frac{I_0(\nu)}{I(\nu)}$$

Eq. 3.5 $$T(\nu) = \frac{I(\nu)}{I_0(\nu)}$$

Eq. 3.6 $$\tau(\nu) = ln \frac{I_0}{I}$$

In this thesis we will present the IR spectra displaying the absorbance as a function of the wavenumbers.

From equation 3.2 is possible to estimate the column density.

Eq. 3.7 $$N = \frac{\int \tau(\lambda) d\lambda}{\int \sigma_{ab}(\lambda)\, d\lambda} = ln\, 10\, \frac{\int A(\lambda) d\lambda}{\int \sigma_{ab}(\lambda)\, d\lambda}$$

Where $\int \tau\ (\lambda)\ d\lambda$ and $\int A(\lambda) d\lambda$ are, respectively, the area of certain absorption bands on absorbance and optical depth scale. The band strength or A_{value} of a given mode of vibration is defined as the integral of absorption cross section over the wavenumber or wavelength $\int \sigma_{ab}(\lambda) d\lambda$. In this work, we will evaluate the A_{value} of some absorption peak of cytosine and thymine using profilometry (see section 3.8) and IR spectroscopy. For the other nucleobases studied in this thesis, we will adopt values reported in the literature (Saïagh et al. 2015; Saïagh et al. 2014).

We monitor the IR spectra of our samples during the irradiation. According to the Beer-Lambert law, the area of a given absorption peak is directly proportional to the column density (number of molecules per cm^2). We observe that during ion processing of our samples the area of the IR absorption peaks decreases, see Chapters 5 and 6, this is due to the molecule target disappearance caused by either destruction or sputtering. Both effects, destruction and sputtering, can be quantified by introducing the "apparent destruction cross section" (σ_d) (de Barros et al. 2012; Mejia et al. 2013). The evolution of the peak area (A) as a function of the ion fluence can be written as:

Eq. 3.8 $$A = A_0 e^{-\sigma_d F}$$

Where F is the fluence, A_0 is the initial absorption of a given absorption peak area and σ_d is the apparent destruction cross section. At GSI the irradiation of adenine and cytosine was performed with the ion beam at a 45° angle with respect to the sample, in this case a correction of the fluence is mandatory under the form: F' = F cos 45°, where F and F' are the measured fluence and the corrected fluence**.**

In order to compare the effects of different ion irradiation in our samples we will also follow the evolution of the peak area as a function of the local dose, i.e., the energy deposited per molecule. Equation 3.9 shows how to calculate the local dose (L_D). In this work most of the irradiations were performed in the electronic loss energy regime and therefore $S_{total} \approx S_e$. The thicknesses of our samples is much smaller than the penetration depth and we can assume that the deposited energy (ΔE) is much smaller than the projectile energy. Under these assumptions we have $\Delta E \approx S_e\, d$, where d is the thickness of the solid, and we can easily calculate the local dose:

Eq. 3.9 $$L_D = \frac{F\, S_e\, MM}{\rho\, n_a} \times 10^7$$

Where ρ is target density (g cm^{-3}), MM the molar mass (g mol^{-1}), n_a the Avogrado number, F the fluence (ions cm^{-2}).

3.4 Experimental set-up: CASIMIR

Chamber d'Analyse par Spectroscopie Infrarouge de Molecules IRradiées (CASIMIR) was one of the sets-up used in our experiments. It consists of a high vacuum steel chamber with a cold head and a sample holder which allows to reach temperatures within the range of 12 – 300 K (the irradiation of the samples occurs in this chamber), a Fourier-transform

infrared spectrometer (FTIR) and a ramp where it is possible to prepare a mixture of gases to be injected in the main chamber, see Figure 3.7. CASIMIR was used in the experiments at GANIL. In the next subsection we will describe this set-up. At GSI, the set-up used is very similar to CASIMIR, therefore it will be described only briefly at the end of this section.

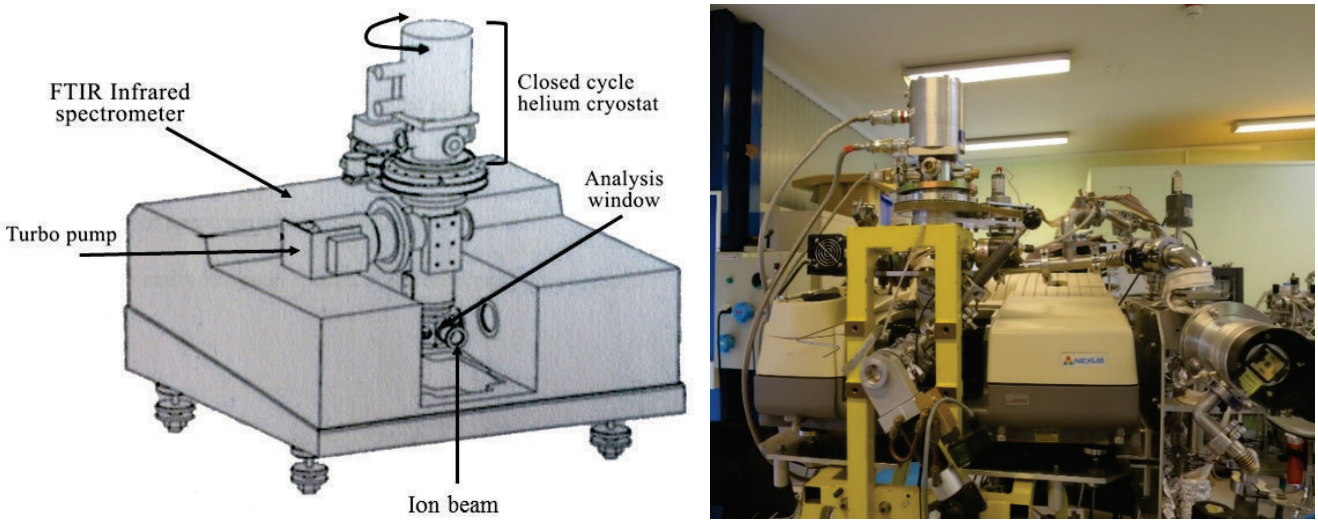

Figure 3.7 - Scheme of CASIMIR (adapted from Seperuelo, 2009) and photo.

3.4.1 High vacuum chamber

The samples are irradiated and monitored by IR absorption spectroscopy in a stainless steel high vacuum chamber. A primary pump can reach a pressure of $\approx 10^{-2}$ mbar and once it does a turbomolecular pump is activated to reach a chamber pressure about 10^{-7} mbar within a few hours. Then, a closed cycle helium cryostat is switched on, in order to decrease the temperature of the sample mounted on a cold head in the chamber to ≈ 12 K. At these temperatures the gas in the chamber condensates on the sample and on the cryostat. This layering effect reduces the pressure in the chamber, leaving pressures at about 2×10^{-8} mbar.

3.4.2 Cryostat and sample holder

The cryostat functions in principle like a conventional refrigerator but uses liquid helium as the cooling substance. It stabilizes cold cryogenic temperatures of the samples as low as around 12 K. The cryostat works in cycles of compression and expansion of helium. The compressor supplies liquid helium and evacuates heat resulting from compression of helium. The liquid helium expansion under adiabatic conditions at the cold head yield gaseous helium that absorbs heat thus decreasing the temperature.

A copper shield protects the sample against thermal radiation from the chamber which is at room temperature. Figure 3.8 shows a picture of our cryostat without the copper shield.

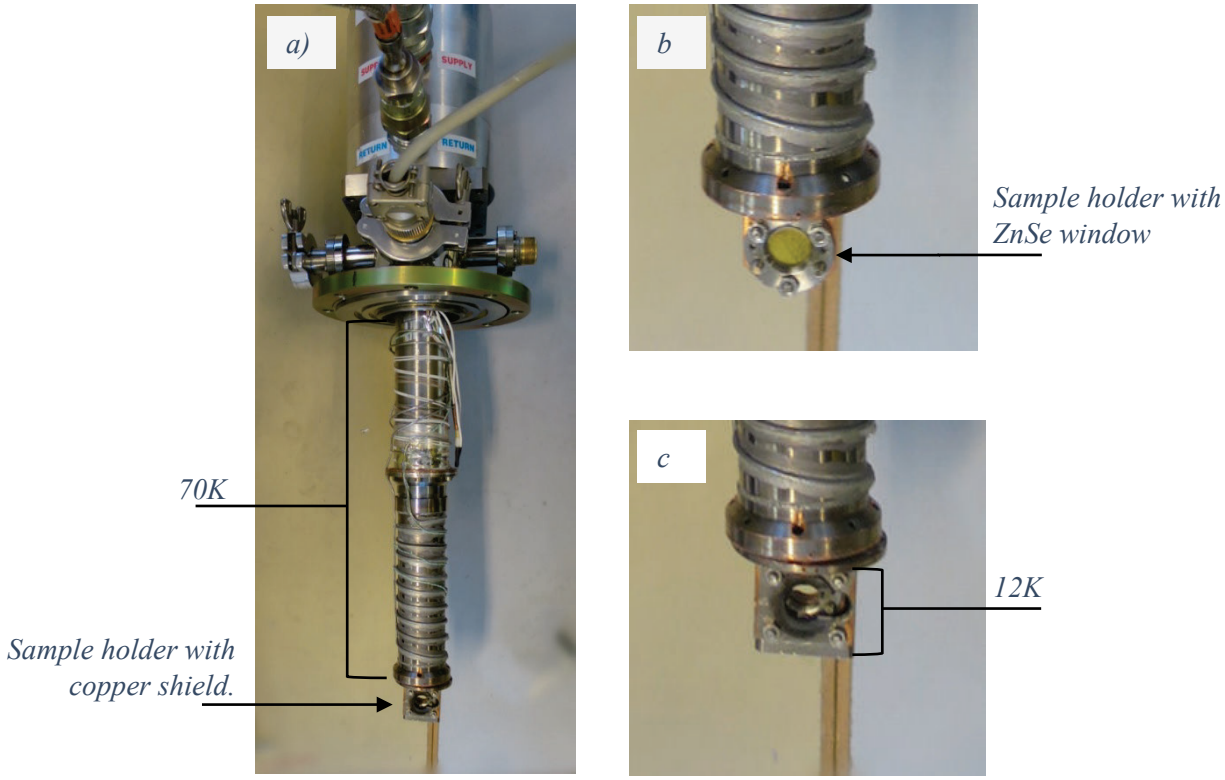

Figure 3.8 – Picture of the cryostat and the sample holder with copper shield (a), sample holder with a ZnSe window without copper shield (b) and detail of sample with copper shield (c).

In order to fix the temperature of the sample at a desired value between 12 K and room temperature, a heating wire with proportional-integral-derivative (PID) temperature control device is looped around the cryostat. A Lakeshore 340 temperature controller was used to control and monitor the temperature of the sample.

The temperature of our samples was measured using a carbon resistance thermometer (CRT) and a cryogenic linear temperature sensor (CLTS) with a precision is of 0.1 K. The CRT stability is extremely affected by the environment therefore is important to calibrate it to be used under vacuum conditions. The CRT resistance increases exponentially (about 1 kΩ at 1 K and nominal resistance at room temperature), the sensitivity increases smoothly with decreasing temperature.

The ensemble (cryostat, sample holder and copper shield) can be turned, as can be seen in Figure 3.9. Irradiation was performed at 0º, the IR analysis at 90º and gas deposition at 180º.

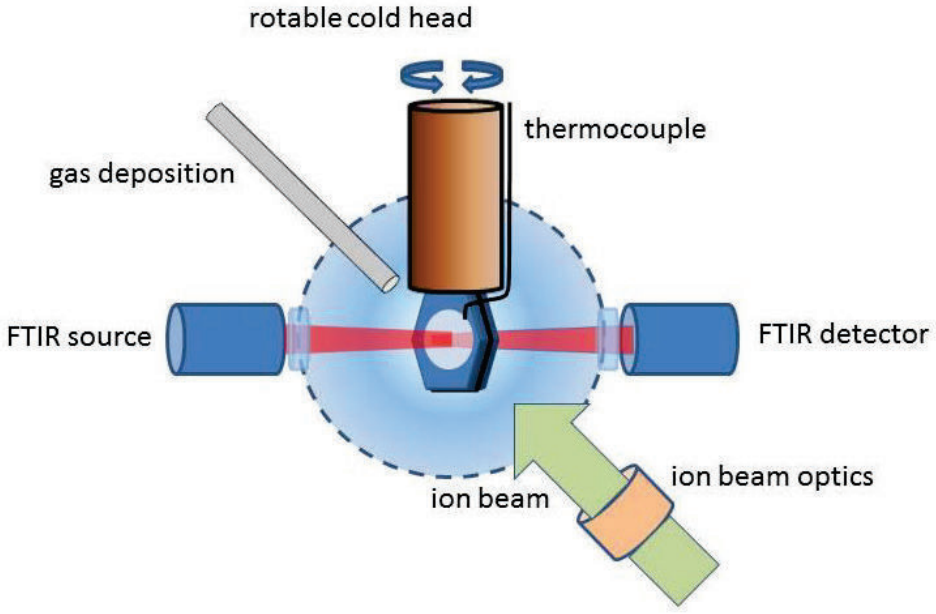

Figure 3.9 - Experimental set-up (schematic) employed for bombardment of solid nucleobases by heavy ions. Figure extracted from Rothard et al. 2017.

3.4.4 Fourier transform infrared (FTIR) spectrometer

The FTIR spectrometer consists of an IR source, a Michelson interferometer and a detector. A computer allows operation of the spectrometer and data acquisition. The Michelson interferometer consists of a beam splitter (half transparent mirror) and two mirrors in a relative movement, Figure 3.10. The IR beam is split into two beams which travel in perpendicular directions. Due to the relative movement of the mirrors there is an interference and the interferogram of the beam is recorded by the detector. Through the software processing by computer using a Fourier transform, the final spectrum is recorded**.** In this work, the IR absorption spectra were obtained before and after irradiation with Nicolet Magna 550 FTIR spectrometer, mercury-cadmium-telluride detector cooled with liquid nitrogen, operating in transmission mode. The spectra were acquired in situ by 128 scans in the wavenumber range from 4000 cm^{-1} to 700 cm^{-1} with a resolution of 1 cm^{-1}.

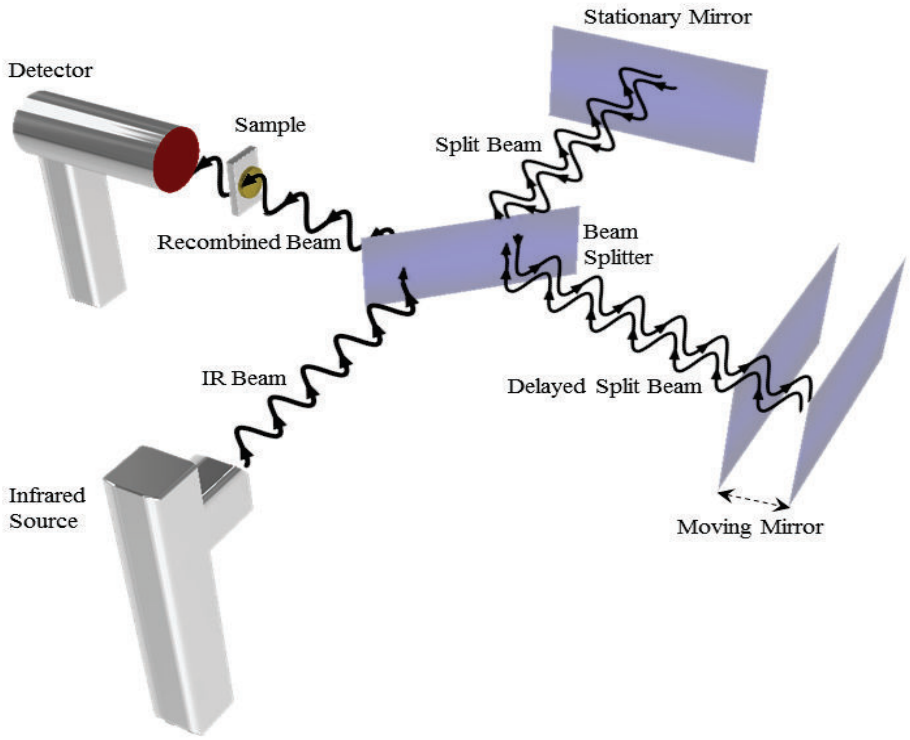

Figure 3.10 – Scheme of FTIR spectrometer.

3.4.5 Ramp at CASIMIR

The preparation ramp is a part of CASIMIR which allows to prepare mixtures of different gases. The ramp has two pre-chambers separated by valves with volumes V_1 and V_2 with ($V_2=2V_1$). It is possible to mix two different gases before depositing them into the main chamber. The ramp allows the connection of three different compounds by using balloons for gases and tubes for liquid compounds, as an example, see Figure 3.11.

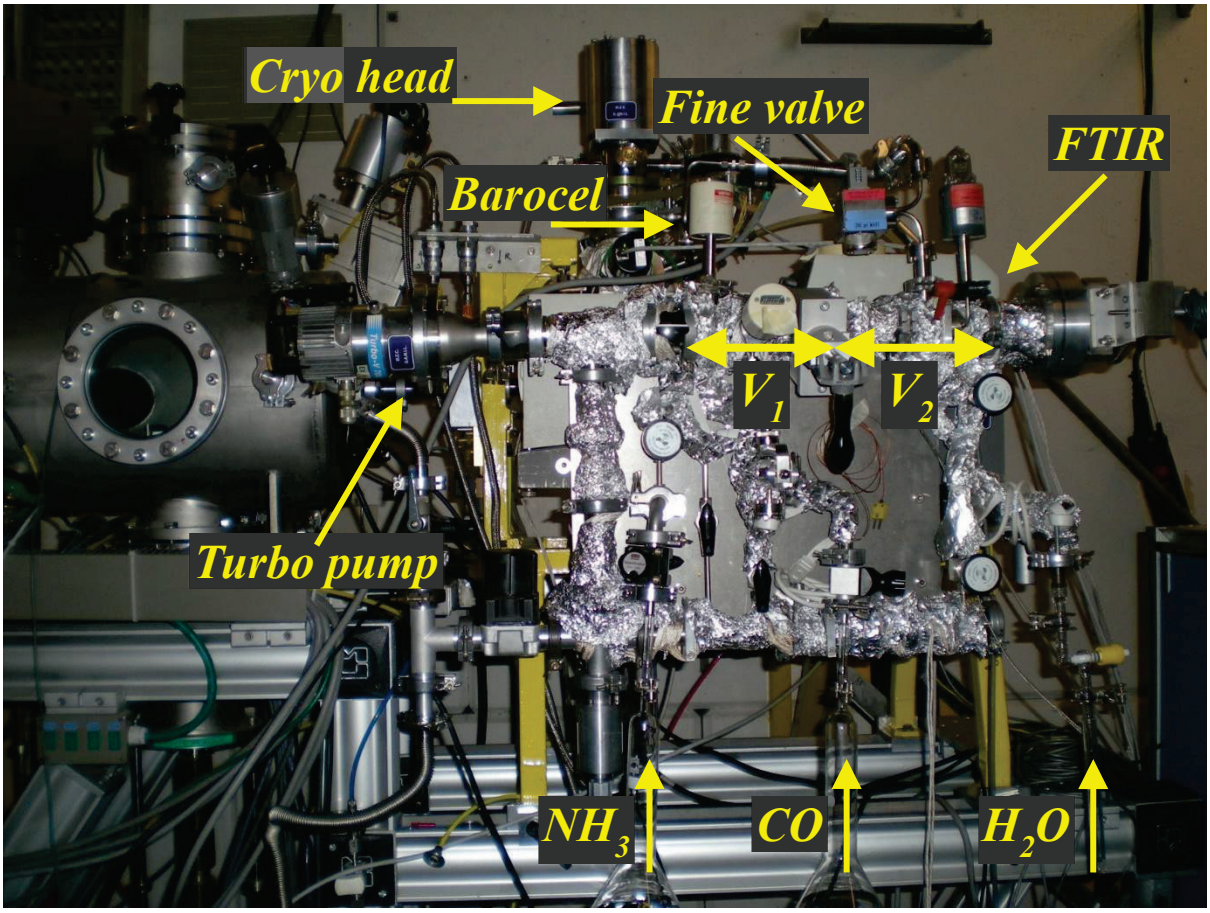

Figure 3.11 – Photo of RAMP of CASIMIR.

Once the balloons and the tubes are connected to the ramp, the pumps coupled to the ramp are switched on and the pressure in the ramp reaches about 10^{-5} mbar. We wait a few hours in order to clean the ramp and avoid contamination from the residual gases from previous experiments which may be trapped inside the ramp. In order to avoid contamination from the gas in the tube, the liquid was frozen using liquid nitrogen and

the tube is pumped several times. Finally, the gas is deposited into a chamber through a thin needle. In order to have an estimation of the amount of the deposited gas in the chamber we monitored the variation of the pressure in the ramp using a gauge (Barocel).

3.5 Experimental procedure

The experimental procedures for the nucleobase experiments:.

1. Virgin window is mounted on to the holder sample.
2. Pumping to reach high vacuum (≈10^{-6} mbar)
3. Background recorded at room temperature.
4. Cooling down to ≈ 12 K.
5. Background recorded at low temperature.
6. Warm up to room temperature.
7. Break the vacuum
8. Our sample is mounted on to the holder sample with the same type of window.
9. Primary pump is switched on and the spectrum is recorded at room temperature with the respective background (room temperature).
10. Pumping to reach high vacuum (≈10^{-6} mbar)
11. Cooling down to ≈ 12 K
12. Spectrum recorded at low temperature (with the respective background, 12 K).
13. The sample is turned at 0º and irradiated.
14. The beam is stopped at intermediate fluences and the sample is turned to 90º and then the spectrum is recorded.

In the experiments with pyridine which is liquid at room temperature, a tube containing this liquid was connected to the ramp, then frozen with liquid nitrogen and pumped

several times to assure that we do not have contamination from the air in the tube and the residual air from the old experiments in the ramp, as described at section 3.3.5. Finally the valve between the tube and the pre-chamber is opened, the pressure is increased and the pyridine is deposited though a needle into a chamber and condenses on the ZnSe window which is at a low temperature of about 12 K.

3.6 Experimental procedure at GSI

At GSI the set-up is very similar to the set-up at GANIL, therefore it will be described only briefly here, for more details see Mejía et al.(2015). The set-up consists in a high vacuum chamber with a cryostat and sample holder, a preparation ramp and an IR spectrometer.

Three samples can be mounted onto the cold head at the same time inside the chamber, therefore it is not mandatory to break the vacuum to perform a new irradiation. Figure 3.12 shows the sample holder used at GSI. The samples are sandwiched between two aluminum plates. Between the aluminum plates and the samples we place manually prepared indium rings to improve its thermalisation. Indium is a metal with a high thermal conductivity. The temperature of Sample 1 that is closest to the cold head (see Figure 3.12) is about 12 K while that of the Sample 3 is about 25 K.

The samples can be moved along the Z axis and can be turned around the azimuth angle. First, the samples were positioned at a specific position on the Z axis; Sample 1 (45.6 mm), Sample 2 (32.5 mm) and Sample 3 (18.5 mm). A piece of alumina (Al_2O_3) was placed below to the last sample. Alumina emits light when irradiated allowing us to check if the ion beam is being delivered correctly. In all our experiments at GSI the Sample 2 was a virgin window allowing us to record a background at low

temperature as well as to check the deposition of any residual gas in the chamber (this will be discussed in Chapter 6). The samples were positioned at 0º for irradiation and for IR measurements at 90º. Gas can be admitted into the chamber through a thin valve. Typically, the pressure in the chamber was increased by about two orders of magnitude (from 10^{-8} to 10^{-6} mbar) during the deposition.

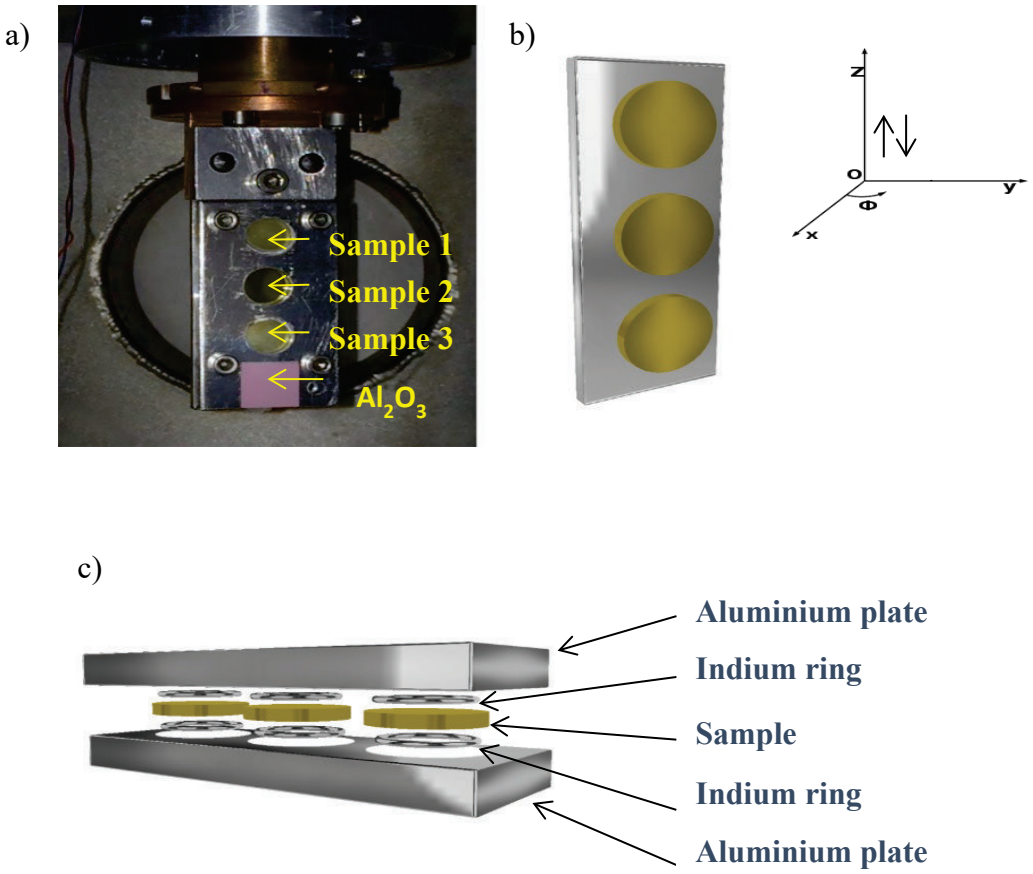

Figure 3.12 – Photo of the sample holder at GSI (a), Scheme of the sample holder and its possible movements (b), Sample holder mounting scheme (c).

The procedure adopted was:

1. The three samples are mounted inside the high vacuum chamber and the pump is switched on.
2. When the pressure reached 10^{-7} mbar we recorded the background of the sample 2 (virgin window) at room temperature and recorded the spectra of the samples at room temperature.
3. Start cooling down procedure.
4. Recording of the background at low temperature and recording the spectrum at low temperature.
5. In one of our experiments at GSI we deposited water vapour inside the chamber before the irradiation and the spectrum was recorded.
6. Positioning of the desired sample and start the irradiation.
7. At a given fluence the beam was switched off and the sample turned at 90º. IR spectra recorded.

3.7 Profilometry

In order to characterize our samples we used the profilometry technique, which allows to determine the thickness of our samples as well as their rugosity. The profilometer device used was a Dektak 150 surfacer from Veeco (Fig. 3.13). Those experiments were performed at the GREYC laboratory (ENSICAEN, Caen, France).

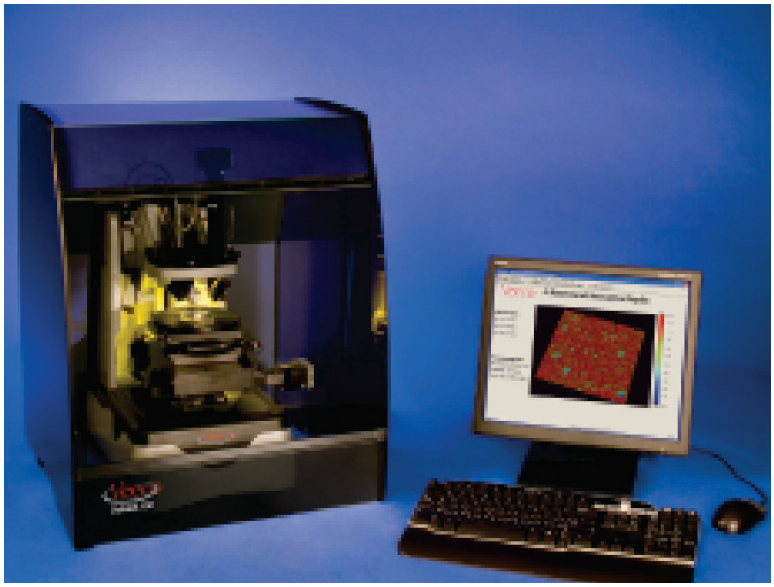

Figure 3.13 – Picture of the Dektak 150 surfacer profilometer.

The operation basically consists of a diamond tip moving along of the samples, this can detect steps of dozen of Angströms. As the diamond tip moves along the sample an electrical signal corresponding to the profile of the sample is generated.

A computer records the electrical signal and a software converts it in thickness (the software registers the difference of steps, which in our case corresponds to the thickness of our samples). The samples were positioned in the center of the profilometer, the limit between the film and the window is clearly visible to the naked eye. Using the microscope coupled to the profilometry makes it easier to see this limit (the step between the window and the film), thus the tip went through at least four different positions at the same film. The results are the average of those measurements. Figure 3.14 displays a profile of cytosine film. Sample characterization is discussed in the next chapter.

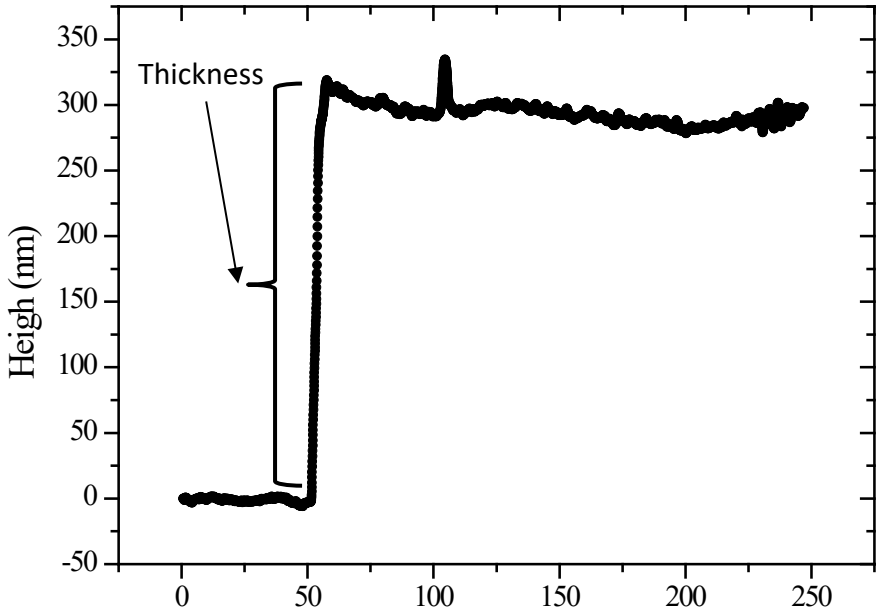

Figure 3.14 – Profile of cytosine film.

3.7 Time of-flight experiments: AODO

The irradiation provokes two main effects on our samples: physico-chemical modifications in the bulk of our solid samples. These modifications can be monitored by IR absorption spectroscopy as described in the previous sections. On the other hand, the

bombardment of solid samples causes sputtering. With the AODO set-up, we can obtain information about of sputtered material. We have the opportunity to apply two complementary techniques: IR to study the modification in the bulk, time-of-flight (TOF) to monitor the cations.

AODO (Fig. 3.15) consists of an ultra-high vacuum steel chamber with a cryostat which allows to reach temperatures in the range of 12 – 300 K (irradiation of the samples occurs in this chamber), a preparation ramp for vapor deposition, a time-of-flight (TOF) mass spectrometer, a quadropole mass analyzer. The cryostat and the temperature controller are very similar as described in 3.3.2 for CASIMIR. For more details about this set-up, see Akcöltekin et al. (2009) and (Hijazi et al. 2011)

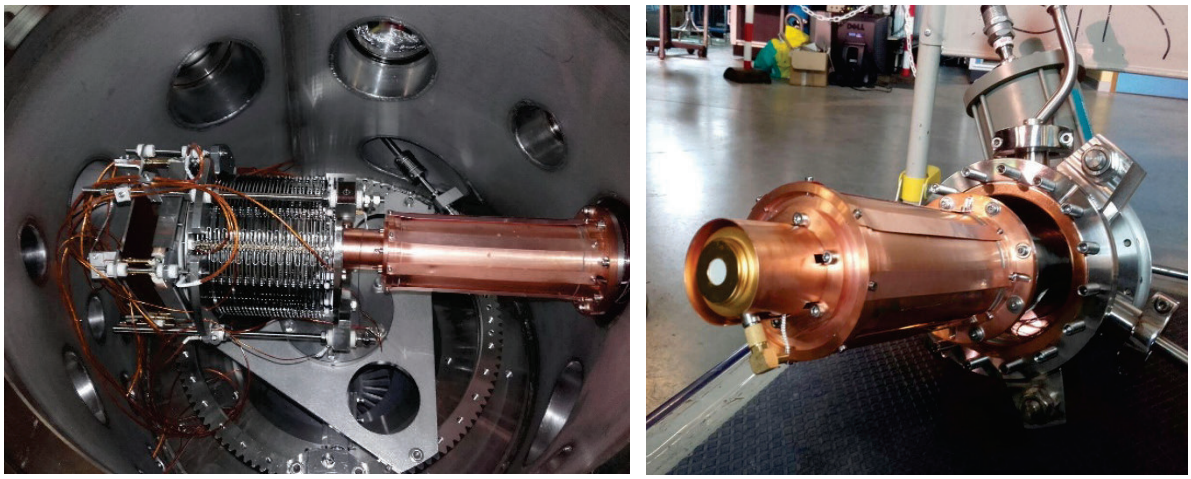

Figure 3.15 – Picture of the interior of AODO – TOF spectrometer, the cryostat and the quartz-crystal microbalance.

3.7.1 Ramp of AODO set-up

The preparation ramp of AODO is similar to that of CASIMIR. It enables mixture and preparation of different gases for deposition into the chambers. The AODO the ramp has two pre-chamber with one same volume. The deposition of the gas on the substrate is made by the opening of the valve between the ramp and the chamber, the pressure is increased from 10^{-8} to 10^{-6} mbar until the desired thickness is reached (the thickness is

monitor by QCM, see the following section). Since pyridine is liquid at room temperature it was possible to perform experiments using AODO. The nucleobases are solid, therefore for its deposition into the chamber, it necessitates a technical modification of the current set-up.

3.7.2 Quartz-crystal microbalance (QCM)

The quartz-microbalance is installed on the cold-finger, (see Fig. 3.15). It is possible to deposit gas into the chamber which condenses on the crystal. The QCM allows to study the variation of small amounts of mass (about 1 ng), i.e. deposition or loss of mass for example by sputtering. The QCM works very well at low pressures and in a large range of temperatures, making this device a simple and popular way to detect mass variation (Hayderer et al. 1999). Here we will describe it only briefly, for more details see Allodi et al. (2013).

The physical principle of this device is simple. It is based on the mass dependent change of the resonance frequency of the quartz crystal. Its resonant frequency occurs when the wavelength is equal to twice of the crystal thickness d. As long the variation of the mass is smaller than the mass of the crystal we can apply the following approximation:

Eq. 3.10
$$\frac{\Delta f}{f} = \frac{-\Delta m}{M_q}$$

Where M_q is the quartz crystal mass. The change of mass Δm is given by:

Eq. 3.11
$$\Delta m = -\Delta f \times \rho \times v/2f^2$$

Here ρ is the density of the quartz crystal. It is important to point out that the crystal is sensible to variation of the temperature, therefore is mandatory to work under temperature controlled conditions. The thickness of pyridine ice was determined by means of QCM (1.4 μm), see Figure 3.16.

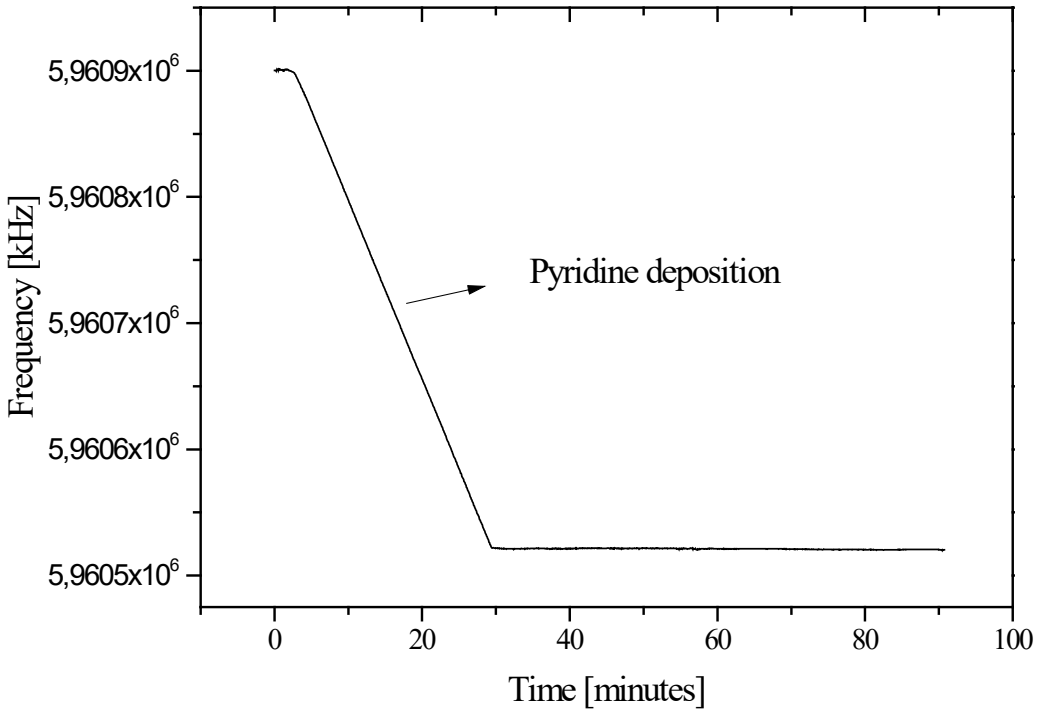

Figure 3.16 – Variation of the frequency of the QCM as a function of the time.

3.7.3 Mass spectrometer – Time-of-flight (TOF)

TOF technique – Principles

Time-of-flight mass spectrometry technique separates the ions and molecular ions upon their time of flight. The time of flight for a secondary ion take to travel the distance between the sample and the detector is a proportional of its (mass/charge)$^{0.5}$ ratio. The spectrometer has two regions of different electric fields ($\overrightarrow{E_1}$ and $\overrightarrow{E_2}$) as illustrated in Figure 3.17.

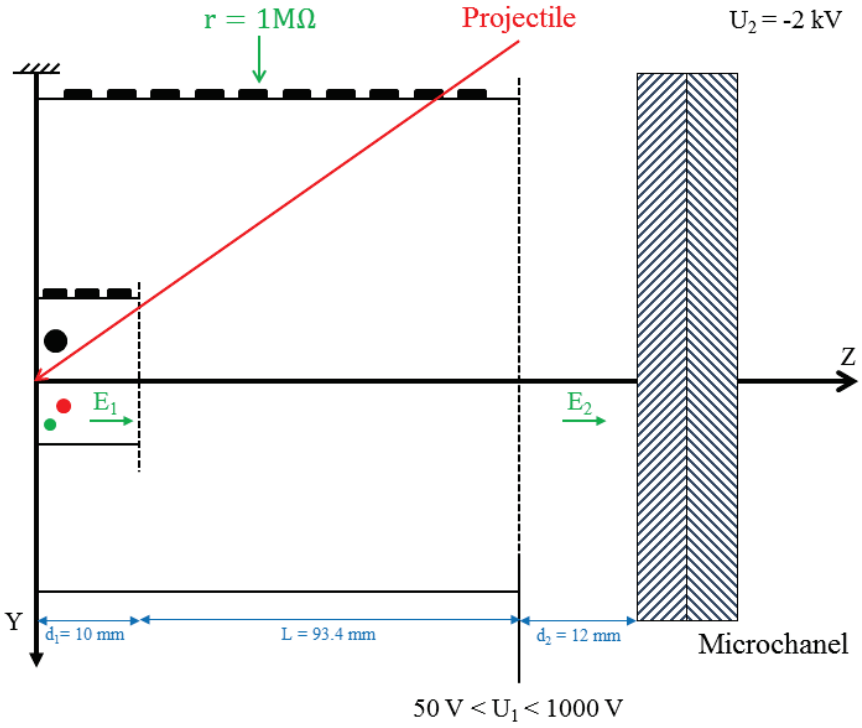

Figure 3.17 – Principle of extraction of secondary ions by spectrometry of time-of-flight.

The electric field $\overrightarrow{E_1}$ extracts the ions accelerating them, the electric field $\overrightarrow{E_2}$ accelerates the ions and increase the efficiency of the set-up.

The time-of-flight of a sputtered ion corresponds to the interval time between the start and the stop signals. The start signal is provided by the frequency generator of the ion beam pulsing device. When the secondary ions impinge the microchannel plates, this generates a ultra-fast pulse used as the stop signal (Langlinay 2014).

We used the TOF to investigate the secondary cation emission from the irradiation of pyridine ice at 12 K, see Chapter 6. To calibrate the mass spectrum converting channels to mass charge^{-1}, we assumed that the highest peak is protons, the second is ionized pyridine and the third is a cationic dimer of pyridine, Figure 3.18 shows the calibration of our system. Using the values obtained by the linear regression we calibrated our mass spectrum, see Chapter 6**.**

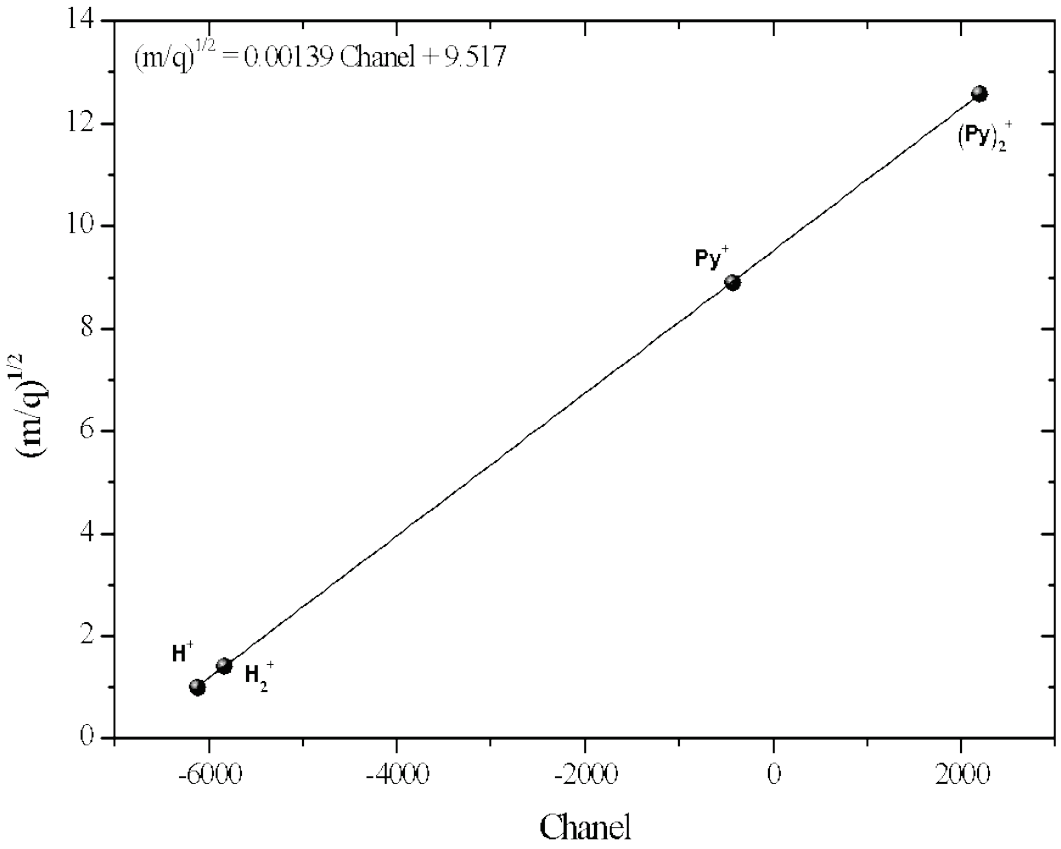

Figure 3.18 – Calibration curve for TOF experiments.

References

Akcöltekin, S., I. Alzaher, B. Ban d'Etat, T. Been, P. Boduch, A. Cassimi, H. Hijazi, et al. 2009. "AODO: Secondary Ion Emission and Surface Modification." *Nuclear Instruments and Methods in Physics Research Section B: Beam Interactions with Materials and Atoms* 267 (4): 649–51. doi:10.1016/j.nimb.2008.11.018

.

Allodi, M. A., R. A. Baragiola, G. A. Baratta, M. A. Barucci, G. A. Blake, P. Boduch, J. R. Brucato, et al. 2013. "Complementary and Emerging Techniques for Astrophysical Ices Processed in the Laboratory." *Space Science Reviews* 180 (1–4): 101–75. doi:10.1007/s11214-013-0020-8.

Barros, A. L. F. de, P. Boduch, A. Domaracka, H. Rothard, and E. F. da Silveira. 2012. "Radiolysis of Astrophysical Ices by Heavy Ion Irradiation: Destruction Cross Section Measurement." *Low Temperature Physics* 38 (8): 759. doi:10.1063/1.4743476.

Dartois, E., J. J. Ding, A. L.F. de Barros, P. Boduch, R. Brunetto, M. Chabot, A. Domaracka, et al. 2013. "Swift Heavy Ion Irradiation of Water Ice from MeV to GeV Energies: Approaching True Cosmic Ray Compaction." *Astronomy & Astrophysics* 557 (September): A97. doi:10.1051/0004-6361/201321636.

Griffiths, D. J. 2017. *Introduction to Quantum Mechanics*.

Günzler, H., and H.-U. Gremlich. 2002. *IR Spectroscopy: An Introduction*. Weinheim: Wiley-VCH.

Hayderer, G., M. Schmid, P. Varga, Hp. Winter, and F. Aumayr. 1999. "A Highly Sensitive Quartz-Crystal Microbalance for Sputtering Investigations in Slow Ion–surface Collisions." *Review of Scientific Instruments* 70 (9): 3696. doi:10.1063/1.1149979.

Hijazi, H., H. Rothard, P. Boduch, I. Alzaher, F. Ropars, A. Cassimi, J.M. Ramillon, et al. 2011. “Interaction of Swift Ion Beams with Surfaces: Sputtering of Secondary Ions from LiF Studied by XY-TOF-SIMS.” *Nuclear Instruments and Methods in Physics Research Section B: Beam Interactions with Materials and Atoms* 269 (9): 1003–6. doi:10.1016/j.nimb.2010.12.062.

Mathlouthi, M., A. M. Seuvre, and J. L. Koenig. 1986. “F.T.-I.R. and Laser-Raman Spectra of Cytosine and Cytidine.” *Carbohydrate Research* 146 (1): 1–13. doi:10.1016/0008-6215(86)85019-4.

Mejía, C., M. Bender, D. Severin, C. Trautmann, Ph. Boduch, V. Bordalo, A. Domaracka, X.Y. Lv, R. Martinez, and H. Rothard. 2015. “Radiolysis and Sputtering of Carbon Dioxide Ice Induced by Swift Ti, Ni, and Xe Ions.” *Nuclear Instruments and Methods in Physics Research Section B: Beam Interactions with Materials and Atoms* 365 (December): 477–81. doi:10.1016/j.nimb.2015.09.039.

Mejia, C. F., A. L. F. de Barros, V. Bordalo, E. F. da Silveira, P. Boduch, A. Domaracka, and H. Rothard. 2013. “Cosmic Ray-Ice Interaction Studied by Radiolysis of 15 K Methane Ice with MeV O, Fe and Zn Ions.” *Monthly Notices of the Royal Astronomical Society* 433 (3): 2368–79. doi:10.1093/mnras/stt902.

Pilling, S., D. P. P. Andrade, E. M. do Nascimento, R. R. T. Marinho, H. M. Boechat-Roberty, L. H. de Coutinho, G. G. B. de Souza, et al. 2011. “Photostability of Gas- and Solid-Phase Biomolecules within Dense Molecular Clouds due to Soft X-Rays: Photostability of Biomolecules in ISM.” *Monthly Notices of the Royal Astronomical Society* 411 (4): 2214–22. doi:10.1111/j.1365-2966.2010.17840.x.

Saïagh, K., H. Cottin, A. Aleian, and N. Fray. 2015. “VUV and Mid-UV Photoabsorption Cross Sections of Thin Films of Guanine and Uracil: Application on Their Photochemistry in the Solar System.” *Astrobiology* 15 (4): 268–82. doi:10.1089/ast.2014.1196.

Seperuelo Duarte, E., P. Boduch, H. Rothard, T. Been, E. Dartois, L. S. Farenzena, and E. F. da Silveira. 2009. “Heavy Ion Irradiation of Condensed CO_2 : Sputtering and Molecule Formation.” *Astronomy and Astrophysics* 502 (2): 599–603. doi:10.1051/0004-6361/200811359.

T. Langlinay. 2014. “Effects de L’irradiation Par Des Ions Lourds Multichargés Sur Des Cristaux et Des Glaces D’intérêt Astrophysique.”

Chapter 4 - Sample characterization

This chapter will present the preparation of grainy and film samples, their absorption spectra and the results from the different techniques used for their characterization. Our solid nucleobase samples were prepared using two different methods in order to condensate onto ZnSe windows: (1) by evaporation of the nucleobase solution onto ZnSe window heated to 100ºC and (2) by sublimation use of an oven under vacuum (10^{-5} mbar). Nucleobase powders were sublimated. Samples prepared using method (1) are observed under optical microscopy, see Figure 4.1. These samples are referred to as grainy due to their "grainy" aspect whereas "film" samples possess a smooth surface.

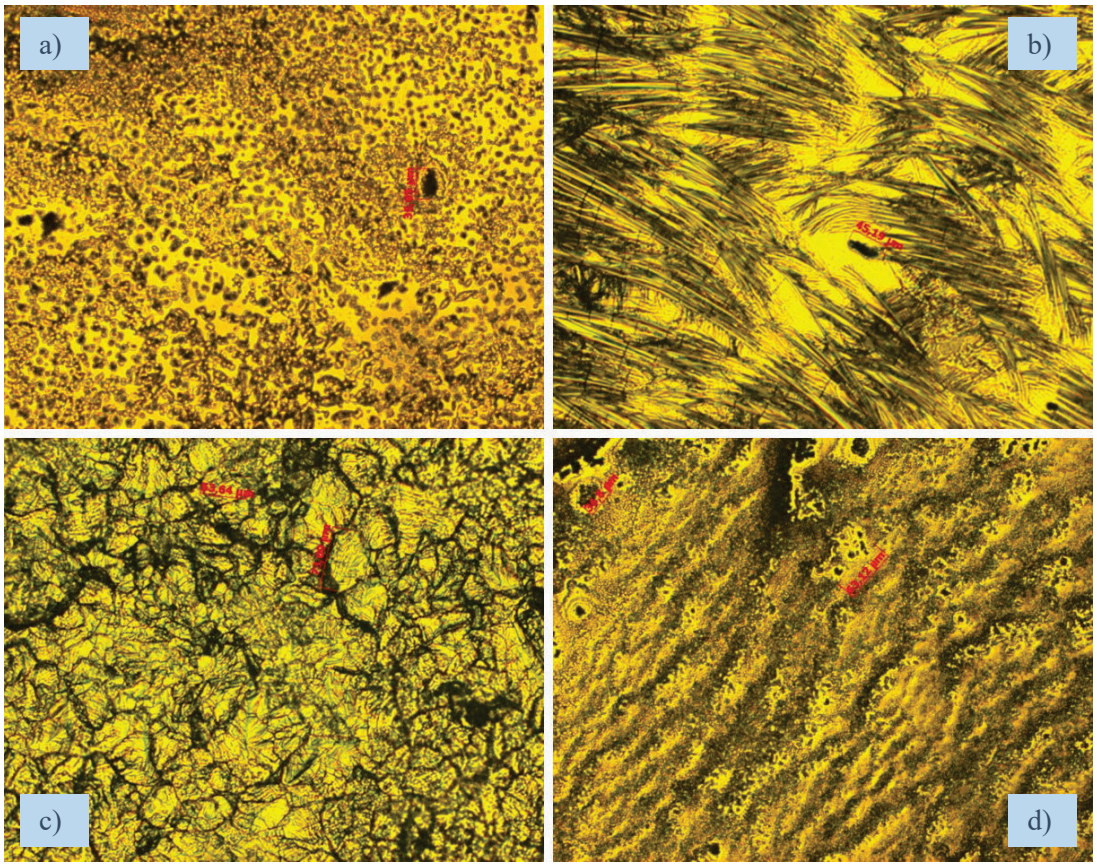

Figure 4.1 – Photos taken using optical microscopy, magnification of 100X. Grainy samples of adenine (a), cytosine (b), thymine (c), uracil (d).

The baseline of the grainy samples escalates (increases) in the shorter wavelengths (higher wavenumbers). This effect is due to the light scattering at the sample surface

caused by their irregular surface. For this reason, a base line correction was applied to the IR spectra of grainy samples in this work. Moreover, the relative intensity of the IR absorption peaks of grainy and film samples are different. This is likely due to the different environments of the molecules. We refer the reader to the Appendix for more details (from Appx. 2 to 4).

4.1 Adenine

Adenine ($C_5H_5N_5$) is a purine nucleobase formed by two heterocyclic rings. Figure 4.2 shows schematically the adenine molecule structure.

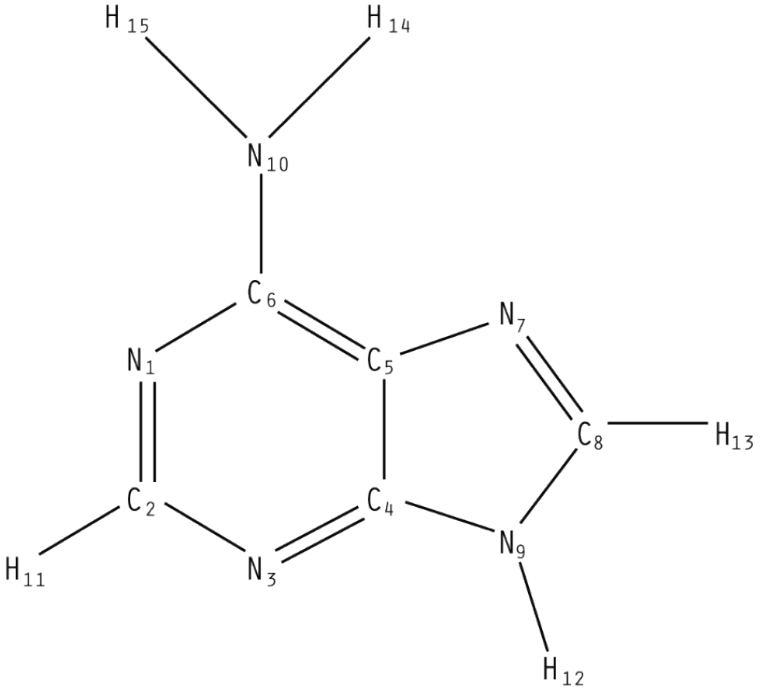

Figure 4.2 – The structure of the adenine molecule (schematic).

The IR spectra of grainy and film samples of adenine are very similar, see Figure 4.3. Both samples display a large absorption band between 3600 and 2000 cm^{-1}. In literature, this is known as the alpha (α) band (Saïagh *et al*. 2014). Within the alpha band, the adenine grainy sample is shifted to smaller wavenumbers (≈ 8 cm^{-1}). However, this

spectrum does not exhibit any shift in the region between 1800 and 700 cm^{-1}. The adenine film sample does not exhibit absorption peaks at 872 and 847 cm^{-1}. The IR spectrum of adenine in a KBr pellet, (Mohammed Mathlouthi, Seuvre, and Koenig 1984; Mohamed et al. 2009).

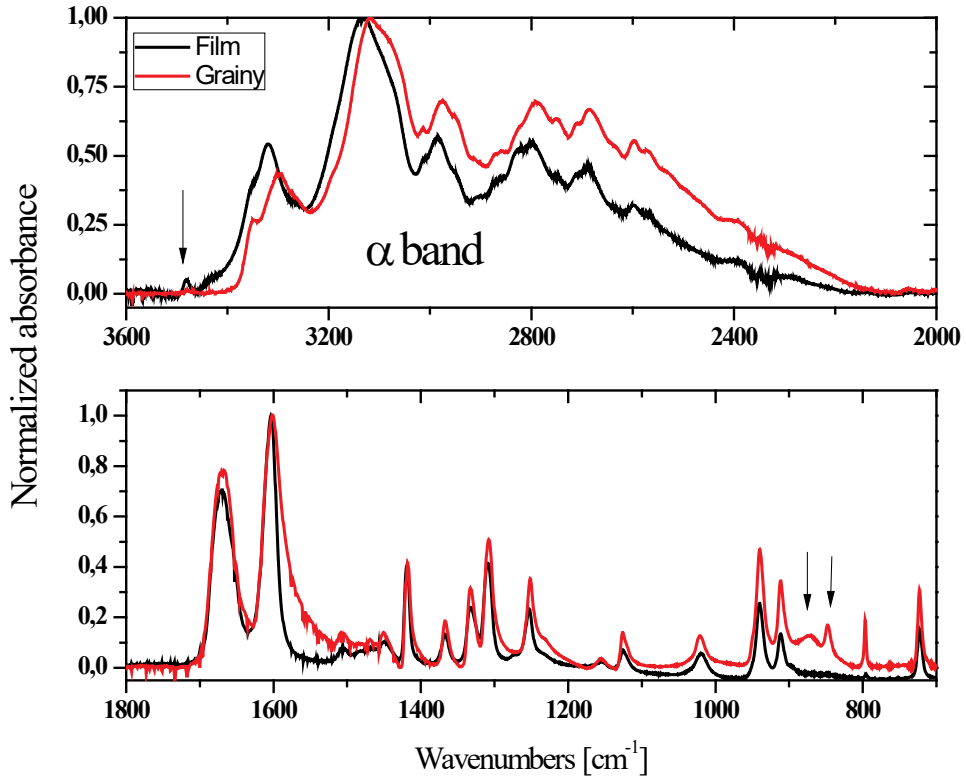

Figure 4.3 – Normalized absorption spectra of grainy and film adenine at room temperature. The arrows indicate the different absorption peaks observed in grain and film sample.

These vibrations correspond to the out-of-plane wagging of C_8H (846 cm^{-1}) and NCN deformation of ring **6** of adenine (872 cm^{-1}). This last absorption peak displays a shoulder at 896 cm^{-1}. Adenine film and grainy samples have small absorption peaks at 3481 cm^{-1} but the intensity of absorption at this peak in the grainy sample is too weak to be observed. Moreover, IR absorption spectrum shows that the band intensity differs between the adenine grainy and film samples, see Table 4.1. The minor variations are plausibly due to the different micro environments of the adenine molecules.

We used the linear relationship reported by Saïagh et al. (2014) between the thickness of the adenine samples and the area of the alpha band. In the case of the grainy samples, a solution at a specific concentration, allowed to determine the mass of adenine deposited on the ZnSe window.

Table 4.1 – Absorption peak position of grainy and film samples of adenine and a comparison with spectra reported in the literature at room temperature.

Assignment	*Definition*	*Mohamed et al (2009)*	*Saiägh et al (2014)*	*Grainy adenine*	*Film adenine*
NH_2	anti-symmetric stretch	3426vw			
N_9H	Stretch	3347sh		3347	3348
NH_2	Symmetric stretch	3296s	3314	3293	3432
C_8H	Stretch	3119vs	3122	3115	3130
		2980	2984	2975	2985
			2798	2790	2799
			2689	2685	2691
C_2H	Stretch	2980s	2984		2985
NH_2	deformation (scissors)	1673vs	1665	1668	1670
CN R(6)	ring stretch	1603vs	1600	1600	1603
CC R(6)	ring stretch	1603vs	1600	1600	1603
CN R(5)	ring stretch	1506sh		1508	1500
CN R(6)	ring stretch	1483sh			
CC R(6)	ring stretch	1451m		1451	1448
C_2H	in-plane deformation	1420s	1417	1418	1419
C_6N_{10}	Stretch	1368w	1366	1367	1367
CN R(5)	ring stretch	1335s	1330	1332	1333
CN R(6)	ring stretch	1309s	1307	1308	1309
C_8H	in-plane deformation	1252s	1251	1252	1252
CN R (5)	ring stretch	1252s	1251	1252	1156
CN R (5)	ring stretch	1126m	1120	1126	1126
N_9H	in-plane deformation	1065sh			
NH_2	Rock	1025m	1023	1022	1020
C_2H	Wagging	939s		939	939
NCN R(5)	ring deformation	913s		911	911
NCN R(6)	ring deformation	872sh		874	895
C_8H	Wagging	846sh		847	849
R(6)	ring torsion	797w		797	796
R(6) breath	ring breathing	723m		723	723

Now let us look at the small modifications in the adenine spectrum between room temperature and at low temperature T = 12 K, see Figure 4.4.

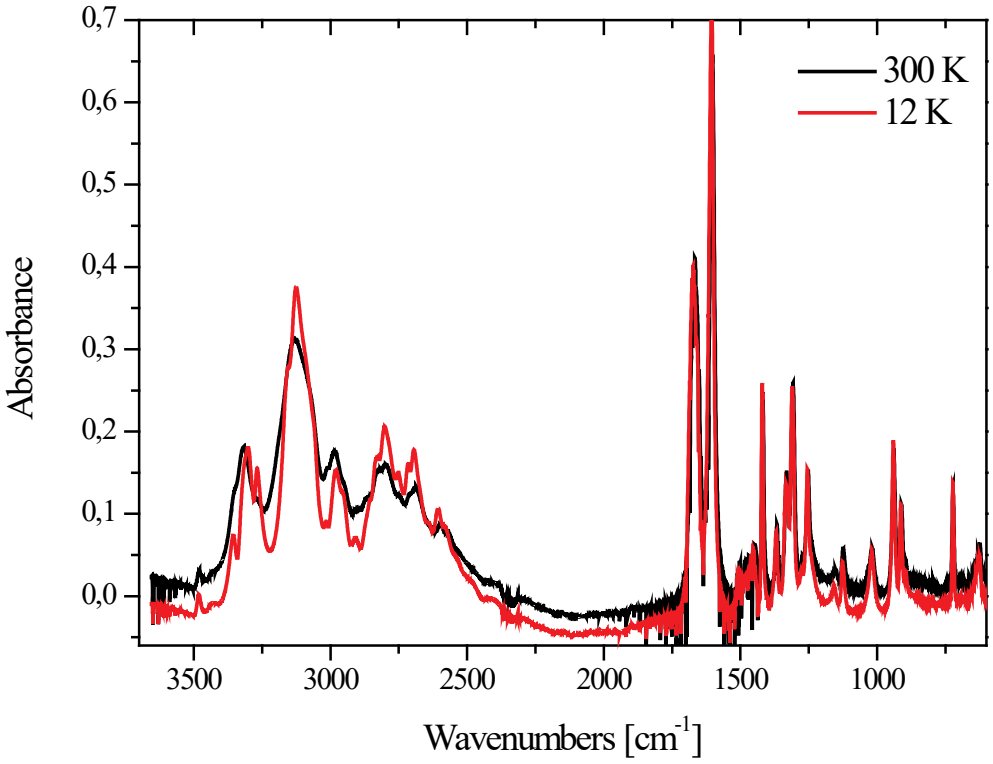

Figure 4.4 – Adenine film IR spectra at room temperature and at 12 K.

The spectrum of adenine at 12 K exhibits a new absorption band at 3260 cm^{-1} and a small shift to higher wavenumbers. The band at 3115 cm^{-1} becomes thinner and the absorption peak in the alpha band is better resolved. Within the region of 1600-800 cm^{-1} a small shift to higher wavenumbers ($\Delta\kappa \approx 2$ cm^{-1}) is observed.

4.2 Cytosine

Cytosine ($C_4H_5N_3O$) is a pyrimidine nucleobase formed by a single heterocycle ring, see Figure 4.5.Grainy and film cytosine display similar spectra, however as compared to the adenine samples the differences are more evident. Figure 4.6 displays the grainy and film

cytosine IR absorption spectra.

We will refer to the large absorption band of cytosine samples between 3600 and 2000 cm^{-1} as χ band, this is region is characteristic of vibration modes of C-H,N-H and O-H.

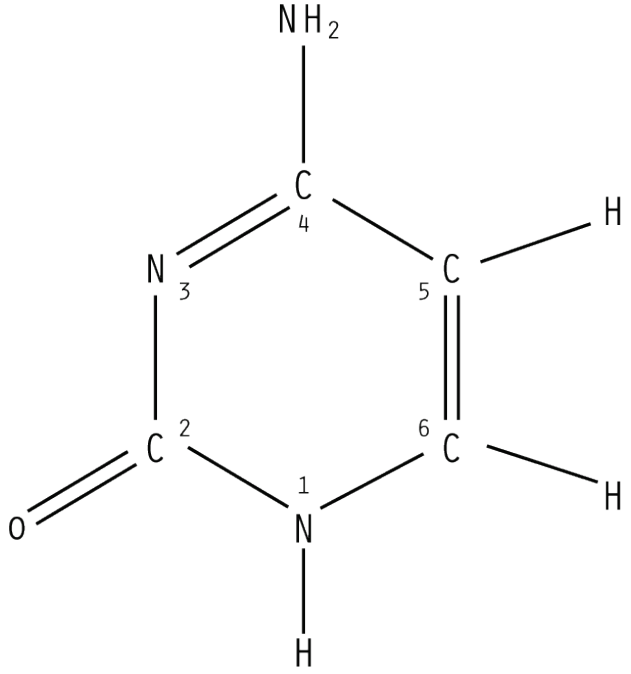

Figure 4.5 – The molecular structure of cytosine (schematic).

From the Figure 4.6 it is clear that grainy and film cytosine samples display absorption spectrum with different band absorption intensities. The cytosine film exhibits an absorption peak at 3381 cm^{-1} which has a shoulder at 3345 cm^{-1}; whereas grainy cytosine displays two peaks in the same region, 3381 and 3345 cm^{-1}.

In the region of 1800 and 600 cm^{-1} grainy cytosine shows an absorption peak at 1703 cm^{-1} that is not observed in the spectrum of cytosine film, this absorption peak is also observed in the IR absorption spectrum of cytosine in KBr pellet (Mohamed Mathlouthi, Seuvre, and Koenig 1986). The cytosine film neither exhibits an absorption peak at 1626 cm^{-1} nor at 820 cm^{-1}. Table 4.2 displays the absorption peaks of grainy and film cytosine spectrum and includes the peaks reported by Mohamed Mathlouthi, Seuvre, and Koenig

(1986) for cytosine in KBr pellet.

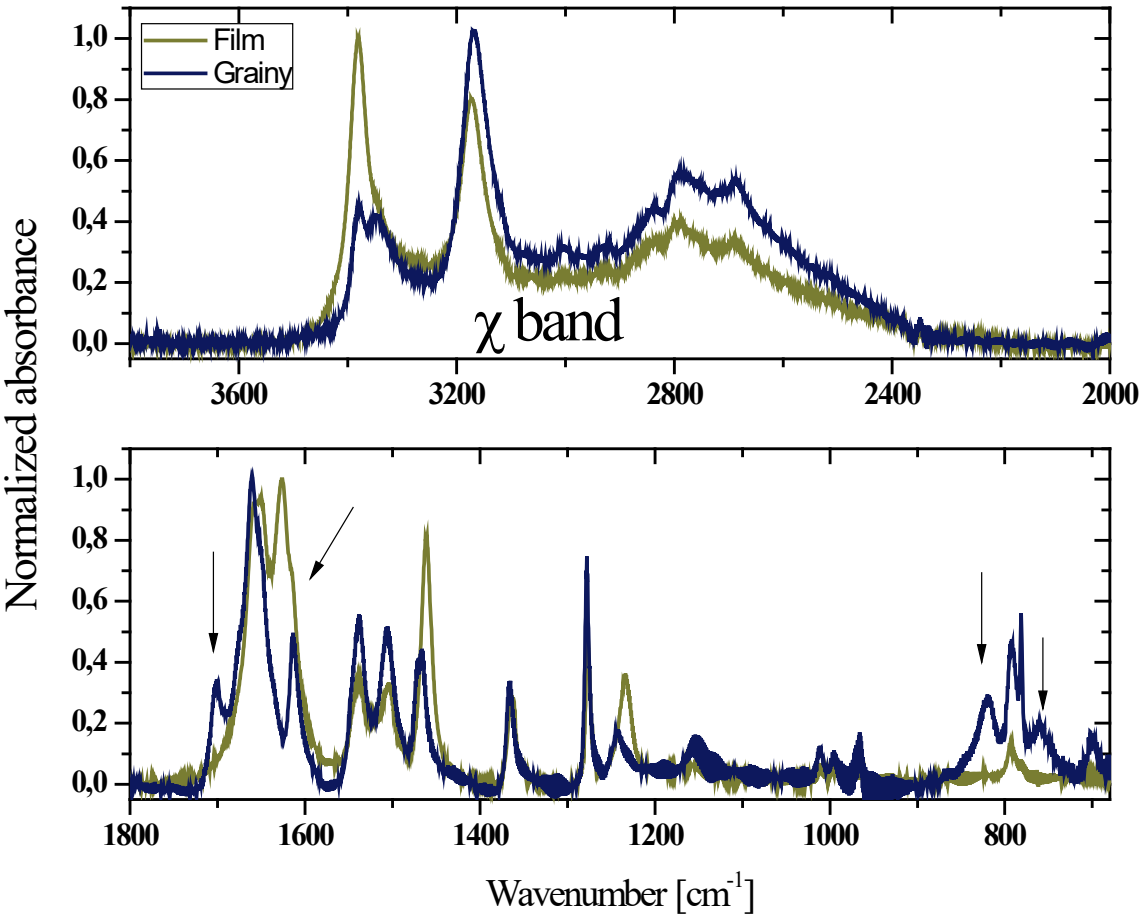

Figure 4.6 – Normalized IR absorption spectra at room temperature of grainy and film cytosine samples.

Table 4.2 – Absorption peak position of grainy and film samples of cytosine and a comparison with spectra reported in the literature at room temperature.

ν_i	*Assignment*	*Definition*	(Mohamed et al. 1986)	*Grainy cytosine*	*Film cytosine*
	NH_2	anti-symmetric stretching	3384	3381	3381
				3346	3349sh
	NH_2	symmetric stretching	3180	3170	3173
			2840	2840	2840
	CH	stretching	2796	2793	2794
	CH	stretching	2690	2686	2688
	NH_2	Bending	1705	1703	
	C_2O	stretching	1667	1660	1658
					1627
	$C_5=C_6$	stretching	1616	1614	1615sh
	NH	bending in plane	1540	1539	1538
	$C_4=N_3$ and C_4-N_4	stretching	1505	1508	1506
	C_4-N_3 and C_2-N_3	stretching	1469	1469	1463
	C=C-H	bending	1366	1366	1365
	C_2-N_1 and C_6-N_1	stretching	1280	1277	1276
	C_4-N_4	Stretching	1240	1242	1235
	C-O	stretching	1155	1154	1157
	NH_2	rocking mode	1100		1100
	N_1-C_6-H	Bending in plane	1012	1011	1010
	C_4-C_5-H	Bending in plane	995	996	993
	C_4-C_5	Stretching	966	967	961
	NH	bending	822	820	825
	Ring	Stretching breathing mode	794	793	794
			783	781	781
			758	762	
	C_5-C_4-N_4	bending	700	700	703

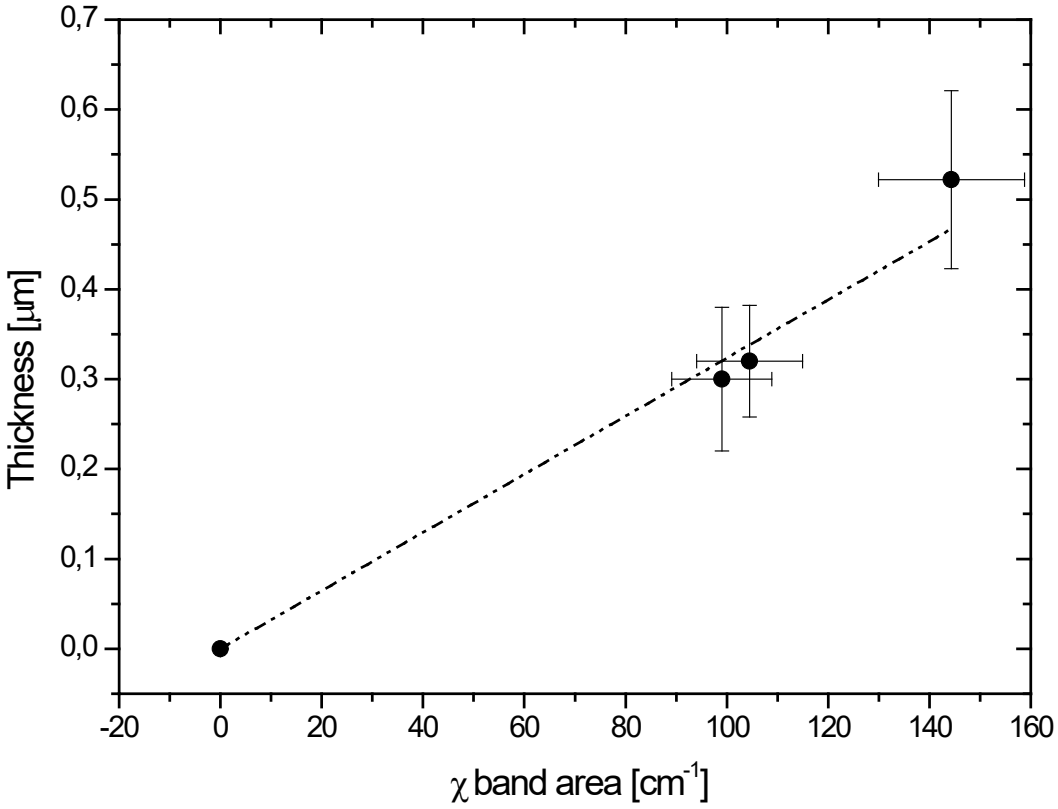

Figure 4.7 – Cytosine film thickness measured by profilometer as a function of IR χ band area.

We were able to determine a linear relationship between the thickness (d), obtained by profilometry, of our cytosine film samples and its IR absorption of the χ band, Figure 4.7 under the form: $d = (3.2 \pm 0.4) \times 10^{-3}$ X, where X is the χ band area. As far we know, the band strength of cytosine in solid condensed phase was not reported in the literature. To determine it, we adopted the cytosine density as 1.5 g cm^{-3}, calculated the column density, and correlated it with the χ band, Figure 4.7.

The linear regression gives an angular coefficient equal to $(3.7 \pm 0.2) \times 10^{-16}$, the equation 4.1 shows the relationship between the A_{value} and the column density, using ($\ln 10 \approx 2.3$), we have:

Eq. 4.1

$$A_{value\,\chi} = 2.3\ \frac{Area_{\chi}}{N}$$

We determined that $A_{value\ \chi} = (8.5 \pm 0.5) \times 10^{-16}$ cm molecule^{-1}. Additional A_{value} absorption peaks of cytosine film at room temperature are available in Appx. 5.

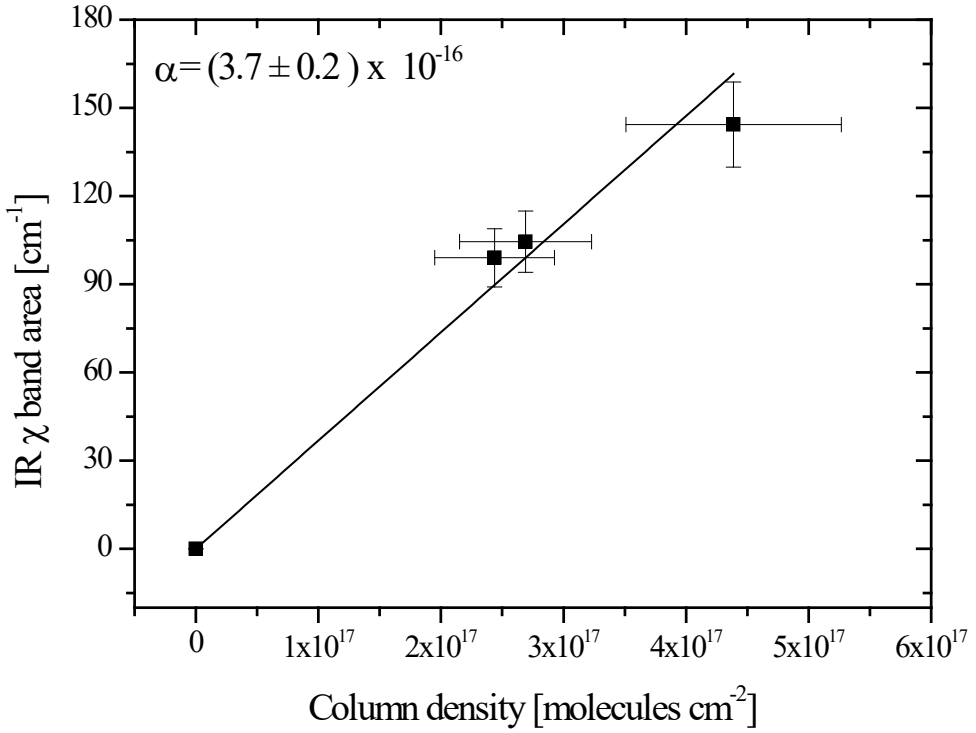

Figure 4.8 – IR χ band area (3600-2000 cm^{-1}) as a function of the column density.

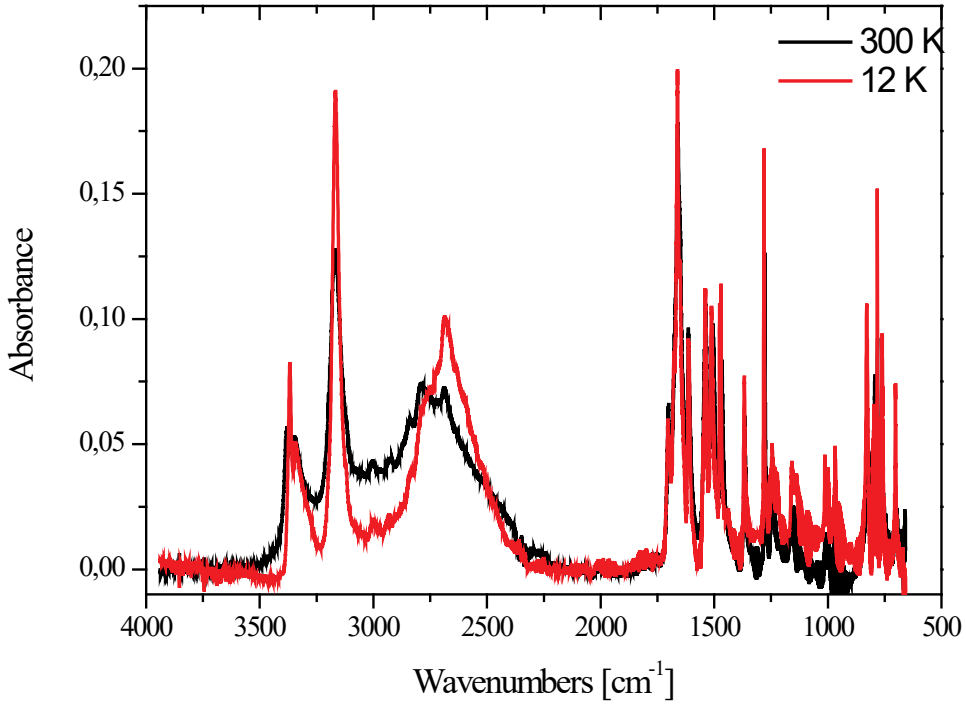

Figure 4.9 – Grainy cytosine IR spectra at room temperature and at 12 K.

At low temperature (12 K) the IR absorption spectrum of cytosine samples present small modifications, Figure 4.9. Absorption peaks of the cytosine spectrum become better resolved, the χ band was shifted to smaller wavenumbers ($\Delta\kappa \approx 3$ cm^{-1}). At region of 1600-800 cm^{-1} we observed a shift of 2 cm^{-1} in the peak positions.

4.3 Thymine

Thymine ($C_5H_6N_2O_2$) is a pyrimidine nucleobase, Figure 4.10. Being very similar to the nucleobase uracil (see Chapter 3), thymine is often referred to as 5-methyl uracil.

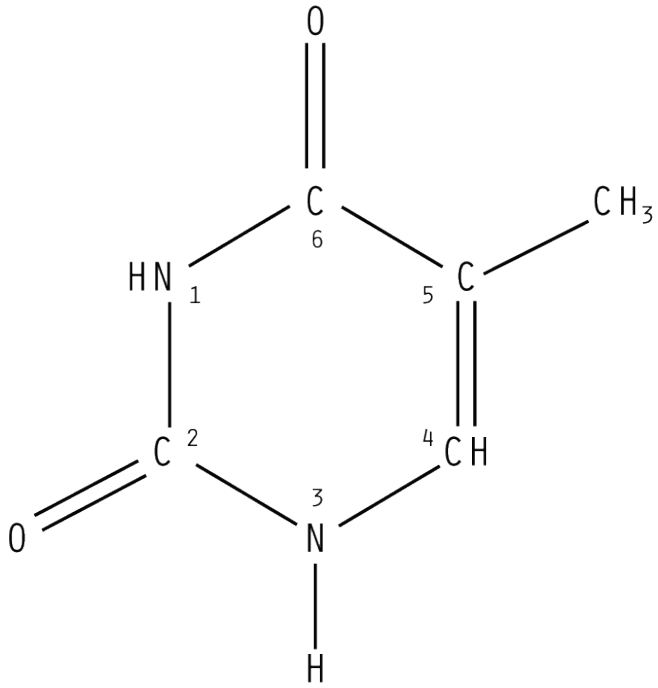

Figure 4.10 – The molecular structure of thymine (schematic).

Samples of grainy and film thymine display very similar IR absorption spectra, Figure 4.11. The IR absorption peak of the thymine film sample is better resolved, whereas the grainy sample is presented as a shoulder. It is observed that the IR absorption spectra is in agreement with those reported in literature, however the absorption peak at 1758 cm^{-1} is shifted by 20 cm^{-1} in comparison with thymine IR spectra embed in KBr matrix, Table 4.3.

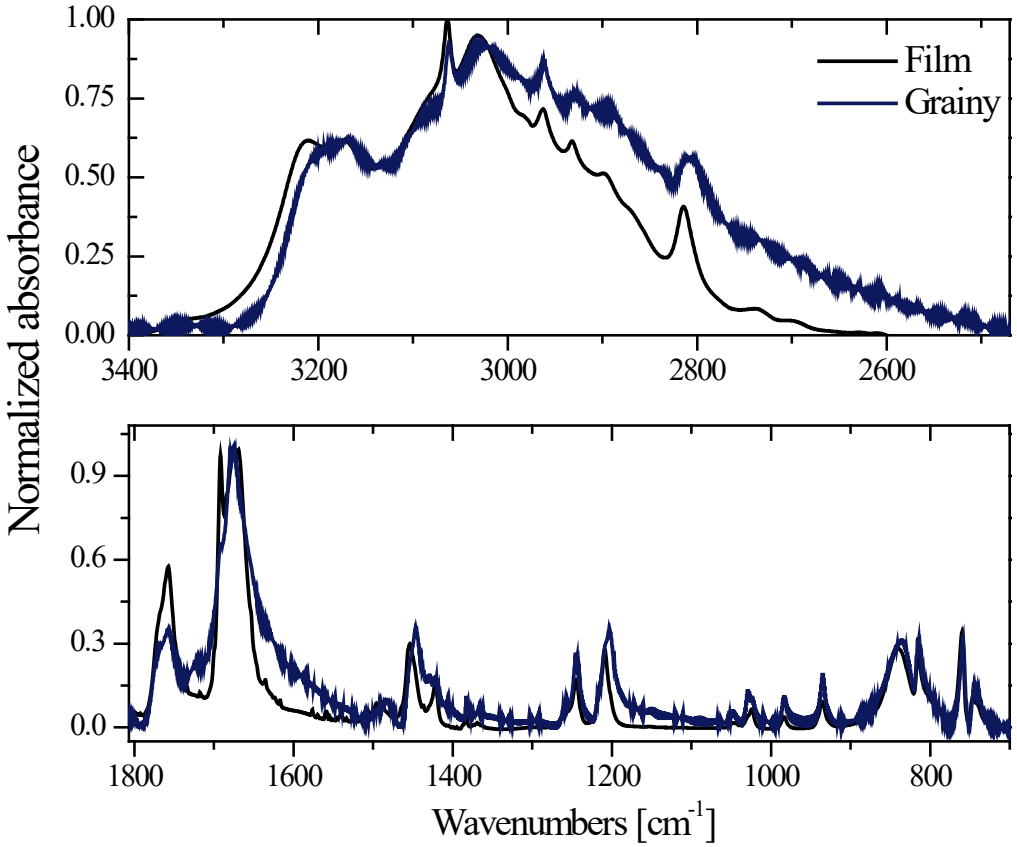

Figure 4.11 – Normalized IR spectra of grainy and film thymine at room temperature.

The observed thymine spectra displays some differences when compared with that reported in the literature (Singh 2008). The band at 1758 cm^{-1} and 1690 cm^{-1} are shifted at 20 cm^{-1} and 10 cm^{-1} in comparison with that bands reported, Table 4.3.

Table 4.3 – Peak position and assignment of our thymine samples and those reported by Singh (2008) at room temperature.

ν_i	*Assignment*	*Definition*	(Singh 2008)	*Film Thymine*	*Grainy Thymine*
	N_1H	Stretching	3185	3211	3211
	N_3H	Stretching	3160	3169	3169
	C_6H	Stretching	3060	3064	3062
				3029	3025
				2961	2962
	CH_3	anti-symmetric	2925	2932	2930
	CH_3	anti-symmetric	2895	2896	2892
				2814	2810
	$C_2=O_7$	Stretching	1738	1758	1758
	$C_5=C_6$	Stretching	1640		
	$C_4=O_8$	Stretching	1680	1676	1676
				1690	1690
	N_1H	in-plane bending	1505	1496	1495
	CH_3	Deformation	1465	1453	1453
	ring	Stretching	1445	1445	1446
	CH_3	Deformation	1430	1430	1428
	N_3H	in-plane bending	1420	1423	1423
	CH_3	deformation umbrella	1380	1382	1383
	C_5-CH_3	Stretching	1360	1367	1367
	ring	Stretching	1300	1292	
	ring	stretching Kekuele	1240	1244	1244
				1215	
	C_6H	in-plane bending	1195	1209	1202
	CH_3	Rocking	1145	1150	
				1047	1046
	ring	Stretching	1030	1024	1027
	ring	angle bending	985	983	981
	C_6H	out-of-plane bending	940	935	934
	CH_3	Rocking	910		
	N_3H	out-of-plane bending	850	839	836
	N_1H	out-of-plane bending	815	815	814
	$C_2=O_7$	out-of-plane bending	760	759	759
	$C_4=O_8$	out-of-plane bending	745	745	744

At 20 K thymine (film and grainy) presents a similar behaviour. We observed an increase of absorption in the large absorption band between 3400 cm^{-1} and 2000 cm^{-1}. Figure 4.12 shows the IR spectra of thymine film at 300 K and 20 K, respectively. We also observed an increase of the absorption peak at 3029 cm^{-1}. At smaller wavenumbers (from 1800 cm^{-1} to 700 cm^{-1}) we also observed a small shift to higher wavenumbers (≈4 cm^{-1}) and the absorption peaks are better resolved at low temperature (20 K).

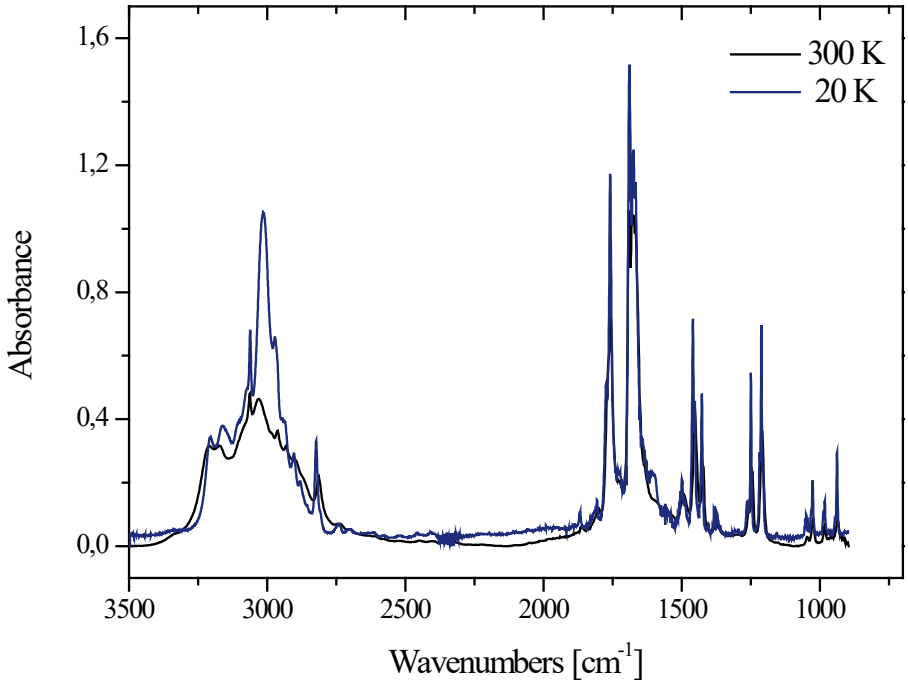

Figure 4.12 - IR absorption spectra of thymine film at 300 and 20 K.

4.4 Uracil

The pyrimidine nucleobase uracil ($C_4H_4N_2O_2$) is found in the composition of RNA macromolecule but is absent in DNA. As previous stated, uracil is very similar to thymine with the slight molecular difference that in uracil the radical methyl at C_5 position is substituted by a hydrogen atom, Figure 4.13.

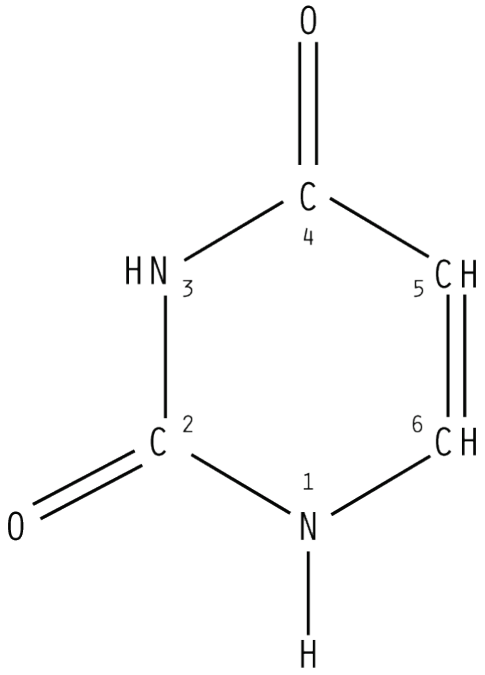

Figure 4.13 – The molecular structure of uracil (schematic).

Only grainy samples of uracil were prepared for our experiences because of its high solubility in water and ethanol. Figure 4.14 shows the normalized IR of grainy uracil and a spectrum of uracil extracted from NIST database.

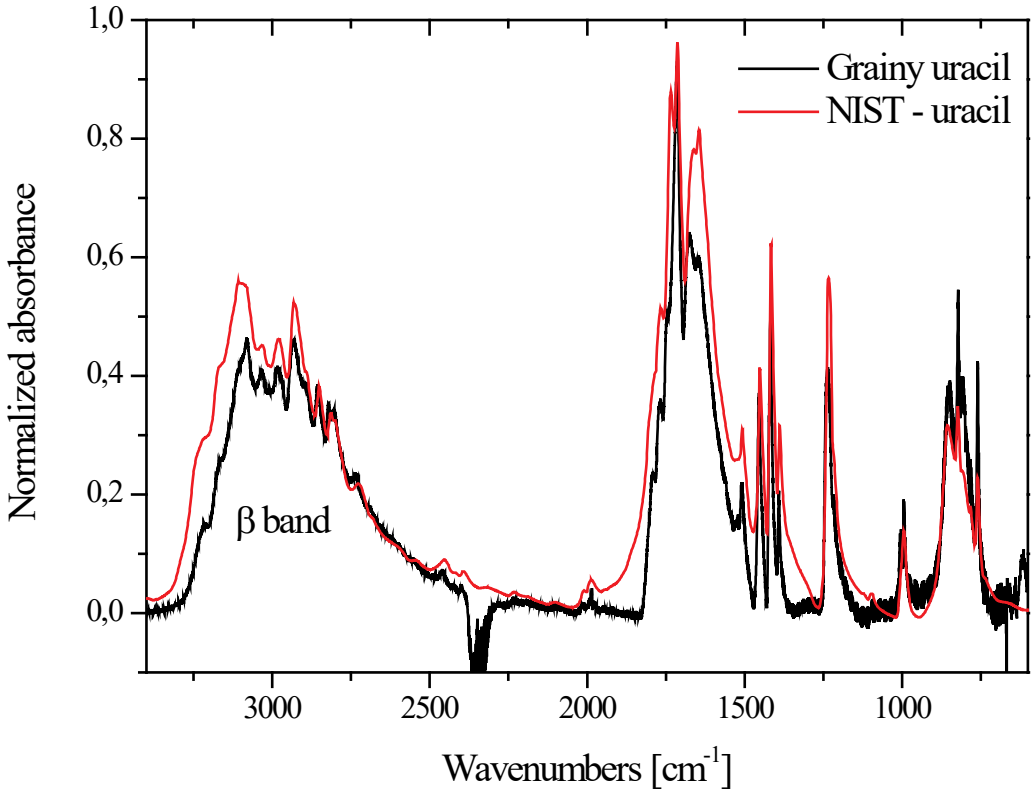

Figure 4.14 - IR grainy uracil and uracil spectra extracted from NIST database.
Ref: http://webbook.nist.gov/cgi/inchi?ID=C66228&Type=IR-SPEC&Index=2#IR-SPEC

From Figure 4.14 is possible to see that our uracil sample is in good agreement with that published in the NIST database. Some differences in the relative intensities of the peak positions appear. The large absorption peak between 3400-2500 cm^{-1} is referred to as beta (β) band by Saïagh et al. (2015). They reported a linear relationship between the β band area and the thickness of their uracil film. Table 4.4 displays the peak positions and assignments of uracil IR spectrum.

Table 4.4 – Peak position and assignment of our grainy uracil samples and those reported in literature at room temperature.

Assignment	*Definition*	(Singh 2008)	(Susi and Ard 1971)	(Saïagh et al. 2015)	*Grainy uracil*
NH	Stretching	3180			
NH	Stretching	3160	3160	3160-	3160
	Stretching	3095	3100		3106
	Stretching	3060	3080	3080	3080
	Stretching				3037
	Stretching				2984
	Stretching				2896
C=O	Stretching			1790	1791
					1770
	stretching	1735			1745
C=O	stretching	1690	1716	1716	1715
C=C	stretching			1675-	1677
C=C		1650			1642
	bending				1615
NH	stretching	1510	1508	1508	1509
ring	bending	1445	1453	1453	1454
NH	bending	1420	1417	1417	1417
CH	stretching	1310	1390	1390	1391
ring	bending out-of-phase	1235	1238	1238	1237
			1217		1217
ring	stretching	1090	1099		
ring		1010	1003		1003
ring	angle bending	995			994
NH	bending out-of-plane	865			859
NH	bending out-of-plane	820			821
			781		809
C=O	bending out-of-plane	765			759

The differences observed in uracil (Table 4.4) and thymine (Table 4.3) can be due to different environments of the molecules: embedded in a matrix of KBr, in a form of crystalline form or as thin film. Furthermore, there is a possibility of the presence of different tautomeric forms. Indeed, Saïagh et al. (2015) have observed two different tautomers in their uracil films. A decrease of 1.2 % of the β band area at 12 K is observed although that the intensity of the absorption peak area at 2941 cm^{-1} increases, Figure 4.15. Within the wavenumber range from 1600 to 600 cm^{-1}, it is observed that the spectrum at 12 K is shifted by 2 cm^{-1} to higher wavenumbers.

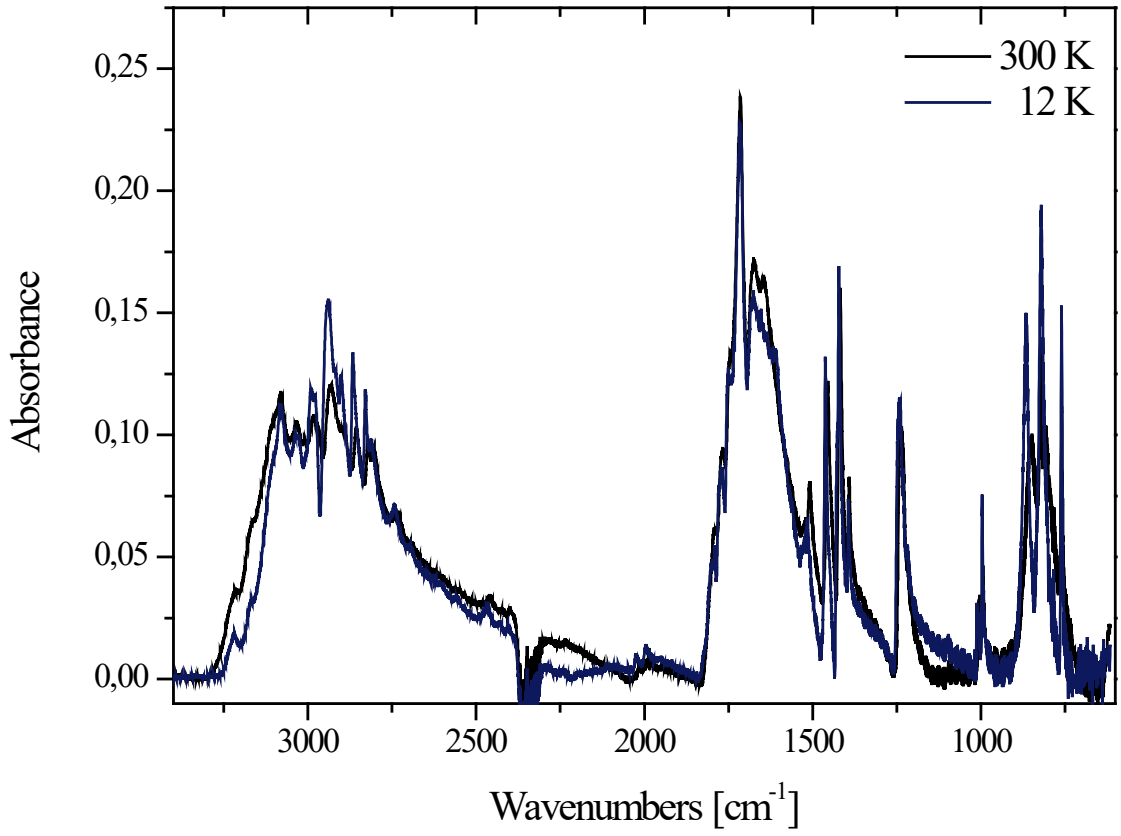

Figure 4.15 - IR spectra of uracil grainy sample at 300 K and 12 K.

4.5 Guanine

Guanine ($C_5H_5N_5O$) is a purine nucleobase formed by two heterocyclic rings, Figure 4.16. Due to the insolubility of guanine in water or ethanol, only film samples of guanine were prepared for our experiments.

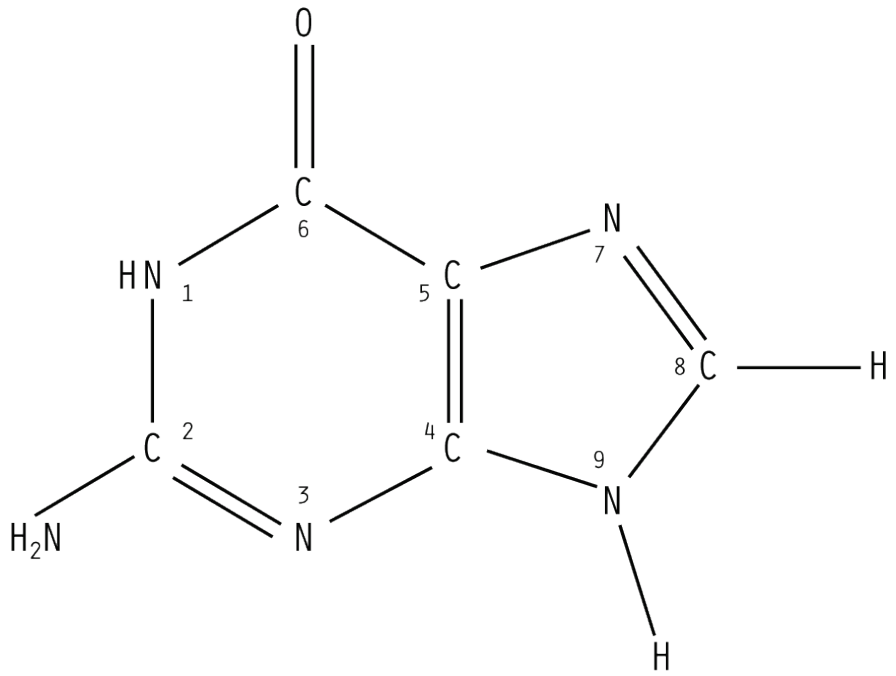

Figure 4.16 – Molecular structure of guanine (scheme).

The IR spectrum of guanine, Figure 4.17, is very similar to that reported by Saïagh et al. (2015). In their work, they refer to the large absorption band between 3600 and 2000 cm^{-1} as "α band". To avoid any confusion with the alpha band of adenine. We will refer to this large absorption band as the gamma (γ) band. Moreover, they reported a linear relationship between the area of the γ band and the film thickness. Here, it will be used in order to determine the thicknesses or the column density of our guanine film samples.

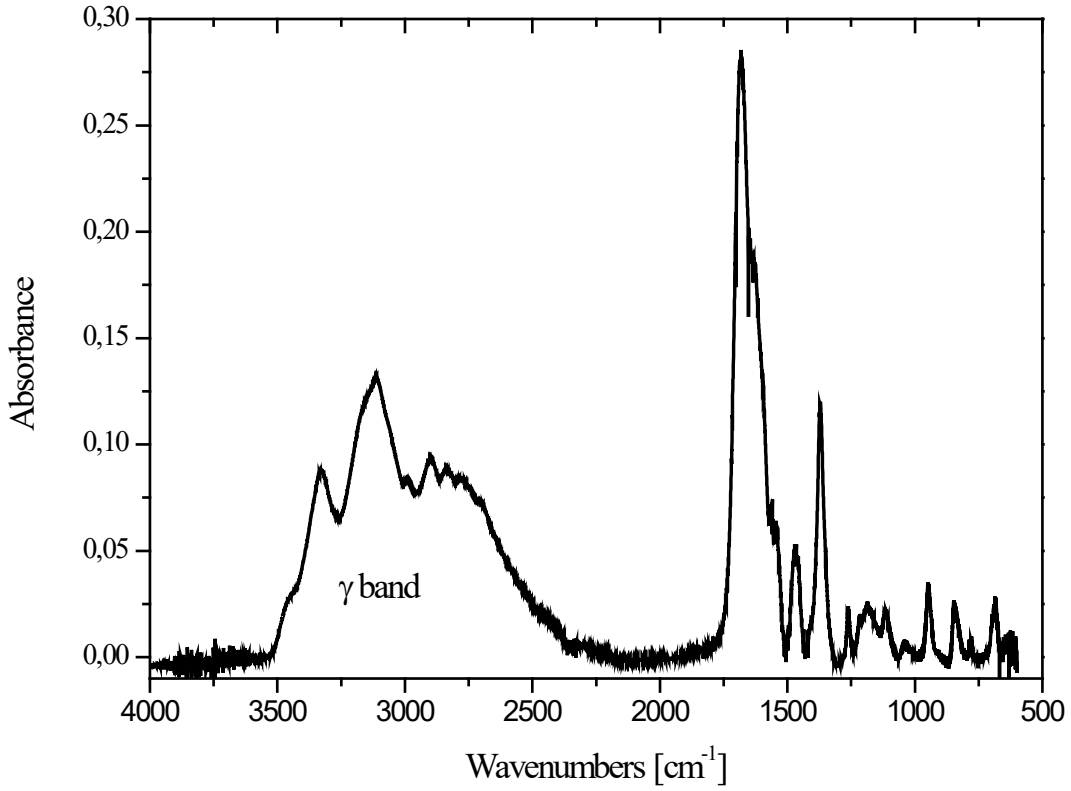

Figure 4.17 – Guanine film IR absorption spectrum at room temperature.

Table 4.5 displays the peak position and possible assignments of our guanine film and those reported in the literature. Table 4.5 includes the works of Mathlouti et al. (1986b) where they reported the IR absorption spectrum of guanine in a KBr pellet and the work of Saïagh et al. (2015) reporting the IR absorption of guanine film. From the Table 4.5, we can also see the peak positions are closer than those reported in their literature, the small differences observed between guanine film IR spectra of our work and that reported by Mohamed et al. (1986b) is probably due to differences of the micro neighborhood of the molecules as they were embed in a KBr matrix. In the present work, the guanine molecules are surrounded by other guanine molecules.

Table 4.5 – Peak position and assignment of guanine film samples and those reported in literature at room temperature.

Assignment	*Definition*	*(Mohamed et al. 1986)*	*(Saïagh et al. 2015)*	*Guanine film*
NH2	antisymmetric stretching	3334	3330	3329
NH2	Stretching	3122		3117
NH	Stretching	2912	2898	2899
		2852		2840
CH	stretching	2780	2699	2782
CH	stretching	2700		2697
C=O and NH	stretching and bending	1700	1674	1682
C=O	stretching	1676		1626
C=N	stretching	1566	1563	1564
C=C	stretching	1554		1542
N=C and C-N	Stretching	1480		
CNH	bending	1465	1467	1467
N=CH	bending	1420		
CNH, CH and CN	bending and stretching	1375	1372	1370
CNH, CH and CN	bending and stretching	1358		
C-N	stretching	1264	1263	1261
C-NH_2	stretching	1216		1214
CH	bending in plane	1175	1180	1189
		1150		1115
C-N=C	bending	1120		
NH_2	rocking	1043		1046
N-C=N and N-C-N	bending	950		
NH	bending out-of-plane	880		
C-C	stretching	852		849
NH	bending	790		
		780		779
		727		
ring	bending	704		
	breathing	690		686

The change of the temperature, from 300 K to 12 K, does not have a big impact in the IR spectrum of guanine, Figure 4.18. It was observed that the γ band area increased and within the γ band area there was slight shift toward smaller wavenumbers (≈ 4 cm^{-1}).

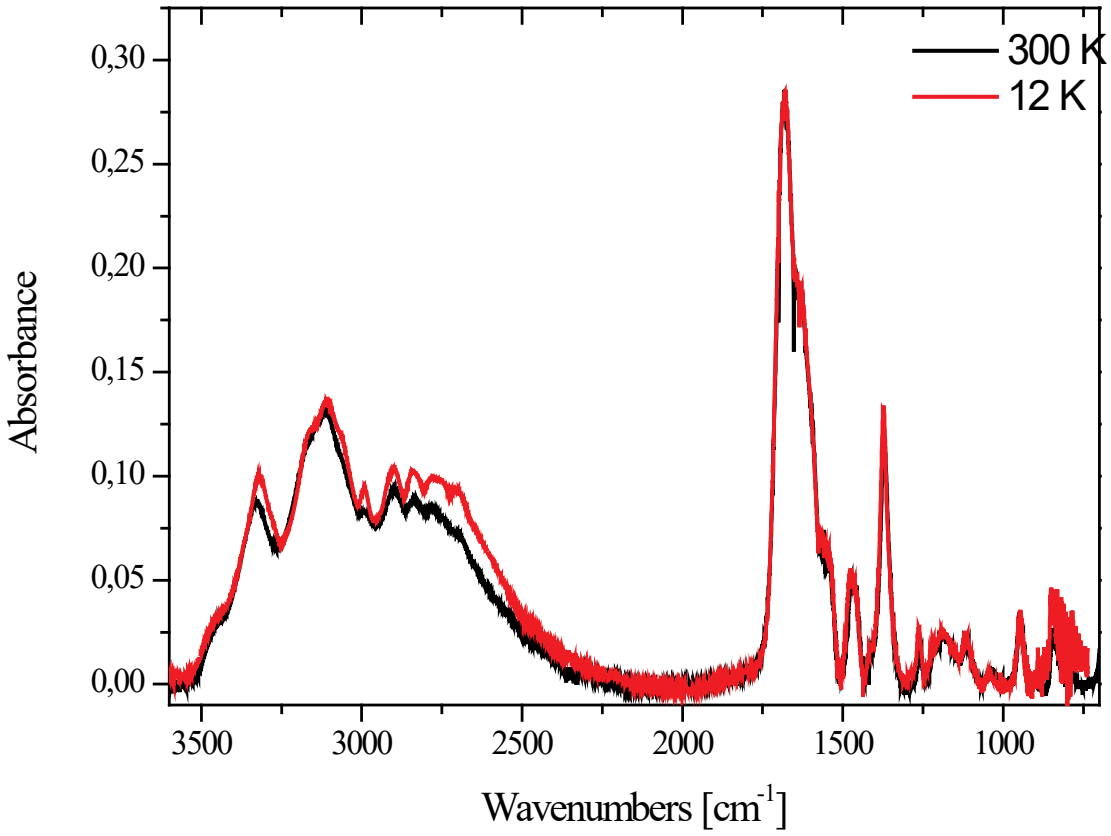

Figure 4.18 - IR spectra of guanine film sample at 300 K and 12 K.

4.6 Pyridine

Pyridine (C_5H_5N) is an AHM isoelectronic similar to benzene (C_6H_6), Fig 4.19.

a)

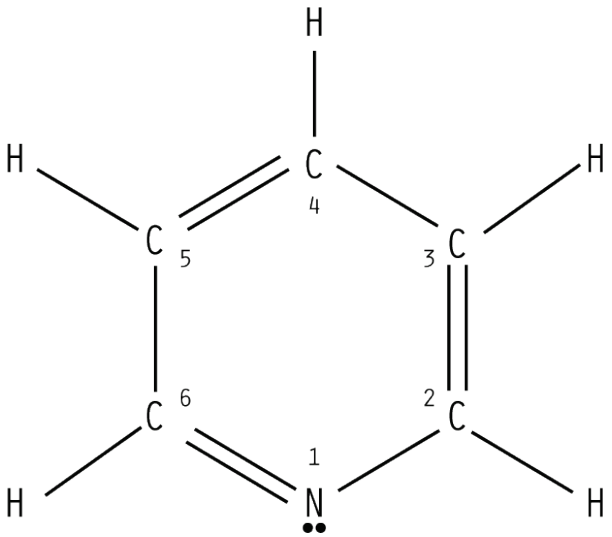

b)

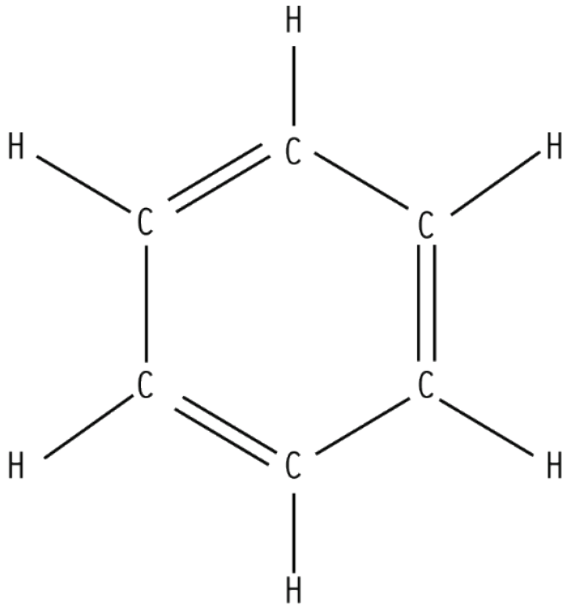

Figure 4.19 – Molecules of pyridine (a) and benzene (b).

The IR absorption spectrum of pyridine ice at 12 K, Fig. 4.20, is similar to that reported by Smith et al. (2014) and McMurtry et al. (2016). These groups performed an energetic processing of CO_2 and pyridine at proportions of 1:1 and 8:1, respectively. Table 4.6 outlines the peak position and assignments of pyridine ice of our experiment and those reported in the literature.

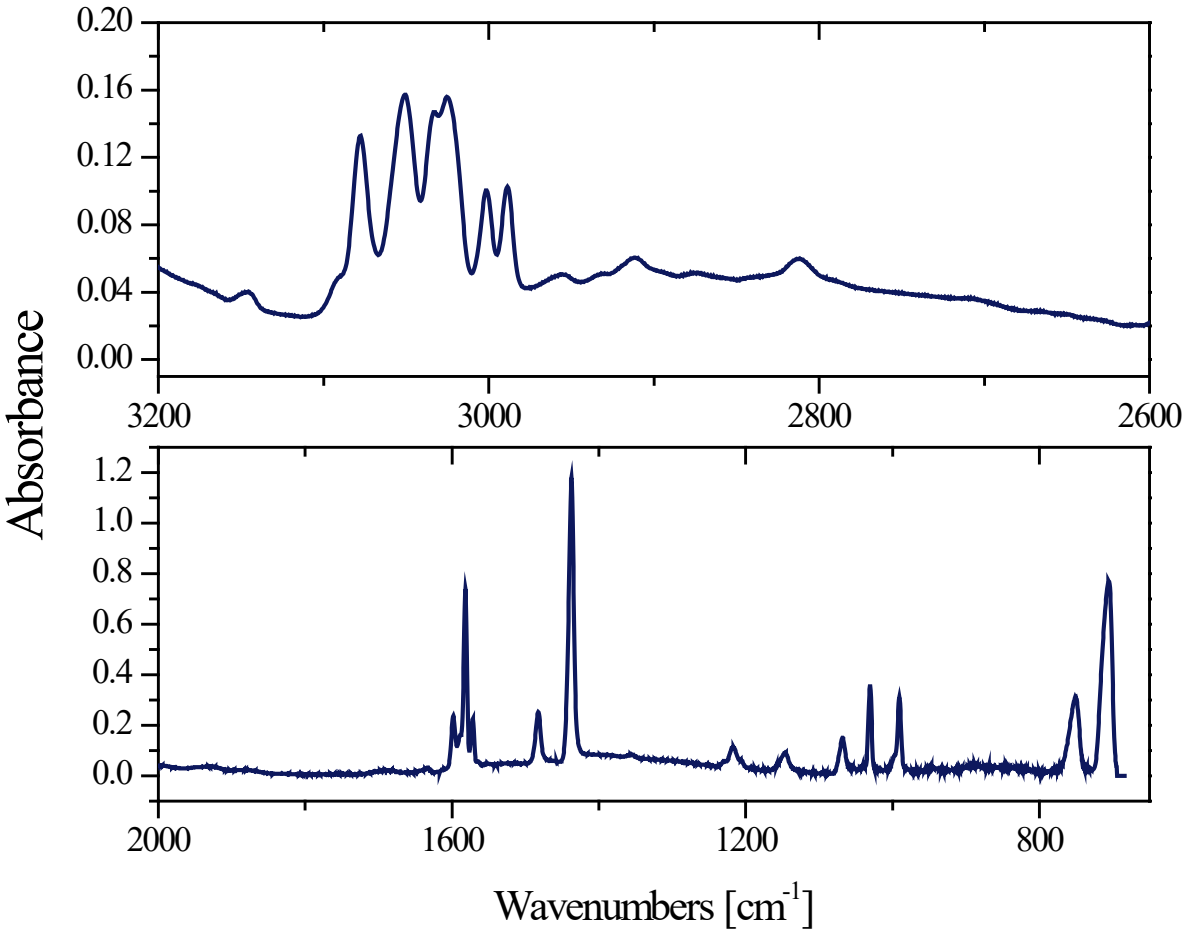

Figure 4.20 - IR absorption spectrum of pyridine ice at 12 K.

Table 4.6 – Peak position and assignment of pyridine ice samples and those reported in literature at room temperature.

Assignment	*Definition*	(McMurtry et al. 2016)	*Pyridine ice*
C-H	stretching	3089	3089
C-H	stretching	3062	3055
	stretching	3044	
	stretching	3034	3033
			3025
C-H	stretching	3009	3001
	stretching and bending	2995	2989
	stretching	2460	2430
		1938	1930
		1639	1634
		1603	1598
ring	stretching	1585	1581
ring	stretching	1574	1571
ring	stretching	1484	1482
ring	stretching	1441	1438
ring	stretching	1358	1356
			1216
C-H	deform	1147	1146
C-H	deform	1071	1068
ring	breathing	1032	1030
ring	breathing	993	991
ring	twist	755	750
C-H	out-of-deform	711	706
	bending		

The differences between our spectrum and that reported by McMurtry et al. (2016) are more likely due to the fact that their pyridine ice was in a matrix of CO_2 mixed ice. To estimate the amount and thickness of our pyridine samples, we adopted the band strength reported by McMurtry et al. (2016), with the assumption that the presence of CO_2 in their sample did not change the band strength of the peaks at 755 and 711 cm^{-1}. Using Equation 4.1 we estimated a pyridine column density to be equal to 1.1×10^{19} molecules cm^{-2}, assuming pyridine density of 1g cm^{-3} (Smith et al. 2014) . These values can be overestimated since we use the band strength for pyridine in CO_2 matrix. The thickness of the pyridine ice is thus estimated to be 14.4 μm. The penetration depth of 116 MeV U^{32+} is much higher than the thickness (P_d = 60.4 μm).

References

Mathlouthi, M., A. M. Seuvre, and J. L. Koenig. 1986a. “F.T.-I.R. and Laser-Raman Spectra of Cytosine and Cytidine.” *Carbohydrate Research* 146 (1): 1–13. doi:10.1016/0008-6215(86)85019-4.

Mathlouthi, M., A. M. Seuvre, and J. L. Koenig. 1986b. “F.T.-I.R. and Laser-Raman Spectra of Guanine and Guanosine.” *Carbohydrate Research* 146 (1): 15–27. doi:10.1016/0008-6215(86)85020-0.

Mathlouthi, M., A.-M. Seuvre, and J. L. Koenig. 1984. “F.t.-I.r. and Laser-Raman Spectra of Adenine and Adenosine.” *Carbohydrate Research* 131 (1): 1–15. doi:10.1016/0008-6215(84)85398-7.

McMurtry, B. M., A. M. Turner, S. E.J. Saito, and R. I. Kaiser. 2016. “On the Formation of Niacin (Vitamin B3) and Pyridine Carboxylic Acids in Interstellar Model Ices.” *Chemical Physics* 472 (June): 173–84. doi:10.1016/j.chemphys.2016.03.010.

Mohamed, T. A., I. A. Shabaan, W. M. Zoghaib, J. Husband, R. S. Farag, and A. El-Nasser M.A. Alajhaz. 2009. “Tautomerism, Normal Coordinate Analysis, Vibrational Assignments, Calculated IR, Raman and NMR Spectra of Adenine.” *Journal of Molecular Structure* 938 (1–3): 263–76. doi:10.1016/j.molstruc.2009.09.040.

Saïagh, K., H. Cottin, A. Aleian, and N. Fray. 2015. “VUV and Mid-UV Photoabsorption Cross Sections of Thin Films of Guanine and Uracil: Application on Their Photochemistry in the Solar System.” *Astrobiology* 15 (4): 268–82. doi:10.1089/ast.2014.1196.

Saïagh, K. M. Cloix, N. Fray, and H. Cottin. 2014. “VUV and Mid-UV Photoabsorption Cross Sections of Thin Films of Adenine: Application on Its Photochemistry in the Solar System” 90. doi:10.1016/j.pss.2013.11.002.

Singh, J.S. 2008. “FTIR and Raman Spectra and Fundamental Frequencies of Biomolecule: 5-Methyluracil (Thymine).” *Journal of Molecular Structure* 876 (1–3): 127–33. doi:10.1016/j.molstruc.2007.06.014.

Smith, K. E., M. P. Callahan, P. A. Gerakines, J. P. Dworkin, and C. H. House. 2014. “Investigation of Pyridine Carboxylic Acids in CM2 Carbonaceous Chondrites: Potential Precursor Molecules for Ancient Coenzymes.” *Geochimica et Cosmochimica Acta* 136 (July): 1–12. doi:10.1016/j.gca.2014.04.001.

Susi, H., and J.S. Ard. 1971. “Vibrational Spectra of Nucleic Acid constituents—I.” *Spectrochimica Acta Part A: Molecular Spectroscopy* 27 (9): 1549–62. doi:10.1016/0584-8539(71)80211-8.

Chapter 5 - Results – Irradiation of nucleobases

This chapter will show the results of the irradiation of five different nucleobase samples; adenine, cytosine, uracil, guanine and thymine by swift heavy ions. The solid nucleobase samples were irradiated at low temperature by different heavy swift ions and the destruction and appearance of new species was followed by IR absorption spectroscopy as a function of the projectile fluence. One sample of adenine film was irradiated at room temperature. Table 5.1 summarizes the experimental parameters. As previously discussed in 2.2.1, by using different ions, it is possible to expand the electronic stopping power range which allows us to study the disappearance of molecules as a function of electronic stopping power.

Table 5.1 – Summary of targets and projectile characteristics.

Sample	Ion	Energy (MeV)	Electronic stopping power (10^3 keV µm^{-1})	Nuclear stopping power (keV µm^{-1})	Penetration depth (µm)	Temperature (K)	Water layer ice (µm)	Thickness (µm)	Column Density (10^{17} cm^2)
Adenine Grainy	Xe^{23+}	92	11.2	71	16	12	-----	0.29	1.9
Adenine Grainy	Kr^{33+}	820	5.8	3.6	120	12	-----	0.45	3.0
Adenine Grainy	Ca^{10+}	190	3.1	2.2	51	12	-----	0.22	1.4
Adenine Grainy	Ca^{10+}	190	3.1	2.2	51	12	0.2	0.25	1.7
Adenine Film	Ni^{24+}	632	3.4	2.0	137	12	-----	0.28	1.9
Adenine Film	Ni^{24+}	632	3.4	2.0	137	300	-----	0.45	3.0
Adenine Grainy	C^{4+}	12	1.0	0.9	12	12	-----	0.28	1.9
Adenine Grainy	C^{4+}	12	1.0	0.9	12	12	-----	0.09	0.6
Cytosine Grainy	Xe^{23+}	92	11.3	73	15.5	12	-----	0.8	6.5
Cytosine Film	U^{32+}	116	13.4	250	16.7	12	-----	0.34	2.8
Cytosine Film	Ni^{8+}	17	4.8	44	9.2	12	-----	0.28	2.3
Cytosine Grainy	Ni^{8+}	17	4.8	44	9.2	12	-----	0.20	1.6
Cytosine Grainy	Ca^{10+}	190	3.2	2.3	51	12	-----	1.1	9.1
Uracil Grainy	Xe^{23+}	92	9.5	62.2	18	12	-----	0.31	2.2
Thymine Grainy	Ca^{10+}	190	3.1	2.2	52.2	12	-----	0.60	3.5
Thymine Film	Ca^{10+}	190	3.1	2.2	52.2	12	-----	0.55	3.23
Guanine Film	Ca^{10+}	190	3.5	2.5	46.2	12	-----	0.42	2.9
Guanine Film	Ca^{10+}	190	3.5	2.5	46.2	12	-----	0.33	2.3
Pyridine ice	U^{32+}	116	9.6	171	22.9	12	-----	14.4	110
Pyridine ice	O^{6+}	0.9	0.21	57	0.33	12	-----	1.4	10.7

5.1 Adenine fragmentation

The irradiation of a solid by corpuscular radiation provokes several effects, notably physical-chemical modifications, fragmentation, formation of radicals and new molecules, material sputtering and compaction (Mejía et al., 2015). During energetic heavy ion irradiation of adenine, its overall IR absorption intensity decreases (Figure 5.1). Furthermore, new IR absorption bands clearly arise between 2300 cm^{-1} and 2000 cm^{-1}.

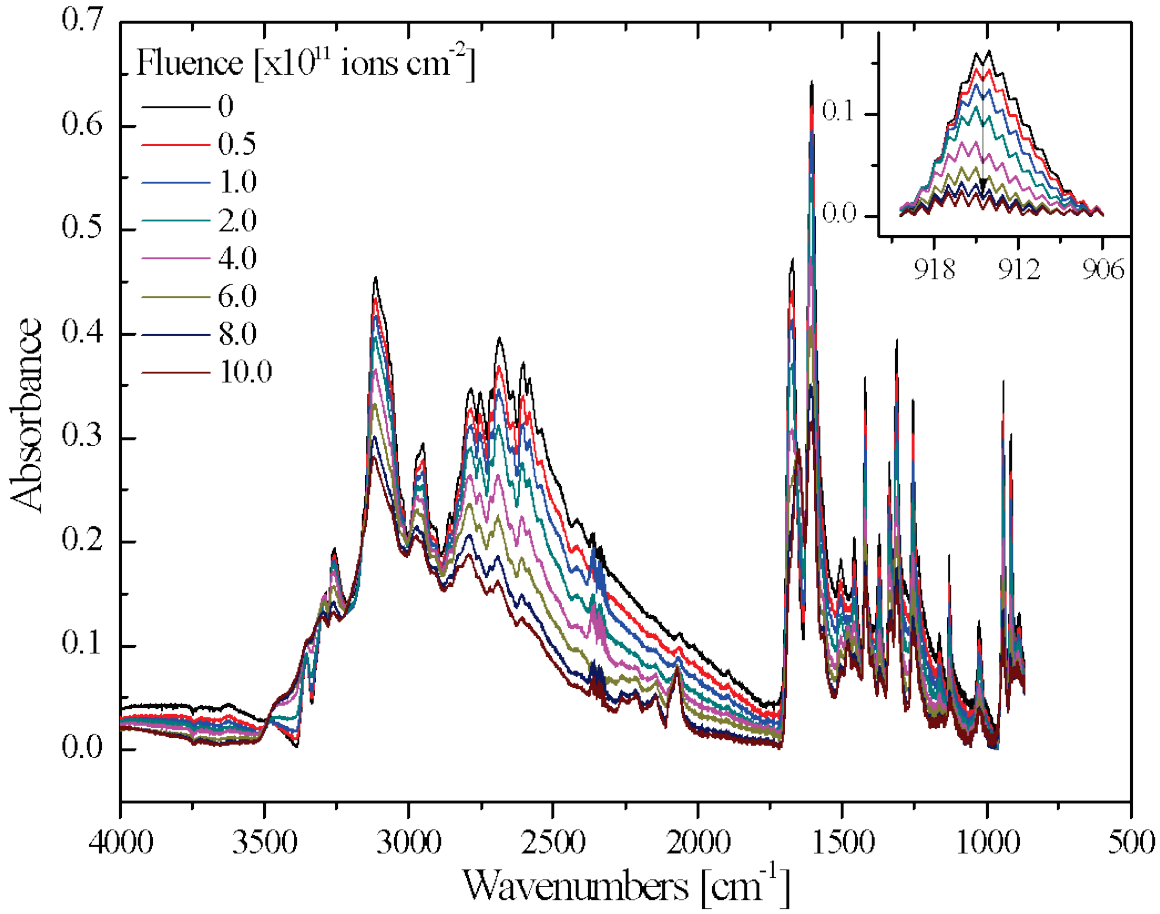

Figure 5.1 – Infrared absorption spectra of grainy adenine at 12 K under irradiation of 92 MeV Xe^{23+} at different fluences.
Inset: Infrared absorption peaks at 914 cm^{-1} at different projectile fluence.

To extract the apparent cross sections we followed the evolution of several peak areas during the irradiation as function of ion fluence. The intensity of certain bands decreases more rapidly than that of others, yielding different values of the apparent destruction cross section, see Appx. 6. We chose the cross section which corresponds to the dissociation of NCN at R5

(914 cm^{-1}), because it not only shows one of the highest observed values, but also because the band located at 914 cm^{-1} is not overlapped by water ice IR absorption bands and thus can be analyzed in a straightforward way without deconvolution. **Figure** 5.2 displays the normalized IR absorption peak area at 914 cm^{-1} as a function of the accumulated ions per square centimeter. The error bars in Figure 5.2 were suppressed for clarity. However, we adopted in this work a margin of error of 15% for the IR peak area and for the ion fluence.

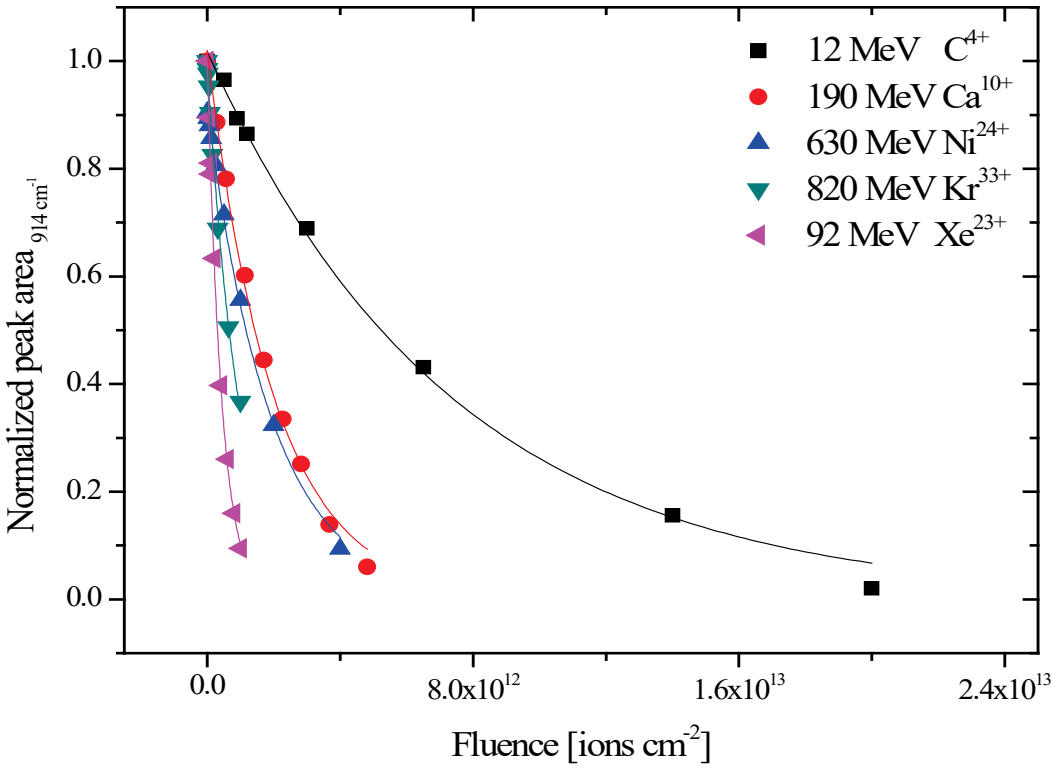

Figure 5.2 – Evolution of the IR absorption peak area at 914 cm^{-1} under the irradiation of different heavy ions at 12 K.

Figure 5.2 clearly shows that the projectiles with higher electronic energy loss (Table 5.1) provokes a faster and stronger decay in the IR absorption peak area, corresponding to a higher apparent destruction cross section. We used Equation 3.8 to extract the apparent destruction cross sections by a best fit procedure.

Table 5.2 – Apparent destruction cross sections of adenine for different ion beams at different energies at 12 K.
** Corresponds to the irradiation of adenine covered with water ice layer.*

Projectile	Apparent destruction cross section ($\cdot 10^{-13}$ cm^2)	Average apparent destruction cross section ($\times 10^{-13}$ cm^2)	S_e ($\times 10^3$keV µm^{-1})
Xe^{23+}	22.2 ± 0.3	14 ± 1	11.4
Kr^{33+}	10.9 ± 0.2	7.8 ± 0.9	5.8
Ni^{24+}	5.2 ± 0.1	3.8 ± 0.8	3.6
Ca^{10+}	4.5 ± 0.4	3.0 ± 0.8	3.1
Ca^{10+} *	4.9 ±0.1	----	3.1
C^{4+}	1.24 ± 0.06	0.87 ± 0.02	1.0

The apparent destruction cross section gives us an information about the disappearance of the initial molecules, but using just single exponential (Eq. 3.8) we are unable to separate and determine the sputtering and the destruction cross section per incoming ion. In order to determine the contribution of sputtering to the evolution of our samples under heavy ion irradiation, one of our samples was covered with a thin water ice layer (0.22 µm). Since sputtering is a phenomenon which occurs at the surface, we expect to avoid adenine sputtering. A similar methodology was applied by Loeffler et al. (2005): they covered their samples with an argon layer before the irradiation by 200 keV protons to prevent sputtering. Figure 5.3 shows the evolution of the peak area at 914 cm^{-1} of pure adenine and adenine covered with water ice as a function of 190 MeV Ca^{10+} fluence. The penetration depth of the incoming ions are much higher than the thickness of the water layer ice (Table 5.2). Therefore, we are sure that the projectiles are reaching the adenine sample.

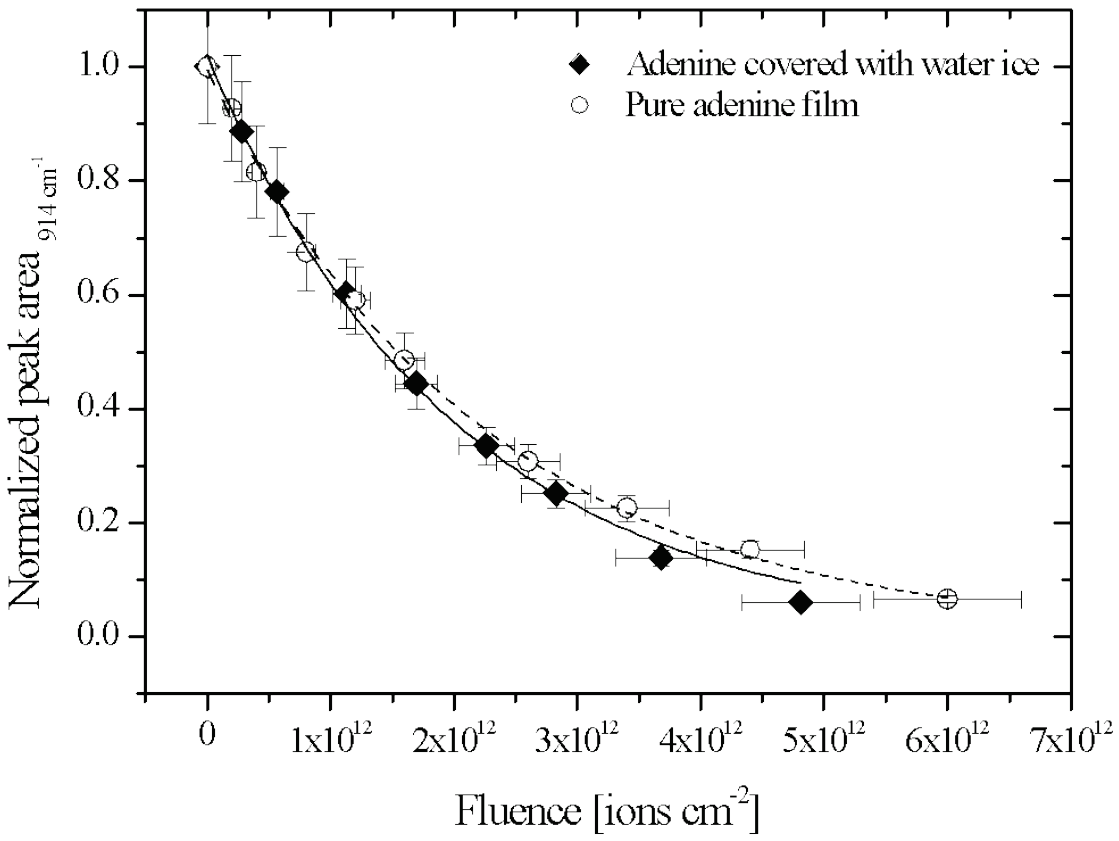

Figure 5.3 – Evolution of the normalized peak area at 914 cm^{-1} of grainy adenine under bombardment of 190 MeV Ca^{10+} at 12 K.

The difference between the two curves is within the error bar, showing that the evolution of adenine under irradiation is dominated by radiolysis. Moreover, since the difference between the two curves is insignificant, it is not possible to determine the adenine sputtering yield per incoming ion. It is important to mention that under the conditions of our experiments (12 K and 10^{-8} mbar) there is a layering from the residual gas in the chamber, therefore the "pure adenine" sample is also covered with a thin ice layer and this may be the explanation why the evolution of our two samples under irradiation are very similar.

We plotted the normalized area (914 cm^{-1}) as a function of the local dose, i.e. the energy per number of molecules, Figure 5.4.

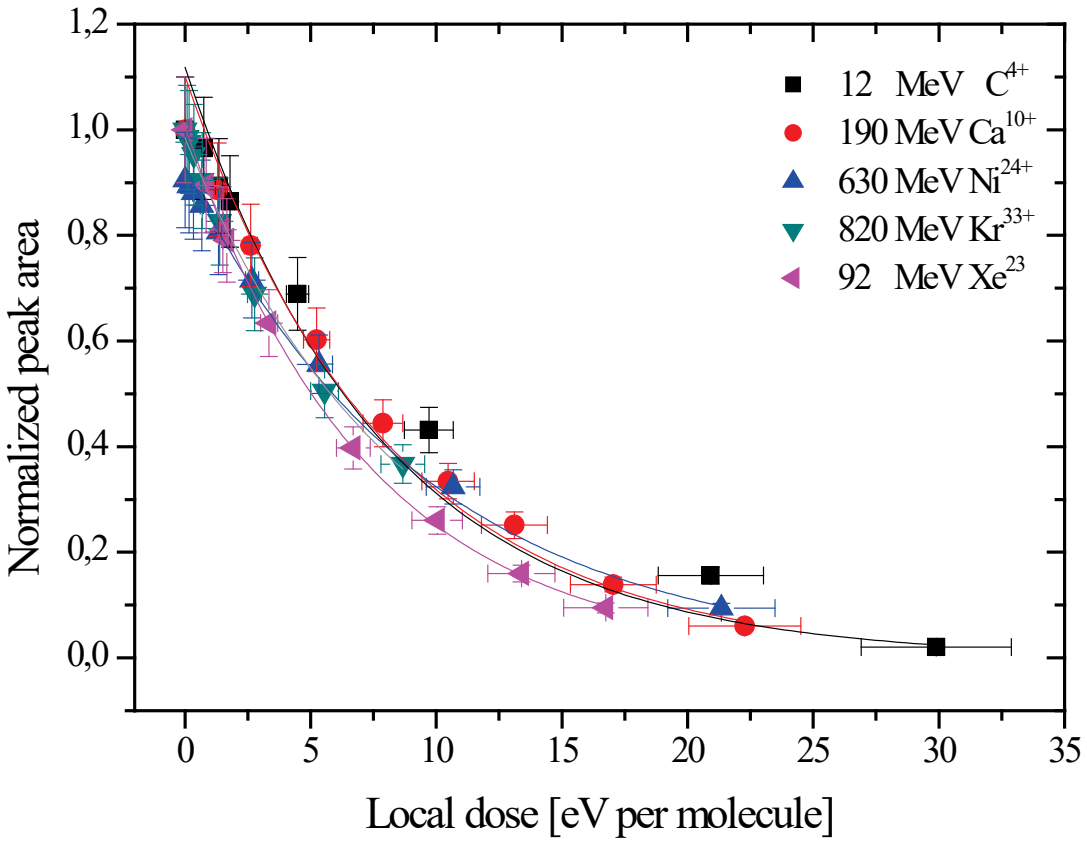

Figure 5.4 – Normalized peak area at 914 cm^{-1} as a function of the local dose at 12 K.

Note that the decay of the peak area as a function of the local dose is very similar for the different projectiles. The results reported in this figure suggest that the local dose is a key parameter: the evolution of adenine molecules under corpuscular radiation depends on the deposited energy.

5.1.1 – Adenine fragmentation – temperature dependence

The damage induced by ionizing radiation in aromatic compounds is temperature dependent. In fact, Fryer *et al.* (1992) exposed films of aromatic molecules (coronene, ovalene and metal-free phthalocyanine) at different temperatures in the range of 4 to 295 K using 100 keV electrons, observing the diffraction pattern and measuring the time required to destroy the crystalline order. Fryer *et al.* (1992) reported cryoprotective effects in the aromatic compounds exposed to

100 keV electrons. Gerakines et al. (2012) irradiated films of glycine, alanine and phenylalanine with 0.8 MeV H^+ and they also irradiated these three amino acids in a water matrix. With the exception of phenylalanine, the cross sections at 15 K are about twice as high as the cross sections at 140 K. Although a decrease of the destruction cross section with increasing temperature is observed the cross sections at 15 and 140 K are of the same order of magnitude. Pilling et al. (2013) also irradiated films of glycine at room temperature (300 K) with 1 MeV H^+ and reported a cross section equal to 2.5×10^{-14} cm^2. This value is, however, one order of magnitude higher than the values reported by Gerakines *et al*. (2012).

Portugal *et al*. (2014) performed irradiations of glycine with heavy ions (46 MeV Ni^{11+}) and curiously, they observed the opposite behavior concerning temperature dependence: the destruction cross section of glycine is about 7 times higher at 15 K than at 300 K. Obviously, in this case a cryoprotective effect is not observed, the molecules are more sensitive to irradiation at lower temperatures.

To check if the radiolysis of adenine presents a temperature dependence, we bombarded adenine films with 632 MeV Ni^{24+} at 12 K and 300 K. Figure 5.5 shows the evolution of the absorption band at 914 cm^{-1} (at room temperature this absorption band is at 912 cm^{-1}, see Chapter 4 – Sample characterization).

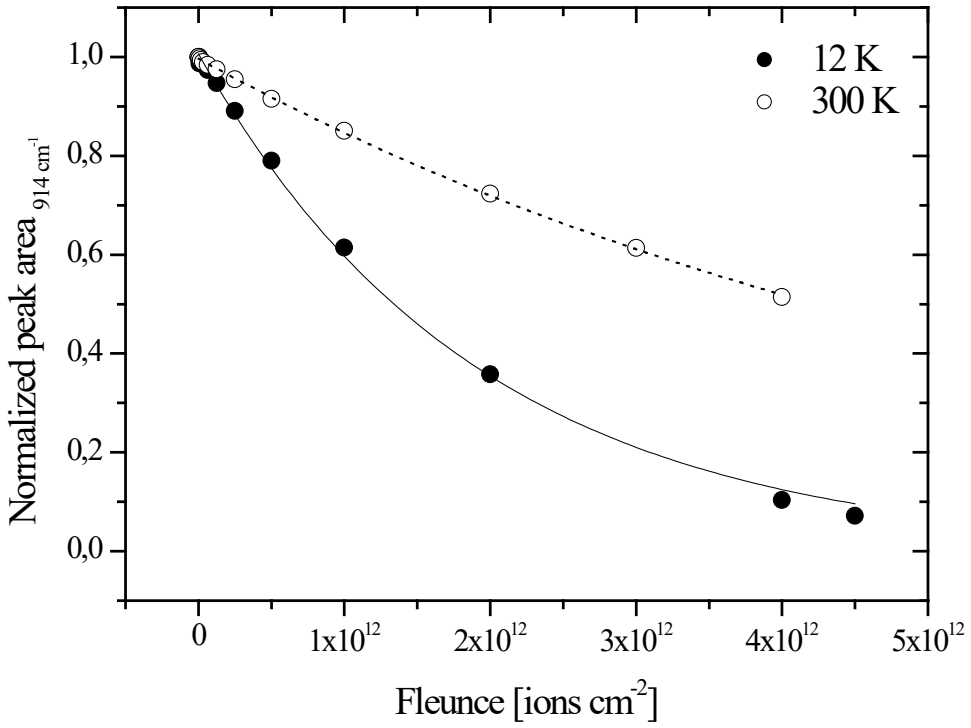

Figure 5.5 - Evolution of the normalized peak area at 914 cm^{-1} of adenine film under bombardment of 632 MeV Ni^{24+} at 12 and 300 K.

It is evident that there is a temperature dependence: at 12 K, adenine is more sensible to heavy ion radiation. The cross sections were $(5.2 \pm 0.1) \times 10^{-13}$ and $(1.63 \pm 0.01) \times 10^{-13}$ cm^2 at 12 and 300 K, respectively. The cross section at low temperature is 3.2 times higher than at room temperature. This effect is similar to that observed by Portugal et al. (2014) : under heavy ion irradiation adenine and glycine present a higher radioresistance at room temperature. This is the opposite behavior as that observed for irradiation of organic molecules with light projectiles, i.e., protons and electrons. Heavy ions deposit more energy per unit of length (see Chapter 2). Furthermore, specific effects connected to strong perturbation occurs:, multiple ionizations and a high yield of secondary electrons. However, it is not yet clear why the damage provoked by light and heavy projectiles exhibit different dependences with temperature. More experiments and theoretical approaches are needed to resolve this question and explain this astonishing finding.

5.2 Cytosine irradiation

5.2.1 – Compaction

In Chapter 4, we explained the differences between grainy and film samples. In this sub-chapter, we will present the results of bombardment of our cytosine samples by swift heavy ions.

Three cytosine film samples were irradiated by 17 MeV Ni^{8+} and 116 MeV U^{23+} (see Table 5.1). Figure 5.6 displays the evolution of the cytosine film absorption peak area at 1539 cm^{-1} under bombardment of 17 MeV Ni^{8+}. From this Figure, a small increase in the absorption peak area is observed at the beginning of irradiation. Then, the peak area starts to decreases exponentially for fluences higher than 2.4×10^{10} ions cm^{-2}.

The two films irradiated by 17 MeV Ni^{8+} present an increase in the area of the absorption spectra area at low fluences (local dose smaller than 0.35 eV per molecule). At local doses higher than 0.35 eV per molecule the peak area starts to decrease, and therefore the film is compacted and

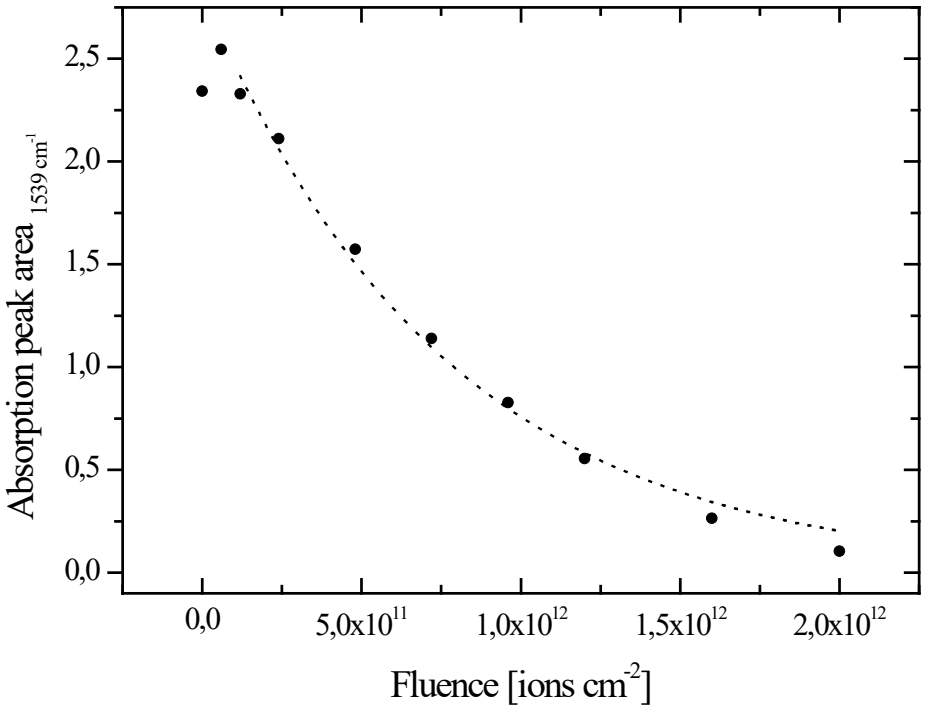

Figure 5.6 – Absorption peak area of cytosine film as a function of the fluence of 17 MeV Ni^{8+} at 12 K.

the disappearance of cytosine molecules are observed. We do not observed the increased of the peak area in the cytosine film irradiated by 116 MeV U^{32+}. This is due to the fact that the first spectrum was recorded a local dose equal to 0.66 eV per molecule. At this deposited local dose, the film is already compacted. This effect (increase of the area of the spectrum) was not observed in the grainy samples, even in the grainy sample irradiated by the same projectile 17 MeV Ni^{8+} at the same conditions of flux, fluence and temperature.

The column density is proportional to the absorption peak area and of course under irradiation we do not create more cytosine molecules. One possible explanation for the increase of the absorption spectra area is the film compaction due to corpuscular radiation. In fact, Mejía et al. (2015) observed a similar increase in the absorption peak area in the spectra of different ices composed of mixtures of water and different organic molecules. They correlate this area increase with a variation of the band strength due to the compaction of the ices under heavy ion radiation. We believe that we are observing the same phenomenon, compaction of the cytosine film.

The compaction is a phenomenon that occurs at low fluences and low deposited energy, therefore we can use the approximation that the column density does not change at those fluences. Using the equation 4.1 with this approximation we obtain equation 5.1:

Eq. 5.1

$$\frac{N(F_1)}{N(0)} \cong 1$$

$$\frac{A\,value_0}{Avalue_1} = \frac{Area_0}{Area_1}$$

$N(F_1)$ is the column density at the maximum peak area and N(0) is the initial column density. $Area_1$ and $Area_0$ refer to the maximum peak area and the initial area, respectively. A_{value1} and A_{value0} are the band strengths concerning the compacted and non-compacted film, respectively. This effect of compaction does not have a big impact on the band strength, taking into account

that the ratio of the initial area and the maximum of the peak area at 1539 cm^{-1} (Fig. 5.6) is 0.92. The compaction provokes a variation of just 8 % in the band strength of 1539 cm^{-1}. This is much smaller than the usual error adopted for the band strength of 50%. The variation of the band strength of different absorption peaks are of the same order of magnitude and therefore within the error bar.

5.2.2 – Cytosine Fragmentation

As discussed in last sub-section, swift heavy ion irradiation provokes firstly an increase in the area of the cytosine film spectra, at the beginning of the irradiation. After the deposition of an energy density superior to 0.35 eV per molecule the evolution of the film and grainy cytosine IR absorption spectra are very similar, the intensity of the peaks decrease as a function of the ion fluence. Figure 5.7 displays the evolution of the IR absorption spectra of grainy and film cytosine under 17 MeV Ni^{8+}.

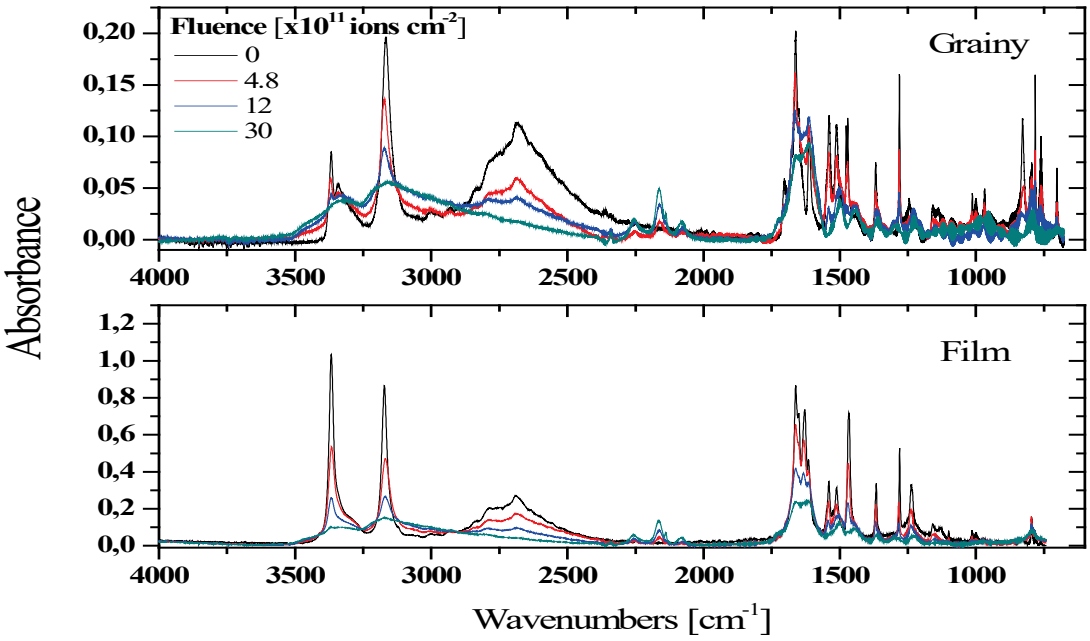

Figure 5.7 – Grainy and film cytosine spectra during the irradiation by 17 MeV Ni^{8+} at different fluences at 12 K.

All samples, grainy or film, exhibit new absorption bands which clearly emerge between 2300 - 2000 cm^{-1} after a dose of 1 eV per molecule has been deposited. The peak areas of the band at 1539, 1367, 1281, 1236, 702 cm^{-1} and the χ band were followed during irradiation. These bands also are not overlapped with possible contaminates such as water and CO_2 from the layering of the residual gas and new absorption bands are not observed emerging in these region. The evolution of the peak areas as a function of the accumulated ions were fitted by equation 3.8. It is important to point out that in the case of the films irradiated by 17 MeV Ni^{8+}, the fitting procedure included only the points after the maximum peak area, see sub-section 5.2.1. As an example the peak area of 1281 cm^{-1} is plotted as a function of the different ions fluences in Figure 5.8.

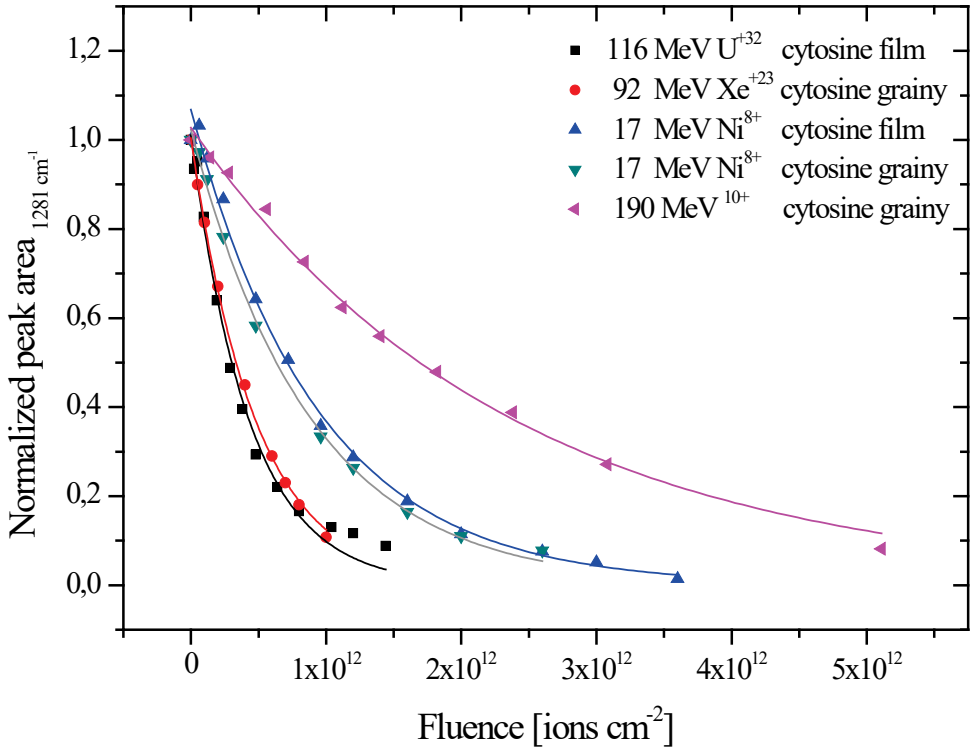

Figure 5.8 – Peak area at 1281 cm^{-1} evolution as a function of the fluence for different ions at 12 K.

Once again, it is obvious that ions with a higher electronic stopping power induce faster decays of the areas corresponding to a faster destruction of cytosine.

Table 5.3 displays the apparent cross section corresponding to different absorption peaks and the average apparent cross section for different projectiles. Since grainy and film cytosine exhibit different IR absorption spectra, it is natural to inquire if the radio sensibility of these samples (apparent destruction cross section) are different.

Table 5.3 – Cytosine destruction cross section for specific IR absorption peak or band.

Peak position	σ [x10^{-12} cm^2] U Film	σ [x10^{-12} cm^2] Xe Grainy	σ [x10^{-12} cm^2] Ni Grainy	σ [x10^{-12} cm^2] Ni Film	σ [x10^{-12} cm^2] Ca Film
1539	(3.50 ± 0.09)	(3.2 ± 0.3)	(1.17 ± 0.03)	(1.31 ± 0.06)	(0.57 ± 0.01)
1367	(1.9 ± 0.2)	(1.48 ± 0.03)	(1.07 ± 0.06)	(1.57 ± 0.08)	(0.33 ± 0.01)
1281	(1.7 ± 0.2)	(1.69 ± 0.02)	(0.91 ± 0.03)	(0.92 ± 0.02)	(0.44 ± 0.02)
1236	(2.4 ± 0.1)	(2.1 ± 0.1)	(1.27 ± 0.02)	(1.24 ± 0.01)	(0.72 ± 0.04)
X	(2.4 ± 0.1)	(2.20 ± 0.06)	(1.40 ± 0.02)	(1.09 ± 0.05)	(0.55 ± 0.02)
$<\sigma>$	(2.4 ± 0.7)	(2.1 ± 0.6)	(1.3 ± 0.2)	(1.2 ± 0.1)	(0.5 ± 0.1)

Note that we performed irradiation of grainy and film cytosine by the same projectile at the same energy (17 MeV Ni^{8+}). This also allows to compare directly the effects of heavy ion irradiation of our two cytosine samples. Although in this case differences in the cross sections are observed for different absorption bands, the average cross sections is identical within error bars.

Let us now study the evolution of cytosine as a function of the deposited dose. Figure 5.9 shows the decay of the absorption peak area as a function of deposited energy per molecule.

Note that the evolution of adenine (Fig 5.4) and cytosine (Fig 5.9) under ion energetic seems irradiation depends only on the deposited energy. This confirm that the local dose is a key parameter.

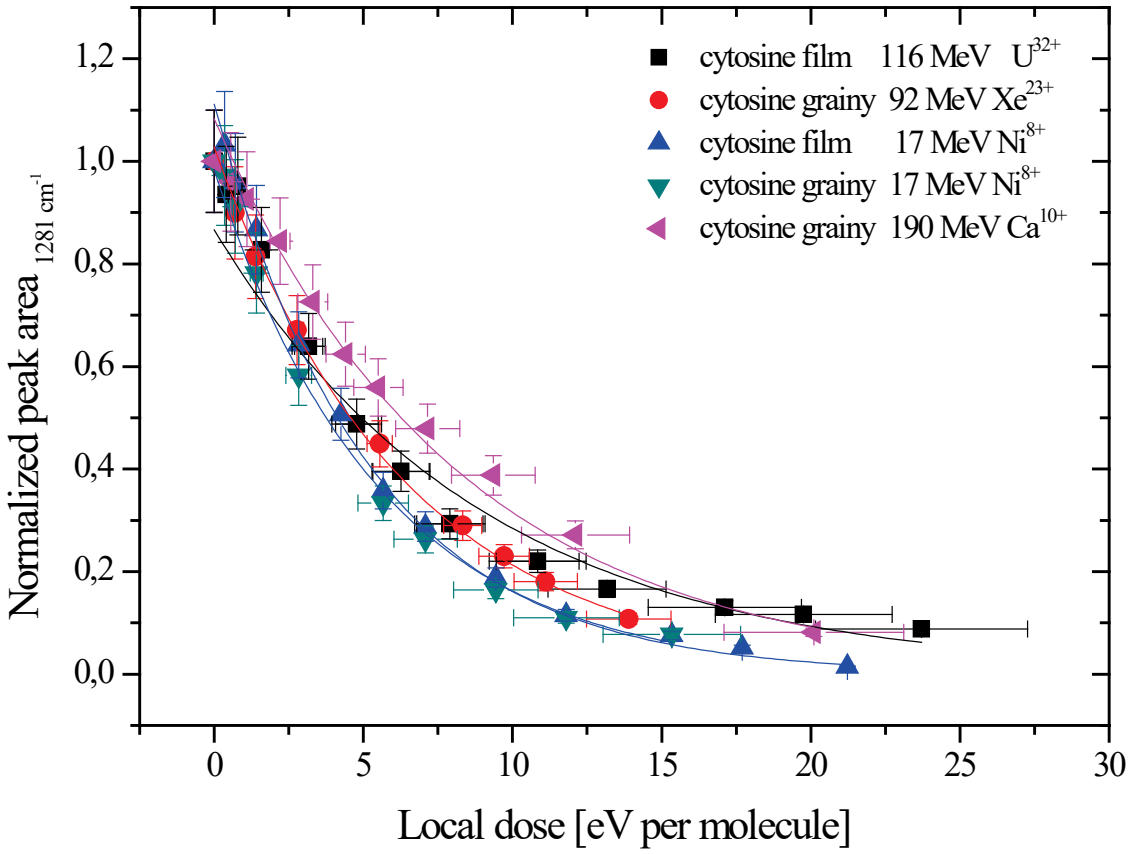

Figure 5.9 - Normalized peak area of 1281 cm^{-1} as a function of the local dose at 12 K.

5.3 – Irradiation of guanine, thymine and uracil samples

We also irradiated other nucleobases (guanine, thymine and uracil). However, just one projectile was used. Nevertheless, we irradiated each nucleobase at least two times with the same projectile under the same conditions of temperature, pressure, ion flux, and fluence to ensure the reproducibility of our results.

Guanine film, grainy and film thymine were irradiated using 190 MeV Ca^{10+} ion beams at GSI, whereas uracil was irradiated at GANIL by 92 MeV Xe^{23+} projectiles. Similar to adenine and cytosine the decay of the absorption peak area of these nucleobases follows a single exponential decay. Table 5.4 displays the respective cross sections. Purine nucleobases (guanine and

adenine) are formed by two heterocyclic rings, whereas pyrimidine nucleobases (cytosine, uracil and thymine) are formed by just one heterocyclic ring. Note that we followed the evolution of different absorption bands taking into account some conditions. Firstly, no new absorption bands emerged at the position of these absorption peaks and secondly, those peaks are not overlapped with water ice bands.

As observed for adenine and cytosine, grainy or film thymine, the average destruction cross sections are approximately equal within error bars. In Chapter 7, we will discuss about the radiosensibility of the different nucleobases and perform a comparison with the results available in the literature.

Table 5.4 – Apparent destruction cross sections of guanine, uracil and thymine for selected IR absorption peaks irradiated by different ions.

Target	Projectile	Peak position [cm^{-1}]	Destruction cross section [cm^2]
Guanine	190 MeV Ca^{10+}	947	$(1.2 \pm 0.1) \times 10^{-13}$
Guanine	190 MeV Ca^{10+}	1117	$(1.5 \pm 0.1) \times 10^{-13}$
Guanine	190 MeV Ca^{10+}	1373	$(9.3 \pm 0.7) \times 10^{-14}$
Guanine	190 MeV Ca^{10+}	1768-1508	$(5.1 \pm 0.2) \times 10^{-14}$
Guanine	190 MeV Ca^{10+}	Part of the γ (2956-2394)	$(2.62 \pm 0.07) \times 10^{-13}$
Guanine	190 MeV Ca^{10+}	Average	$(1.3 \pm 0.8) \times 10^{-13}$
Thymine Film	190 MeV Ca^{10+}	1250	$(5.0 \pm 0.3) \times 10^{-13}$
Thymine Film	190 MeV Ca^{10+}	938	$(4.8 \pm 0.1) \times 10^{-13}$
Thymine Film	190 MeV Ca^{10+}	847	$(5.4 \pm 0.1) \times 10^{-13}$
Thymine Film	190 MeV Ca^{10+}	818	$(6.6 \pm 0.2) \times 10^{-13}$
Thymine Film	190 MeV Ca^{10+}	760	$(5.0 \pm 0.1) \times 10^{-13}$
Thymine Film	190 MeV Ca^{10+}	749	$(6.5 \pm 0.3) \times 10^{-13}$
Thymine Film	190 MeV Ca^{10+}	Average	$(5.5 \pm 0.8) \times 10^{-13}$
Thymine Grainy	190 MeV Ca^{10+}	1250	$(4.1 \pm 0.3) \times 10^{-13}$
Thymine Grainy	190 MeV Ca^{10+}	938	$(4.0 \pm 0.3) \times 10^{-13}$
Thymine Grainy	190 MeV Ca^{10+}	847	$(2.7 \pm 0.3) \times 10^{-13}$
Thymine Grainy	190 MeV Ca^{10+}	818	$(5.1 \pm 0.3) \times 10^{-13}$
Thymine Grainy	190 MeV Ca^{10+}	760	$(4.0 \pm 0.2) \times 10^{-13}$
Thymine Grainy	190 MeV Ca^{10+}	749	$(6.0 \pm 0.2) \times 10^{-13}$
Thymine Grainy	190 MeV Ca^{10+}	Average	$(4 \pm 1) \times 10^{-13}$
Uracil	92 MeV Xe^{23+}	760	$(1.9 \pm 0.2) \times 10^{-12}$
Uracil	92 MeV Xe^{23+}	820	$(1.6 \pm 0.1) \times 10^{-12}$
Uracil	92 MeV Xe^{23+}	866	$(2.5 \pm 0.1) \times 10^{-12}$
Uracil	92 MeV Xe^{23+}	1393	$(2.1 \pm 0.2) \times 10^{-12}$
Uracil	92 MeV Xe^{23+}	1421	$(1.3 \pm 0.1) \times 10^{-12}$
Uracil	92 MeV Xe^{23+}	1461	$(2.8 \pm 0.1) \times 10^{-12}$
Uracil	92 MeV Xe^{23+}	Average	$(2.0 \pm 0.6) \times 10^{-12}$

5.4 – Radioproducts – New molecules from nucleobases degradation

In this sub-section, we present the results concerning the new absorption peaks which appear in the nucleobases's spectra under ion irradiation. Here we will highlight the new absorption bands and possible candidates for these peaks and bands. Moreover, IR spectroscopy has its limitation especially to detect symmetric molecules such as H_2, O_2, N_2, etc. Therefore, we need to stress that the formation of these molecular species is a possibility but the detection by IR is very difficult. A detailed discussion will be given in Chapter 7.

5.4.1 – New molecules from adenine radiolysis

As previously stated, due to the complexity of the IR absorption spectrum of adenine, it is very difficult to identify unequivocally the molecules responsible for the new absorption features. It is nevertheless possible to propose on some candidates of new molecular species responsible for the observed absorption. After a deposition of 1 eV per molecule we observe in all adenine samples new absorption features emerging from its degradation. We observe an increasing absorption peak at 1478 cm^{-1}, this absorption can be assigned to a vibration of primary amine (Günzler and Gremlich 2002) or to NH_4^+ (Gerakines, Moore, and Hudson 2004). We also observe a band emerging about 1654 cm^{-1}, which is characteristic to a vibration of C=N. A broad absorption band emerges between 2300 and 2000 cm^{-1}, Figure 5.10.

We deconvoluted the large band (2300 - 2050 cm^{-1}) appearing when adenine is irradiated by Xe^{23+} at high fluence (1×10^{12} ions cm^{-2}, 16.7 eV $molecule^{-1}$) to analyze the formation of new molecules as shown in Figure 5.17. This region is characteristic of C≡N and C≡C absorption, observable through the deconvolution of absorptions at 2044 cm^{-1}, 2070 cm^{-1}, 2092 cm^{-1}, 2100 cm^{-1}, 2124 cm^{-1}, 2144 cm^{-1}, 2174 cm^{-1}, 2212 cm^{-1}, 2240 cm^{-1} and 2262 cm^{-1}.

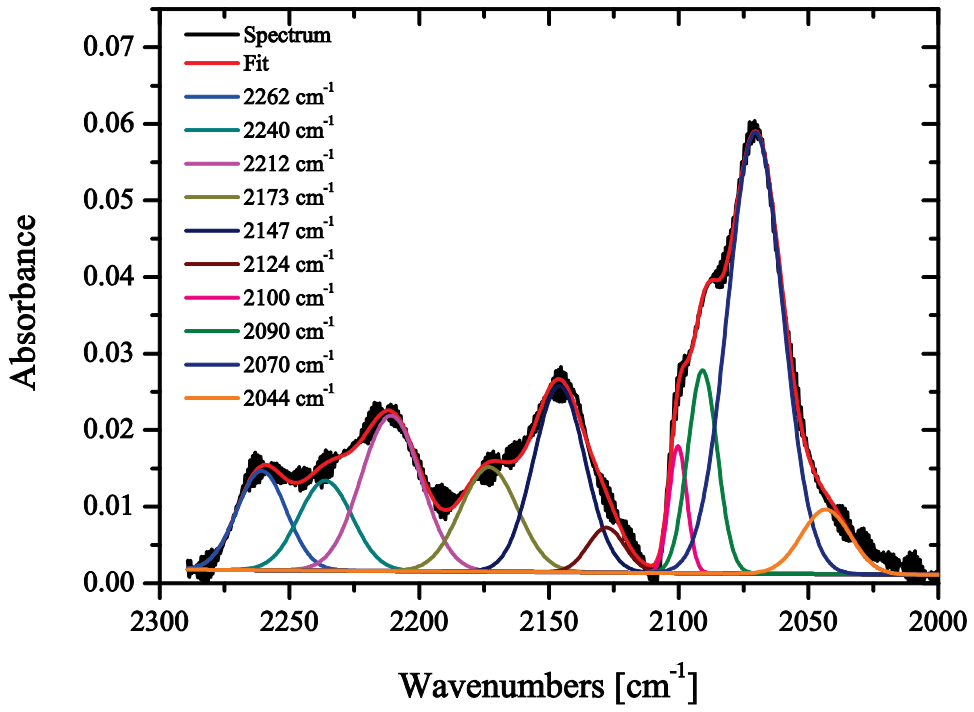

Figure 5.10 - Deconvolution of the band between 2300-2000 cm^{-1} of grainy adenine irradiated with 92 MeV Xe^{23+} at fluence of 1.0 × 10^{12} ions cm^{-2} (deposited energy 16.2 eV per molecule) at 12 K.

The absorption peaks at 2090 and 2100 cm^{-1} are used assigned as CN^- and HCN species (Burgdorf et al., 2010; Gerakines et al., 2004; Moore and Hudson, 2003), respectively. Due to the deconvolution is not possible to determine accurately the amount of CN^- or HCN species. The presence of the peak at 1478 cm^{-1} and 2090 cm^{-1} is a clue that NH_4CN is present. The absorption peak at 2240 cm^{-1} is certainly a nitrile, this peak is also observed by Evans et al. (2011) in the adenine degradation by 5 keV electrons. The peaks at 2212 and 2173 cm^{-1} can be assigned to $C_2H_4N_4$ (2212 and 2174 cm^{-1}) (Gerakines et al., 2004). The absorption peak at 2147 cm^{-1} can be assigned to nitrile or isonitrile (Hudson and Moore 2004). The absorption peak at around 2260 cm^{-1} is the typical vibration of C≡N, for example some molecules and radicals like HCNO (Peeters et al. 2003) and cyanomethyl radical (CH_2-C≡N) (Pilling et al. 2012) exhibit this absorption band. It is important to mention that despite the absence of oxygen in an adenine molecule, pollution from residual gases like water and CO_2 is not excluded, therefore formation of molecules containing oxygen cannot be excluded.

To eliminate the contamination of the residual gas (layering) we performed an irradiation of adenine film at room temperature. Under this condition no considerable condensation of the residual gas in the chamber on the adenine sample is possible, and therefore the pollution by oxygen species can be excluded. Figure 5.11 displays the IR absorption spectrum of adenine irradiated at room temperature by 632 MeV Ni^{24+} at 3×10^{12} ions cm^{-2} (15.2 eV $molecule^{-1}$).

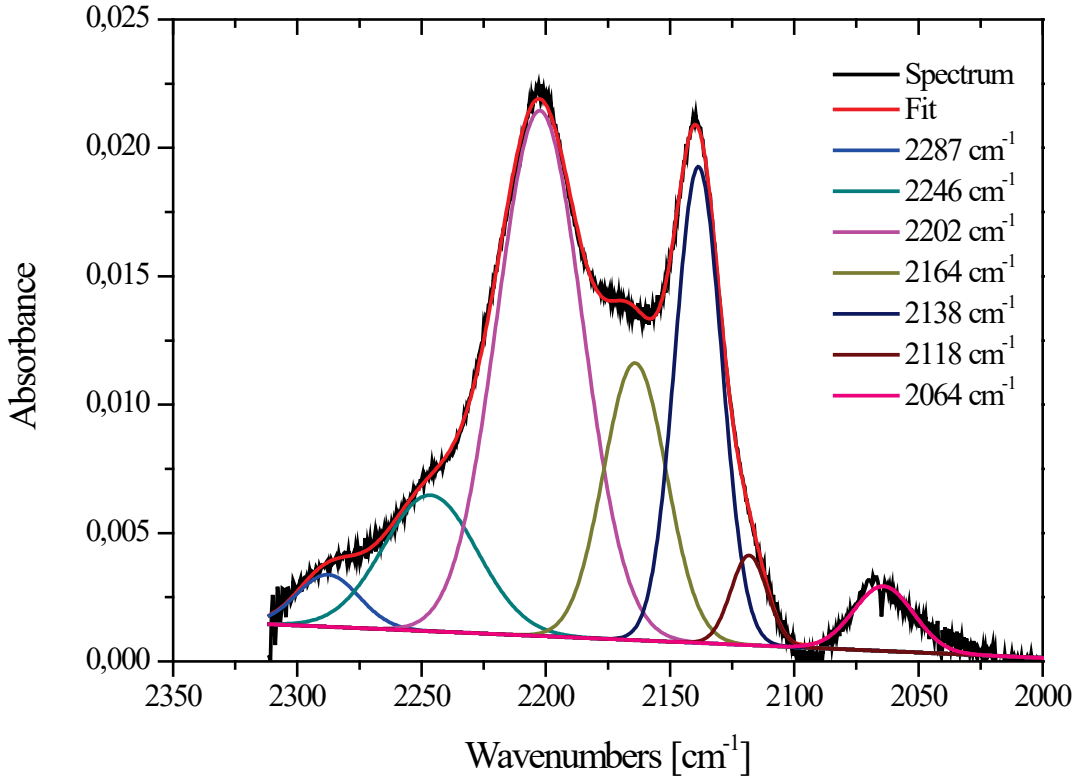

Figure 5.11 - Deconvolution of the band between 2300-2000 cm^{-1} of adenine film irradiated with 632 MeV Ni^{24+} at fluence of 3.0×10^{12} ions cm^{-2} (15.2 eV per molecule) at room temperature.

It is interesting to note that we observed new absorption peaks here, which are usually assigned to molecules which containing oxygen, such as OCN^- which has an absorption peak at 2164 cm^{-1}, (Hudson, Moore, and Gerakines 2001) and CO (2138 cm^{-1}), (van Broekhuizen et al. 2006). At room temperature, we can exclude a strong contamination with water or CO_2. Also, adenine ($C_5H_5N_5$) does not contain oxygen. These molecules thus cannot be responsible for the observed IR absorption spectrum, this is also a clue that the observed IR spectrum of adenine irradiated at low temperature is composed by nitriles and isonitriles. Indeed, Poch et al. (2014) reported

new broad IR absorption band between 2165 and 2180 cm^{-1} from the adenine UV photolysis. They assigned that particular absorption to nitriles, isonitriles and possible extended conjugated system (-C=C--C=N-). Similar to their observation (Poch et al. 2014) we also observed a change in the colour of adenine after the energetic processing, the initially white adenine sample becomes darker, see Figure 5.12.

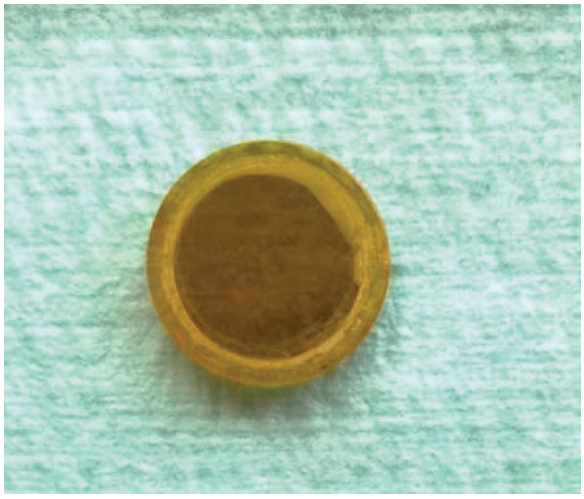

Figure 5.12 - Picture of adenine after ion processing.

5.4.2- New molecules from guanine radiolysis

The irradiation of guanine film did not produced any new absorption peak within the wavenumbers region of 1800 – 720 cm^{-1} (with maybe one exception at 825 cm^{-1}), Figure 5.13.

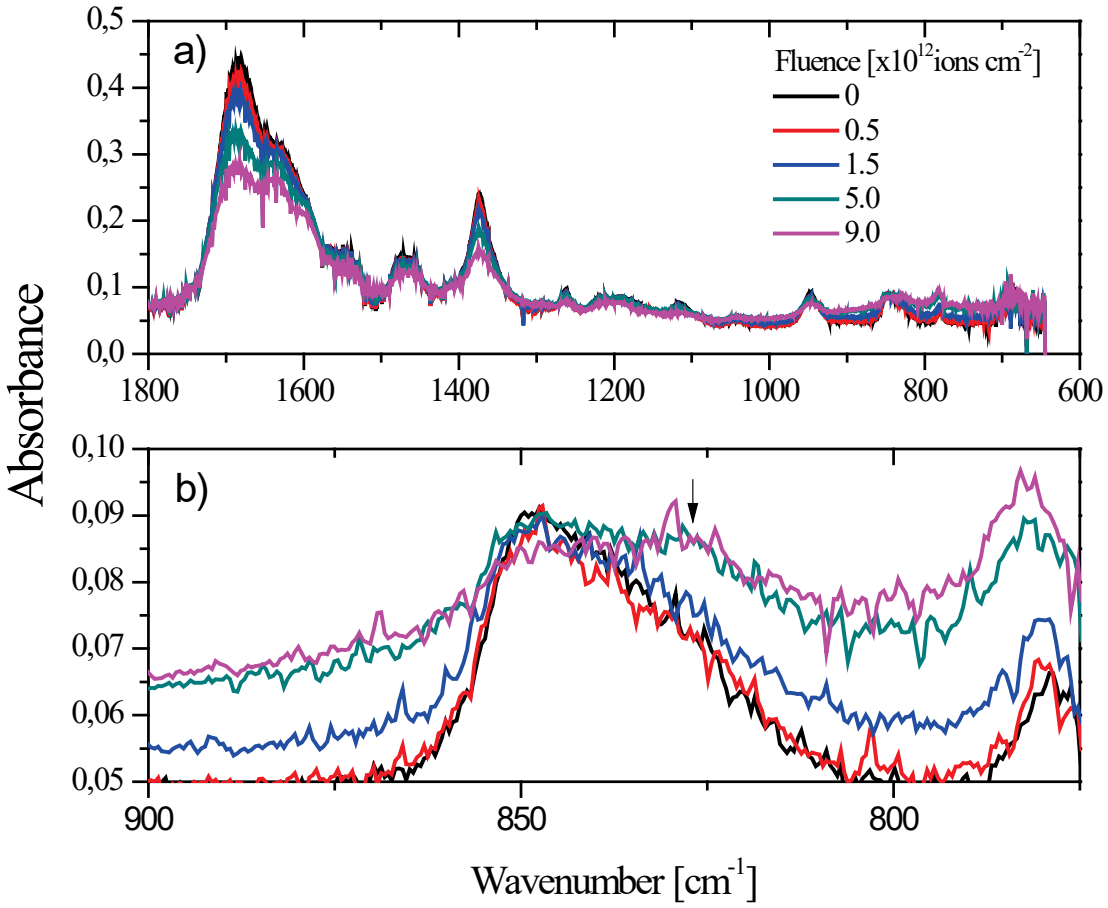

Figure 5.13 - IR absorption of film guanine before and during the irradiation by 190 MeV Ca^{10+} within the wavenumber range from 1800 to 600 cm^{-1} (a) and (b) a zoom in the range of 900 to 700 cm^{-1}. The arrow indicates a possible small absorption peak at 825 cm^{-1} at 20 K.

The possibly observed small peak could be due to a contribution from the water layering, in fact water ice has a broad absorption band centered at about 800 cm^{-1}. Energetic processing of guanine films produced new absorptions band within wavenumbers range from 2300 to 2000 cm^{-1}. We show in Figure 5.14 the IR absorption spectrum of guanine processed by 190 MeV Ca^{10+} at a fluence of 7×10^{12} ions cm^{-2}.

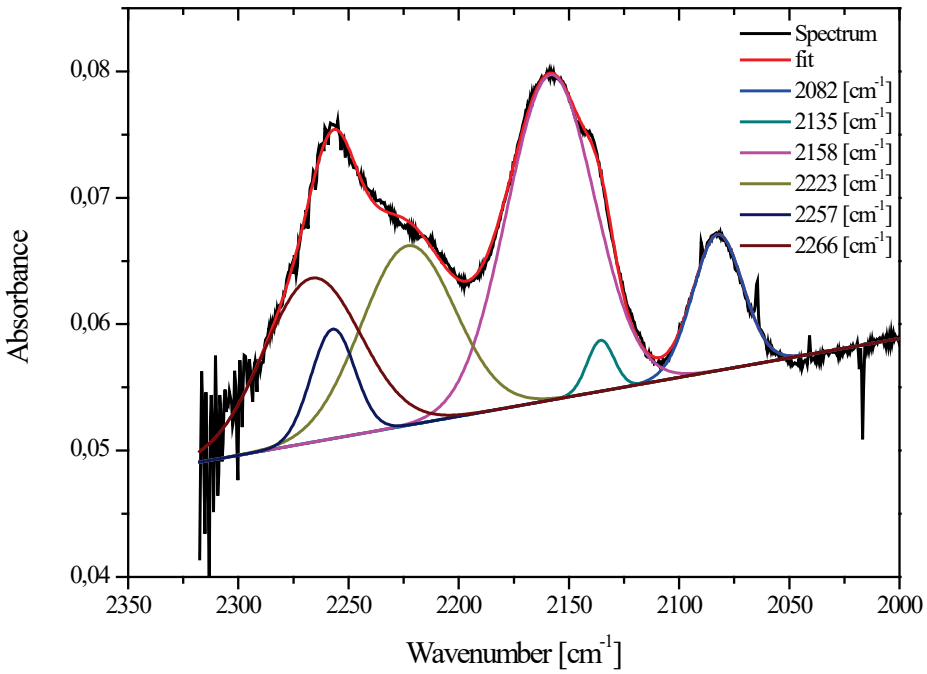

Figure 5.14 - Deconvolution of the band between 2300-2000 cm^{-1} of guanine film irradiated with 190 MeV Ca^{10+} at fluence of 7.0×10^{12} ions cm^{-2} (36.1 eV per molecule) at 20 K.

We observe (through the deconvolution) absorption bands centered at 2082 cm^{-1}, 2135 cm^{-1}, 2158 cm^{-1}, 2223 cm^{-1}, 2257 cm^{-1}, and 2266 cm^{-1}. We also observed a new IR band at 2346 cm^{-1}, this band can be attributed to CO_2. The band centered about 2082 cm^{-1} is a vibration of nitrile and used in the literature assigned as CN^- ion (Moore and Hudson 2003), the peaks at 2135 and at 2158 cm^{-1} probably are vibrations of nitriles and isonitriles (Hudson and Moore 2004). The vibrations at 2257 cm^{-1} and 2266 cm^{-1} are assign of vibration of isontitrile (νN≡C). Isocyanic acid (HNCO) at low temperature presents a vibration at 2254 cm^{-1} (Lowenthal, Khanna, and Moore 2002). In contrast to adenine (Fig. 4.13), the energetic processing of guanine films makes the films “whiter”, Figure 5.15.

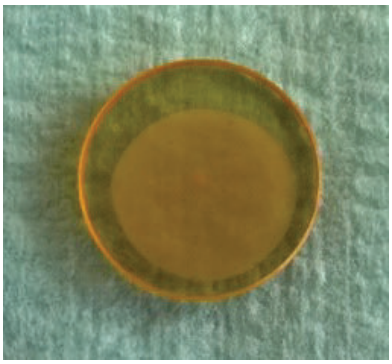

Figure 5.15 - Photo of guanine film after the ion processing by 190 MeV Ca^{10+}.

5.4.3 - New molecules from cytosine radiolysis

The energetic processing of cytosine samples produced new absorption peaks in the region of 2300-2000 cm^{-1}. Figure 5.16 displays the evolution of the IR absorption spectra of cytosine irratiated by 116 MeV U^{32+} at different fluences.

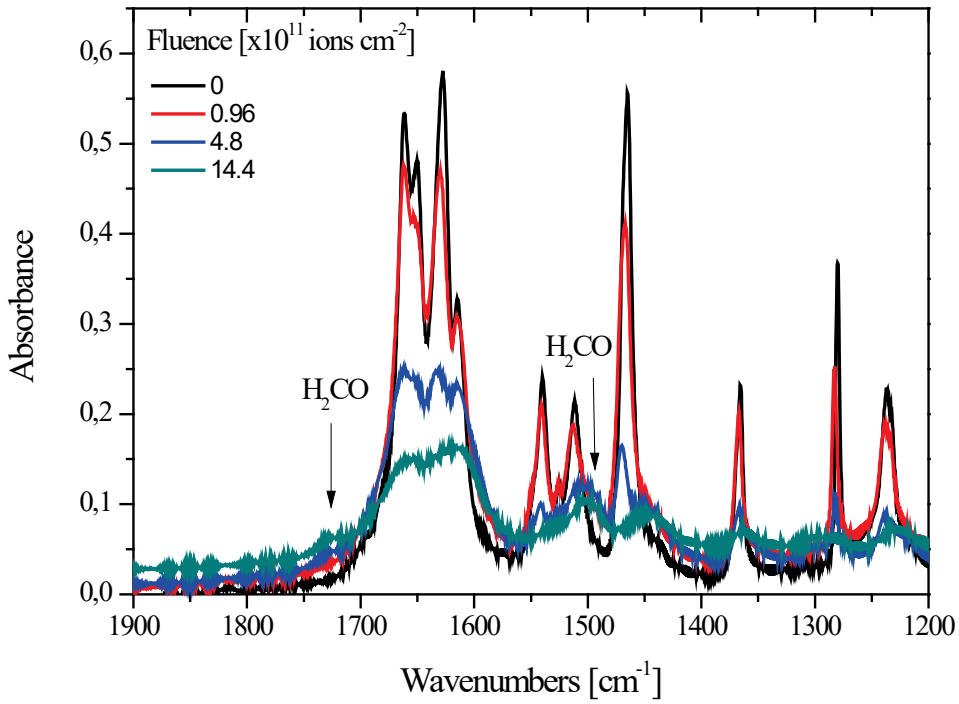

Figure 5.16 – Cytosine film IR absorption spectra before and during the irradiation by 116 MeV U^{32+} at selected fluences at 12 K.

Small peaks are emerging at about 1720 and 1500 cm^{-1}, which can be attributed to H_2CO (de Barros et al., 2012; Gerakines et al., 1996), as can be seen in Fig.5.16. In our experiments, we observed new features emerging between 2300 and 2000 cm^{-1}, the region characteristic of isonitriles and nitriles. Figure 5.17 shows the IR cytosine absorption spectra before and during the bombardment by 116 MeV U^{32+}.

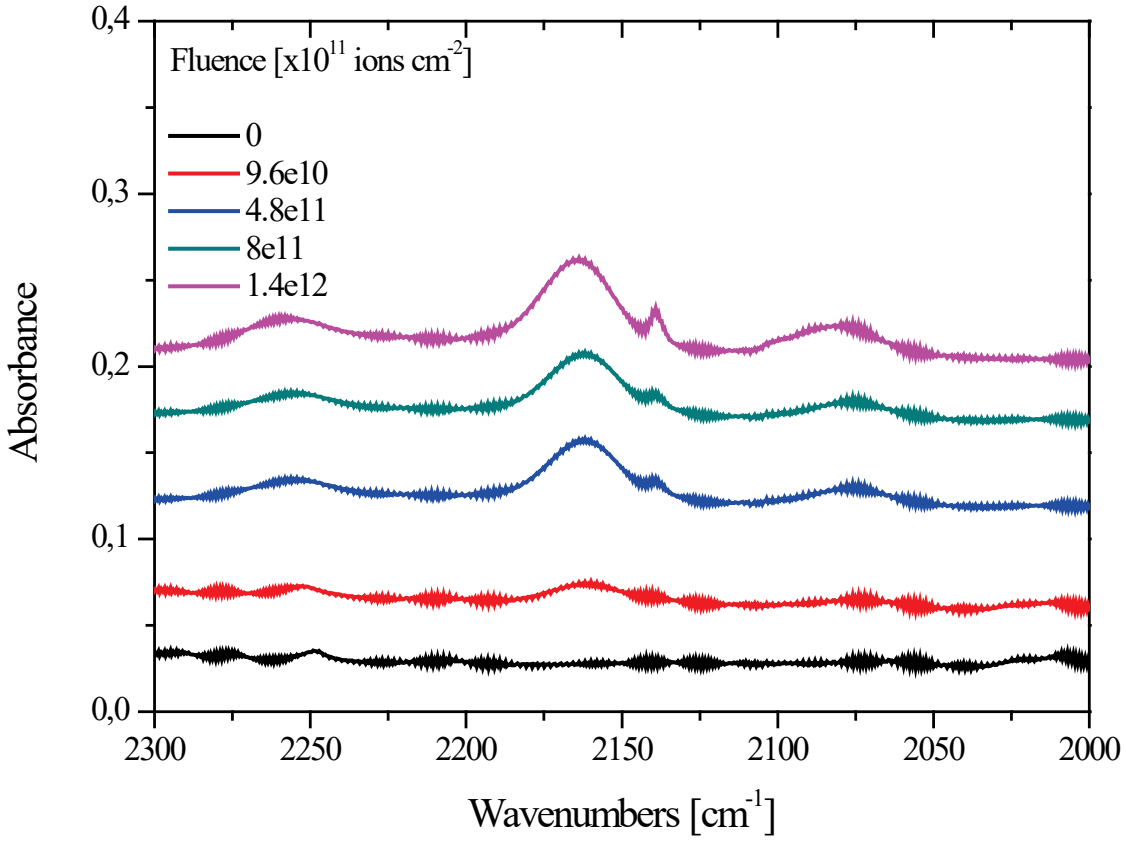

Figure 5.17 – Cytosine film IR absorption spectra irradiated by 116 MeV U^{32+} at different fluences within wavenumbers ranging from 2355 to 2050 cm^{-1}.

The cytosine IR absorption spectrum does not exhibit absorption peaks within this region. Nevertheless, with the radiodegradation of solid cytosine absorption peaks emerge and their intensity increases with the deposited dose. To try to identify the responsible radioproducts for these absorptions we deconvoluted the absorption IR spectrum at high fluence (1.4×10^{12} ions cm^{-2}, 19.6 eV $molecule^{-1}$), Figure 5.18.

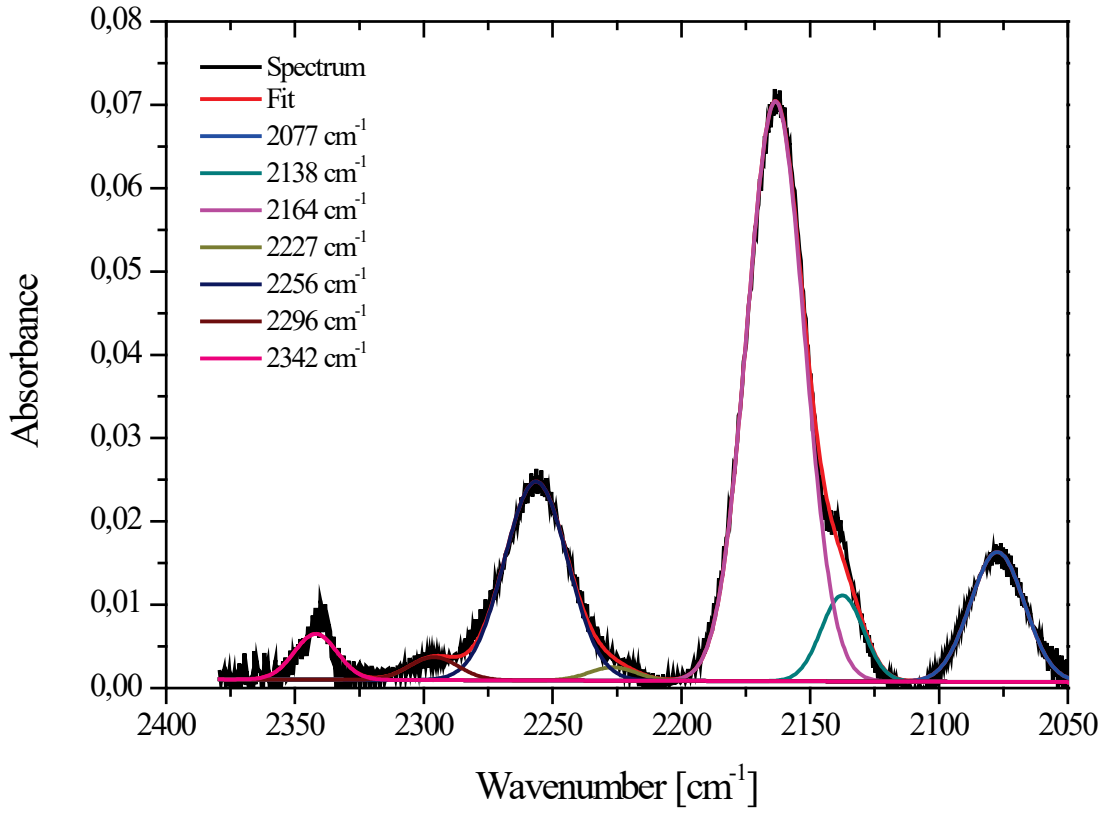

Figure 5.18 - Deconvolution of the band between 2300-2000 cm^{-1} of cytosine film irradiated by 116 MeV U^{32+} at fluence of 1.2 × 10^{12} ions cm^{-2} (19.6 eV per molecule) at 12 K.

The following absorption peaks are observed: 2080, 2094, 2139, 2165, 2222, and 2258 cm^{-1}. The peaks at 2080 and 2094 cm^{-1} may be assigned to CN^- and HCN (Danger *et al.*, 2011; Gerakines *et al.*, 2004; Noble *et al.*, 2013). The FWHH of the absorption peak at 2139 cm^{-1} is 4.4 cm^{-1}, accordingly this seems to be the IR absorption peak of CO (Seperuelo Duarte et al., 2010). The absorption peak at 2165 cm^{-1} may be assigned to OCN^- (Danger et al. 2011; Portugal et al. 2014), indeed, the formation of OCN^- from the destruction of cytosine ring is plausible, see Figure 4.6. The absorption peak at 2258 cm^{-1} is attributed to HNCO (Peeters et al. 2003; Lowenthal, Khanna, and Moore 2002).

5.4.4 - New molecules from uracil radiolysis

Uracil was irradiated by 92 MeV Xe^{23+}. We do not observe any new absorption bands at

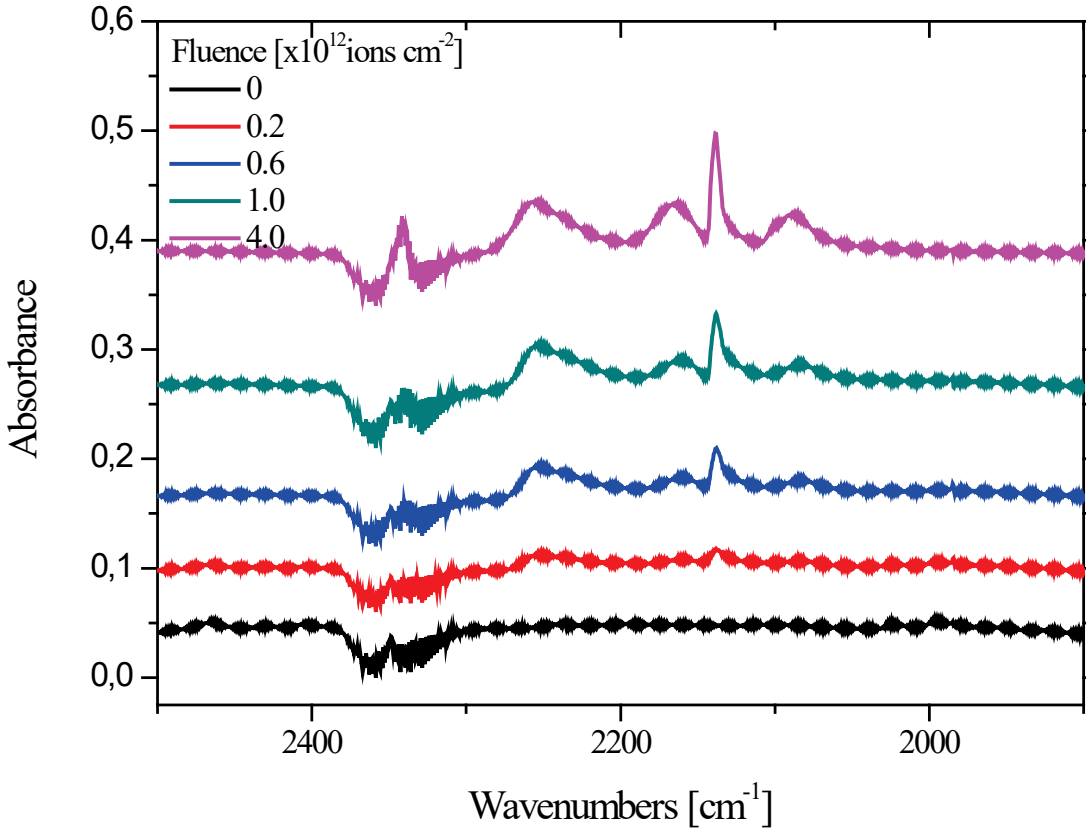

Figure 5.19 - IR absorption spectra of grainy uracil irradiated by 92 MeV Xe^{23+} at different fluences within wavenumbers ranging from 2500 to 2050 cm^{-1} at 12 K.

wavenumber region from 1600 to 700 cm^{-1}. In Figure 5.19 it is evident that a new absorption band emerges from the uracil degradation during irradiation. Also the IR spectrum of irradiated uracil shows an absorption peak at 2342 cm^{-1}, this absorption peak is probably due to the CO_2 formation from uracil fragmentation. To try to identify the radioproducts responsible for these absorptions we deconvoltuded the IR spectrum of uracil irradiated by 92 MeV Xe^{23+} at the fluence equals to 4×10^{12} ions cm^{-2} (53.4 eV $molecule^{-1}$), Figure 5.20.

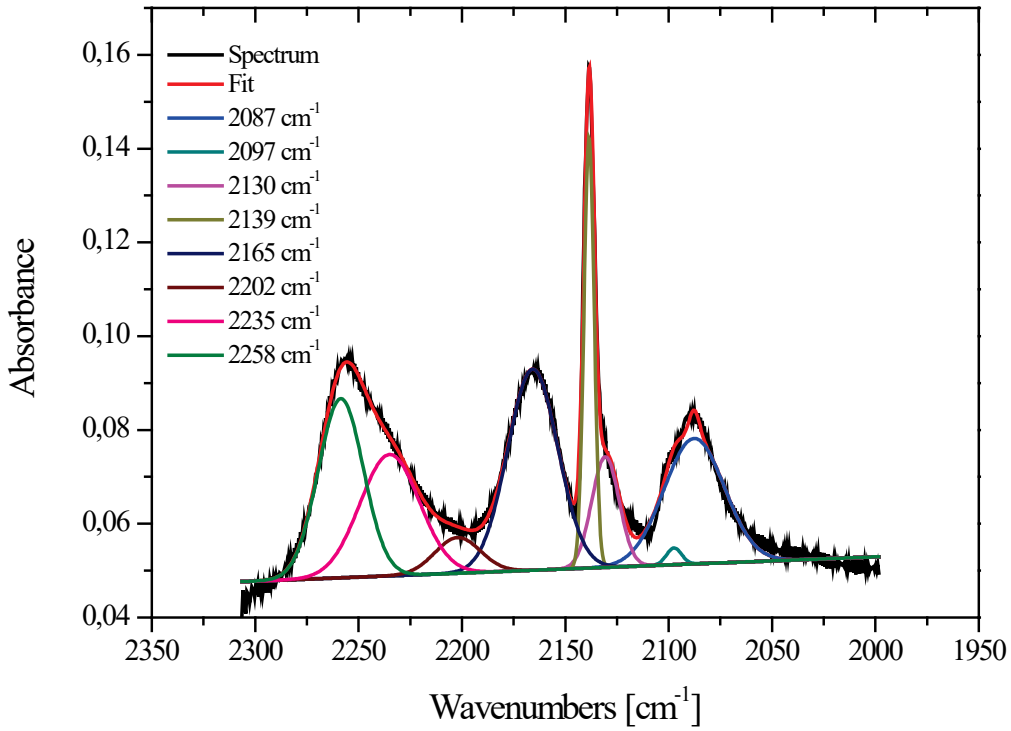

Figure 5.20 - Deconvolution of the band between 2300 and 2000 cm^{-1} of grainy uracil irradiated by 92 MeV Xe^{23+} at a fluence of 4.0×10^{12} ions cm^{-2} at 12 K.

We observed a peak at 2139 cm^{-1} which is an indication of formation of CO (Seperuelo Duarte et al., 2010), the bands at 2087 and 2097 cm^{-1} as said before may be assigned as CN^- and HCN, 2130 cm^{-1} probably may be attributed to an isonitrile or nitrile (Hudson and Moore 2004), 2165 cm^{-1} to OCN^-, 2235 and 2258 cm^{-1} is a vibration of nitrile and isonitrile (Peeters et al. 2003; Hudson and Moore 2004).

5.4.5 - New molecules from thymine radiolysis

Thymine was processed by 190 MeV Ca^{10+}. The evolution of thymine's spectrum under irradiation is shown at Figure 5.21.

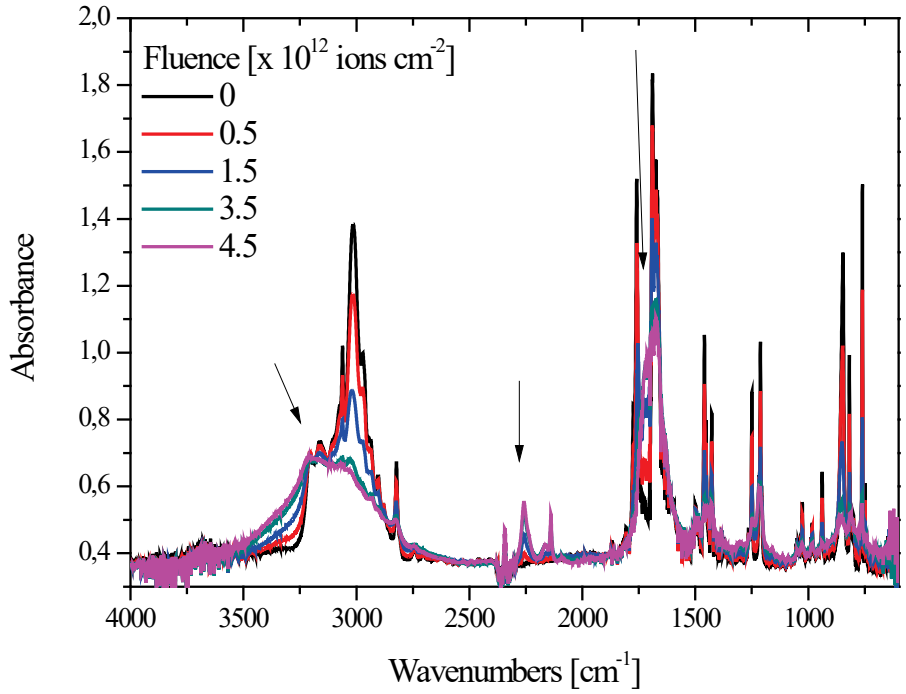

Figure 5.21 – IR spectra of thymine film before and during the ion irradiation at different fluences at 12 K. Arrows indicate new absorption peaks.

From Figure 5.21 it is possible to see new absorption bands growing with increasing projectile fluence. Let us now look at different wavenumbers range thus evidencing the observed new absorption features, Figure 5.22.

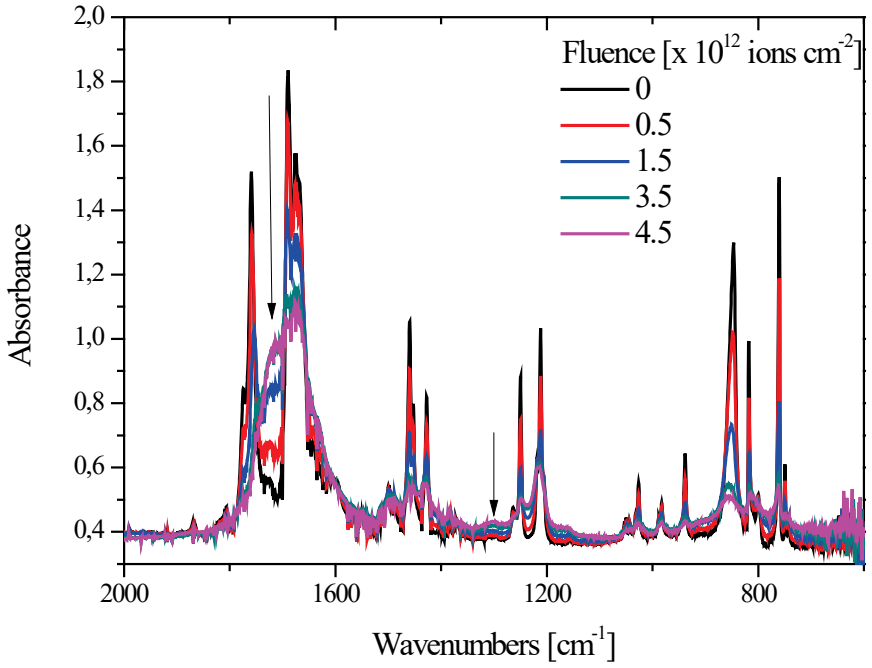

Figure 5.22 – IR spectra of thymine film before and after irradiation within the wavenumber range from 2000 to 600 cm^{-1} at 20 K. Arrows indicate new absorption bands.

We observe a new broad absorption centered about 1712 cm^{-1}. This absorption is probably due to a vibration of C=O (Günzler and Gremlich 2002). Small peaks are observed at 1306 cm^{-1} and 1234 cm^{-1}, these vibration are typical of C-H. For example, methane exhibits an absorption band in 1303 cm^{-1} (Mejia et al. 2013).

We deconvoluted the large absorption band located between 2300 and 2050 cm^{-1}, see Figure 5.23.

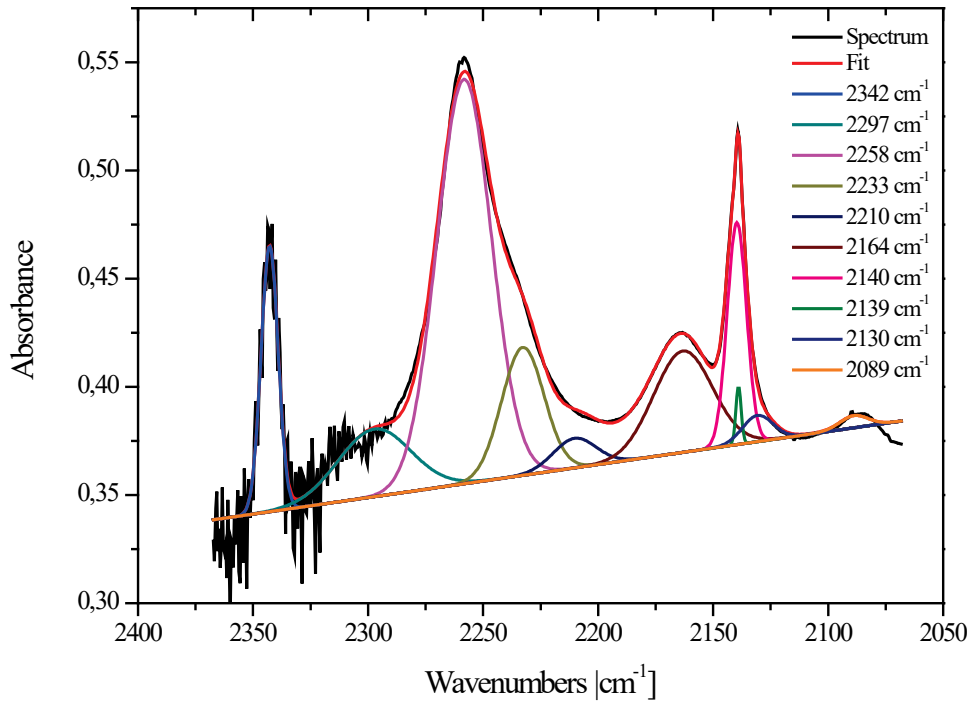

Figure 5.23 – Deconvolution of IR spectrum of thymine film irradiated by 190 MeV Ca^{10+} at fluence of 4.5 × 10^{12} ions cm^{-2}at 20 K.

From the deconvolution, we observed absorption peaks centered at 2342, 2297, 2258, 2233, 2210, 2164, 2140, 2139, 2130 and 2089 cm^{-1}. As said before, these bands may be assigned to CO_2 (2342 cm^{-1}), νN≡C (2258 cm^{-1}), OCN^- (2164 cm^{-1}), CO (2139 cm^{-1}), νC≡N (2130, 2140, 2233, and 2210 cm^{-1}), and CN^- (2089 cm^-). The irradiation of thymine film darkens the color of the sample, this can be correlated to formation of new molecules or even to structural changes in the film, Figure 5.24.

Note that, the white part seen in Figure 5.24 is the non-irradiated part of the film shielded by the sample holder, whereas the irradiated area corresponds to the darker region.

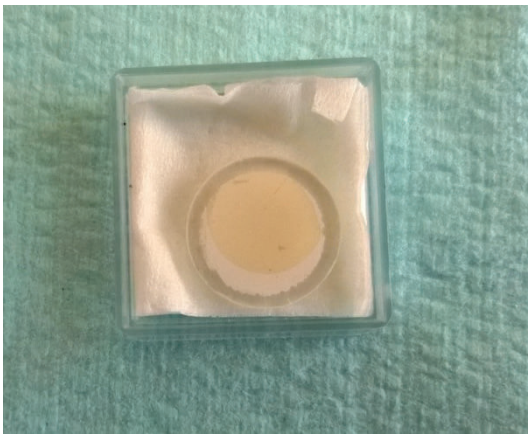

Figure 5.24 - Thymine film irradiated by 190 MeV Ca^{10+}.

References

Barros, A. L. F. de, P. Boduch, A. Domaracka, H. Rothard, and E. F. da Silveira. 2012. "Radiolysis of Astrophysical Ices by Heavy Ion Irradiation: Destruction Cross Section Measurement." *Low Temperature Physics* 38 (8): 759. doi:10.1063/1.4743476.

Broekhuizen, F. A. van, I. M. N. Groot, H. J. Fraser, E. F. van Dishoeck, and S. Schlemmer. 2006. "Infrared Spectroscopy of Solid CO–CO $_2$ Mixtures and Layers." *Astronomy and Astrophysics* 451 (2): 723–31. doi:10.1051/0004-6361:20052942.

Burgdorf, M., D. P. Cruikshank, C. M. Dalle Ore, T. Sekiguchi, R. Nakamura, G. Orton, E. Quirico, and B. Schmitt. 2010. "A TENTATIVE IDENTIFICATION OF HCN ICE ON TRITON." *The Astrophysical Journal* 718 (2): L53–57. doi:10.1088/2041-8205/718/2/L53.

Danger, G., J.-B. Bossa, P. de Marcellus, F. Borget, F. Duvernay, P. Theulé, T. Chiavassa, and L. d'Hendecourt. 2011. "Experimental Investigation of Nitrile Formation from VUV Photochemistry of Interstellar Ices Analogs: Acetonitrile and Amino Acetonitrile." *Astronomy & Astrophysics* 525 (January): A30. doi:10.1051/0004-6361/201015736.

Evans, N. L., C. J. Bennett, S. Ullrich, and R. I. Kaiser. 2011. "On the interaction of adenine with ionizing radiation: mechanistical studies and astrobiological implications." *The Astrophysical Journal* 730 (2): 69. doi:10.1088/0004-637X/730/2/69.

Fryer, J.R., C.H. McConnell, F. Zemlin, and D.L. Dorset. 1992. "Effect of Temperature on Radiation Damage to Aromatic Organic Molecules." *Ultramicroscopy* 40 (2): 163–69. doi:10.1016/0304-3991(92)90057-Q.

Gerakines, P. A., Schutte, W. A., and Ehrenfreund, P. 1996. “Ultraviolet Processing of Interstellar Ice Analogs.” *Astronomy and Astrophysics* 312 (January): 289–305.

Gerakines, P.A., M.H. Moore, and R.L. Hudson. 2004. “Ultraviolet Photolysis and Proton Irradiation of Astrophysical Ice Analogs Containing Hydrogen Cyanide.” *Icarus* 170 (1): 202–13. doi:10.1016/j.icarus.2004.02.005.

Gerakines, Perry A., Reggie L. Hudson, Marla H. Moore, and Jan-Luca Bell. 2012. “In Situ Measurements of the Radiation Stability of Amino Acids at 15–140K.” *Icarus* 220 (2): 647–59. doi:10.1016/j.icarus.2012.06.001.

Günzler, Helmut, and Hans-Ulrich Gremlich. 2002. *IR Spectroscopy: An Introduction*. Weinheim: Wiley-VCH.

Hudson, R. L., M. H. Moore, and P. A. Gerakines. 2001. “The Formation of Cyanate Ion (OCN^-) in Interstellar Ice Analogs.” *The Astrophysical Journal* 550 (2): 1140–50. doi:10.1086/319799.

Hudson, R.L., and M.H. Moore. 2004. “Reactions of Nitriles in Ices Relevant to Titan, Comets, and the Interstellar Medium: Formation of Cyanate Ion, Ketenimines, and Isonitriles.” *Icarus* 172 (2): 466–78. doi:10.1016/j.icarus.2004.06.011.

Loeffler, M. J., G. A. Baratta, M. E. Palumbo, G. Strazzulla, and R. A. Baragiola. 2005. “CO_2 Synthesis in Solid CO by Lyman-α Photons and 200 keV Protons.” *Astronomy and Astrophysics* 435 (2): 587–94. doi:10.1051/0004-6361:20042256.

Lowenthal, M.S, R.K Khanna, and Marla H Moore. 2002. “Infrared Spectrum of Solid Isocyanic Acid (HNCO): Vibrational Assignments and Integrated Band Intensities.” *Spectrochimica Acta Part A: Molecular and Biomolecular Spectroscopy* 58 (1): 73–78. doi:10.1016/S1386-1425(01)00524-8.

Mejía, C., A.L.F. de Barros, E. Seperuelo Duarte, E.F. da Silveira, E. Dartois, A. Domaracka, H. Rothard, and P. Boduch. 2015. “Compaction of Porous Ices Rich in Water by Swift Heavy Ions.” *Icarus* 250 (April): 222–29. doi:10.1016/j.icarus.2014.12.002.

Mejia, C. F., A. L. F. de Barros, V. Bordalo, E. F. da Silveira, P. Boduch, A. Domaracka, and H. Rothard. 2013. “Cosmic Ray-Ice Interaction Studied by Radiolysis of 15 K Methane Ice with MeV O, Fe and Zn Ions.” *Monthly Notices of the Royal Astronomical Society* 433 (3): 2368–79. doi:10.1093/mnras/stt902.

Moore, M.H., and R.L. Hudson. 2003. “Infrared Study of Ion-Irradiated N2-Dominated Ices Relevant to Triton and Pluto: Formation of HCN and HNC.” *Icarus* 161 (2): 486–500. doi:10.1016/S0019-1035(02)00037-4.

Peeters, Z., O. Botta, S. B. Charnley, R. Ruiterkamp, and P. Ehrenfreund. 2003. “The Astrobiology of Nucleobases.” *The Astrophysical Journal* 593 (2): L129–32. doi:10.1086/378346.

Pilling, S., D. P. P. Andrade, E. F. da Silveira, H. Rothard, A. Domaracka, and P. Boduch. 2012. “Formation of Unsaturated Hydrocarbons in Interstellar Ice Analogues by Cosmic Rays: *Unsaturation Induced by Cosmic Rays*.” *Monthly Notices of the Royal Astronomical Society* 423 (3): 2209–21. doi:10.1111/j.1365-2966.2012.21031.x.

Pilling, S., L. A.V. Mendes, V. Bordalo, C. F.M. Guaman, C. R. Ponciano, and E. F. da Silveira. 2013. “The Influence of Crystallinity Degree on the Glycine Decomposition Induced by 1 MeV Proton Bombardment in Space Analog Conditions.” *Astrobiology* 13 (1): 79–91. doi:10.1089/ast.2012.0877.

Poch, O., S. Kaci, F. Stalport, C. Szopa, and P. Coll. 2014. “Laboratory Insights into the Chemical and Kinetic Evolution of Several Organic Molecules under Simulated Mars Surface UV Radiation Conditions.” *Icarus* 242 (November): 50–63. doi:10.1016/j.icarus.2014.07.014.

Portugal, W., S. Pilling, P. Boduch, H. Rothard, and D. P. P. Andrade. 2014. “Radiolysis of Amino Acids by Heavy and Energetic Cosmic Ray Analogues in Simulated Space Environments: Glycine Zwitterion Form.” *Monthly Notices of the Royal Astronomical Society* 441 (4): 3209–25. doi:10.1093/mnras/stu656.

Chapter 6 - Pyridine irradiation

Pyridine is a liquid at room temperature with a vapor pressure close to that of water (20 mmHg at 25 °C). Therefore, it is easy to prepare pyridine ices. Due to the low temperature (12 K) pyridine condenses on the substrate forming an ice layer. Due to the easy manipulation of this substance, we had a great opportunity to deposit pyridine ice inside the AODO chamber controlling its thickness by QCM. The sample was irradiated by 90 keV O^{6+} using the ion beam of the ARIBE facility. With the AODO TOF-SIMS set-up we studied the ionic species sputtered from the pyridine ice by the ion irradiation. We also performed another experiment with pyridine; we irradiated it by 116 MeV U^{32+} at IRRSUD and analyzed the ice degradation by FTIR. Note that time-of-flight and FTIR are complementary techniques, i.e., FTIR provides information about the modification in the bulk whereas time-of-flight provides information about the cationic species sputtered from the ice. It is very important to mention here that the comparison between the TOF-SIMS and IR results need to be examined carefully. Indeed, the energy deposition mechanism might differ significantly for the two projectiles, 116 MeV U^{32+} is in the electronic stopping power regime, whereas 90 keV O^{6+} the electronic stopping power is indeed higher than the nuclear stopping power, however the latter cannot be neglected.

6.1 – Pyridine irradiation - 116 MeV U^{32+} - IR experiment

Pyridine was irradiated by 116 MeV U^{32+} and its evolution during the irradiation was followed using the IR absorption spectroscopy. During the irradiation we first observe an increase in the area of the absorption spectrum, as we did earlier with cytosine, see 4.21. We correlate this phenomenon with the compaction of the ice with a change of the band

strength and we applied the same method to evaluate the variation of the band strength than that used in the study of cytosine irradiation. To study the pyridine ice deterioration by ion bombardment, we followed the evolution of four absorption peaks: 1030, 1068, 1437, and 1482 cm^{-1}. These peaks correspond different modes of vibrations of distinct parts of the pyridine ring, see in Chapter 4.

We present in Table 6.1 the relative variation of the band strength due to the compaction.

Table 6.1 – Variation of the peak area at the begging of the irradiation of pyridine ice and the relative increase of its band strength.

Peak position [cm^{-1}]	Relative variation of the area	Relative increase in the band strength
1030	0.92	8%
1068	0.86	14%
1437	0.93	7%
1482	0.90	10%

First at very low fluences the area of peak area increases, and then starts to decrease exponentially as a function of the projectile ion fluence. As an example, we plotted the peak area at 1030 cm^{-1} as a function of the projectile ion fluence, Figure 6.1

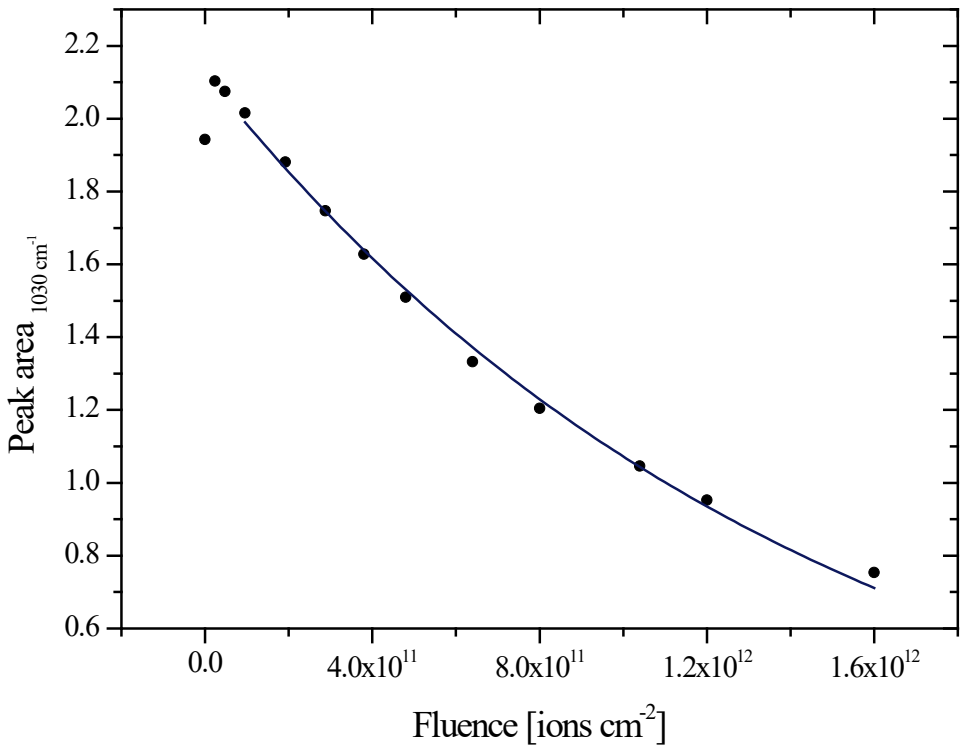

Figure 6.1 – IR absorption peak area of pyridine at 1030 cm^{-1} as a function of the accumulated projectiles.

Using equation 3.8 we determined the apparent destruction cross section. Table 6.2 displays the apparent destruction cross sections for the selected absorption peaks and the associated average value.

Table 6.2 – Pyridine destruction cross-section for selected peaks area and its average.

Peak position [cm^{-1}]	Apparent destruction cross section [$\times 10^{-13}$ cm^2]
1030	(6.8±0.1)
1068	(6.3±0.2)
1437	(5.8±0.2)
1482	(7.1±0.2)
Average	(6.5±0.6)

6.2 – Formation of new molecules from pyridine degradation

At end of the irradiation of the cytosine film, we recorded a background, then turned the ZnSe window to 180° C in order to deposit pyridine ice on the clean face of the ZnSe window, as described at Chapter 3. Finally, the window was turned 90º and the pyridine ice was irradiated by 116 MeV U^{32+}. Due to the presence of the cytosine film on the other face of the window, it was not possible to obtain the information of the annealing of the pyridine ice after the energetic ion process. Adopting a layering rate of 1 monolayer per 100 seconds, we obtained that pyridine was deposited on 100 monolayers of water ice, 1×10^{17} water molecules per cm^2. Therefore, we need to take into consideration the possibility of formation of new molecules containing oxygen in this composition, even in view of absence of oxygen in the pyridine. We also need to keep in mind that pyridine contains only one nitrogen atom itself.

Let us now present the evolution of the pyridine ice during the irradiation (Fig. 6.2).

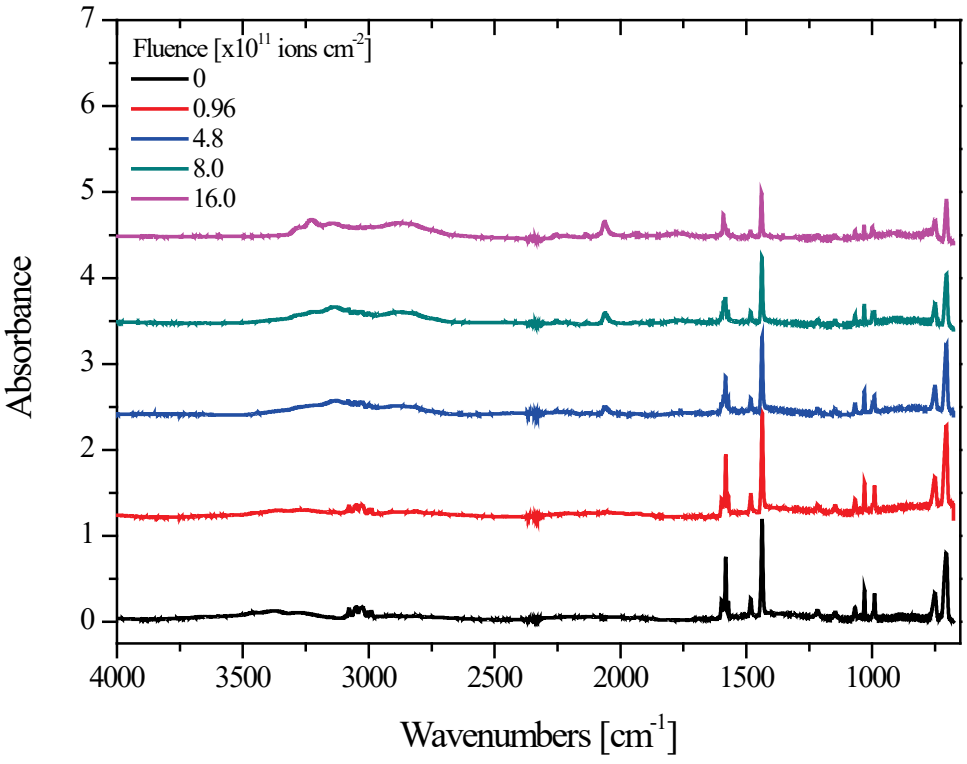

Figure 6.2 – IR absorption spectra of pyridine ice irradiated by 116 MeV U^{32+} at different fluences.

We observed a decrease in the IR absorption intensity of the peaks with the increase of the accumulated ions per square centimeters. In the region from 1620 to 670 cm^{-1}, we observe new bands emerging at 1590 cm^{-1} and at 999 cm^{-1}. Figure 6.3 is a zoom in these regions, which allow to focus on the new absorptions bands which emerge from pyridine ice degradation.

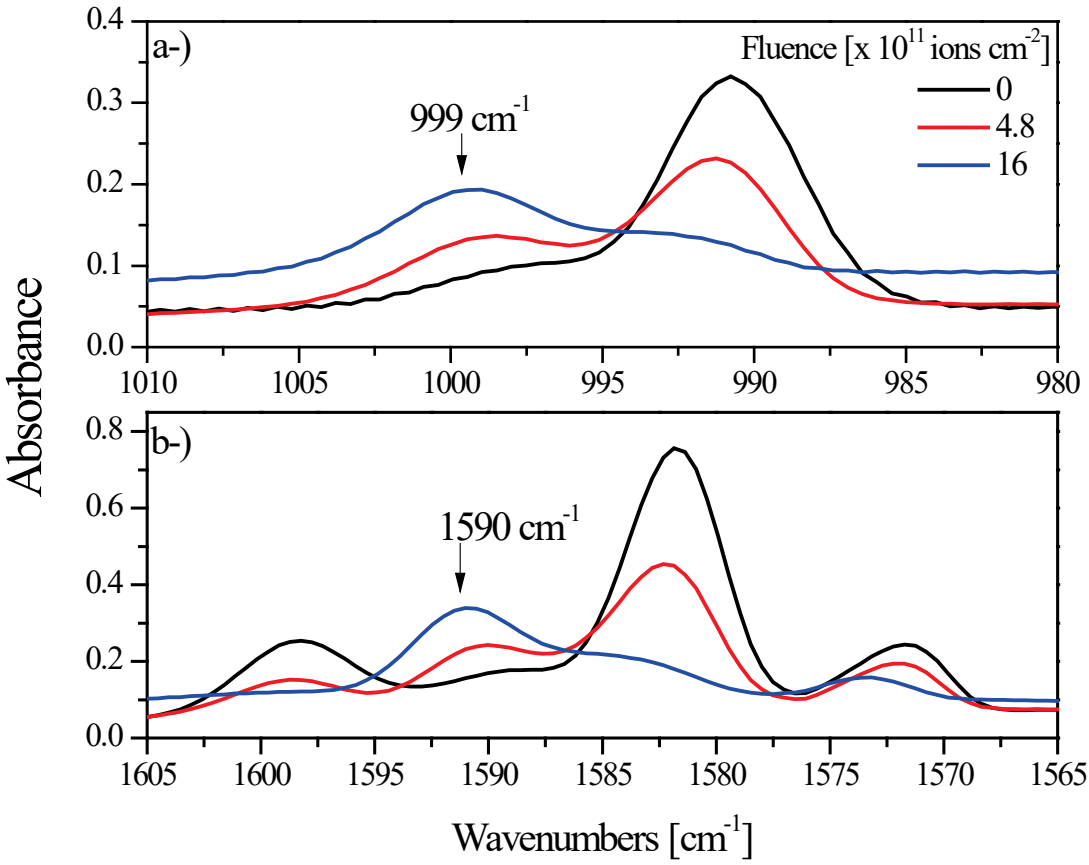

Figure 6.3 – IR absorption spectra of pyridine ice irradiated by 116 MeV U^{32+} at different fluences. We give a zoom at regions of (a) 1010 to 980 cm^{-1} and of (b) 1605 and 1565 cm^{-1}.

The new absorption peaks are indicated in Figure 6.3. In view of to the complexity of the pyridine spectrum we again indicate the intrinsic limitation of IR absorption spectroscopy to identify complex molecules. It is indeed very difficult to assign a specific molecule to the new absorption bands observed. Also, contamination from the residual gas contributes

to this difficulty. Smith et al. (2014) irradiated a mixture of pyridine and CO_2 (1:1) with 0.8 MeV protons, they deposited a final dose in their ice of 36 eV per molecule. They exhibit the spectra of pyridine + CO_2 before and after the irradiation within the wavenumber range from 800 to 2000 cm^{-1}. They point out the similarity of the IR spectrum of pyridine + CO_2 processed by the proton irradiation with the IR spectra of nicotid acid and picolinic acid, both molecules contain pyridine and oxygen in their composition. In our experiment we just achieved 20.1 eV per molecule, also the source of oxygen becomes from the pollution. Nevertheless, we also observe the same structure pointed out by Smith et al. (2014) as being similar to those present in the IR absorption spectra of of nicotid acid and picolinic acid. Here, we show the IR absorption spectra of pyridine before and during the ion energetic process (Figure 6.4), the asterisks in the figures are the structures similar to those present in the picolinic acid spectrum or observed by Smith et al. (2014)

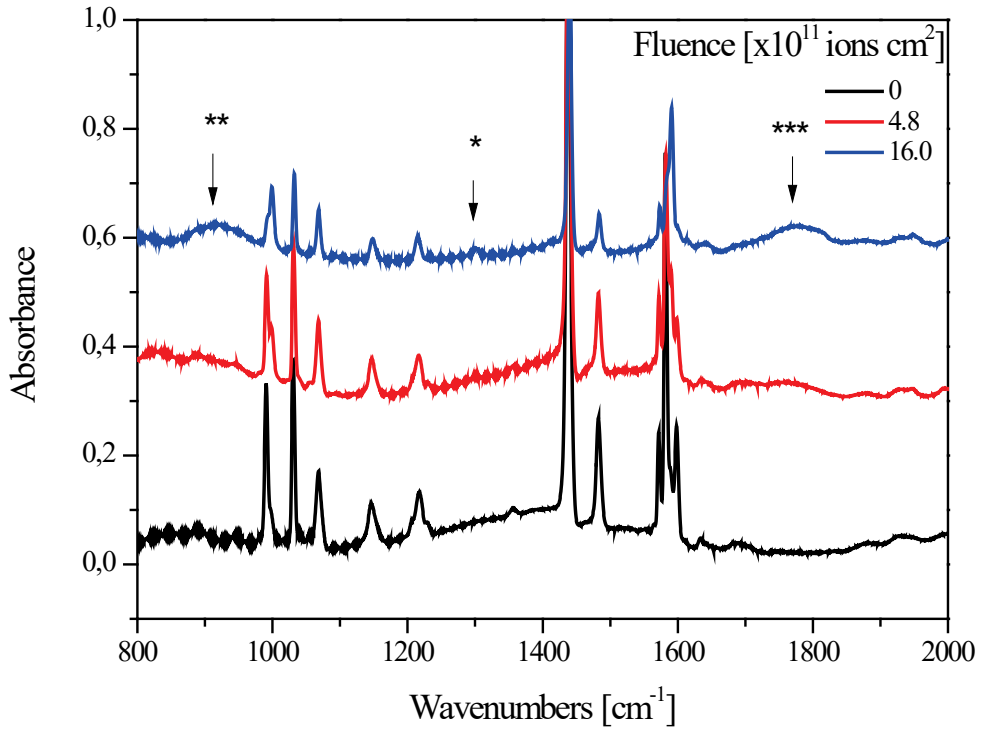

Figure 6.4 – IR spectra of pyridine ice before and during the ion bombardment with 116 MeV U^{32+}. The asterisks indicate the structures similar to those observed by Smith et al. (2014) or present in the picolinic acid IR absorption spectrum .

The large absorption band centered about 1200 cm^{-1}, (Fig. 6.4) was also observed for picolinic acid. The absorption peak centered at 1300 cm^{-1} is observed in the pyridine + CO_2 ice processed by 0.8 MeV protons moreover, nicotic acid, isonicotic acid and picolnic acid present absorption in this region. Nicotic acid, isonicotid acid and pyridine + CO_2 ice irradiated by 0.8 MeV protons show an absorption band about at 1750 cm^{-1}.

As previously said, the contamination by oxygen species cannot be neglected and seems to play an important role in the formation of new molecules due the similarity of our results and those obtained by Smith et al. (2014). Let us now zoom in on the different relevant wavenumber regions in different parts of the IR spectra of pyridine ice before and during the energetic processing.

Figure 6.5 displays the IR spectra of pyridine ice, before and after ion bombardment, within the wavenumber range of 2400-1610 cm^{-1}.

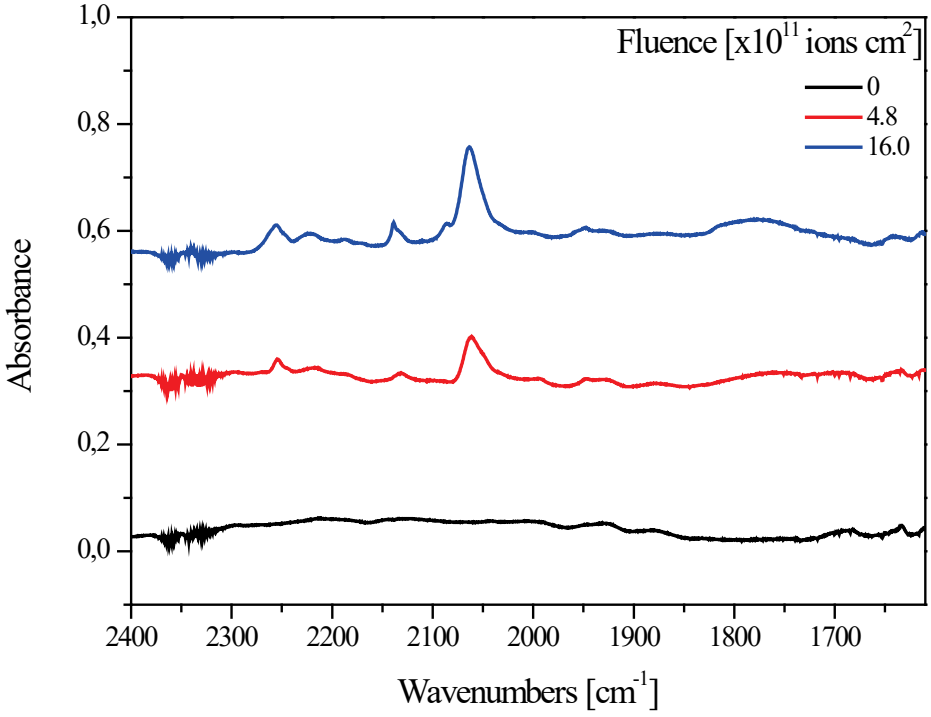

Figure 6.5 - IR spectra of pyridine ice before and during the ion bombardment 116 MeV U^{32+} at different fluences within wavenumbers range from 2400 to 1610 cm^{-1}

This wavenumber region 2300 – 2100 cm^{-1} is a region of vibration of nitrile, isonitriles and triple bonds between carbons (Günzler and Gremlich 2002). Also, molecules such as CO, CO_2 (Mennella, Palumbo, and Baratta 2004) , HNCO (Peeters et al. 2003) exhibit absorption peaks in this region. In Figure 6.5 it is possible to see an increase about 2340 cm^{-1}, this can be assigned as CO_2. Using the band strength of 7.6×10^{-17} cm per molecule (Lv et al. 2014), at the end of the experiment there are 1×10^{16} molecules of CO_2 per cm^2. It is established that the irradiation of carbon subtracts covered with water layer is an effective via of CO_2 formation (Gomis and Strazzulla 2005). However, the CO_2 observed may come from the residual gas in the chamber.

We deconvoluted the absorption band between 2300 and 1850 cm^{-1}, Figure 6.6.

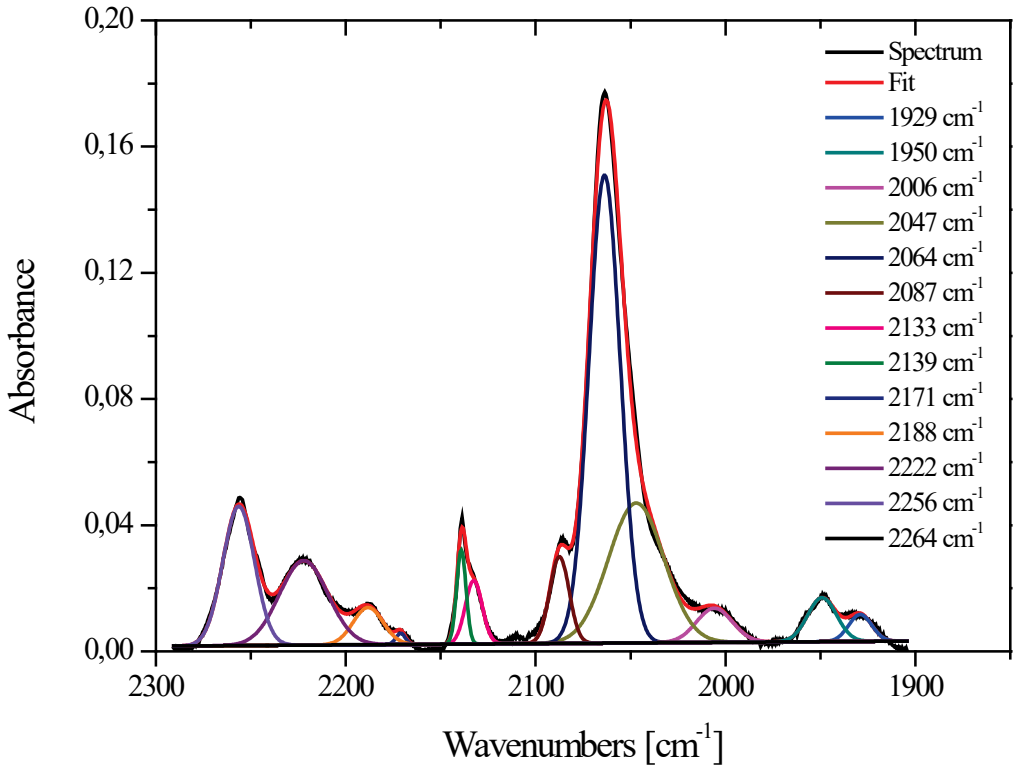

Figure 6.6 – Deconvolution of the IR band of pyridine ice irradiated by 116 MeV U^{32+} at fluence of 1.6×10^{12} ions cm^{-2}.

With the deconvolution shows the presence of absorptions peaks centered at 1929, 1950, 2006, 2047, 2064, 2087, 2133, 2139, 2171, 2188, 2222, 2256, and 2264 cm^{-1}. This region contains vibrations of C≡C, C≡N or N≡C. Indeed, we are able to assigned some of these band like C_3H_4 (1950 cm^{-1}) (Hudson, Moore, and Raines 2009) or C_6 (Trottier and Brooks 2004). Furthermore, C_5O_2 exhibits an IR absorption peak at 2060 cm^{-1} (Palumbo et al. 2008), C_3 presents an absorption peak at 2039 cm^{-1} (Seperuelo Duarte 2009 and the references therein). CN^- at 2087 cm^{-1}, 2133, 2171, 2256, and 2264 νCN or νNC (Moore and Hudson 2003). The wavenumber region from 4000 and 2500 cm^{-1} is characteristic of vibrations of N-H, C-H and O-H. Here, we show the modification induced by the irradiation in this region, Figure 6.7.

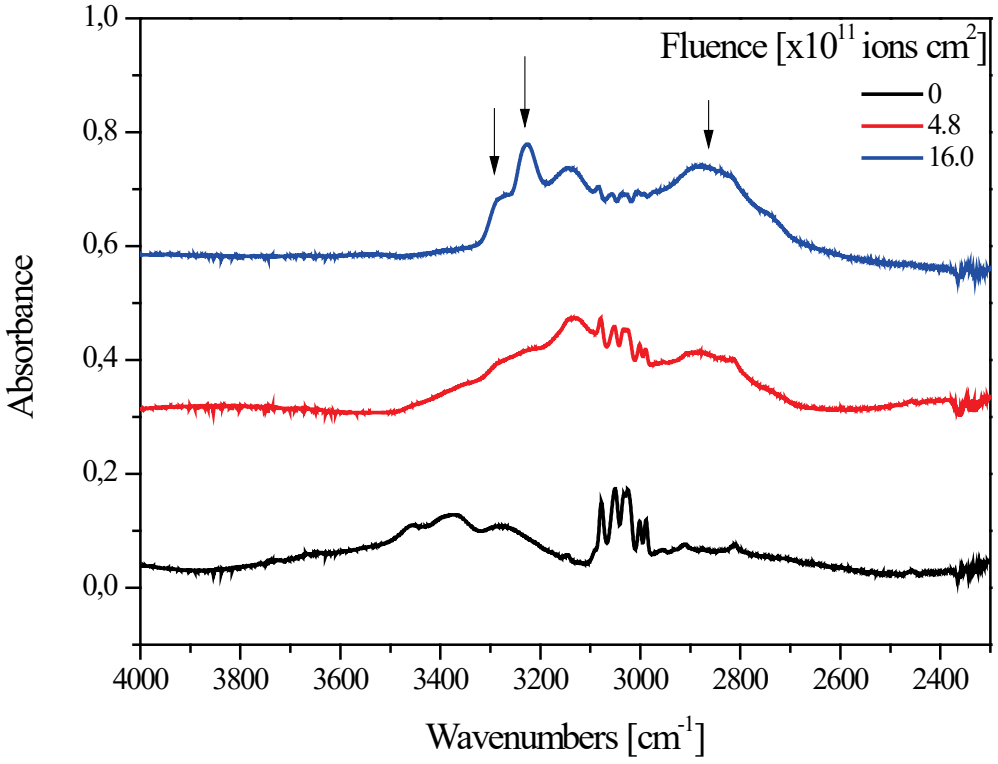

Figure 6.7 - IR spectra of pyridine ice before and during the ion bombardment with 116 MeV U^{32+} at different fluences within wavenumbers ranging from 4000 to 2300 cm^{-1}.

At high fluences (1.6×10^{12} ions cm^{-2}) pyridine spectrum exhibits new absorption peaks, see the narrows in the Figure 6.7. These peaks are centered at about 3276 cm^{-1}, 3226 cm^{-1} and for a broad band at 2877 cm^{-1}.

As said before it, was not possible to obtain the spectrum of the residue of the pyridine irradiation at 300K because on the other face of the window we have the residue of the cytosine. Figure 6.8 displays the picture the residue of the energetic ion processing of pyridine ice. The black color is a strong indication of carbonization of the pyridine sample. That is expected as pyridine is mostly composed by carbon and hydrogen atoms.

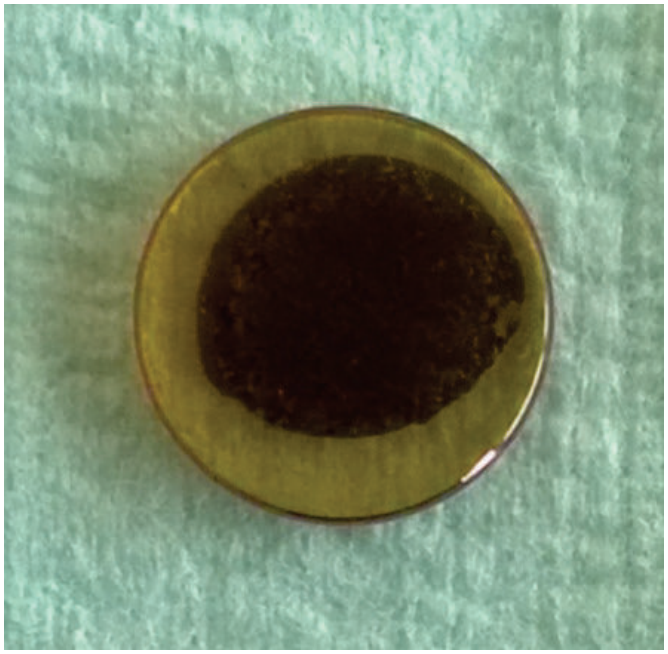

Figure 6.8 – Picture of the residue of the irradiation of pyridine ice.

6.3 - TOF experiment

When the vacuum in the irradiation chamber of AODO was at 5×10^{-9} mbar and the cold head at 12 K, we opened the fine valve towards the tube with liquid pyridine was connected. The pressure in the chamber was increased to 1×10^{-6} mbar. After 13 hours under these conditions the QCM showed that we had a pyridine ice with a thicknesses of 1.4 μm. Note that the thickness is much higher than the penetration depth of 90 keV O^{6+} in pyridine. With TOF-SIMS we will monitor the secondary cation emissions. Figure 6.9 shows the secondary ion mass spectrum from pyridine ice irradiated with 90 keV O^{6+} projectiles.

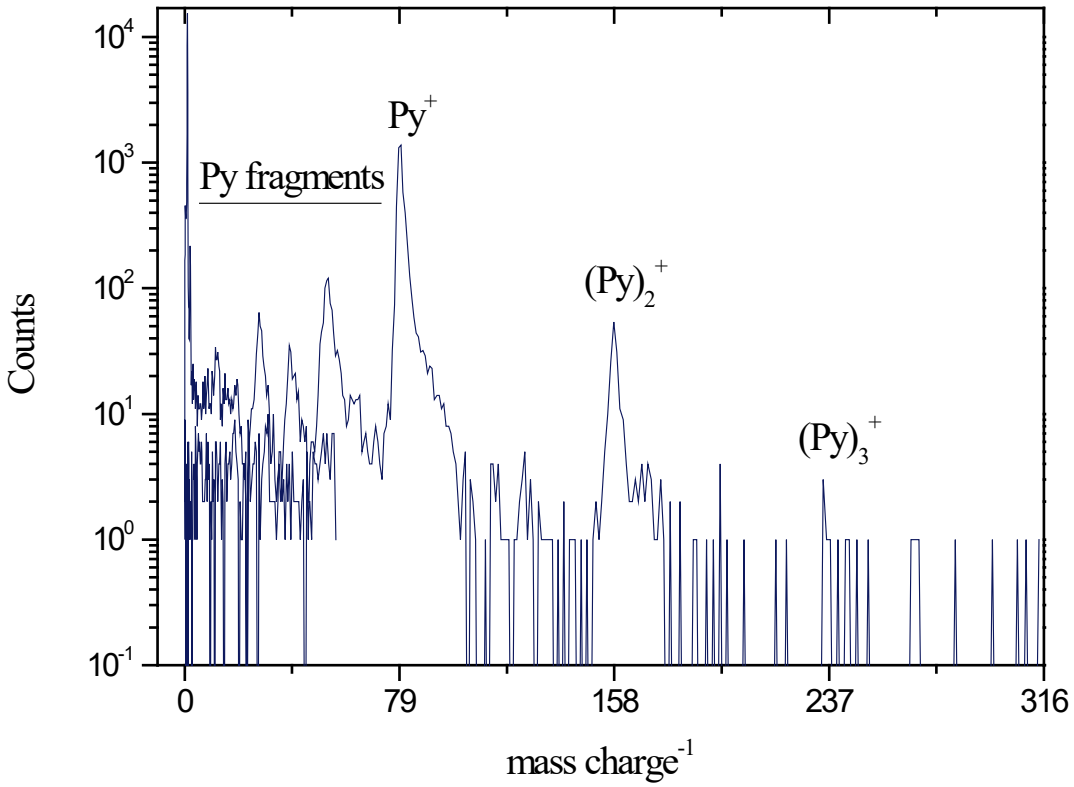

Figure 6.9 – Time-of-flight spectrum of pyridine irradiate by 90 keV O^{6+}.

Let us now analyze this mass spectrum and summarize the possible fragments and observed peaks, see Table 6.3.

Table 6.3 – Cationic fragments detected by TOF.

Mass charge^{-1}	Intensity	Possible fragments or clusters
12	31	C^+
14	16	N^+ or CH_2^+
39	35	$C_3H_3^+$ or $C_2H_2N^+$
52	115	$C_4H_4^+$ or $C_3H_3N^+$
65	13	$C_5H_5^+$ or $C_4H_4N^+$ or $C_4H_3N^+$
79	1382	Py^+
92	24	$(Py + CH)^+$
158	54	$(Py)^+_2$

It is important to point out that the mass resolution is not good enough to distinguish between molecules or radicals like HCN^+ or CN^+. In particular, the peaks are very broad.

Among the fragments, we observe a highest contribution for $C_4H_4^+$ or $C_3H_3N^+$, these fragments correspond to the loss of N and CH_2 from the pyridine molecule. The loss of the heteroatom (nitrogen) is expected, since normally in cyclic molecules the fragmentation occurs mainly in the heteroatom. $C_3H_3^+$ or $C_2H_2N^+$ are complementary fragments forming together pyridine. We also observe formation of a complex between pyridine and CH but in low abundance, appearing as a shoulder in the big peak which corresponds to ionized pyridine.

REFERENCES

Gomis, O., and G. Strazzulla. 2005. "CO_2 Production by Ion Irradiation of H_2O Ice on Top of Carbonaceous Materials and Its Relevance to the Galilean Satellites." *Icarus* 177 (2): 570–76. doi:10.1016/j.icarus.2005.04.003.

Günzler, H., and H.-U. Gremlich. 2002. *IR Spectroscopy: An Introduction*. Weinheim: Wiley-VCH.

Hudson, R.L., M.H. Moore, and L.L. Raines. 2009. "Ethane Ices in the Outer Solar System: Spectroscopy and Chemistry." *Icarus* 203 (2): 677–80. doi:10.1016/j.icarus.2009.06.026.

Lv, X. Y., P. Boduch, J. J. Ding, A. Domaracka, T. Langlinay, M. E. Palumbo, H. Rothard, and G. Strazzulla. 2014. "Sulfur Implantation in CO and CO2 Ices." *Monthly Notices of the Royal Astronomical Society* 438 (2): 922–29. doi:10.1093/mnras/stt2004.

Mennella, V., M. E. Palumbo, and G. A. Baratta. 2004. "Formation of CO and CO_2 Molecules by Ion Irradiation of Water Ice–covered Hydrogenated Carbon Grains." *The Astrophysical Journal* 615 (2): 1073–80. doi:10.1086/424685.

Moore, M.H., and R.L. Hudson. 2003. "Infrared Study of Ion-Irradiated N2-Dominated Ices Relevant to Triton and Pluto: Formation of HCN and HNC." *Icarus* 161 (2): 486–500. doi:10.1016/S0019-1035(02)00037-4.

Palumbo, M. E., P. Leto, C. Siringo, and C. Trigilio. 2008. "Detection of C_3O in the Low-Mass Protostar Elias 18." *The Astrophysical Journal* 685 (2): 1033–38. doi:10.1086/591017.

Peeters, Z., O. Botta, S. B. Charnley, R. Ruiterkamp, and P. Ehrenfreund. 2003. “The Astrobiology of Nucleobases.” *The Astrophysical Journal* 593 (2): L129–32. doi:10.1086/378346.

Seperuelo Duarte, E. 2009. Thése “Etude Par Spectroscopie Infrarouge Des Effets D’irradiation de Glaces D’intérêt Astrophysique Par Des Ions Lourds.” France: Université de Caen Normandie et Université Catholique de Rio.

Smith, K. E., M. P. Callahan, P. A. Gerakines, J. P. Dworkin, and C. H. House. 2014. “Investigation of Pyridine Carboxylic Acids in CM2 Carbonaceous Chondrites: Potential Precursor Molecules for Ancient Coenzymes.” *Geochimica et Cosmochimica Acta* 136 (July): 1–12. doi:10.1016/j.gca.2014.04.001.

Trottier, A., and R. L. Brooks. 2004. “Carbon-Chain Oxides in Proton-Irradiated CO Ice Films.” *The Astrophysical Journal* 612 (2): 1214–21. doi:10.1086/422680.

Chapter 7 – Discussion

This chapter presents the compilation of results obtained after irradiating different AHMs (Chapters 5 and 6). Further we will compare the results of our experiments with those reported in literature concerning energetic processing of these molecules using different ionizing agents such as slow and swift projectiles, UV photons, X-rays, and electrons. The examination of the half-life of adenine exposed to ionizing radiation of different regions of outer space like DCs and ISM is covered at the end of this chapter.

7.1 Destruction cross section as a function of electronic stopping power

In Chapter 5 we presented the results of irradiation of the nucleobases. Figures 5.2 and 5.5, clearly show that projectiles with high electronic stopping powers provoke a faster decay in the peak area. Indeed, several authors reported that the destruction cross section obeys a power law: $\sigma_d = C\, S_e^n$, from a best fit of this formula to our experimental results, we can obtain the input needed to estimate survival half-life time.

Adenine

Adenine was exposed to five different projectiles with stopping power range from 10^3 to 1.12×10^4 keV μm^{-1}. Figure 7.1 displays the destruction cross section (914 cm^{-1}) and the average apparent destruction cross section as a function of the electronic stopping power. The error adopted for the electronic stopping power and for the destruction cross section was 10%, whereas the error for the average destruction cross section is the standard deviation.

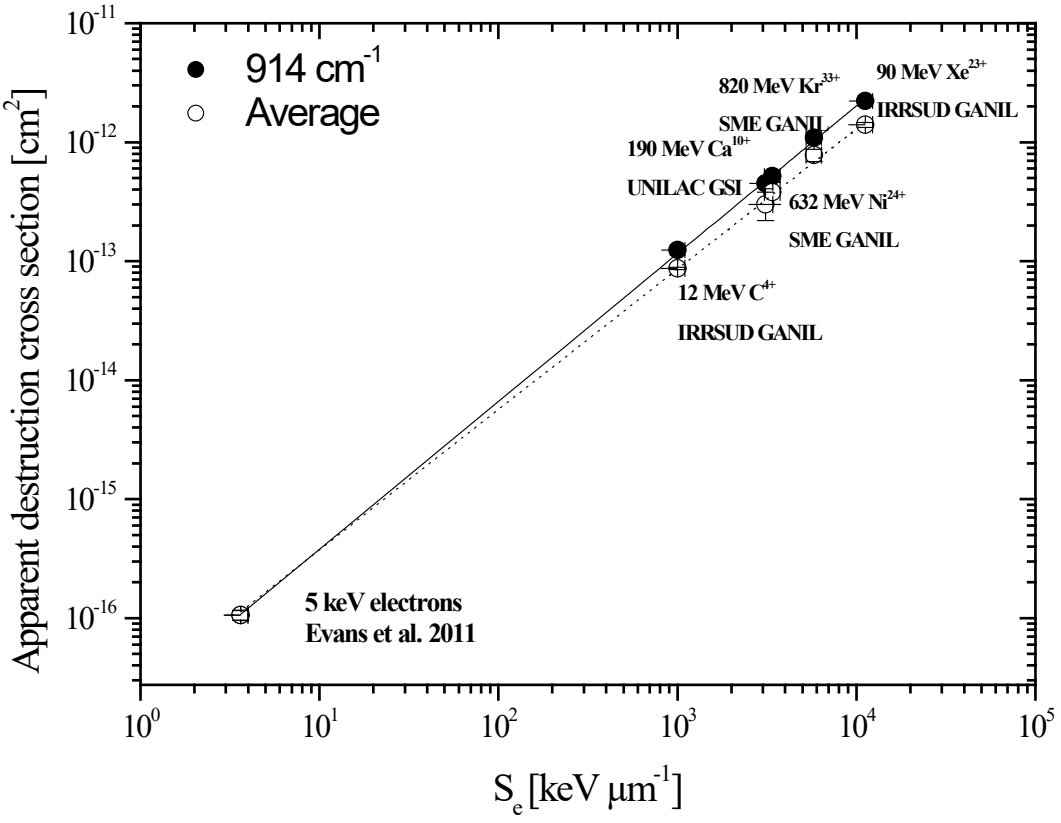

Figure 7.1 – The destruction cross section (914 cm^{-1}) and the average apparent destruction cross section as a function of the electronic stopping power of adenine.

The adenine destruction cross section for 5 keV electrons (Evans et al. 2011) is also included in Figure 7.1. Using the power law, we obtained an adenine destruction cross section $\sigma = (2.0 \pm 0.4) \times 10^{-17} S_e^{(1.24 \pm 0.01)}$.

Note that adenine destruction cross sections obtained from the two different accelerators and with two different experimental set-ups (GANIL and GSI) fall onto the same curve, showing high consistency and reproducibility of our experiments.

Evans *et al.* (2011) also estimated the destruction cross section for 1 MeV and 1 keV protons under the assumption that they could be obtained by scaling the 5 keV electron data with the stopping power ratio. We can also estimate the destruction cross section for protons using our findings (Fig. 7.1). Calculating the electronic stopping power of protons

using the SRIM code (Ziegler *et al.* 2012) together with the observed power law allowing to estimate the destruction cross section for protons at those energies (1 MeV and 1 keV). The obtained values were: $\sigma = 1.0 \times 10^{-15}$ and $\sigma = 1.8 \times 10^{-15}$ cm^2 for 1 keV and 1 MeV protons, respectively. The cross sections reported by (Evans et al. 2011) are about 60% lower than these results, however, this approximation is of the same order of magnitude as our calculations, showing the validity of their extrapolation. It is important to say that the observed power law is only valid in the electronic stopping power domain. In the case of 1 MeV and 1 keV protons, the electronic stopping power is at least one order of magnitude higher than the nuclear stopping power.

Cytosine

We also irradiated cytosine with four different projectiles in the electron stopping power ranging from 3.2×10^3 to 1.34×10^4 keV μm^{-1}. Figure 7.2 shows the destruction cross section of cytosine corresponding the highest observed value (this was the case for the absorption at 1539 cm^{-1}) as a function of the electronic stopping power.

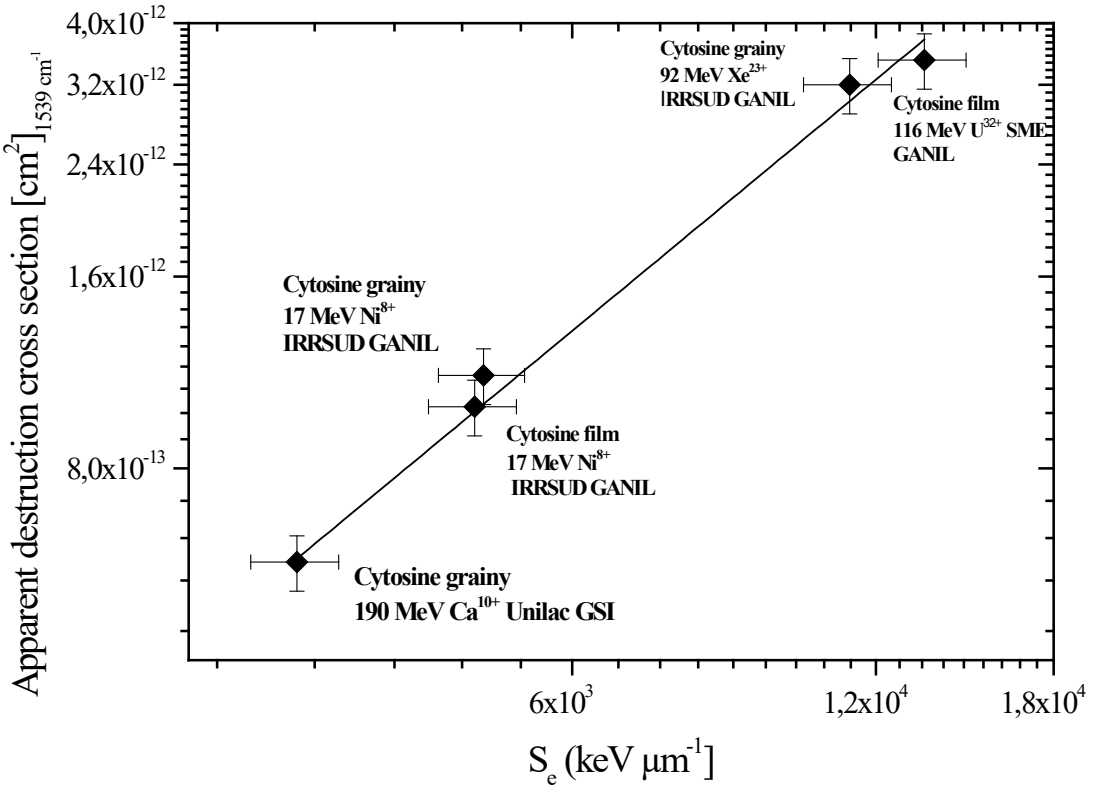

Figure 7.2 – The destruction cross section of cytosine corresponding the highest value (1539 cm^{-1}) as a function of the electronic stopping power.

Using the above mentioned power law to fit our data, we the obtained a destruction cross section as function of the electronic stopping power: $\sigma_d = (1.5 \pm 1.0) \times 10^{-17} S_e^{(1.3 \pm 0.08)}$. This behavior is similar to that reported for small molecules and also for the amino acid glycine (Portugal et al. 2014). Cytosine and adenine destruction cross sections display a similar dependence on the electronic stopping power: approximately $\sim S_e^{1.2}$. Indeed, since cytosine and adenine are similar molecules, aromatic and with the same electronic stopping power within error bars, it is expected that the dependence on the electronic energy loss would be very similar.

7.2 Radiosensibility of the AHMs

Four nucleobases (adenine, cytosine, guanine, and thymine) were irradiated under the same conditions. At GSI, the four nucleobases were exposed to 190 MeV Ca^{10+}. This allows us to directly compare the obtained cross sections. Data from Chapter 5 is exhibited again below (Table 7.1) to facilitate the comparison between the destruction cross sections.

Table 7.1 – The average destruction cross sections for the nucleobases exposed to 190 MeV Ca^{10+}.

AHM	Average destruction cross sections [$\times 10^{-13}$ cm^2]
Guanine	(1.3 ± 0.8)
Adenine	(3.0 ± 0.8)
Thymine grainy	(4 ± 1)
Thymine film	(5.5 ± 0.8)
Cytosine	(5 ± 1)

The values of the destruction cross sections are of the same order of magnitude. It can be observed that guanine is the least sensitive nucleobase to 190 MeV Ca^{10+} irradiation followed by adenine. Both are slightly smaller than cytosine and thymine, these last two nucleobases are the same within the error bars.

$$\sigma_d^{guanine} < \sigma_d^{adenine} < \sigma_d^{thymine} \approx \sigma_d^{cytosine}$$

Uracil, adenine, and cytosine were also exposed to the ion beam (92 MeV Xe^{23+}). The observations are that guanine is more radioresistant than adenine and furthermore uracil and cytosine are the same within error bars (Table 7.2).

Table 7. 2 – The average destruction cross sections for different nucleobases exposed to 92 MeV Xe^{23+}.

AHMs	Average destruction cross sections [× 10^{-12} cm^2]
Adenine	(1.4 ± 0.4)
Cytosine	(2.1 ± 0.6)
Uracil	(2.0 ± 0.6)

Thymine and uracil are very similar molecules differing by a methyl radical (thymine is also known as 5-methyl uracil). Therefore, this result is not surprising.

Table 7.3 displays the average destruction cross section of pyridine and cytosine irradiated by 116 MeV U^{32+}.

Table 7.3 – Average destruction cross sections of cytosine and pyridine exposed to 116 MeV U^{32+}.

AHM	Destruction cross section [×10^{-12} cm^2]
Cytosine film	(2.4 ± 0.7)
Pyridine	(0.65 ± 0.06)

Note that the destruction cross section of pyridine amounts only about 30% of the destruction cross section of cytosine, this shows that pyridine is more radioresistant than cytosine. This difference is almost the same as observed between the destruction cross sections of guanine and cytosine exposed to 190 MeV Ca^{10+}. Therefore, we can suggest the following chain of radioresistance against corpuscular radiation,

$$\sigma_d^{pyridine} \approx \sigma_d^{guanine} < \sigma_d^{adenine} < \sigma_d^{thymine} \approx \sigma_d^{uracil} \approx \sigma_d^{cytosine}$$

Huang et al. (2014) performed irradiation of solid nucleobases (adenine, cytosine, guanine and thymine) at room temperature with 30 keV Ar^+. They estimated the number of damaged molecules following the IR peak area decays as a function of the deposited dose. They reported a radioresistance in the respective order adenine < cytosine < thymine < guanine. Our findings are not in agreement with this report. However, it is important to mention that their experiments were performed in the nuclear energy loss domain. Therefore, the mechanism of deposition of energy is different in our experiments. In the nuclear energy loss domain, the energy is deposited by elastic collisions of the projectile and the target nuclei, see Chapter 2. In contrast, in the electronic energy loss domain the projectiles deposit energy via interaction with the electronic cloud of the target atoms. Moreover, the molecular damage also depends on the temperature.

7.3 Comparison between different irradiation sources

As far as we know, only a small number of studies have been performed about the irradiation of nucleobases and pyridine in the solid phase. Here our results will be compared with those from the literature:

- Peeters et al. (2003) exposed organic molecules embedded in an argon matrix to UV photons: adenine, uracil, and glycine.
- Guan et al. (2010) irradiated films of organic molecules, including adenine, with UV photons.
- Pilling et al. (2011) exposed solid samples of different amino acids and the nucleobases adenine and uracil to soft X-rays.
- Evans et al. (2011) exposed adenine samples with and without thin layers of oxygen to 5 keV electrons.

- Smith et al. (2014) processed ices of pyridine + CO_2 with 0.8 MeV protons.
- Recently, McMurtry et al. (2016) irradiated different mixtures of pyridine and CO_2 with 5 keV electrons.
- Peteers el al. (2005) also exposed AHMs, including pyridine, in an argon matrix to UV photons.

Let us now compare the destruction cross sections of our experiments with those available in the literature, Table 7.4 displays the destruction cross sections of different AHMs for different ionizing agents, and for the sake of convenience, average cross sections previously presented have been incorporated.

Table 7.4 – Destruction cross sections and radiation G yield of different molecules irradiated by different ionizing agents.

Target	Ionizing agent	Destruction cross section [cm^2]	Radiation G yield [eV^{-1}]	Reference
Adenine grainy	820 MeV Kr^{33+}	$(1.1 \pm 0.2) \times 10^{-12}$	12.56	(Vignoli Muniz et al. 2017)
Adenine film	632 MeV Ni^{24+}	$(4.5 \pm 0.4) \times 10^{-13}$	9.70	
Adenine grainy	190 MeV Ca^{10+}	$(1.24 \pm 0.06) \times 10^{-13}$	8.29	(Vignoli Muniz et al. 2017)
Adenine grainy	5 keV electrons	$(1.07 \pm 0.24) \times 10^{-16}$	1.98	(Vignoli Muniz et al. 2017; Evans et al. 2011)
Adenine film	10.2 UV photons	$(5 \pm 2) \times 10^{-22}$	4.9×10^{-5}	(Guan et al. 2010)
Adenine in an Argon matrix	10.2 UV photons	2.7×10^{-18}	0.26	(Peeters et al. 2003)
Adenine grainy	150 eV photons	3×10^{-19}		(Pilling et al. 2011)
Uracil grainy	92 MeV Xe^{23+}	$(2.8 \pm 0.1) \times 10^{-12}$		This work
Uracil in an Argon matrix	10.2 eV photons	1.1×10^{-17}	1.08	(Peeters et al. 2003)
Uracil grainy	150 eV photons	1.2×10^{-18}		(Pilling et al. 2011)
Cytosine grainy	116 MeV U^{32+}	$(3.50 \pm 0.09) \times 10^{-12}$	21.96	This work
Cytosine grainy	92 MeV Xe^{23+}	$(3.2 \pm 0.3) \times 10^{-12}$	24.03	This work
Cytosine grainy	17 MeV Ni^{8+}	$(1.17 \pm 0.03) \times 10^{-12}$	20.08	This work
Cytosine film	17 MeV Ni^{8+}	$(1.31 \pm 0.06) \times 10^{-12}$	22.48	This work
Cytosine grainy	190 MeV Ca^{10+}	$(5.7 \pm 0.1) \times 10^{-13}$	14.98	This work
Thymine film	190 MeV Ca^{10+}	$(6.6 \pm 0.2) \times 10^{-13}$	12.52	This work
Thymine grainy	190 MeV Ca^{10+}	$(6.0 \pm 0.2) \times 10^{-13}$	11.38	This work
Guanine film	190 MeV Ca^{10+}	$(1.5 \pm 0.1) \times 10^{-13}$	3.76	This work
Adenine grainy	X-rays 150 eV	3×10^{-19}		(Pilling et al. 2011)
Uracil grainy	X-rays 150 eV	1.2×10^{-18}		(Pilling et al. 2011)

From Table 7.4 it is clear that heavy ions are highly efficient in the destruction of the studied molecules. The destruction cross sections obtained in this work are around 10^4 times higher than for 5 keV electrons (Evans et al. 2011), 10^9 times higher than for UV photons (Guan et al. 2010), 10^5 times higher than for X-rays (Pilling et al. 2011) and 10^6 times higher than for UV photon degradation of adenine and uracil in argon matrix (Peeters et al. 2003). Note that the nucleobases embedded in an argon matrix are more photosusceptible than the solid molecule samples. Due to the low penetrability in the matter, the photodegradation takes places in the first layers of the solids. According to Poch et al. (2014) the photoproducts of adenine still absorb the UV photons and protect the bulk from the photodegradation. Guan et al. (2010) also point out that hydrogen bonds and the Van der Waals of molecules in a noble gas matrix are weaker when compared with the solid or a film molecules. In a noble gas matrix, the molecules seems to be isolated like in the gas phase. When they are exposed to UV radiation field they are rapidly degraded, since in this case there is no protection effects of the previous molecules layers. The weak bounds between the molecules and the matrix would not be favorable to dissipate energy thus making the degradation more probable. For example, phosphorescence of adenine in argon and nitrogen matrices at low temperature (77 K) has been reported (Polewski et al. 2011). For phosphorescence to take place, the electronic cloud needs to be in an excited state for adequately long time period, since the transition from a triplet state to a singlet is a forbidden transition. Therefore, it seems that when the molecule is embedded in a noble gas matrix, the non-radiative mechanisms of dissipation of energy are less efficient.

Peeters et al. (2005) exposed pyridine, pyrimidine and s-triazine ($C_3H_3N_3$) in an argon matrix to UV photons (10.2 eV). These aromatic molecules are very similar differing only by the number of nitrogen (heteroatom) present in the ring: 1, 2, and 3, respectively. They

observed that the presence of the heteroatom in the ring leads to a higher photon susceptibility. The proportion of the number of atoms in the ring relative to the number of heteroatoms in molecules studied in this thesis are: pyridine (5), adenine and guanine (2.25), cytosine, uracil and thymine (3). In this case, we have similarities in our experiments; cytosine, uracil and thymine present the same proportion of heteroatoms in their rings and present the same destruction cross sections. Although guanine and adenine have the same proportion of heteroatoms in their rings, we observed that guanine is more radioresistant. It important to point out, that Peeters et al (2003) also exposed adenine and uracil to UV radiation under the same conditions of the experiments performed by Peeters et al. (2005). The destruction cross section of adenine is one order of magnitude smaller than that for pyridine, while the cross section of pyridine has the same value that was reported for uracil. Therefore, the behavior that they reported seems to work for simple molecules with just one type of heteroatom, keeping in mind that nucleobases are a more complex system.

The comparison of the molecular damage provoke by different radiation sources needs to be analyzed with attention because corpuscular and electromagnetic radiation have different mechanism of deposition of energy in the matter. UV photons also interact via electronic excitations like swift heavy ions but also there is differences. A long to the ion track the electrons are stripped by swift ion irradiation. That provokes a high production of secondary electrons and radicals which can diffuse from the ion track and interacts with neighboring molecules, this is known as secondary effects. Furthermore, fast electrons can induce secondary ionizations from the track core.

In the case of the experiment of Peeters et al. (2005), the molecules are in an argon matrix in a proportion of (1:750), the molecules are isolated from each other. The secondary

effects from the exposure to UV field radiation is less probable since the molecules are less abundant and isolated from each other.

To compare the sensibility of the different AHMs to different ionizing agents we calculated the radiation G yield using our results and those available in the literature, see Chapter 2. The radiation G yield in the present case is defined as the number of adenine molecule destroyed per 100 eV absorbed. Table 7.4 displays the radiation G yield and the destruction cross sections for different projectiles. In order to estimate the adenine destruction cross section and the G value for photons of 10.2 eV, we used the results of Guan *et al.*(2010) and Saïagh *et al.* (2014). To calculate the radiation G yield for adenine and uracil in an argon matrix exposed to UV radiation field we assumed that the absorption cross section of these molecules are the same as that reported for those molecules in a thin film Saïagh *et al.* (2014, 2015). This finding clearly shows that even at a low abundance, heavy ions play an important role in the destruction of AHMs due to large value of destruction cross sections. It was impossible to calculate the radiation G yield for solid adenine irradiated with 150 eV photons, because its absorption cross section is unknown. Moreover, the irradiation of adenine by soft X-rays (Pilling et al. 2011) and UV photons (Guan et al. 2010) was performed at room temperature and the radiation damage is dependent on temperature (Fryer et al. 1992; Portugal et al. 2014).

We observe that adenine is less susceptible to radiation than uracil. Note that the radiation G yield of adenine in an argon matrix is one order of magnitude smaller than uracil in the same conditions to UV photons. The purine nucleobases display smaller radiation G yield values than pyrimidines, indeed the radiation G yield of guanine exposed to 190 MeV Ca^{10+} is one order of magnitude smaller in comparison with other nucleobases exposed to the same ion beam.

7.4 New molecules from radiodegradation of AHMs

In chapters 5 and 6, new absorption peaks emerging from the AHMs radiolysis was reported. Since the molecules here are similar and formed essentially by carbon, hydrogen, nitrogen, and oxygen atoms. The role of oxygen in the formation of new molecular species was examined, As an example, guanine ($C_5H_5N_5O$) differs from adenine ($C_5H_5N_5$) by a simple oxygen atom. Pyridine (C_5H_5N) differs with adenine from the number of nitrogen atoms. Cytosine ($C_4H_5N_3O$), uracil ($C_4H_4N_2O_2$) and thymine ($C_5H_6N_2O_2$) differ from each other by the number of carbon and oxygen atoms.

Here it will be discussed the results of adenine irradiation, irradiated at 300 and 12 K

Adenine

Adenine in an argon matrix was exposed to UV radiation, its photolysis produced new IR absorption band at 904, 1092, 1141 cm^{-1}, the two firsts peaks were assigned to HAr^+, the authors were unable to assign any molecule to the later peak. Guan et al. (2010) exposed solid films of adenine to UV photons in the laboratory. They also exposed adenine films directly to the solar winds of Earth's orbit by using the BIOPAN 6 facility, which was set outside the automated Russian science satellite Foton M3. They did not observe any new IR absorption peak emerging from adenine photolysis. Pilling et al. (2011) exposed solid samples of adenine to soft X-rays, they did not observed new IR absorption peaks.

Poch al. (2014) also exposed thin films of complex organic molecules to UV radiation. Among those molecules adenine was also photolyzed for a long time (2.5 days). Their results are in agreement with ours; for example, they observed a new IR absorption band that emerged from the adenine radiolysis. They assigned those absorption peaks to the vibration of isonitrile groups (R-N≡C) and/or nitrile groups (R-C≡N), the stretching of

C=C and C=N. They also observed a new absorption band emerging from adenine degradation between 2165 and 2180 cm^{-1}, they assigned it to formation of OCN^- from the adenine destruction and the residual pollution. Moreover, another indication of the absence of new absorption peaks in the experiments of Guan et al. (2010) and Pilling et al. (2011) is a low susceptibility of adenine to UV photons (Table 7.4). The photon fluence used by Poch et al. (2014) was around 1 order of magnitude higher than that used by Guan et al. (2010) and 4 orders of magnitude higher than that employed by Pilling et al. (2011).

The exposure of adenine to swift heavy ions produced new absorption bands (Fig. 5.11). Some bands could be attributed to molecular species of oxygen. To eliminate this possibility we performed one irradiation at room temperature, where the contamination with the residual gas is too small and can be neglected (Fig. 5.12). Augé et al. (2016) irradiated ices of N_2 and CH_4 at different proportions (90:10) and (98:2) with 44 MeV Ni^{11+} and 160 MeV Ar^{15+} at 14 K. The ice processing produced an IR absorption spectrum very similar to that observed by us after the heavy ion processing of adenine. Figure 7.3 shows the IR absorption spectra of adenine film irradiated by 632 MeV Ni^{24} at a fluence of 4.5×10^{12} ions cm^{-2} and the $N_2 - CH_4$ (90:10) irradiated by 44 MeV Ni^{11+} (54 eV $molecule^{-1}$).

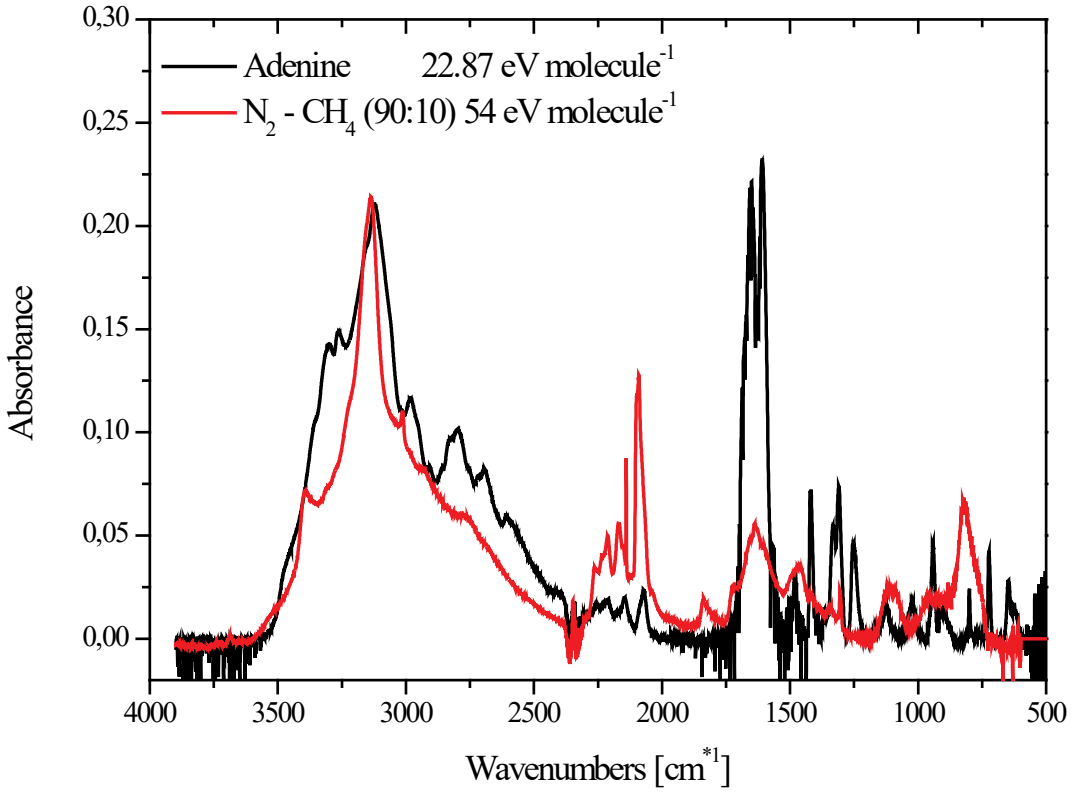

Figure 7.3 – IR spectra of adenine film irradiated by 632 MeV Ni^{24+} at a fluence of 4.5×10^{12} ions cm^{-2} (22.87 eV $molecule^{-1}$) and $N_2 – CH_4$ ice irradiated by 44 MeV Ni^{11+} at a fluence of 3×10^{13} ions cm^{-2} (54 eV $molecule^{-1}$).

Note that adenine is composed by the atoms (CNH) also present in the ices irradiated by Augé et al. (2016). They assigned some of the new absorption peaks to molecules containing oxygen like HNCO and CO. Indeed, the shape of the peak at 2139 cm^{-1} in their spectrum is very similar to that observed in the IR spectrum of CO ice, which means that the oxygen from the residual gas is reacting with the ice during the energetic ion processing. Moreover, they assigned the absorption peak at 2260 cm^{-1} to HNCO. Our experiment at 300 K (Fig. 5.12) strongly suggests that the absorption peak in that region could be due to the presence of nitrile or isonitrile since that at 300 K our set-up does not generate layering at this temperature.

We suggested that the absorption peaks observed through the deconvolution process could be attributed to CH_3CN and $(CH_3)_3CNC$ (Vignoli Muniz et al. 2017). However, if

we adopt the band strength suggest by Moore and Hudson (2003) to nitrile and isonitriles (~10^{18} cm molecule^{-1}), the column density of those molecules would be too high in comparison with the initial adenine column density. Therefore, the responsible for the observed new IR absorption peak are not these molecules or the interaction of these molecules with the residual adenine changes their band strength.

Evans et al. (2011) performed an irradiation of adenine by 5 keV electrons following three different protocols: one pure sample of adenine was exposed to 5 keV electrons from where they determine the destruction cross section, other sample was covered with an oxygen layer (90 nm) before the irradiation, and finally another sample of pure adenine was irradiated and at intermediary fluences they stopped the electron beam, and covered the adenine with an oxygen layer and continued with the electron processing. The irradiation of pure adenine film produced one absorption band at 2235 cm^{-1}, we also observed this absorption peak (Fig. 5.11). The sample covered by oxygen layer before the irradiation did not produced new absorption bands, in this case the oxygen layers were thicker than the electrons penetration depth. Therefore, they observed that the indirect effects on adenine film is small. However, when they covered adenine with oxygen after the beginning of the irradiation the observed a plethora of new IR absorption peaks which can be attributed to oxygen species. That means that the fragments of adenine are very reactive with oxygen, readily forming new molecules.

We performed irradiation of pure adenine and adenine covered with water ice at GSI. We did not observe significant differences between these experiments. We observed the same destruction cross section within error bars and in terms of new absorption peaks we did not observe differences, as said before probably contamination with water from the residual gas in the pure adenine film is possible. However, we safely can state that the new absorption peaks observed are not the same than that reported by Evans et al. (2011)

suggesting that the interaction of the reactive fragments from adenine radiolysis have a completely different behaviour when reacting with oxygen or water.

Guanine

Huang et al. (2014) exposed films of adenine, guanine, cytosine, and thymine to 30 keV Ar^+ and monitored the evolution of the film of nucleobases by IR absorption spectroscopy. They did not observe any new absorption band emerging from the nucleobases radiolysis. Indeed, this is an astonishing result since they observe a disappearance between 16 to 70% of the IR peak areas of different nucleobases.

Adenine and guanine are very similar molecules, differing by a presence of one atom of oxygen in guanine molecule. This allow us to try to probe the role of this one only oxygen atom in the molecule. In this work, we pointed out that guanine was the most radioresistant nucleobase, indeed the radiation G yield of adenine is two times higher than that observed for guanine.

We observe in the IR spectrum of adenine after the irradiation a peak at 1478 cm^{-1} and 2090 and 2100 cm^{-1} these could be assigned to NH_4^+, CN^- and HCN, possibly forming NH_4CN. We do not observe the absorption peak corresponding to NH_4^+ in the IR spectrum of guanine after the heavy ion processing. We observed new absorption peaks which can be attributed to nitrile and isonitriles, with or without oxygen in their composition.

Uracil

Let us now discuss about the formation of new molecules from degradation of pyrimidine nucleobases. Uracil in an argon matrix was exposed to UV photons. Peeters et al. (2003)

reported new absorption peaks at 904, 1092, 1141, 2143, 2345, and 2263 cm^{-1}. The two first peaks were attributed to HAr^+, the peaks at 2143 and 2345 cm^{-1} were assigned as CO and CO_2, respectively. The peak at 2263 cm^{-1} was assigned to HNCO, they were unable to identify the responsible vibrations for the absorption at 1141 cm^{-1}. We also observed formation of CO, CO_2 and possibly HNCO. Moreover, peaks which can be attributed to nitriles and isonitriles, probably also contributed to the formation of CN^- and HCN (2087, 2097 cm^{-1}), OCN^- (2164 cm^{-1}), moreover we observed new absorption peaks at 1656 and 1214 cm^{-1} which can be attributed to vibration of CN.

Thymine

Thymine and uracil are similar molecules, thymine is also known as 5-methyl uracil. Comparing the thymine and cytosine spectra after the energetic ion processing we can try to evaluate the role of the radical CH_3 on the formation of new molecules. After the irradiation thymine presented a large absorption band (Fig. 5.24). Through the deconvolution, we observed almost the same peaks as for uracil. We can probably assign CN^- , CO, nitriles and isonitriles. We observed a big peak at 2342 cm^{-1} which can be attributed to CO_2. Note that we observed a small peak at 2342 cm^{-1} in IR absorption spectrum of uracil after the ion irradiation. Moreover, we observed a peak at 2210 cm^{-1}, whereas in uracil we observed a peak at 2202 cm^{-1}. We also observed in the Thymine degraded IR spectrum an absorption peak at 2297 cm^{-1}, this peak is not present in the degraded IR spectrum of uracil. We also observed at degraded thymine peak which can be attributed to the stretch of C-H such as 1306 cm^{-1} (CH_4) and 1234 cm^{-1} , also an absorption peak at 1712 cm^{-1} (C=O) is observed.

Cytosine

Cytosine presents new absorption peaks in which can be attributed to CO, CO_2, OCN^-. We also observed the presence of the absorption peak at 2296 cm^{-1}. This later peak is also present in the IR absorption spectrum of irradiated thymine. Moreover, absorption peaks at 1720 and 1500 cm^{-1} are observed; H_2CO could be the responsible for these absorption peaks.

Pyridine

Pyridine ice (C_5H_5N) does not have oxygen in its composition, but under our experimental conditions, (see Chapter 6), pyridine was deposited on an ice from the residual gas, and therefore we cannot excluded the formation of oxygen species. Indeed, we observed formation of CO_2. As expected we observed several peaks which can be attributed to C≡C. Note also that the proportion of the absorption peak at 2087 cm^{-1} (CN^-) is much smaller than the that observed in IR spectra of the irradiated nucleobases, this is evident due to the presence of only one nitrogen in pyridine. As already pointed out in Chapter 6, we observed in the IR spectrum of irradiated pyridine structures similar to those observed by Smith et al. (2014) from the proton irradiation of pyridine-CO_2 ices. McMurtry et al. (2016) irradiated pyridine-CO_2 ices with 5 keV electrons, they reported a plethora of new IR absorption band. We observed did not observe the IR absorption band reported by them. They also observed a large absorption band between 1618 and 1578 cm^{-1} and assigned it to o-C_5H_4NCOOH, this molecule presents an IR absorption peak at 1595 cm^{-1} (Lewandowski et al. 2005), we observed trough the deconvolution a peak area at 1590 cm^{-1}.

As previously discussed, all AHMs after energetic swift heavy ion irradiation present a large new absorption peak within the wavenumber range from 2350 to 1900 cm^{-1}. Figure 7.4 presents the new absorption band of AHMs after the irradiation process within this wavenumber region.

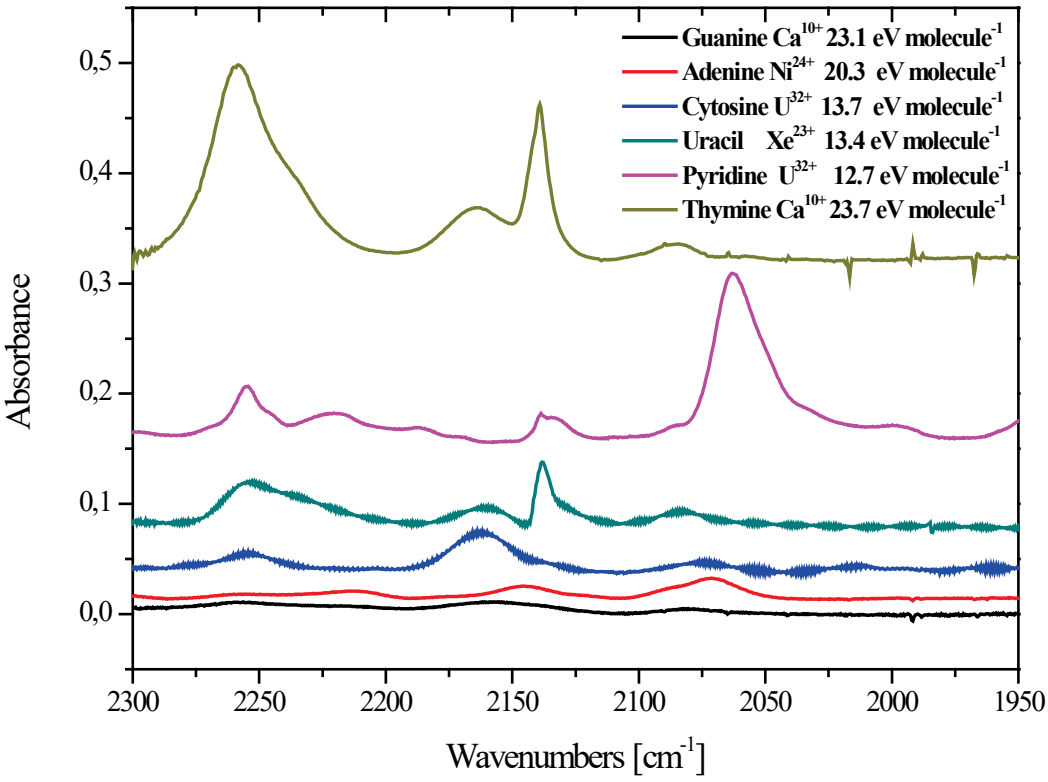

Figure 7.4 – IR spectra within wavenumber range from 2300 to 1950 cm^{-1} of guanine, adenine, cytosine, uracil, pyridine and thymine irradiated by different projectiles. The deposited dose are indicated in the figure.

A word of caution is necessary here. Firstly the deposited doses were not the same for the different AHMs, this can lead to different results. Second, the initial amount of the AHMs molecules are not identical and of course the production of new molecules is proportional to the column density of the mother molecule. It was observed that small molecules under irradiation become more complex. Polymerization also has been proposed after analysis at radioproducts of ices and complex molecules irradiation (Augé et al. 2016; Poch et al. 2014). Therefore, the possibility exists of the formation of a long conjugated system from

the AHMs degradation. However, to confirm this hypothesis new approaches are necessary.

7.5 Astrophysical implications

Currently, rotational spectroscopy is the most accurate technique to detected molecules in outer space. Several theoretical studies have been conducted to determine the rotational transitions of AHMs (Brünken et al. 2006; Ye et al. 2005). The attempt to detected AHMs in outer space were not successful (Peeters et al. 2005; Charnley et al. 2005; Kuan et al. 2003). It should be reminded that there is an intrinsical limitation of the rotational spectroscopy: molecules in condensed phase are very difficult to detect through radiospectroscopy. IR spectroscopy has been used to detected several molecules in outer space. The principle is simple: a neighboring star provides a source of IR light, the light crossing a region of space is absorbed by molecules present in this region, when observed from Earth it is possible to identify the molecules responsible for the observed absorptions. Thus, several molecules have already been detected. However, IR spectroscopy is not the most accurate technique to detect complex molecules in outer space. We already discussed about the complexity of the IR absorption spectrum of complex molecules and their absorption peaks would be overlapped with those of other molecules, and through IR, it is only possible to detect a molecule with a column density above 1×10^{15} cm^{-2}. At last, it is known that the absorption spectrum of nucleobases are dependent of their subtracte (Fornaro et al. 2013): nucleobases adsorbed in different substrates display different spectra than those observed in solid nucleobase film or in KBr pellet.

We can extrapolate our laboratory results to astrophysical environments. This procedure can give us a clue about the possibility of the detection or presence of AHMs within astrophysical environments, where ionizing radiation is omnipresent.

We now first shortly present different astronomical environments, especially in terms of presence of ionizing radiation.

ISM – Interstellar Medium

Interstellar medium comprehends the space among the stars, it has 10 % of the mass of our galaxy, most of it in form of gas (99%) and 1% in the form of submicrometer sized grain particles. The average densities of this region is 1 hydrogen atom per cm^3 and 10^{-11} grains cm^{-3}. The typical temperatures are about 10 K. The composition of the gas consists of 93.38% neutral hydrogen, (6.49%) helium. Oxygen, carbon and nitrogen contribute with 0.11% respectively with proportion of 7:3:1. (Kaiser 2002). The grain cores are formed by silicates and carbonaceous dust, at low temperatures these grains are covered by a mantle formed by simple molecules, notably water, CO and ammonia, PAHs are also expected (Tielens, 2010). Although, the matter and energy in the ISM are not constant and evolves with time, it has been attributed to this region a UV photon flux in the order of 1×10^8 s^{-1} cm^{-2} (Ehrenfreund et al. 2001; Palumbo et al. 2008; Peeters et al. 2003)

DCs – Dense clouds or Giant molecular clouds

In short, clouds are regions of a concentration of gas and dust (Irvine 2011). Usually the definition of different clouds lies in their densities and temperature: diffuse clouds have

a density range of 1 to 1000 cm^{-3}. Composed essentially of hydrogen, their typical temperatures are over 100 K. Dense or molecular clouds are more dense agglomerates of gas and dust with a density over 1000 cm^{-3} and temperatures of about tenths of Kelvin (Cottin et al. 1999). At such low temperatures and at that pressure the gases condensate into grains forming "dirty" ice mantles, the gas phase of a DC consists almost of molecular hydrogen. In these regions, DCs, several molecules were already detected from small molecules such water, CO, and more complex ones such as PAHs (Tieles, 2010). The scattering provoked by the dust shield the core of the DCs against the X-rays and UV photons coming from neighboring stars, but the collision of GCRs with H_2 leads to the production of secondary UV photons. Indeed, secondary UV photons play an important role in these environments but their flux is five orders of magnitude smaller in comparison with the UV flux in the interstellar medium. It was estimated to about 1.4 to 4.8×10^3 UV photons s^{-1} cm^{-2}. (Ehrenfreund et al. 2001; Moore, Hudson, and Gerakines 2001; Palumbo et al. 2008).

Survival of AHMs at astronomical environments

In the beginning of this Chapter we presented the results obtained from our laboratory experiments. Let us extrapolate our findings to astrophysical environments. We use our findings about the adenine destruction cross section to estimate its half-life time when exposed to GCRs. We will also compare the half-life time of adenine exposed to GCRs with the extrapolations previously reported in the literature.

Since the observed power law is only valid in the electronic energy loss regime, we will simulate the electronic stopping power of the ten most abundant ions in GCRs in solid adenine within the energy range of 10^{-1} to 10^3 MeV per nucleon, where the nuclear energy

loss is at least two orders of magnitude smaller than the electronic one. Figure 7.5 displays the electronic stopping power (a) and the destruction cross section as a function of the projectile energy.

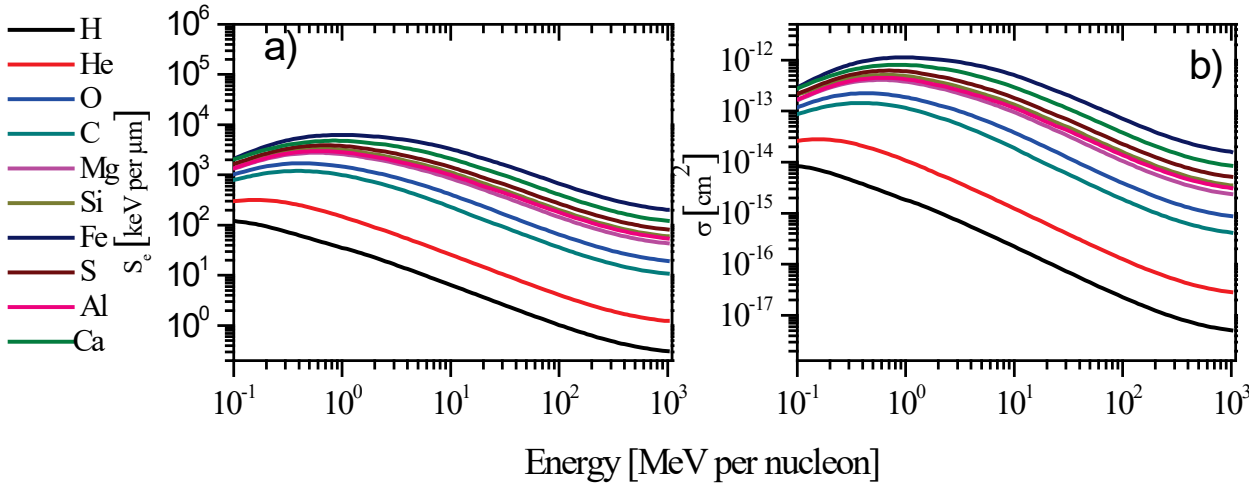

Figure 7.5 – Electronic stopping power of the ten most abundant ions of GCRs in solid adenine (a) and the destruction cross section calculated by our observed power law.

The destruction rate, i.e. the product of the destruction cross section and the flux of cosmic rays ($\sigma\,(Z, E)\,\Phi(Z, E)$) , will determine the survival of adenine exposed to cosmic rays. The half-life time ($\tau_{1/2}$) of adenine exposed to GCRs can be estimated by the following equation

Eq. 7.1 $$\tau_{1/2} = \ln 2\,(4\,\pi\,\sum_Z \int_{10^{-1}}^{10^3} \sigma\,(Z, E)\,\Phi\,(Z, E)\,dE)^{-1}$$

We take into consideration the ten most abundant ions in the GCRs. In order to estimate the destruction rate we will use the equation 2.1 to simulate the spectrum of GCRs. To have a better evaluation of the half-life time we will simulate the flux using three different values (200, 400, and 600 MeV/n) for the parameter E_0. Figure 7.6 shows the destruction rate ($\sigma_d \times \Phi$) as a function of energy for different ions**.**

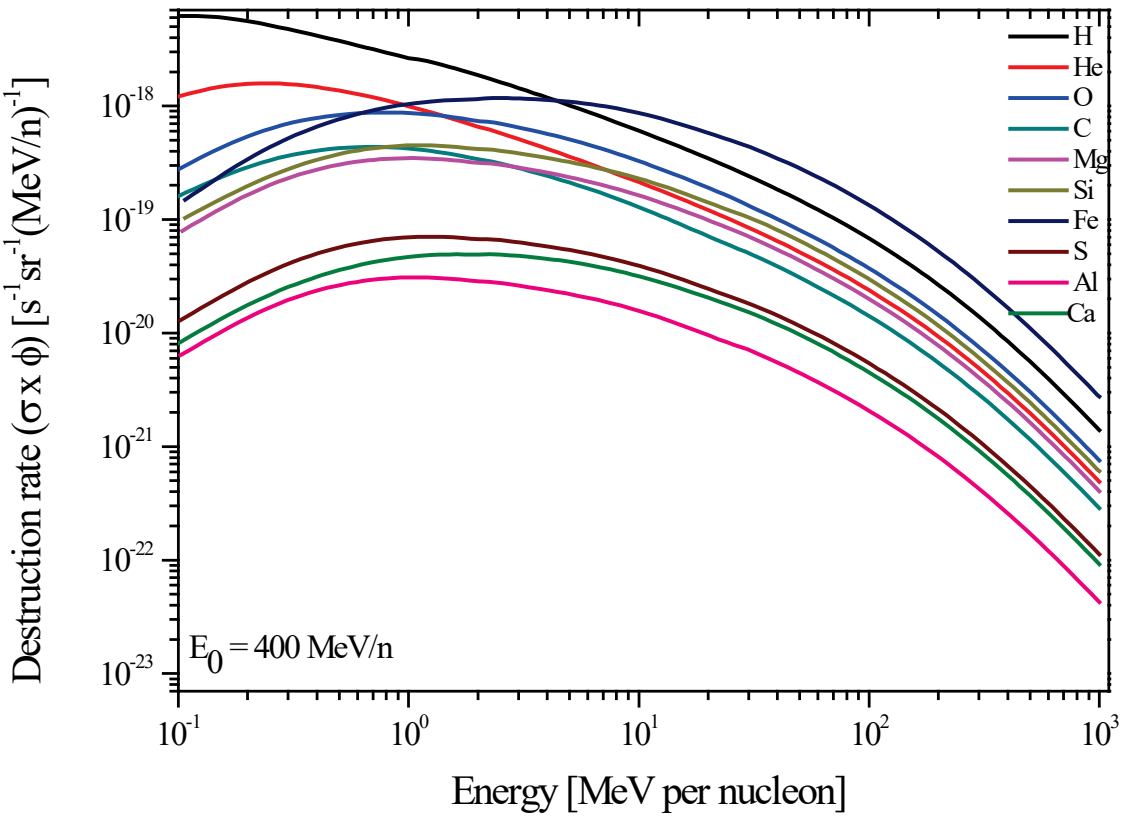

Figure 7.6 – Adenine destruction rate for the ten more abundant ions of GCRs. E_0 = 400 MeV/n.

In Figure 7.6, protons at energies below 1 MeV per nucleon protons are the biggest contributors to adenine destruction, whereas at higher energies, iron becomes the dominant ion to the destruction of adenine. This finding confirms that even at low abundance, about 10^{-4} times less abundant than protons, heavy ions have a key role in the survival of AHMs in ISM. Table 7.5 displays the half-life time of solid adenine exposed to cosmic rays for different values of E_0 in the ISM and the average adenine half-life time.

Table 7.5 - The half-life time of solid adenine exposed to cosmic rays for different values of the parameter E_0 and the average adenine half-live time.

E_0 (MeV/n)	*Half-life time $\tau_{1/2}$ (million years)*
200	1.96
400	10.5
600	29.6
Average adenine half-life time (Myears)	14 ± 11

The half-life time of solid adenine exposed to GCRs are of the same order of magnitude as the half-life time of dense clouds. As discussed by (Peeters et al. 2003) the half-life time of adenine is different within distinct regions of outer space due to UV deterioration. We can estimate the half-life time of adenine exposed to UV photons in ISM and in the core of DCs. It is important to pay particular attention to adenine film and adenine embedded in an argon matrix that exhibit distinct radioresistance. This is probably due to the low penetrability of photons in the matter, the shielding effect due to the first photoproducts and the different forces between the molecules in their neighbourhood. Therefore, we can assume here the half-life time of adenine in a film as a superior limit for the cosmic half-life time. Using the results of Peeters et al.(2003) together with the UV destruction cross section of solid adenine that we calculated by referring to the work of (Guan et al. 2010). We estimated the half-life time of solid adenine exposed to UV photons in the ISM and DC**s**, see Table 7.6.

Table 7.6 – Half-life time of different AHMs under experimental conditions and its extrapolation to astrophysical environments.

Molecule	Half-life time in laboratory [s]	Half-life time in ISM [years]	Half-life time in DCs [years]	Reference
Adenine film	---	4.5×10^5	4.5×10^{10}	Vignoli Muniz e al. 2017; Guan et al. 2010
Adenine in argon matrix	518	8.27×10^1	8.27×10^6	Peeters et al. 2003
Uracil in argon matrix	127	2.03×10^1	2.03×10^6	Peeters et al. 2003
Pyridine in argon matrix	123	1.8×10^1	1.8×10^6	Peeters et al. 2005

It has been proposed that if AHMs exist in outer space, they would most likely be in a condensed phase in ice mantle grains (Chakrabarti et al. 2015; Peeters et al. 2003). As previously discussed, the half-life of adenine exposed to electromagnetic radiation strongly depends on its state (in a film or in a noble gas matrix). However, the extrapolations of the half-life time of adenine in a film and in a matrix for ISM show that adenine would be easily photolyzed much faster than the destruction provoked by GCRs. In contrast, in the core of the DCs, the minimum value for adenine half-life time is 8.26×10^6 years, indeed this time is in the same order of magnitude according to our evaluations (Table 7.5). The half-life of adenine film shows adenine could survive 10^4 years more when exposed to UV flux in ISM and DCs. This also suggests that if AHMs molecules are deep within the ice mantles or inside astronomical ice bodies like comets, these molecules survival rate increased for even longer periods of time. The attenuation of CGRs in the DCs is small, the GCRs can penetrate into the ice mantle. Thus, the half-life time of adenine exposed to GCRs in ISM and DCs is esteemed to be very similar. Moreover, when in the dirty mantle, the AHMs would be in a matrix of different elements,

notably water. Hence, more experiments and studies need to be performed in order to achieve more realistic half-life time for AHMs in these astrophysical environments. Taking into account the destruction cross sections of the nucleobases determined in this theses and the errors in the GCRs flux, the half-life times of solid nucleobases exposed to GCRs will be essentially the same.

REFERENCES

Augé, B., E. Dartois, C. Engrand, J. Duprat, M. Godard, L. Delauche, N. Bardin, et al. 2016. "Irradiation of Nitrogen-Rich Ices by Swift Heavy Ions: Clues for the Formation of Ultracarbonaceous Micrometeorites." *Astronomy & Astrophysics* 592 (August): A99. doi:10.1051/0004-6361/201527650.

Brünken, S., M. C. McCarthy, P. Thaddeus, P. D. Godfrey, and R. D. Brown. 2006. "Improved Line Frequencies for the Nucleic Acid Base Uracil for a Radioastronomical Search." *Astronomy and Astrophysics* 459 (1): 317–20. doi:10.1051/0004-6361:20065777.

Chakrabarti, S. K., L. Majumdar, A. Das, and S. Chakrabarti. 2015. "Search for Interstellar Adenine." *Astrophysics and Space Science* 357 (1). doi:10.1007/s10509-015-2239-1.

Charnley, S. B., Y.-J. Kuan, H.-C. Huang, O. Botta, H. M. Butner, N. Cox, D. Despois, et al. 2005. "Astronomical Searches for Nitrogen Heterocycles." *Advances in Space Research* 36 (2): 137–45. doi:10.1016/j.asr.2005.09.005.

Cottin, H, M.C Gazeau, and F Raulin. 1999. "Cometary Organic Chemistry: A Review from Observations, Numerical and Experimental Simulations." *Planetary and Space Science* 47 (8–9): 1141–62. doi:10.1016/S0032-0633(99)00024-0.

Ehrenfreund, P., M. P. Bernstein, J. P. Dworkin, S. A. Sandford, and L. J. Allamandola. 2001. "The Photostability of Amino Acids in Space." *The Astrophysical Journal* 550 (1): L95–99. doi:10.1086/319491.

Evans, N. L., C. J. Bennett, S. Ullrich, and R. I. Kaiser. 2011a. "On the interaction of adenine with ionizing radiation: mechanistical studies and astrobiological implications." *The Astrophysical Journal* 730 (2): 69. doi:10.1088/0004-637X/730/2/69.

Fornaro, T., J. R. Brucato, E. Pace, M. C. Guidi, S. Branciamore, and A. Pucci. 2013. "Infrared Spectral Investigations of UV Irradiated Nucleobases Adsorbed on Mineral Surfaces." *Icarus* 226 (1): 1068–85. doi:10.1016/j.icarus.2013.07.024.

Fryer, J.R., C.H. McConnell, F. Zemlin, and D.L. Dorset. 1992. "Effect of Temperature on Radiation Damage to Aromatic Organic Molecules." *Ultramicroscopy* 40 (2): 163–69. doi:10.1016/0304-3991(92)90057-Q.

Guan, Y. Y., N. Fray, P. Coll, F. Macari, D. Chaput, F. Raulin, and H. Cottin. 2010. "UVolution: Compared Photochemistry of Prebiotic Organic Compounds in Low Earth Orbit and in the Laboratory." *Planetary and Space Science* 58 (10): 1327–46. doi:10.1016/j.pss.2010.05.017.

Huang, Q., X. Su, G. Yao, Y. Lu, Z. Ke, J. Liu, Y. Wu, and Z. Yu. 2014. "Quantitative Assessment of the Ion-Beam Irradiation Induced Direct Damage of Nucleic Acid Bases through FTIR Spectroscopy." *Nuclear Instruments and Methods in Physics Research Section B: Beam Interactions with Materials and Atoms* 330 (July): 47–54. doi:10.1016/j.nimb.2014.03.012.

Irvine, W. M. 2011. "Dense Clouds." In *Encyclopedia of Astrobiology*, edited by Muriel Gargaud, Ricardo Amils, José Cernicharo Quintanilla, Henderson James Cleaves, William M. Irvine, Daniele L. Pinti, and Michel Viso, 419–419. Berlin, Heidelberg: Springer Berlin Heidelberg. doi:10.1007/978-3-642-11274-4_409.

Kaiser, R. I. 2002. "Experimental Investigation on the Formation of Carbon-Bearing Molecules in the Interstellar Medium via Neutral−Neutral Reactions." *Chemical Reviews* 102 (5): 1309–58. doi:10.1021/cr970004v.

Kuan, Y.-J., C.-H. Yan, S. B. Charnley, Z. Kisiel, P. Ehrenfreund, and H.-C. Huang. 2003. "A Search for Interstellar Pyrimidine." *Monthly Notices of the Royal Astronomical Society* 345 (2): 650–56. doi:10.1046/j.1365-8711.2003.06975.x.

Lewandowski, W., G. Świderski, R. Świslocka, S. Wojtulewski, and P. Koczoń. 2005. "Spectroscopic (Raman, FT-IR and NMR) and Theoretical Study of Alkali Metal Picolinates." *Journal of Physical Organic Chemistry* 18 (9): 918–28. doi:10.1002/poc.918.

McMurtry, B. M., A. M. Turner, S. E.J. Saito, and R. I. Kaiser. 2016. "On the Formation of Niacin (Vitamin B3) and Pyridine Carboxylic Acids in Interstellar Model Ices." *Chemical Physics* 472 (June): 173–84. doi:10.1016/j.chemphys.2016.03.010.

Moore, M.H., and R.L. Hudson. 2003. "Infrared Study of Ion-Irradiated N_2-Dominated Ices Relevant to Triton and Pluto: Formation of HCN and HNC." *Icarus* 161 (2): 486–500. doi:10.1016/S0019-1035(02)00037-4.

Moore, M.H, R.L Hudson, and P.A Gerakines. 2001. "Mid- and Far-Infrared Spectroscopic Studies of the Influence of Temperature, Ultraviolet Photolysis and Ion Irradiation on Cosmic-Type Ices." *Spectrochimica Acta Part A: Molecular and Biomolecular Spectroscopy* 57 (4): 843–58. doi:10.1016/S1386-1425(00)00448-0.

Palumbo, M E, G A Baratta, D Fulvio, M Garozzo, O Gomis, G Leto, F Spinella, and G Strazzulla. 2008. "Ion Irradiation of Astrophysical Ices." *Journal of Physics: Conference Series* 101 (February): 012002. doi:10.1088/1742-6596/101/1/012002.

Peeters, Z., O. Botta, S. B. Charnley, Z. Kisiel, Y.-J. Kuan, and P. Ehrenfreund. 2005. "Formation and Photostability of N-Heterocycles in Space: I. The Effect of Nitrogen on the Photostability of Small Aromatic Molecules." *Astronomy and Astrophysics* 433 (2): 583–90. doi:10.1051/0004-6361:20042443.

Peeters, Z., O. Botta, S. B. Charnley, R. Ruiterkamp, and P. Ehrenfreund. 2003a. "The Astrobiology of Nucleobases." *The Astrophysical Journal* 593 (2): L129–32. doi:10.1086/378346.

Pilling, S., D. P. P. Andrade, E. M. do Nascimento, R. R. T. Marinho, H. M. Boechat-Roberty, L. H. de Coutinho, G. G. B. de Souza, et al. 2011. “Photostability of Gas- and Solid-Phase Biomolecules within Dense Molecular Clouds due to Soft X-Rays: Photostability of Biomolecules in ISM.” *Monthly Notices of the Royal Astronomical Society* 411 (4): 2214–22. doi:10.1111/j.1365-2966.2010.17840.x.

Poch, O., S. Kaci, F. Stalport, C. Szopa, and P. Coll. 2014. “Laboratory Insights into the Chemical and Kinetic Evolution of Several Organic Molecules under Simulated Mars Surface UV Radiation Conditions.” *Icarus* 242 (November): 50–63. doi:10.1016/j.icarus.2014.07.014.

Polewski, Krzysztof, David Zinger, John Trunk, and John C. Sutherland. 2011. “Ultraviolet Absorption and Luminescence of Matrix-Isolated Adenine.” *Radiation Physics and Chemistry* 80 (10): 1092–98. doi:10.1016/j.radphyschem.2011.02.007.

Portugal, W., S. Pilling, P. Boduch, H. Rothard, and D. P. P. Andrade. 2014. “Radiolysis of Amino Acids by Heavy and Energetic Cosmic Ray Analogues in Simulated Space Environments: -Glycine Zwitterion Form.” *Monthly Notices of the Royal Astronomical Society* 441 (4): 3209–25. doi:10.1093/mnras/stu656.

Saïagh, K., M. Cloix, N. Fray, and H. Cottin. 2014. “VUV and Mid-UV Photoabsorption Cross Sections of Thin Films of Adenine: Application on Its Photochemistry in the Solar System.” *Planetary and Space Science* 90 (January): 90–99. doi:10.1016/j.pss.2013.11.002.

Saïagh, K., H. Cottin, A. Aleian, and N. Fray. 2015. “VUV and Mid-UV Photoabsorption Cross Sections of Thin Films of Guanine and Uracil: Application on Their Photochemistry in the Solar System” 15. doi:10.1089/ast.2014.1196.

Smith, K. E., M. P. Callahan, P. A. Gerakines, J. P. Dworkin, and C. H. House. 2014. "Investigation of Pyridine Carboxylic Acids in CM2 Carbonaceous Chondrites: Potential Precursor Molecules for Ancient Coenzymes." *Geochimica et Cosmochimica Acta* 136 (July): 1–12. doi:10.1016/j.gca.2014.04.001.

Tielens, A. G. G. M, and Cambridge University Press. 2010. *The Physics and Chemistry of the Interstellar Medium*. Cambridge, UK; New York: Cambridge University Press.

Vignoli Muniz, G. S., C. F. Mejía, R. Martinez, B. Auge, H. Rothard, A. Domaracka, and P. Boduch. 2017. "Radioresistance of Adenine to Cosmic Rays." *Astrobiology* 17 (4): 298–308. doi:10.1089/ast.2016.1488.

Ye, E., R. P.A. Bettens, F. C. De Lucia, D. T. Petkie, and S. Albert. 2005. "Millimeter and Submillimeter Wave Rotational Spectrum of Pyridine in the Ground and Excited Vibrational States." *Journal of Molecular Spectroscopy* 232 (1): 61–65. doi:10.1016/j.jms.2005.02.004.

Ziegler, J. F., M. D. Ziegler, and J. P. Biersack. n.d. *SRIM 2012. Www.srim.com*.

Chapter 8 - Conclusion & Outlook

In this thesis, we presented a study of the evolution of AHMs at low temperature under heavy ion irradiation. Using beam lines of GANIL and GSI we exposed solid samples of different AHMs to different projectiles within the energy loss range from 10^3 to 10^4 keV μm^{-1}. The solid nucleobases samples were prepared using two different methods: drops of nucleobase solutions were applied directly onto ZnSe windows. Afterwards, the windows were heated to 100ºC until to the entire evaporation of the solvent, thus obtaining a solid sample. These samples are referred to as "grainy" because of their grainy aspect under optical microscopy. Due to low solubility of guanine in water or ethanol. Uniform "films" of nucleobases were prepare by the sublimation of nucleobase powders in a vacuum by heating with subsequent condensation of the molecules onto a ZnSe window.

Profilometry experiments were performed to determine the thickness of our cytosine film and combined with the results of IR absorption spectroscopy we establish a liner law between the thicknesses of cytosine film samples and their χ band area, in the form: $d = (3.2 \pm 0.4) \times 10^{-3} X$ [μm]. From this we also addressed a value for the band strength of χ band: $A_\chi = (8.5 \pm 0.5) \times 10^{-16}$ cm molecule^{-1}.

The film samples under irradiation first displayed an increase in the area of the IR absorption spectra, this effect was correlated with the film compaction, later inducing a change in the band strength in the order of 10%. Moreover, compaction was not observed in the "grainy" samples.

Upon our first approach, we observed that the evolution of the AHMs under swift heavy ion irradiation depends upon the deposited energy. However, more experiments under controlled conditions are required to confirm this.

A temperature dependence of adenine destruction cross section was also observed. From the results published it seems that organic molecules irradiated by heavy and light projectiles display different temperature dependences.

Our results suggest a destruction cross sections of the AHMs exposed to swift heavy ions in the following order:

$$\sigma_d^{pyridine} \approx \sigma_d^{guanine} < \sigma_d^{adenine} < \sigma_d^{thymine} \approx \sigma_d^{uracil}\ \sigma_d^{cytosine} .$$

Adenine and cytosine destruction cross sections follow the power law $\sim S_e^n$, n = (1.24 ± 0.01) and (1.31 ±0.08), respectively. We did not observe any differences of destruction cross sections nor find any formation of new molecular species from pure adenine and adenine covered with a thin water ice layer. This also suggests that the effects of sputtering is a minor.

From the AHMs radiolysis, we observed new IR absorption bands and peaks. These peaks can be attributed to vibrations of N≡C, C≡N, C≡C. There is a possibility of the formation of conjugated systems, but further experiments applying different techniques would be necessary to identify the radioproducts.

We used the observed power law to estimate the lifetime of adenine exposed to GCRs as (14 ± 11) Myears. In ISM adenine would be quickly destroyed by UV radiation field. This suggests that the detection of nucleobases in ISM is improbable. Inside the core of DCs the UV decreases by five orders of magnitude increasing the damaging effects of GCRs. Moreover, adenine in a noble gas matrix and in a solid film exhibit distinct

radiosensibility. This also suggests that if AHMs are within the inner layer of ice mantles or inside cold bodies the effects of UV would be strongly attenuated. According to our results, adenine inside DCs exhibits a half-life comparable with the lifetime of these environments favoring its survival.

Outlook

We observed a temperature dependence in the destruction of adenine when exposed to swift heavy ions. This temperature dependence remains unclear: from the literature, it seems that organic molecules at low temperatures present a high resistance to light projectiles. Surprisingly, we observed an inverse behavior for heavy ion irradiation: at low temperature, adenine was more sensitive to radiation when exposed to 632 MeV Ni^{24+}. More experiments with light and heavy projectiles under the same experimental conditions and protocol are necessary to resolve this question and determine the destruction cross section as a function of the temperature and the electronic stopping power.

We also observed formation of new molecules from AHMs radiolysis. Due to the intrinsic limitation of FTIR it was not possible to accurately analyse them. Therefore, different approaches are required to identify the radioproducts. UV-vis absorption spectroscopy and chromatography would be suggested techniques that would enable the identification of these new molecular species in the residue left from the irradiation of AHMs.

The irradiation of solid samples of AHMs give us a clue to the survival of these molecules in astronomical environments. Note of course that we do not except these molecules to be present as “grainy” or “thin film” in outer space. In fact, it is expected that they are in

a matrix of different elements, especially water. Therefore, the irradiation of AHMs in a water matrix would be a natural evolution of this work. Moreover, since PAHs have been proposed to be an important source of carbon in space, it would be very interesting to study their radioresistance in water matrix of different proportions.

It was also presented for the first time the mass spectrum of secondary emission from pyridine ice irradiated by 90 keV O^{6+}. We also studied the evolution of pyridine ice under swift heavy ion irradiation using FTIR. TOF-SIMS are complementary techniques and provide information from the sputtered ionic species and the modification of molecules in bulk. It would be important to study the evolution of the pyridine ice irradiate by the same ion beam using these two techniques. In our experiments, we employed ions in different energy loss domains. Moreover, TOF-SIMS can provide information about secondary ion emission using QCM, we would be able to determine the total sputtering, neutral and ionic species.

We followed the evolution of AHMs under irradiation using IR absorption spectroscopy, enabling us to determine the apparent destruction cross section, quantity. This provides information about the sputtering yield and molecular destruction. From our experiments it seems that the sputtering is a minor effect. To quantify and be certain about this, it would be very interesting to exploit the QCM and TOF-SMS in future experiments.

Appendix

Appx. 1 - Relative abundance and normalization constant of the several constituent of the galactic cosmic rays. Adapted from Portugal et al. 2014

Elements	Relative abundance to 10^6 H atoms	C(Z)
H	10^6	9.42×10^4
He	$10^{4.8}$	5.94×10^3
O	$10^{3.5}$	297.9
C	$10^{3.4}$	236.3
Mg	$10^{2.8}$	59.4
Si	$10^{2.8}$	59.4
Fe	$10^{2.8}$	59.4
S	$10^{1.9}$	7.5
Al	$10^{1.7}$	4.7
Ca	$10^{1.6}$	3.8

Appx. 2 - Relative intensities of the absorption peaks of grainy and film adenine samples

Adenine Grainy position [cm^{-1}]	Adenine Grainy (I/I_{max})	Adenine Film Position [cm^{-1}]	Adenine Film (I/I_{max})
Region 3600 - 2000		Region 3600 - 2000	
		3480	0.05
3347	0.27	3432	0.39
3293	0.42	3130	1.00
3117	1.00	2985	0.56
2977	0.70	2799	0.54
2793	0.69	2691	0.46
2685	0.67	2597	0.46
2598	0.55		
Region 1800-800		Region 1800-800	
1668	0.78	1672	0.69
1600	1.00	1603	1.00
1417	0.41	1419	0.40
1367	0.18	1367	0.13
1332	0.32	1333	0.24
1308	0.51	1309	0.41
1251	0.35	1253	0.23
1126	0.14	1126	0.07
1020	0.12	1020	0.05
939	0.47	723	0.15
912	0.34		
873	0.13		
848	0.17		
796	0.19		
723	0.31		

Appx. 3 - Intensity proportion of absorption peaks of grainy and film cytosine samples

Cytosine Grainy position [cm^{-1}]	Cytosine Grainy (I/I_{max})	Cytosine Film Position [cm^{-1}]	Cytosine Film (I/I_{max})
Region 3600 - 2000		Region 3600 – 2000	
3381	0.45	3381	1.00
3346	0.41	3349	0.46
3170	1.00	3173	0.80
2840	0.44	2843	0.32
2793	0.56	2794	0.40
2687	0.55	2688	0.33
Region 1800-700		Region 1800-800	
1703	0.34		
1660	1.00	1658	0.92
1614	0.48	1627	1.00
1539	0.54	1615	0.70
1508	0.52	1538	0.34
1469	0.42	1504	0.32
1366	0.34	1461	0.82
1277	0.75	1363	0.29
1242	0.18	1276	0.48
1154	0.09	1235	0.36
1106	0.03	1157	0.06
1011	012	1100	0.03
997	0.10	1010	0.036
967	0.16	993	0.12
820	0.29	961	0.04
793	0.47	793	0.13
781	0.56	781	0.08
762	0.19	703	0.03
700	0.15		

Appx. 4 - Relative Intensities of absorption peaks of grainy and film thymine samples

Thymine Grainy position [cm^{-1}]	Thymine Grainy (I/I_{max})	Thymine Film Position [cm^{-1}]	Thymine Film (I/I_{max})
Region 3600 - 2000		Region 3600 – 2000	
3169	0.61	3170	0.61
3062	1.00	3063	1.00
3025	0.92	3029	0.94
2962	0.87	2963	0.71
2892	0.7	2932	0.61
2810	0.56	2896	0.51
Region 1800-800		2815	0.41
1758	0.35	1758	0.57
1676	1.00	1691	0.96
1495	0.07	1676	1.00
1453	0.24	1495	0.07
1445	0.35	1455	0.29
1428	0.19	1424	0.13
1383	0.10	1384	0.03
1245	0.26	1244	0.17
1203	0.34	1209	0.28
1046	0.06	1049	0.014
1029	0.13	1024	0.06
981	0.11	984	0.03
936	0.18	935	0.09
836	0.31	838	0.28
815	0.32	815	0.26
759	0.31	760	034
744	0.14	745	0.11

Appx. 5 - Cytosine band strength for selected absorption peaks

Absorption peak [cm^{-1}]	Band strength [$\times 10^{-17}$ cm $molecule^{-1}$]
1726-1566	9.6
1566-1476	1.8
1462	1.9
1364	0.78
1278	6.2
1233	0.99
792	0.32

Appx. 6 - Apparent destruction cross section of adenine for selected peak areas at 12 K.

Absorption band (cm^{-1})	*Vibration*	*Xe Apparent destruction cross section ($x10^{-14}$ cm^2) Se=1.1×10^4 keV.μm^{-1}*	*Kr Apparent destruction cross section ($x10^{-14}$ cm^2) Se = 5.8×10^3 keV.μm^{-1}*	*Ca Apparent destruction cross section ($x10^{-14}$ cm^2) Se=3.1×10^3 keV.μm^{-1}*	*Ni Apparent destruction cross section ($x10^{-14}$ cm^2) Se=3.4×10^3 keV.μm^{-1}*	*C Apparent destruction cross section ($x10^{-14}$ cm^2) Se=1.0×10^3 keV.μm^{-1}*
724	C6N1, C2N3 – R(6) Breathing	139 ± 6	62 ± 2	24 ± 2		8.9 ± 0.5
797*	C6N10 – R(6) – Wagging	75 ± 6	----------	30 ± 2		6.6 ± 0.3
848	C8H – R(5) – Wagging	150 ± 50	150 ± 10	45 ± 4		11.1 ± 0.5
886	NCN –R(6) – Deformation	139 ± 4	130 ± 3	43 ± 1		10.1 ± 0.6
914	NCN- R(5) – Deformation	222 ± 3	109 ± 2	45 ± 1	52 ± 1	12.4 ± 0.6
940	C2H – R(6) – Wagging	132 ± 5	57 ± 2	21.9 ± 0.6	31 ± 4	6.13 ± 0.02
1025	NH2 – R(6) – Rock	101 ± 4	47 ± 9	19 ± 2		5.6 ± 0.4
1128	CN – R(5) – Stretch	148 ± 7	75 ± 2	29 ± 2		8.0 ± 0.6
1162		182 ± 7	100 ± 4	56 ± 4		15 ± 2
1255	C8H – in plane deformation CN R(5) Stretch	84 ± 4	37.2 ± 0.8	8.4 ± 0.4		4.4 ± 0.1
1309	CN – R(6) – Stretch	135 ± 7	49.4 ± 0.3	24.5 ± 0.9	37 ± 1	7.3 ± 0.1
1335	CN – R(5) – Stretch	116 ± 7	64.6 ± 0.5	25 ± 1		8.5 ± 0.2
1369	C6N10 – Stretch	190 ± 10	99 ± 1	51 ± 1	69 ± 2	14 ± 1
1420	C2H – in plane deformation	98 ± 5	33 ± 1	24.6 ± 0.5	22.8 ± 0.3	6.4 ± 0.2

1457	CC – R(6) – Stretch	270 ± 20	8	----------		9.6 ± 0.9
1503	CN – R(5) Stretch	96 ± 3	----------	----------		IR absorption intensity too weak
1605	CN – R(6) – Stretch CC – R(6) – Stretch	114 ± 5	32 ± 1	6.5 ±0.2	33.2 ± 0.3	8.7 ± 0.3
Part of alpha band**		141.9 ± 0.7	73 ± 4	28.3 ± 0.3	30.9 ± 0.3	6.1 ± 0.1
Average		140.7	78.5	31.0	38	8.7